Tribocorrosion and Tribochemistry of Cobalt-Chromium Alloy used for Total Hip Replacement

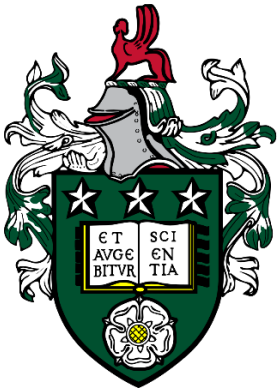

By

Mohamad Taufiqurrakhman

Submitted in accordance with the requirements for degree of

Doctor of Philosophy

School of Mechanical Engineering

University of Leeds, UK

August 2021

The candidate confirms that the work submitted is his own, except where work which has formed part of jointly authored publications has been included. The contribution of the candidate and other co-authors in published work from this thesis has been clearly indicated. The candidate confirms that appropriate credit has been given within the thesis where reference has been made to the work of others.

In the papers contributing to this thesis, the candidate (first author) carried out all the experiments, analysis and preparation of the manuscripts. All other authors contributed by proof reading and providing insight for the discussions.

Papers contributing to this study:

Published

- Taufiqurrakhman M, Bryant M, Neville A. Tribofilms on CoCrMo alloys: Understanding the role of the lubricant. Biotribology. 2019:100104. (The manuscript [1] is part of Chapter 5 in this thesis)

Submitted

- Taufiqurrakhman M, Neville A, Bryant M. The effect of protein structure and concentration on tribocorrosion and film formation on CoCrMo alloys. Bio- and Tribo-Corrosion Journal (submitted: 2021). (The manuscript is part of Chapter 7 in this thesis)

Under preparation

- Taufiqurrakhman M, Bryant M, Neville A. Applied electrochemical potential effect on the tribocorrosion of CoCrMo alloy in organic-containing environment. (The manuscript is part of Chapter 6 in this thesis)
- Taufiqurrakhman M, Thornley B, Beadling A, Neville A, Bryant M. The role of dissolved metal ions on tribocorrosion and surface chemistry at CoCrMo alloys. (The manuscript is part of Chapter 8 in this thesis)

Acknowledgements

In the Name of Allah SWT, the Most Gracious & the Most Merciful, who blessed me with the patience and strength to this point and beyond. Prayers and peace to be devoted to Prophet Muhammad SAW.

First of all, I would like to express my appreciation and gratitude to my PhD supervisor, Dr Michael G. Bryant, for his valuable guidance, cooperation and motivation. Thanks for your friendly guidance and kindness, knowledge and patience every time I collected my writing report. An honourable mention given to my former supervisor, Professor Anne Neville, for accepting me as her student in the first place and giving me more self-confident and idea of how broad the tribology research area can be. For me, both of you have always been the good mentor who I look up to as inspirational researcher. It was privileged to work with both of you.

I would like to express gratitude to Indonesia Endowment Fund for Education (LPDP) for accepting me as a doctorate scholarships awardee.

Special thanks to Prof. David Barton and all IFS colleagues: Fiona and Judith, the technicians' team (Jordan, Mick, Paul, Ryan), research fellows (Rob, Chun, Abimbola, Siavash, Waleed, Amir, M Alkhateeb), Bio-Tribology research group, PhD Office 3.32a, especially Blake, Frank and Asmawi for your supports and always being my best friends. Also, for all supports given from all Indonesian people in the UK: KIBAR Leeds, PPI Leeds, Grup Makan-Makan, Tahsin Leeds, especially Mas Farid, Mas Hizbul, Mas Edo, Mas Fathiro, Mas Emye, Fahri, Kak Teguh, Ranggi and Syihan. Thank you for being my family in Leeds.

Most importantly, I would say uncounted thank to my beloved parents (Ayah Dwi Sutriarga and Ibu Syahminda Lusia Suhro) and my brother, Dr Mohamad Lutfi Ramadhan. Thank you Ayah, Ibu and Dede for your tireless prayers, longing and supports, giving me a chance to achieve my dreams, pursuing PhD degree in the UK. Also, for all prayers and supports given from my beloved family-in-law (Bapak Henry, Ibu Anni and Naufal), as well as the Suhrowirdi and Margono's big families.

Finally, I would like to thank my beloved wife, Ridani Faulika. Thank you for being with me, going all the way to the other side of the world, being away from your family and friends, leaving all your dreams that you might have had back then, so we can be together. Thank you so much for your prayers, patience, unwavering supports and loving encouragements whenever I am feeling down. Dear my 'forever best friend', you are essential to my life and to everything we accomplish. I am and will always be proud of you!

Abstract

Cobalt-based metallic biomaterials are mostly employed as bearing materials for Total Hip Replacement (THR) owing to their high strength, their biocompatibility, as well as their wear and fatigue resistance. Cobalt-chromium-molybdenum (CoCrMo) alloys also have excellent passivity characteristics as an oxide layer can form on the surface spontaneously, reducing corrosion. Nevertheless, mechanical interaction, such as friction and wear, can damage the passive oxide layer and also causes metal products used in such replacements to be released into the human body. The repeated removal of the oxide layer due to joint articulation leads to wear and corrosion; a process termed 'tribocorrosion'.

Due to the complex working environment, as well as the presence of organic elements or species, there remains a lack of knowledge regarding tribocorrosion and the surface film mechanisms. An understanding upon these mechanisms is important since studies have reported that the tribochemical film, a complex metal-protein compound, can enhance the surface protection towards tribocorrosive processes. However, the behaviour is still debatable depending on the working conditions (e.g. temperature, pH, contact load and organic species in the lubricant).

The fundamental mechanisms of wear and corrosion are recognised to solve the longevity problem of the orthopaedic implants. Tribocorrosion and tribochemistry of CoCrMo alloys were investigated in various conditions. A reciprocating tribometer, electrochemical cells and surface analysis techniques were employed to observe the tribocorrosive behaviour of CoCrMo samples tested in protein-containing electrolytes. Conditions were applied to investigate various protein-metal interactions regarding behaviour in the tribocorrosion process: (a) in a range of electrochemical potential, (b) with different organic species, (c) protein conditions and (d) with the addition of metal ions in the bulk electrolytes. Results highlighted that a tribocorrosion and tribochemical reactions occurred during sliding are sensitive to the electrolyte composition. These findings contribute to the pre-clinical understanding of protein-metal interactions occurring in tribofilms' formation and the system variables effect on the metallic bearing surfaces.

Table of Contents

List of Figures

List of Tables

Nomenclature

Terms	Definition	Unit
λ	Lambda ratio	-
$\boldsymbol{\alpha}$	Level of significance for ANOVA test	-
A	Active/exposed area	cm^2
at%	Atomic percentage of element	%
$\boldsymbol{\beta_a}$ and $\boldsymbol{\beta_c}$	Tafel constants	mV/decade
CPE	Constant phase element	
C	Pure capacitance in EIS	
$\mathbf{C_0}$	Pure corrosion (not with wear product)	μm^3
$\Delta\mathbf{C_w}$	Wear-enhanced corrosion loss	μm^3
d	Film thickness	nm
$\mathbf{E_{corr}}$	Free-corrosion potential	V
$\mathbf{E_b}$	Breakdown potential	V
$\boldsymbol{\varepsilon}$	Relative dielectric constant of layer	-
$\boldsymbol{\varepsilon_0}$	Permittivity of the vacuum	F/cm
F	Faraday's constant	C/mol
$\mathbf{f_0}$	Characteristic frequency at the maximum imaginary part of the impedance	Hz
$\mathbf{I_{corr}}$	Corrosion current density	$\mu A/cm^2$
$\mathbf{I_T/I_0}$	Raman intensity ratio	-
m	Mass	gram
M	Atomic mass	gram
n	Valence number	-
$\mathbf{P_{mean}}$	Mean Hertzian contact pressure	MPa

$\mathbf{P_{max}}$	Max. Hertzian contact pressure	MPa
$\boldsymbol{\rho}$	Density	g/cm
$\boldsymbol{\rho_0}$	Resistivity of the oxide film/metal surface interface	
Q	Total charge transfer	mC
$\mathbf{R_a}$	Roughness average (RMS)	nm
$\mathbf{R_p}$	Polarisation resistance	Ω
R	Resistance	Ω
$\mathbf{R_s}$	Solution resistance	Ω
$\mathbf{R_{out}}$	Outer layer resistance	Ω
SWR	Archard's specific wear rate	$\mu m^3/N.m$
$\Delta \mathbf{S}$	Sliding run distance	m
t	Time	s
V	Volume	μm^3
$\mathbf{V_{total}}$	Total of volume loss	μm^3
$\mathbf{V_C}$	Corrosion volume loss	μm^3
$\mathbf{V_W}$	Wear volume loss	μm^3
W	Constant normal load	N
$\mathbf{W_0}$	Pure wear (not with corrosion product)	μm^3
$\Delta \mathbf{W_c}$	Corrosion-enhanced wear loss	μm^3
Z	Impedance	$k\Omega.cm^2$

Chapter 1
Introduction

1.1 Motivation

Total Hip Replacement (THR) is a common type of joint surgery, where the natural hip joint is replaced by a prosthesis (implant) [2]. THR has been known as one of the most successful surgical inventions since the early 1960s for the treatment of osteoarthritis; a development which has been through several stages of design and material improvements to date. The purpose of a THR is to restore function and relieve pain when the natural joint becomes damaged or worn. Many conditions can cause the need for hip replacement surgery, such as osteoarthritis, rheumatoid arthritis, septic arthritis, hip fracture and bone dysplasia (unusual bone growth).

The number of procedures for hip replacement has increased in the last 15 years and is expected to keep growing, affecting around 0.20% of the world population per year. On average, the rate of hip replacement increased by 30% between 2000 and 2015 [3]. Over 450,000 hip replacements are carried out in the United States each year [4]. The National Joint Registry (NJR) shows the increasing trend for primary hip procedures in the United Kingdom since 2004 [5]. The NJR data show that more than 90,000 primary hip procedures have been performed annually over the last four years. Despite the estimated period being 15 years of use, an average of 7% of the implanted hip prostheses needs to have their first revision within ten years after the primary hip surgery. The revision surgery shows that the THRs have a shorter use period than expected, a situation which results in a significant increase in costs. Indeed, the chosen materials involved in a THR may well be a major cause of the increased revision rates for hip replacement, as set out above.

Metallic-based alloys are the most common material used for THR, other than polymers and ceramics. The first generation of MoM (Metal-on-Metal) THR configuration was proposed in the 1950s; however, that early generation demonstrated several short-comings, including early loosening failure, limited

design and inefficient manufacturing capabilities at that time. The second generation of MoM, which included large diameter bearings and hip resurfacing, was reintroduced in the 1990s as an alternative model to address the issues associated with polymer wear debris in MoP models (Metal-on-Polymer was introduced in the 1980s) [6]. The second-generation design promised a low rate of aseptic loosening and volumetric wear and was reliable for use with young patients.

However, the problems associated with the early failures and increasing rates of adverse tissue reactions by the released metal ions and debris from the large bearing diameter have attracted press attention and become a matter for concern for both experts and patients. The suitability of such metallic implants was being questioned; thus, several products have been recalled from the market and withdrawn from use. Since 2008, the MoM bearing surfaces turned out to have higher revision rates compared to those of MoPs [5]. Metal products have been associated with adverse reactions, causing deterioration in the bone and tissue around the hip, pseudo tumour, metallosis and other biological infections [7]. Several government authorities have applied guidelines to assist general practitioners, patients and surgeons to monitor the use of the metal-coupled bearings, especially MoM, for hip replacements. As reported by the NJR (Figure 1.1), the number of MoM THRs has decreased drastically since 2009 in the UK. Nevertheless, MoM hip resurfacing and other metallic-coupled bearings (e.g., Metal-on-Polymer (MoP), Ceramic-on-Metal (CoM)) and dual mobility bearings (Ceramic-on-Polymer-on-Metal and Metal-on-Polymer-on-Metal) are still being implanted today, as reported by NJR. These procedures also have a developing risk associated with a patient's body's adverse reaction to the introduction of metal debris.

Since the issues of implant-derived debris, tribology and corrosion of THR have been brought to the fore in the last decade, burgeoning research activities designed to understand the degradation mechanisms associated with THR have been undertaken. These activities mainly consist of tribology and/or corrosion studies attempting to understand the mechanisms of cobalt-chromium-molybdenum (CoCrMo) degradation. Some authors have recently suggested that the success of load-bearing CoCrMo implants is, in part, due to the tribochemical reactions at the surface during sliding [8-11]. Tribochemical reactions resulting from high contact pressure during asperity sliding are hypothesised to result in graphitic carbon

layers and are attributed to the low friction and low wear processes seen in MoM articulations [12, 13]. Whilst it is generally agreed that the presence of proteins and other organic species plays a vital role in reducing the wear and corrosion of CoCrMo, the exact mechanisms in this regard are not yet fully understood. This thesis therefore aims to address this knowledge gap.

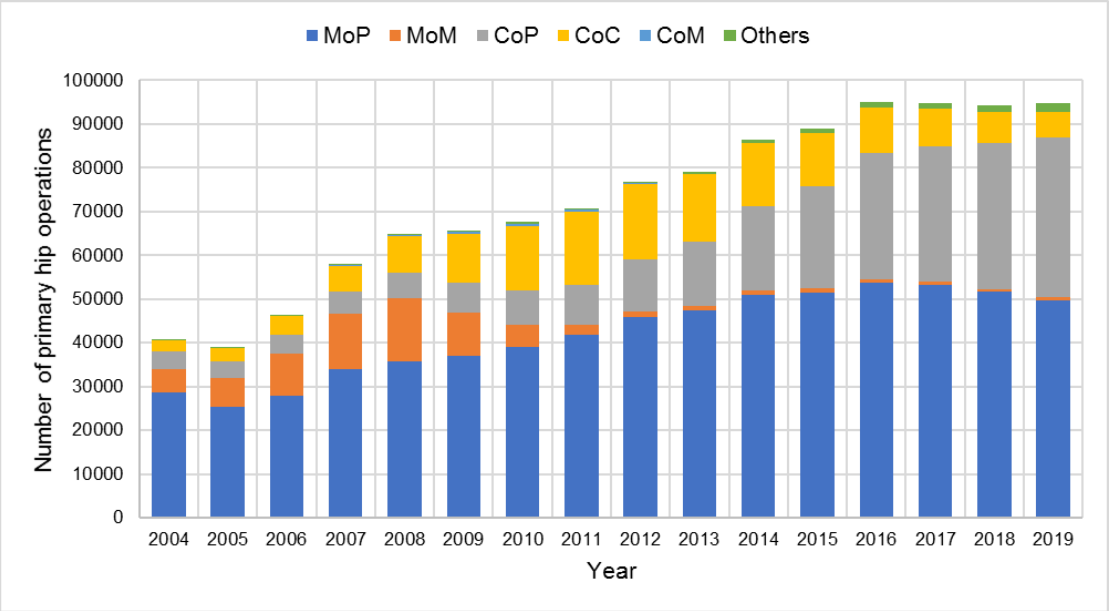

Figure 1.1 Trends in primary hip replacements by bearing materials in England and Wales (2004 - 2019) from NJR 17th Annual Report 2020 [5]

It is essential to manage critical factors, such as the hip bearing design, wear and corrosion phenomena, and interacting biological species, which cause material degradation associated with THR. In this study, one of the most commonly used metallic materials (CoCrMo alloy) is employed as a primary specimen. MoM is indeed the main motive due to its major issues associated with the increasing rates of adverse reactions by the released metal products. However, even though MoM is no longer used, the CoCrMo alloy is still used for implant components, such as the femoral stem and head. This study is also relevant to other situations, where at least one metallic component in hip prosthesis works at the tribological interface. The material degradation mechanisms are still largely unknown due to the complex environment and biological species present inside the human body. Therefore, this

knowledge gap motivated this study to explore factors related to the process of metallic degradation and how it affects prosthesis longevity.

1.2 Outline

- **Chapter 1**: Introduces the research motivation and general structure of the overall study.
- **Chapter 2**: A literature review of recent studies related to tribology-corrosion and metal-protein interactions and surface chemistry in biomedical applications to identify any research gaps.
- **Chapter 3**: States the research hypothesis, aim and objectives to be addressed, extracted from the literature.
- **Chapter 4**: Presents the experimental methodology and analytical techniques to answer all of the research questions.
- **Chapter 5**: Presents the experimental results and discussion related to tribochemistry and tribocorrosion synergistic behaviour at the CoCrMo surface in the organic-containing environments. Parts of Chapter 5 have been published in an original manuscript/paper [1] prior to this thesis's submission.
- **Chapter 6**: Presents the experimental results and discussions to observe the effect of electrochemical potentials on tribochemistry and tribocorrosive behaviour at the CoCrMo samples. This section follows up and has a similar testing condition as Chapter 5.
- **Chapter 7**: Presents the experimental results and discussion to understand the effect of protein structure and concentration on tribocorrosion and surface chemistry.
- **Chapter 8**: Presents the experimental results and discussion to investigate the effect of dissolved metal ions on tribocorrosion and surface chemistry. This section has a similar testing condition as Chapter 7.

In each result chapter (**Chapter 5-8)**, sub-chapters cover the objective, specific testing protocol, results, brief discussion and chapter summary. These sub-chapters allow the reader to understand in depth each chapter's findings before continuing to the general discussion section.

- **Chapter 9**: An overall discussion highlighting the main findings throughout this study, along with a comparison of recent clinical and experimental studies.
- **Chapter 10**: Summarises the overall conclusions and offers suggestions regarding future study.

Chapter 2
Literature Review

2.1 Introduction to the Literature Review

The literature review chapter aims to introduce total hip replacements, including the biomaterials, natural hip joint as the design inspiration, THRs' history and development and emerging issues. In this chapter, the fundamental sciences of tribology and corrosion are explored. The background of the interaction between the tribology and corrosion processes (tribocorrosion), as well as the protein species and metallic surface, are introduced. Furthermore, related *in vitro* studies were discussed to establish the state-of-the-art regarding tribocorrosion and surface chemistry of the hip joint environment. At the end, the literature review is summarised to identify the gaps and objectives in the current study.

2.2 Biomaterials of the THRs

A material which can be suitable while operating inside the living organism is called a biomaterial [14]. Besides being used for THRs, biomaterials have been widely utilised for other applications, e.g., tissue recovery, drug storage and medical and surgical instruments. This sub-section discusses the biomaterials specifically in the THRs' device.

2.2.1 Metal Biomaterials

Metallic-based materials are widely used for THRs' components. The metals and their alloys have a high elastic modulus, yield strength and reliable ductility. Therefore, metals are suitable for handling the load-bearing nature in the human body. Hip joint replacement commonly uses three metal alloys options; i.e. iron-based, titanium-based and cobalt-based alloys [15, 16].

2.2.1.1 Iron-based Alloys

Stainless steel is one of the iron-based alloys. In 1925, Marius Smith-Petersen and Philip Wiles employed stainless steel to create the first THR fitted to bone by using bolt and screw components [17, 18]. There are many different types of stainless steel, depending on the alloying composition and properties. ASTM F138 has standardised the type of stainless steel used for surgical applications [19].

Nowadays, stainless steel alloys are still employed in various medical applications. Stainless steel 316L, for example, is a comparatively ductile, robust material that is easy to manufacture and low-cost [20]. Stainless steel 316L contains chromium, nickel and molybdenum elements, and the 'L' means a lower carbon concentration. The chromium (Cr) is alloyed due to its ability to generate a passive oxide film for corrosion resistance. High nitrogen stainless steel (HNSS) is also commonly used for biomedical devices. The addition of nitrogen is useful for improving fatigue strength and corrosion resistance. The nitrogen can stabilise the passive oxide film by increasing the local pH level and performing a re-passivation process [21, 22]. However, stainless steel is susceptible to fretting or crevice corrosion while the passive film is removed. Therefore, the performance of high corrosion and bio-corrosion has limited the use of stainless steel in the prosthesis material.

2.2.1.2 Titanium-based Alloys

Ti-based alloys are employed for implant devices due to their outstanding mechanical properties, static corrosion resistance and osteointegration [23]. However, titanium alloys have a lower modulus elasticity, as well as poor wear and tribocorrosion properties [24]. One of the most widely-used Ti-based alloys for biomedical devices is Ti-6Al-4V.

Nevertheless, Ti-based alloys are unsuitable for use as femoral head material due to their inadequate self-mating ability [25]. The debris from their surface was also found to affect the local tissue by blackening the tissue surface. Furthermore, the titanium stems are mechanically unstable while fixing in the cement scuff, which can cause the failure of an implant [23, 24, 26].

2.2.1.3 Cobalt-based Alloys

As mentioned earlier, McKee-Farrar designed the first generation of MoM bearings using the cast cobalt-chromium alloys [27]. The cobalt alloy was also employed in the Charnley's 'low-friction arthroplasty' MoP bearings for its femoral stem and head [28]. Cobalt-based alloys are suitable for use in hip joint replacement since they have a high elastic modulus (220 GPa) and hardness (40-50 HRC), especially for articulating bearing surfaces [29].

There are various cobalt alloy composition types, but cobalt-chromium-molybdenum (CoCrMo) is commonly used for implant devices. The addition of chromium (Cr) aims to increase the corrosion resistance by its passive oxide film in the form of chromium oxides (Cr_2O_3) [30]. CoCrMo is usually categorised into high-carbon (C>0.15%), with more hardness, and low-carbon (C<0.15%) alloys [13]. The cobalt-chromium alloys have good wear resistance and toughness, owing to their microstructural composition of dispersed hard particles (Cr_7C_3) in a cobalt-rich (Co>50%) solid solution of Face Centered Cubic (FCC) matrix alloys' structure. Also, the properties are determined by the carbide morphology and volume fraction [31]. Cobalt alloys' strength relies upon the carbides' precipitation along the grain boundaries. Other metal elements are also added into the cobalt alloys to strengthen the solid solution and carbide formation, which also enhances the level of corrosion resistance [32].

However, these alloys are rarely used for a femoral stem body since their high elastic modulus can have stress-shielding consequences [33]. Cobalt-based alloys also have a comparatively low stacking fault strength. Therefore, they can be vulnerable to cut off slip and transform its FCC packing structure into a Hexagonal Close Packed (HCP) structure due to a strain induced-transformation [34]. Since it is also one of the metallic surfaces, cobalt alloys result in corrosion and metal ion removal while rubbing.

This particular study uses Co-28Cr-6Mo alloys as the primary specimen for the experiments and is analysed after testing. The specification of Co-28Cr-6Mo alloy is shown in Table 2.1 and typically used for biomedical implants, such as spinal, hip bone and toe. This alloy class offers excellent mechanical properties, such as strength, hardness and corrosion and temperature resistance [29]. The CoCrMo

alloy fulfils the requirements of ISO 5832-4 [35], ISO 5832-12 [36], or ASTM F75 [37] precisely for alloys in implant applications.

Table 2.1 Material specification of CoCrMo alloys [29]

Physical and Chemical Properties				
Relative Density with Standard Parameters		approx. 100% (8.29 g/cm^3)		
Material Composition		Co 60-65 wt%	Si max 1 wt%	C max 0.16 wt%
		Cr 26-30 wt%	Mn max 1 wt%	Ni max 0.1 wt%
		Mo 5-7 wt%	Fe max 0.75 wt%	
Mechanical Properties at 20°C				
Ultimate Tensile Strength (MPIF 10)	horizontal direction (XY)	1300 MPa ± 50 MPa		
	vertical direction (Z)	1150 MPa ± 50 MPa		
Yield Strength (Rp 0.2%)	horizontal direction (XY)	980 MPa ± 50 MPa		
	vertical direction (Z)	880 MPa ± 50 MPa		
Elongation at Break	horizontal direction (XY)	11% ± 2%		
	vertical direction (Z)	9% ± 1%		
	after HIPping	21-24%		
Young's Modulus	horizontal direction (XY)	220 GPa ± 20 MPa		
	vertical direction (Z)	220 GPa ± 20 MPa		
Fatigue Life*	in vertical direction (Z) at 0-400	approx. 7.2 million cycles		
MPa load range and 20 Hz				
Hardness (DIN EN ISO 6508-1)		40-45 HRC		
Surface Roughness	after shot-peening	approx. R_a 10 µm		
	after polishing	R_z up to < 1 µm		
Thermal Properties				
Coefficient of Thermal Expansion		over 20-500°C	over 500-1000°C	
		13.6 x 10^{-4} m/m°C	15.1 x 10^{-4} m/m°C	
Thermal Conductivity		at 20°C | 13 W/m°C	at 500°C | 22 W/m°C	
		at 300°C | 18 W/m°C	at 1000°C | 33 W/m°C	
Maxioumum Operating Temperature		1150°C		
Melting Range		1350-1430°C		

2.2.2 Ceramic Biomaterials

Ceramics are well known for their hardness, low coefficient of friction, high wear resistance and good biocompatibility [38]. Several ceramics are commonly employed for hip prosthesis, e.g. alumina, zirconia, silicon nitride and zirconia-toughened alumina (ZTA) [39]. Boutin designed the hip joint replacement using alumina (Al_2O_3) in 1972, known as one of the first uses of ceramic materials for hip bearings [40]. Several studies have proven that the combination of ceramics produces less wear debris than when coupled with metal bearing in the articulating hip joint [41-46]. Thus, the ceramic bearing is still used to date, even coupled with other hard and soft materials.

However, several failures were reported by patients who used ceramic bearings in the 1970s. These cases reported an *in vivo* fracture of the ceramic bearings due to

their inadequate toughness and strength [38]. Since then, ceramic materials have been developed. The properties of alumina ceramics were also improved through increasing their density and bending strength, as well as an average grain size reduction [47]. ZTA ceramic is one of the latest generation of alumina ceramics which is employed in implant devices. ZTA consists of 82% alumina and 17% zirconia nano-particles in volume. The zirconia nano-particle can increase the toughness and inhibit crack propagation on the subsurface [47, 48].

This study uses an alumina ball as a counter-sliding against an CoCrMo alloy plate in a wear test. The use of an alumina ball aims to localise the corrosion only at the metallic specimen for experimental and analysis purposes.

2.3 Natural Hip Joints

The hip is one of the largest and highest loaded joints within the human body. It consists of a spherical ball and socket joint, connecting the leg bone to the bottom of the upper body [49]. The hip joint operation is of a complicated, challenging nature for biomechanics. Therefore, it is crucial to understand fully the anatomy of the natural hip joint regarding its mechanical functions and realistic boundary conditions before designing a hip replacement, as well as its kinematics and kinetics aspects.

2.3.1 Hip Joint Anatomy

The natural hip design facilitates standing, walking and performing other lower body movements to support human activities [50]. As seen in Figure 2.2, the hip structure can be divided into the pelvis, acetabulum and femur sections [51]. The pelvis has the acetabulum as a socket for the joint. The acetabulum socket is a large cavity, lined with the articular cartilage as a cover for the femur section. The femur is known as the longest, heaviest bone in the human body [51]. There is a femoral head at the top, with two-thirds of the spherical shape covered by cartilage. The femur neck connects the head and main bone with an inclination of approximately 125°. The femur is attached by ligaments, membranes, muscles and shells of bone.

A synovial membrane is also attached to the femur head, which encloses the hip joint.

The range of motion and loading depends on human activity. However, the hip joint's motion and loading will influence the quality of articulating movement between the acetabulum socket and femur section. The synovial membrane produces synovial joint fluid which lubricates the cartilage and reduces the degree of friction during movement. However, the cartilage interfaces are critically exposed by a tribological condition during activity, so the worn cartilage surface needs to be restored by an implant. Arthritis is the most common reason for severe hip pain and disability, e.g. osteoarthritis, rheumatoid arthritis, post-traumatic arthritis and osteonecrosis [52]. Figure 2.1 shows a comparison of a normal hip joint with one affected by hip osteoarthritis.

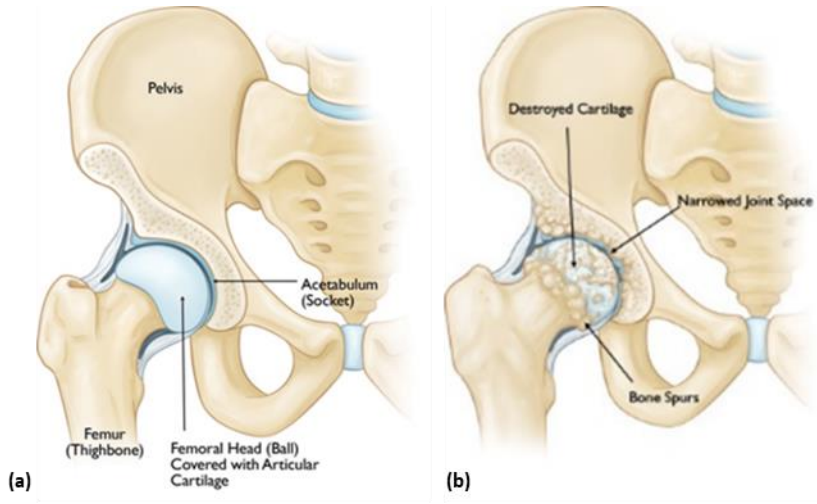

Figure 2.1 Natural hip joint in the (a) healthy condition and (b) with osteoarthritis (reproduced with permission from OrthoInfo. © American Academy of Orthopaedic Surgeons. https://orthoinfo.org/ [52])

2.3.2 Synovial Joint Fluid

Synovial fluid is a thick, stringy fluid within the articulating joint that offers lubrication and reduces friction. This fluid acts as a medium for transporting nutritional substances to the articulating cartilage in the human body, e.g. protein, glucose and uric acid [53]. Since the joint movement is considered a tribological

condition, the synovial joint fluid operates as a natural lubricant between the rubbing surfaces. The synovial fluid has a higher viscosity than the other body fluids produced by the plasma since it contains a high concentration of hyaluronic acid. It consists mainly of proteins, hyaluronic acid, lubricin, collagenases and other proteinaceous or organic substances.

The physical characteristics in a normal condition are listed in Table 2.2. In several studies, synovial fluid has been replicated using a protein serum solution, e.g. foetal bovine serum and bovine calf serum [9, 54]. This solution was assumed to act as a mimic since it contains similar characteristics regarding the protein amount and other chemical properties.

Table 2.2 Characteristics of normal synovial joint fluid [53]

Normal appearances	clear, pale yellow, viscid, and does not clot
Amount	thin film covering surfaces of synovium and cartilage within joint space
Cell count	< 200/mm^3; less than 25% are neutrophils
Protein	1.3-1.7 g/dl (20% of normal plasma protein)
Glucose	within 20 mg/dl of the serum glucose level
Salts	Calcium: 1.2–2.4, Chloride: 87–138, Potassium: 3.5–3.5 and Sodium: 133–139 mmol/L
Temperature	32˚ Celsius (peripheral joints are cooler than core body temperature)
pH	7.4

During surgery, the synovial membrane regenerates and produces a similar liquid characteristic of natural synovial fluid, termed pseudo-synovial fluid. However, several studies have demonstrated that pseudo-synovial fluid has a different lubrication mechanism compared to natural synovial fluid. Therefore, it is important to investigate the effect on hip bearing performance of each biological species contained in the pseudo-synovial fluid. A study found that different protein types in biological electrolyte will display a different protein adsorption behaviour regarding the bearing surfaces, thereby affecting the bearing lubricity [55]. The

proteins could interact with and adsorb to the surfaces, producing a protective tribochemical film on the bearing surface [8, 56]. It is essential to investigate the interaction of physiological species, such as proteins and salts by undertaking a pre-clinical observation since they play a different role in the hip implant.

2.4 Total Hip Replacements (THRs)

Joint replacement is among the most common types of joint surgery, where the original joint is replaced by an implant device or prosthesis [2]. The procedure involves the replacement of the natural joint with an artificial implantation device. Several types of prosthesis can be implanted into the human body; e.g., the knee, hip, ankle and shoulder. These devices can restore function and relieve pain when the natural joint is damaged, worn, or affected by disease.

2.4.1 THRs Development Timeline

A total hip replacement is inspired by the natural hip joint, constructed by a femoral stem, head and acetabular sections. Glück designed the earliest THR in the 1890s, with a carved ivory ball secured by nickel screws on a socket joint. Several experiments followed this first design to improve THR by employing other material combinations [27]. Figure 2.2 illustrates the conventional design of a THR and how it appears while attached.

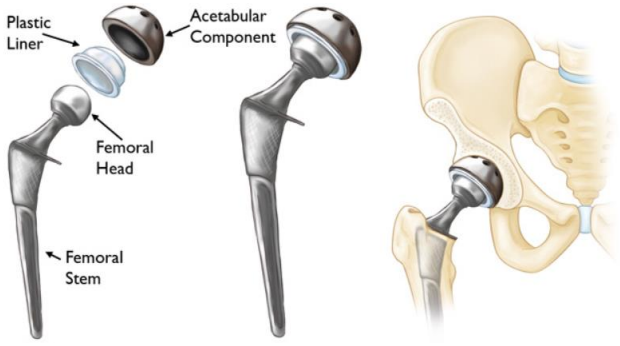

Figure 2.2 The components of a total hip replacement (reproduced with permission from OrthoInfo. © American Academy of Orthopaedic Surgeons. https://orthoinfo.org/ [52])

The THRs with a modular interface consist of the femoral stem, head and acetabular sections. The femoral stem is fixed by inserting it into the leg bone, either cementless or using conventional bone cement as the fixation technique. The femoral head can be inserted to the femoral stem by a Morse taper fitting. A fit taper is also used to fit the two components of the acetabular part; i.e., the acetabular shell and liner. The acetabular shell is fixed to the upper bone. The shell holds the liner part when articulating against the femoral head during walking.

The modular THRs design is beneficial for surgical treatment as it makes it possible to adjust the components to fit better and be more aligned to the user [57, 58]. The femoral head is fitted and can move within an acetabular part, operating in sliding contact. Thus, the contacting femoral head and acetabular cup usually attract attention in the tribological research. The combination of materials can be varied for different behaviour. Total hip replacement has evolved in terms of the materials, shapes and components. There are still many studies that try to improve the system to offer better biocompatibility and longevity.

2.4.1.1 First Generation of Metal-on-Metal (MoM)

In the 1950s, McKee-Farrar designed the first generation of Metal-on-Metal (MoM) bearings with stainless-steel [59]. This was then replaced by the cobalt-based alloy (e.g. CoCrMo alloy) which has better wear resistance [60]. The McKee-Farrar design comprised acetabular parts for the bearing and the fixation using dental cement material. However, McKee-Farrar MoM have been associated with a high early failure rate, showing a 90% success rate during only four years of follow-up [59]. The main reason for the failures was the loosening of the bearing components during articulation. Also, there were concerns about the metal toxicity from the wear debris and high friction in the MoM bearing [61, 62].

2.4.1.2 Metal-on-Polymer (MoP)

In the 1960s, Charnley developed a new bearing configuration of Metal-on-Polymer (MoP) [63]. The Charnley's THR was known as Low Friction Arthroplasty (LFA), consisting of a stainless-steel femoral stem and head and a Polytetrafluoroethylene (PTFE) acetabular cup. The prosthesis modular design has remained mainly

unchanged until today and is believed to be a gold standard for THRs bearing. However, the size and volume of wear from the polymer acetabular cup still limit the implant's longevity to around three years. The increase in the number of younger and more active patients triggered many studies seeking to decrease the polymer wear volume. Since then, the polymer has been upgraded the Ultra-High-Molecular-Weight-Polyethylene (UHMWPE) with a new cross-linking technique [64, 65]. Studies show that the micron-scale of polymer debris can negatively affect the human body, such as provoking an immune response, osteolysis and macrophagic stimulations [46, 60, 65, 66]. As an alternative, there is also the soft-on-hard bearing couple; i.e., CoP (Ceramic-on-Polymer). A ceramic (alumina or zirconia) femoral head is coupled with a acetabular cup made of UHMWPE. The ceramic surfaces in CoP are more rigid and smoother than the metal in MoP, resulting in the reduced wear debris size of the polymer acetabular cup [60, 67].

2.4.1.3 Ceramic-on-Ceramic (CoC)

Boutin designed the hip implant by coupling Ceramic-on-Ceramic (CoC) in the 1970s [60, 68]. Although this was popular initially in Europe, the CoC THRs have been associated with a system failure due to fracture and fixation issues [68]. Thus, the CoC prosthesis was improved by employing high purity alumina with smaller grain sizes in the 1990s [60]. The THRs with CoC bearings are beneficial not only due to their hardness and low roughness [69-71], but also their excellently low wear rate compared with the MoM and MoP designs [60, 68, 69]. Their wear debris is also in nanometre sizes [67, 69] and considerably less biologically sensitive than polymer debris [67, 72]. However, apart from all of these advantages, there are still concerns about using CoC implants long-term. The risk of fracture and a squeaking noise at the contact bearings has not been totally eliminated [73]. Grain pull-out and stripe wear have also been found on the ceramic surfaces [68, 74].

2.4.1.4 MoM Hip Resurfacing

Hip resurfacing is designed to attach at the bone leg without any femoral stem. In the 1990s, Derek McMinn removed the traditional stem and replaced it with a small stem component at the bottom of the femoral head [75]. The aim was to only trim

and cover the original femoral head instead of removing it while implanting, make it easier to revise, decrease the risk of hip dislocation and facilitate more normal walking pattern. This prosthesis is called the Birmingham Hip Resurfacing (BHR) device (Figure 2.3). The BHR design showed good initial success rates for surgical treatment [76]. These BHR devices were targeted to suit younger, more active patients, offering easier revision if needed than the traditional method [77]. Due to its MoM configuration, hip resurfacing also showed a higher revision rate than the other bearing combinations. However, the revision rates are still lower than the traditional THRs design due to the smaller contact interface [78, 79].

Figure 2.3 The McMinn or Birmingham Hip Resurfacing device [76]

2.4.1.5 Second Generation of MoM

MoM prostheses were reintroduced as the second generation, with a new design, in the late of 1990s. Previously, the first generation of MoM had fallen out of favour in the 1970s due to concerns about metal ion generation and the associated carcinogenic risk, hypersensitivity reaction and aseptic loosening [80]. The prosthetic loosening and early failures are now thought to have been caused by the poor design and implantation method used in the first generation MoM, rather than the first MoM bearing itself. The second generation MoM has been reported to produce wear 60 times less compared to the expected rate of MoP implant [81]. The metal femoral head, owing to its less brittle properties compared with other biomaterial, can be made with a larger diameter in order to increase joint stability and decrease the chance of dislocation [82]. This MoM configuration was also known to address peri-prosthetic inflammatory tissue and osteolysis from polymer

debris [83]. However, several reports indicated that an elevated level of cobalt and chromium ion was found in the bloodstream [81]. Since many younger patients are now using MoM prostheses, concerns have arisen about the long-term risk of developing metal ions exposure to biological adverse reactions.

2.4.2 Major Issues and Current Trends

The trend of the bearing material used in primary hip procedures over the last 15 years are shown in Figure 1.1. The second generation of MoM bearings was one of the most widely used hip replacements in the early and mid-2000s. This bearing couple was believed to offer a solution to the polymer debris issue. Midland Medical Technologies (MMT), in 1997, was the earliest company in the UK to bring the MoM to the market. The company was later bought by the UK firm Smith & Nephew in 2004. DePuy Synthes Companies also launched its version of the MoM implant on the market in 2003. The MoM succeeded in Europe after laboratory and simulator testing, rather than conducting clinical trials on people [84].

However, some national joint registries in 2007, e.g., the National Joint Registry (NJR UK) and Australian Orthopaedic Association, claimed that the MoM had twice the revision risk and led to more follow-up procedures compared with using other bearing materials. In 2010, the Depuy company recalled its hip implant with the MoM bearing from the market after several reports and urgent needs for revised surgery among patients. The primary reason for the MoM's failure was due to the femoral ball's rotation with the acetabular cup. The articulating surfaces produce wear and high levels of cobalt and chromium ions in the blood, found in users with the large diameter bearing. Furthermore, several registries mention infection, dislocation, metal sensitivity, and the loosening and fracture of the hip implant as a range of specific diagnoses. Since the MoM implants had higher than anticipated failure levels, many companies recalled their hip implant models or pulled them from the market [85]. Figure 2.4 displays the trend of the bearings used in 2019 in the UK.

Nowadays, MoP and CoP are the main bearing materials used for the hip implant. Figure 2.4 shows that nearly 50,000 MoP bearings were implanted in 2019, even though the material is coupled with a metallic surface. Some experts are also

concerned that the MoP bearings can release metal debris from the metallic stem or head. Although the MoM is no longer commonly used worldwide, there are still plenty of patients who have these implants fitted. MoM hip resurfacing and other metallic-coupled bearings are even being implanted nowadays, as reported by NJR [5]. They must also have the potential to be affected by the corrosion products that may be released after years of use.

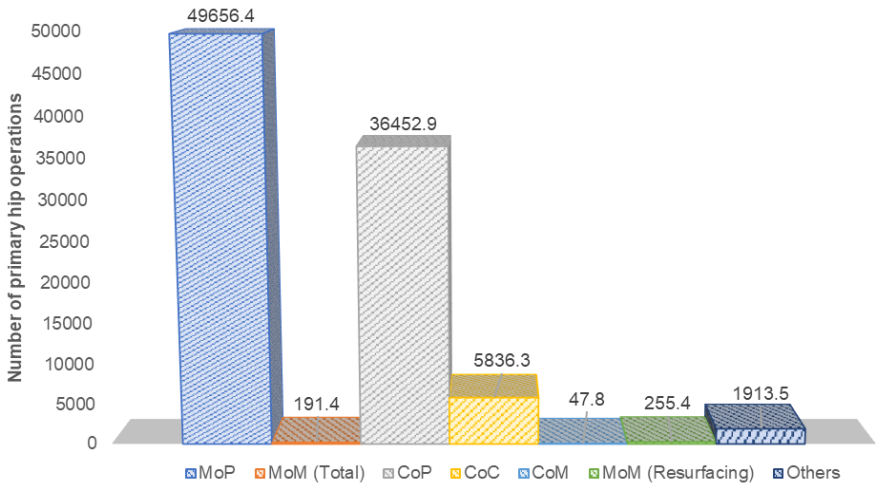

Figure 2.4 Trends in primary hip replacements by bearing materials in England and Wales during 2019 from NJR 17th Annual Report 2020 [5]

2.4.3 Biocompatibility of Metallic Implants

Joint replacement has been acknowledged to be an outstandingly reliable treatment to restore a damaged natural joint's function. However, these devices still need further development due to limited long-term implantation and the potential need for revision surgery. The complication related to the implants is the deterioration of their components, resulting in debris release and the patient's biological reaction. Therefore, the biocompatibility of the used material is questioned.

A material with good biocompatibility will disrupt the normal body function with the minimum effect. In general, biocompatibility in implant biomaterial is influenced by several factors; e.g., implant shape, size, material alloy composition, surface roughness, wettability and charge [86]. On the other hand, the biological environment should not result in the degradation of the biomaterial, e.g., by mechanical, biological or corrosion mechanisms, which reduce the implant

properties. There is no biomaterial which can completely avoid exerting a negative effect on the biological environment. However, each material has its own level of inertness.

This sub-chapter will review the biocompatibility aspect of the metallic implant. A metallic implant can produce metal ions that can damage the human body [87-89]. Hence, metal biocompatibility has been doubted and needs to be controlled. The adverse tissue reactions associated with the metallic implant material found by the clinical assessment are reviewed.

2.4.3.1 Current Understanding of the Role of Metallic Ions

Metal ion release from implanted biomaterials and metal alloys in the human body are crucial issues for implant device users and the industry. The metal alloys made for several typical implants, such as hip, knee and dental implants, can degrade over time, with the metal ions dissolving into the bodily fluids and human tissue [90, 91]. Some alerts about metallic-based hip bearings, both Metal-on-Metal and Metal-on-Polymer, have been issued and studied due to the adverse effect of metallic products (ion and debris particles) related to cobalt and titanium alloys surfaces. Studies also obtained higher failure rates than expected for metal hip replacements, associated with the metal particle and ion release from those alloys [92, 93].

The metallic implants can degrade due to two main mechanisms; mechanical wear enhanced corrosion (tribocorrosion, fretting corrosion and corrosion fatigue) and electrochemical corrosion (crevice, active, galvanic corrosions, and passive dissolution) [94]. Passive metal types, such as CoCrMo alloys, spontaneously generate a passive oxide layer as its secondary reaction. Therefore, the layer dissolves through the corrosion mechanism called passive dissolution [95, 96]. The surrounding cell can also react to the nano- and micron-sized wear particles, generating an oxidising environment. Therefore, the metal debris can release more metallic ions.

Cobalt (Co) is mainly released as a Co^{2+} during passive film formation [30, 97]. Studies have reported that the Co ion concentration in bodily fluid was higher compared to Cr and Mo. Espallargas et al. [94] found that the cobalt ions in all of the tested solutions were one order of concentration higher than the other elements,

after testing CoCrMo under corrosion in saline electrolyte, PBS electrolyte and PBS with albumin electrolytes. In addition, there is an increase in metal ion release when mechanical sliding is applied to the corrosion (tribocorrosion).

The trend is in good agreement with the study by Hedberg et al. [98]. The Co^{2+} ion was found as the abundant ion concentration released from the CoCrMo surface in PBS with a ratio of Co:Cr:Mo = 13:2:1. Furthermore, the Co ion dissolution was even higher with the addition of albumin in PBS. This result indicates that the interaction of cobalt-protein has occurred and influenced the electrochemical reaction of Co ion.

In a hip simulator test, Yan et al. [99] reported a high concentration ratio of Co ion in the synovial fluid after one week tested in tribocorrosion at human body temperature. The majority of recent studies have proven that the ratio of metal ion release after tribocorrosion and hip simulator tests generally lies in an identical range, with Co ion as the highest, followed by Cr and Mo as the lowest concentration [99-102]. Also, the ion concentration increases with the testing time and applied potential.

Chromium (Cr) is the primary element in forming the passive film on the CoCrMo surfaces [103]. Chromium is oxidised during the passive oxide layer formation and becomes the chromium oxide layer while the cobalt ions dissolve [96, 104]. In a static immersion test, Cr^{3+} ion is released from the implant surface at a very low rate compared to the Co^{2+} and Mo ions [105]. Nevertheless, Lhotka et al. [106] reported an elevated concentration of Cr^{3+} ions after a longer period of use. The observation was conducted on the blood and urine of metallic implant patients. The high Cr concentration is attributed to the cyclic removal of the passive film due to mechanical wear. The Cr ion will experience de- and re-passivation multiple times during the articulating process.

Molybdenum (Mo) is known as a stable element in passivity at low pH conditions. However, Mo ion dissolution may occur at a pH higher than 7.0 [107]. Even though there have been only a few studies about the role of Mo ion in the adverse reaction, it was hypothesised that Mo ion in the bulk solution could interact with the proteins. The protein interaction with molybdenum ions was assumed significantly to affect the passivity behaviour on a CoCrMo surface [107, 108]. The molybdenum-protein interaction then increases the tribolayer performance to reduce wear and corrosion

on the metal implant. Indeed, there are specific conditions for sliding and the electrochemical potential applied. The interaction then leads to the growth of surface film formation. A recent study by Martin et al. [109] found that Mo ions can deposit the proteins to the surface compared with the Co and Cr presence. This result shows an independent role for each metal ion type (Co, Cr and Mo in this case) on the protein films' deposition. However, the interaction between the metal ions and the proteins, as well as their effect on material degradation during tribocorrosion, are not well established.

The tribocorrosion tests were also conducted in various applied potentials, from cathodic, OCP, passive and transpassive. Indeed, the corrosion products have a different concentration in each potential condition after being collected and calculated using the ICP-MS technique. Under cathodic condition, the de-passivation effect causes an increase in the metal ion released during mechanical wear. In OCP tribocorrosion, the metal ion release was enhanced due to the galvanic coupling mechanism, with a shift in the electrochemical conditions inside and outside the wear track [110, 111].

Espallargas et al. [94] found that the effect of mechanical action at the applied passive potential (+0.2 V) can increase the Co ion release between 20 and 40 times and Cr ions between 3 and 8 times compared to during static corrosion. This is because the cyclic removal of the oxide layer accelerates wear-enhanced corrosion and allows greater metal dissolution. That study also reported ICP-MS (inductively coupled plasma mass spectrometry) results measuring metal ion release after 30 minutes of corrosion and tribocorrosion tests in Table 2.3. Moreover, it was indicated that the rate of Mo ion release depended on the electrolyte chemistry, but was still higher in the presence of sliding. These results show that the rate of metal ion release is increased when the passive oxide layer is removed. It can also enhance the active dissolution and modifies the potential of the passive surface.

It is useful to monitor the elevated concentration of metallic ions in the bloodstream or other bodily fluids. A comprehensive review by Matusiewicz [112] highlighted the high concentrations of metal ions (e.g. Co, Cr and Ni) in human blood. The number of metal ions can indicate the hip implant performance or signal any upcoming adverse reactions. The Co and Cr ions in the patient's body are often monitored to evaluate MoM hip implant. The UK Medicines and Healthcare

Regulatory Agency (MHRA) issued guidance that limits the cobalt and chromium concentration in the bloodstream to a value of 7 μg/L. Once a higher amount is detected, this means that the MoM patient should undergo further surveillance due to an excessive metallic product [113]. Several American associations related to orthopaedic surgeons suggest a systemic evaluation of the patients and the monitoring of the serum ion levels. Periodic monitoring seems to be needed by surgeons to optimise the management of patients with a metallic implant.

Table 2.3 Metal ion release measured in a study by Espallargas et al. [94]

Condition	Electrolyte	Potential	Co (ppb)	Cr (ppb)	Mo (ppb)
Corrosion	0.9% NaCl	OCP	13.3	2.5	0.4
		+0.2 V	20.5	3.5	1.0
		+1 V	2727.4	991.7	174.7
	PBS	OCP	22.8	5.9	4.0
		+0.2 V	14.2	1.7	0.6
		+1 V	3249.2	1268.3	221.5
Tribocorrosion	0.9% NaCl	OCP	114.4	2.3	5.3
		+0.2 V	671.6	32.3	68.1
	PBS	OCP	142.7	4.9	5.8
		+0.2 V	418.5	18.5	25.8

2.4.3.2 Adverse Local Tissue Reaction

The presence of implant debris in the human body can lead to some physical issues known as Adverse Local Tissue Reactions (ALTRs). ALTRs are an unusual growth of solid fibrotic mass that originates in the patient's synovial tissue [114, 115]. With MoM implants, the ALTR involves an adverse reaction to metallic debris due to the tribocorrosion process. Those metal products can cause cellular toxicity and allergy [116, 117], metal hypersensitivity [118, 119] and chromosomal changes [120]. These issues of concern become a higher risk due to the accumulation of metal ions release after long-term used in the human body. ALTRs have been attributed to

~43% of MoM implant failure [121]. Although the use of MoM implants has been declining since 2008 to less than 5% of implantation procedures, there are still nearly one million patients using MoM bearings [122].

The effect of metal species' toxic effect on the surrounding tissue is not yet fully understood. Furthermore, these ions remain bound to the surrounding tissue and can be transported through protein binding, the bloodstream and the lymphatic system towards the remote organs. Those mechanisms were sourced from several reported cases [123, 124]. Several in-vivo studies have been conducted to assess the spreads of metallic ions from a cobalt-based implant in the human body. The results show that massive metallic ions, e.g. Co and Cr, can be found in the liver, heart, spleen, muscle, lymphatic tissue, lungs and urine [125, 126].

Studies are still focusing on the relationship between corrosion products and the pathological effects of the systemic toxicity of metallic ions. Inflammation and pseudotumours affect most patients with MoM implant. However, inflammation was also found in a few patients with MoP implant [127, 128].

To date, such diseases are believed to be caused by the high concentration of metal ions. The presence of Co ion can cause thyroid hypofunction, myocardiopathy and polycythemia. The Cr ion can initiate, in particular, liver and kidney infection and carcinoma. Cr^{3+} ion can trigger mutagenesis in the nucleus of the cell [109]. Lyvers et al. [129] have proven that metal ions in bulk solution could still interact with the metal surface and biological species (such as protein). Thus, it is vital to justify and control the metallic release due to the risk of spreading its potential toxicity.

2.5 Corrosion in Metallic Hip Replacements

Corrosion entails the destruction or loss of material, which has a chemical reaction upon its surrounding environment [130]. Compared to erosion, galling, or wear process, the material deterioration in corrosion does not include any mechanical movement. All metallic materials generally have a possibility of corroding. The environment can be both aqueous or gaseous media.

When a metal surface is exposed to an aqueous environment, chemical reactions cause the transfer of electrons between the two, called the electrochemistry

process. Electrons transfer typically occurs between the metal as an electrical conductor and electrolyte as an ionic conductor [131]. The electron transfer becomes a primary mechanism between the metals and the environments during the corrosion process.

Corrosion is one of the most problematic issues for metallic implant longevity and biocompatibility. Several passive-type metals are used for the bearing surface material, due to their ability to produce a passive oxide film for corrosion resistance. However, metal alloys with a robust passive oxide film can still experience passive film dissolution and ionic transfer at the interface [132]. The metal ion and debris from the surface indeed harm the local and systemic biological reaction in the human body [133]. Thus, this sub-chapter aims to review the essential aspects, passivity behaviour, measurement techniques and types of corrosion process in the implant environment. Based on clinical observations of the corrosion effect, it is vital to study the roles of electrochemical surface potentials, metal ion release and its interaction with the biological substances under a tribocorrosion condition.

2.5.1 Electrochemistry of Corrosion

The electrochemistry of corrosion involves the electrical aspect and the chemical reaction which occur at the metal-electrolyte solution interface. Corrosion usually takes place between opposing electrochemical reactions, in which the equilibrium between the two determines the corrosion rate. The anodic reaction occurs when a metal is oxidised and releases electrons into the bulk metal. Equation (2.1) represents the oxidation/dissolution of a metal surface (M), which releases the metal ions (M^{n+}). The metal surface also produces 'free' electrons (e^{-}) which stay within the bulk metal. The number of electrons removed is equal to the valence number of the material (n). In short, oxidation means the loss of electrons and the metal surface where its reaction occurs is termed anodic electrodes (anodes) [134].

$$M \rightarrow M^{n+} + ne^{-} \quad \textbf{(2.1)}$$

The cathodic reaction, meanwhile, occurs when an electrolyte species (e.g. H^+ or O_2) is reduced and takes electrons from the bulk metal (cathodes) [134]. The equations in Table 2.4 demonstrate the reduced reactions in the aerated solution, which are affected by the electrolyte chemistry. The reduction process occurs when the oxygen (O_2) and water (H_2O) compounds in the aqueous environment bind to the free electrons, generating the oxide and hydroxide layers, respectively [131]. During corrosion reactions, the metal oxidation will be complimented by cathodic reduction processes. Therefore, at the equilibrium state, the reduction reactions (e.g., involving hydrogen and oxygen) are favourable compared to metal ions. When the anodic and cathodic reactions are in an equilibrium state, the electrons flow from each half-reaction is balanced and no net electron flow (electrical current) occurs.

Table 2.4 Some of the most common cathodic reactions in aqueous environments

Hydrogen evolution	$2H^+ + 2e^- \rightarrow H_2$	**(2.2)**
Oxygen reduction in acid	$O_2 + 4H^+ + 4e^- \rightarrow H_2O$	**(2.3)**
Oxygen reduction in base	$O_2 + H_2O + 4e^- \rightarrow 4OH^-$	**(2.4)**

When the reduction reactions occur, the oxidation reactions can also result in material degradation at the metal surface. Those processes form an Electrical Double Layer (EDL) which can separate the electrical charge, and further develop resistance and capacitance. EDL contains Stern and diffuse layers between the bulk surface and electrolyte, as illustrated in Figure 2.5. The surface charge contains the adsorbed ions due to the chemical interactions at the Stern layer. The diffuse layer is created by the electrical charge of the Coulomb force, comprising other ions, such as metal ions (M^+) and Electrochemically Active Species (EAS). The EAS is involved as the oxidising agent for any species within the electrolyte which has a charge. Free energy can be attributed to the ability of electrons to pass through the two layers of EDL from the material into the solution. The potential of the metal ions passes through the double layers, as well as the Stern and diffuse layer composition within

EDL between the bulk metal and electrolyte. Such metals with passivity behaviour can generate a hydroxide film in an electrolyte, restricting the ions from returning to the metal substrate [131]. The free electrons can be used during the other half-cell (reduction) reactions due to the contact between the oxidising agents and the metal surface.

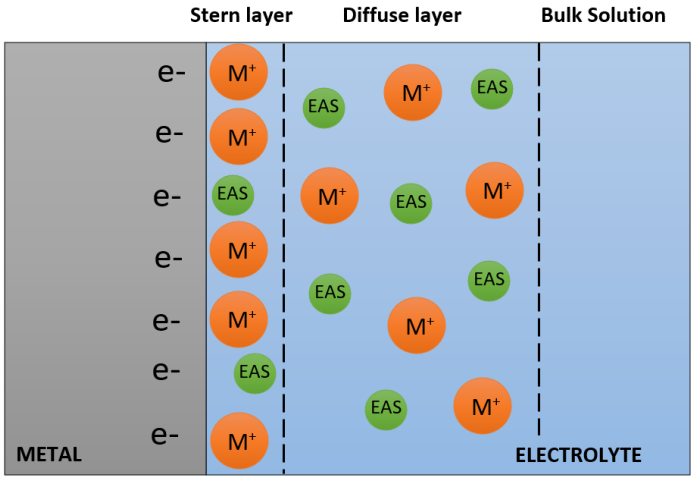

Figure 2.5 Electrical double layer (EDL) illustration

2.5.2 Thermodynamics of Corrosion

A material can be corroded directly or may require thermodynamic force. Equation (2.5) shows that the energy can be determined thermodynamically with an isotherm reaction of the Van Hoff formula, known as Gibbs free energy [131].

$$\Delta G = \Delta G^0 + RT \ln J \qquad \textbf{(2.5)}$$

Where:

ΔG : Gibbs free energy change

ΔG^0 : Standard free energy of all reactants

R : Ideal gas constant (8.3145 J/mol K)

T : Temperature (K)

J : Activity quotient for the reaction

When the following reaction $aA + bB \rightarrow cC + dD$ occurs, the activity quotient (J) of the reactants and products can be calculated using Equation (2.6).

$$J = \frac{[C]^c . [D]^d}{[A]^a . [B]^b} \quad \textbf{(2.6)}$$

The value of Gibbs Free Energy (ΔG) determines whether or not corrosion processes will occur spontaneously. The element is considered stable when the value $\Delta G > 0$. Positive Gibbs Free Energy means that the reaction requires a certain amount of energy to oxidise the metal. On the contrary, the value $\Delta G < 0$ means that the oxidation reaction will occur spontaneously and release some energy. Therefore, the material is degraded because the ions can diffuse from the bulk surface into an electrolyte. The change in energy between the reactants and products, either released or added, determines the reaction behaviour over time.

The chemical energies are in equilibrium due to the potential obtained at an electrode. The electrode potential in the electrochemical reaction is identified as the reduced Gibbs free energy of the charge transferred. Thus, the free energy can be determined in corresponding electrical terms as in Equation (2.7). That equation also leads to the Nernst Equation to measure an electrical potential at the metal-solution interface in electrochemistry reactions. The formula also reveals the opposite behaviour of the E value compared to the ΔG value. The negative electrode potential $E < 0$ means that the reaction requires a certain amount of energy to oxidise the metal. On the contrary, the positive potential $E > 0$ means that the oxidation reaction will occur spontaneously and release some energy. When the reaction direction is reversed, the E value also becomes negative.

The Nernst equation is used in equilibrium, relating both the chemical aspect in EDL and electrical potential [134]. In a standard state (pressure 1 atm at 25°C), the potential of an electrode is the total of the reduction and oxidation potentials in the half-reactions. The Nernst equation in Equation (2.8) can also be used to determine the cell potential when the conditions are non-standard state or not in equilibrium,

i.e. the reactions of two electrodes. The E calculation involves the standard potential, temperature condition, valence number of electrons and reaction quotient. The reaction quotient is the relative amount of reactants and products existing at such point in a reaction [135].

$$\Delta G = -nFE \text{ and } \Delta G^0 = -nFE^0 \quad \textbf{(2.7)}$$

$$\Delta E = \Delta E^0 - \frac{RT}{nF} \ln J \quad \textbf{(2.8)}$$

Where:

n : Valence number

F : Faraday's constant (96,485 C / mol)

E : Potential difference of an electrode (V)

E^0 : Standard potential difference of an electrode (V)

2.5.3 Material Passivity

As mentioned in the Nernst equation, the metal will be more reactive with increasing negative cell potential. Table 2.5 shows a list of potential values for each material as a half-cell electrode. The standard potential value can be used for the Nernst equation. For instance, gold and platinum are found to have standard electrode potentials above +1.20 V vs the Standard Hydrogen Electrode (SHE). Those metals are well established to have very little corrosion due to their low driving force to corrode. In the orthopaedic implant, most of the materials used can be found in the middle of Table 2.5 e.g., Co, Cr, Ti and Fe, which are commonly added to a metal alloy composition owing to their corrosion resistance ability.

Table 2.5 The list of standard electrode potential for some metal half-reactions

Metal	Half Reaction	Standard Electrode Potential (E^0)
Gold	$Au^{3+} + 3e^- \rightarrow Au$	+1.50
Platinum	$Pt^{2+} + 2e^- \rightarrow Pt$	+1.20
Mercury	$Hg^{2+} + 2e^- \rightarrow Hg$	+ 0.85
Silver	$Ag^+ + e^- \rightarrow Ag$	+ 0.80
Copper	$Cu^+ + e^- \rightarrow Cu$	+ 0.34
Hydrogen	$2H^+ + 2e^- \rightarrow H_2$	0.00
Lead	$Pb^{2+} + 2e^- \rightarrow Pb$	- 0.13
Tin	$Sn^{2+} + 2e^- \rightarrow Sn$	- 0.14
Nickel	$Ni^{2+} + 2e^- \rightarrow Ni$	- 0.25
***Cobalt**	$Co^{2+} + 2e^- \rightarrow Co$	- 0.28
***Iron**	$Fe^{2+} + 2e^- \rightarrow Fe$	- 0.44
***Chromium**	$Cr^{3+} + 3e^- \rightarrow Cr$	- 0.74
Zinc	$Zn^{2+} + 2e^- \rightarrow Zn$	- 0.76
Aluminium	$Al^{3+} + 3e^- \rightarrow Al$	-1.66
Magnesium	$Mg^{2+} + 2e^- \rightarrow Mg$	-2.36
Sodium	$Na^+ + e^- \rightarrow Na$	-2.71
Calcium	$Ca^{2+} + 2^{e-} \rightarrow Ca$	-2.87
Barium	$Ba^{2-} + 2e^- \rightarrow Ba$	-2.90
Potassium	$K^+ + e^- \rightarrow K$	-2.92
Lithium	$Li^+ + e^- \rightarrow Li$	-3.05

Biomedical alloys, such as Co, Fe and Ti-based alloys, are known as passive materials due to their ability to form corrosion-reducing, passive films. Those materials can rely on their film formation of metal oxide for corrosion resistance. The thin film acts as a protective barrier to inhibit the charge transferred from the bulk metal surface to the electrolyte. Equation (2.9) describes the reaction of

passivation with the metal ions. However, this passivity is a secondary reaction, following the metal oxidation as the primary reaction. For instance, the Cr element is added to an alloy material for an implant device due to its self-passivate ability. Equation (2.10) demonstrates how the oxidised Cr from the metal surface reacts with the water or oxygen from the environment at the metal-solution interface. The reaction produces a passive oxide film containing chromium oxide (Cr_2O_3), which protects the underlying surface from corrosion [136].

$$\frac{1}{2}M^{n+} + \frac{n}{2}H_2O \rightarrow \frac{n}{2}MO + nH + ne^- \quad \textbf{(2.9)}$$

$$2Cr^{3+} + 3H_2O \rightarrow Cr_2O_3 + 6H + 6e^- \quad \textbf{(2.10)}$$

The passive film characteristics are known to vary, depending on the interacting species in the environment and exposure time to the electrolyte and its metal alloy composition [137]. The passive film mainly contains an inner oxide layer and hydroxide in the outer layer [138]. Passive films thickness was found to range typically from 1-5 nm [139, 140]. Nevertheless, although the passive film is commonly demonstrated as an inert layer at the metal surface, it is more complicated in reality [103].

Understanding the corrosion initiation is one of the least known aspects within the corrosion process. The passive film breakdown is on a very small scale, even close to zero during the static passive condition. However, some external processes can degrade the passive film, such as mechanical (i.e., pressure or wear) and chemical removal (i.e., pH level reduction or driving force change). The passive films have a low ionic conductivity, which provides a protective barrier to the oxidation of the metal surface. On the other hand, the films tend to be unstable while interacting with aggressive ions such as high chloride concentrations. Figure 2.6 illustrates the mechanism theories of passive film breakdown.

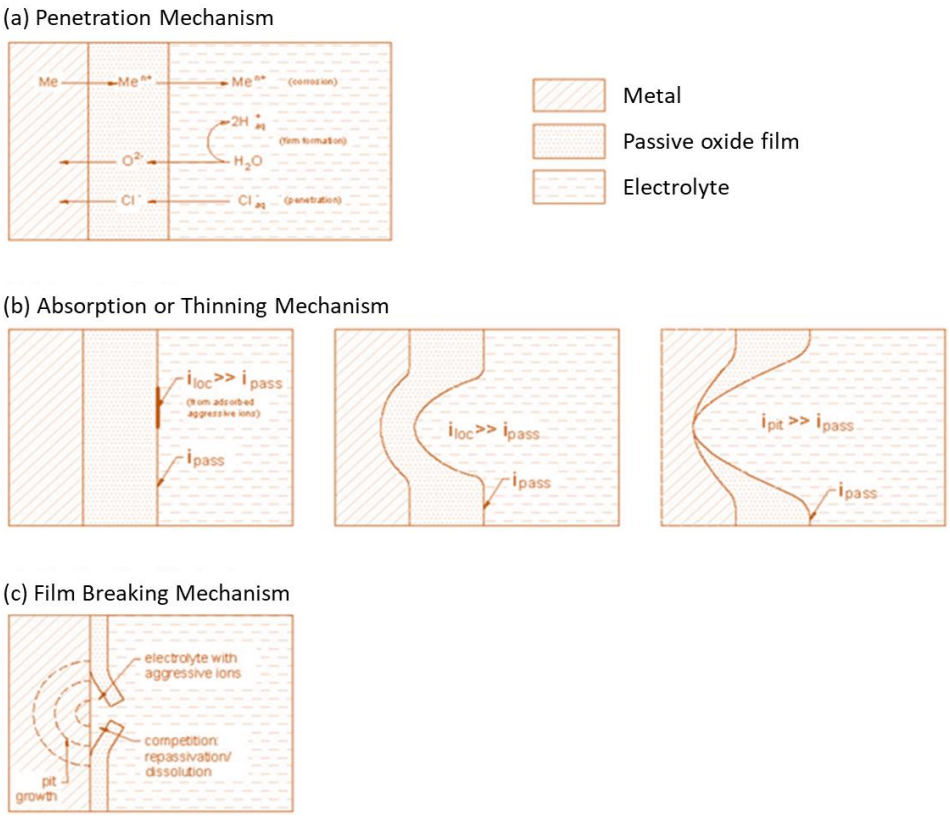

Figure 2.6 Schematic illustration for the breakdown mechanisms of the passive film and pit initiation by (a) penetration, (b) absorption and (c) breaking

The primary mechanism theories which have been established for passive film dissolution and pit initiation are categorised into [137, 141]:

- A penetration mechanism [142]; involving the penetration process by the aggressive anions in the electrolyte into the metal-oxide interface through the passive film. At that point, the pitting will be helped to grow.
- An absorption or thinning mechanism [143]; involving the absorption of local species, such as chloride and oxygen, through the passive film. This mechanism can reduce passive film thickness, and even lead to the complete breakdown of the films and pit initiation.
- A film breaking mechanism [144]; involving film breaking initiated by mechanical stress at the surface. The re-passivation will occur in the absence of an aggressive environment. Otherwise, the pitting corrosion will start to grow.

The re-passivation of the film will occur once the passive film has been removed. Passive formation happens so rapidly in the micro-second scale, which thickens over a longer exposure time. However, not every metal ion from the surface can contribute to re-passivation. The re-passivation kinetics, degree and extension of that oxide reformation are influenced by the surrounding environment, thermodynamic aspects and applied load in an articulating condition [135].

In vivo, the initial and re-passivation processes are more complicated due to the presence of the biological environment. The biological species, as well as phosphate, chlorides and oxygen, can interact and be adsorbed into the surface, resulting in a change in the native passive film properties [95]. It has been established that the various ionic species and protein presences have significantly affected the susceptibility and kinetics of corrosion at the metal surface. Although the protein tends to enhance the corrosion rate at the metal surface under a static condition, the protein provides protection via the formation of tribofilms under mechanical wear instead [8, 95].

2.5.4 Types of Corrosion

In this section, different types of corrosion will be discussed based on each initiation mechanism. Although there are at least eight corrosion types [130], this section will focus only on some of the most relevant corrosion types in biomedical devices.

2.5.4.1 General/Uniform Corrosion

General or uniform corrosion is caused by the degradation of chemical or electrochemical reactions that uniformly occur in the exposed material. General corrosion is usually found on metallic materials that fail to generate a protective oxide layer [130]. This type of corrosion changes the physical appearance of some metal-based material. For instance, surfaces of steel and cast iron become rusty when exposed to the open air, particularly when in contact with oxygen. Furthermore, the general corrosion rate is influenced by the thickness of the material, material surface condition and surrounding environment (pH and oxygen level) [130]. Although there are few general corrosion examples in metallic

implants, a localised attack can be performed on a passive-type metal surface where the local dissolution rates increase uniformly.

2.5.4.2 Pitting Corrosion

Pitting corrosion is indicated by forming small holes and cavities in the localised area at a metal surface. Pitting corrosion is commonly found on the passive-type metals that rely on a protective oxide film for corrosion resistance. When chemically or mechanically removed, their passive film needs time to re-passivate. The film degradation produces an anodic site which is coupled with the remaining passive film as a cathode. Thus, a local galvanic couple in that localised area is created [130].

On a metallic implant, the passive film can be damaged by the interaction between such aggressive anions, e.g. chloride (Cl^-), with the metal surface. The pits can initially pierce a metastable phase, where the passive film can still be restored. However, the pit geometry and chemistry become stable once the local potential exceeds the pitting potential. It then leads to increase the width and depth of the cavity and pit, resulting in a higher corrosion rate [145]. Pitting corrosion can also form into various shapes of pit geometries, as referred to in ASTM G46. Figure 2.7 illustrates the pit types, i.e. narrow, elliptical, wide, subsurface, undercutting, horizontal and vertical [146].

Pitting corrosion is known as the most challenging type to prevent and predict. The material selection should be suitable for the surrounding conditions. It is well established that the chloride ion and pH level can influence metal surface resistance upon pitting corrosion [147], since the pH level can change the pitting potential at the metal surface. Pitting holes can lead to severe weakness in the system structure, causing system or component failure.

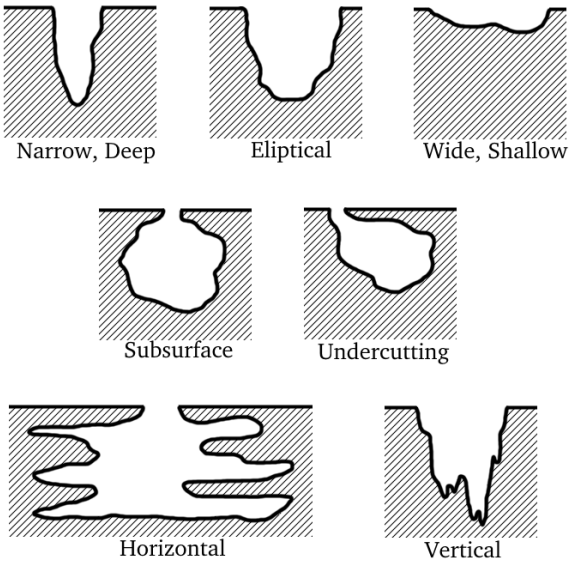

Figure 2.7 Various types of pit geometries as categorised in ASTM G46 [146]

2.5.4.3 Crevice Corrosion

Crevice corrosion generally occurs in a gap in the connection between two metals [148]. Similar to pitting corrosion, crevice corrosion operates on passive-type metal which owes its corrosion resistance to passive film formation. It is well established that crevice corrosion will occur after being initiated by the following conditions [130]:

- An electrical connection must appear between the metal substrate with the material at the outside of a crevice.
- The focused solution within the crevice must be stagnant in order to allow ionic species migration.
- The outer material of the crevice stays passive because of ions transportation.

Crevice corrosion can also occur when the concentrated solution within the crevice is starved of oxygen [149, 150]. This condition is compared to the oxygen-rich concentration in the bulk solution outside the crevice. Therefore, ions are transported from the bulk solution into the crevice to maintain the minimum potential energy and charge conservation. The oxygen levels outside the gap will be higher than those inside, so it acts as a cathode. The pH level will also be higher, resulting in a more alkaline environment on the outside. On the contrary, a low

oxygen concentration prevents re-passivation and an acidic environment occurs within the gap. This process results in complex ions and metal dissolution, leading to the formation of a corrosion product. The metal surface inside the crevice eventually begins to corrode.

For instance, Figure 2.8 shows crevice corrosion which occurs in a small gap between the neck of the stem and femoral head in the hip implant. The small concentration of aqueous fluid fits the two components that lead to an oxygen gradient in the crevices. The metal component will eventually more rapidly corrode once crevice corrosion is initiated.

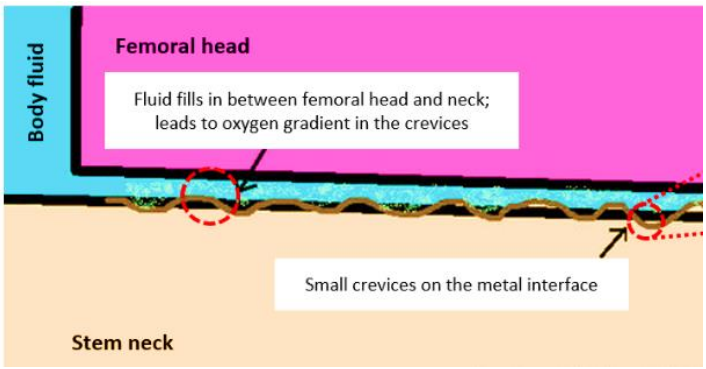

Figure 2.8 Crevice corrosion occurs in a small gap between the neck of the stem and femoral head in the hip implant [151]

2.5.4.4 Intergranular Corrosion

Intergranular corrosion occurs due to damage to the grain boundaries of a metal alloy. This corrosion creeps within the boundary due to the fact that the metal consists of many grains or crystal structures. Therefore, the corrosion must be viewed through a microscope since the material cracks occur at a microstructural scale. The results of this corrosion depend on the composition of the elements in the material.

A clear example is the Cr-containing alloy for a biomedical implant, which deposits chromium carbides ($Cr_{23}C_6$) along the grain boundaries. Chromium carbide precipitation uses Cr elements from thin sections over the boundary. As a result, the chromium-depleted regimes become anodes due to the potential difference with the bulk material. Those localised regimes are thus in a galvanic circuit and exposed

to intergranular corrosion [130]. CoCrMo alloy is claimed to be more vulnerable to this corrosion than Ti-based alloys [152, 153].

2.5.4.5 Galvanic Corrosion

Galvanic corrosion occurs when two different types of metal are immersed and electrochemically connected in an electrolyte/solution. An electrical circuit can take place due to the potential difference between the two metals. Ions from the metal will move through the electrolyte solution as a route. This interaction is called an electrochemical reaction. As shown in Figure 2.9, each electrode potential in two metals determines which one has a more active role.

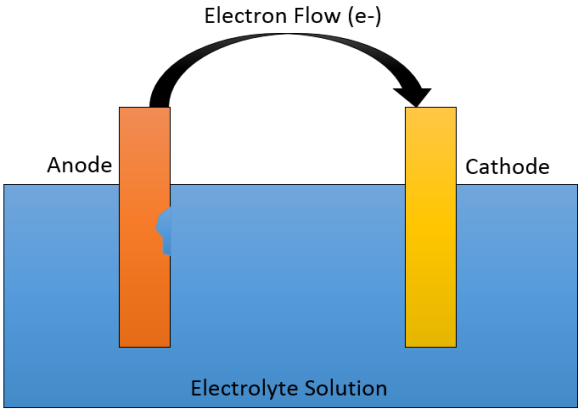

Figure 2.9 Galvanic corrosion on the two dissimilar metals in an electrolyte solution

The electrons do not usually travel through the electrolyte as individual entities, instead they will be transferred via the transport of the ions that are present in the electrolyte. Metal with the lower potential will have a positively charged electrode (anode). The electrons from the anodic electrode will move due to the potential difference between the two electrodes, resulting in galvanic corrosion at the metal surface. On the contrary, the other metal with higher potential will be a negatively charged electrode due to receiving the electrons. That second metal thus acts as a net cathode and is protected from corrosion.

An engineer must know the potential magnitude of each metal used to control the galvanic corrosion. A suitable metal pair must be appropriately chosen to minimise corrosion in one of the metals [130]. On the other hand, the metal with the lower potential is employed as a 'sacrificial anode' to prevent corrosion in the primary metal. Consequently, the sacrificial metal will be exposed to corrosion and replaced periodically in the galvanic couple [154].

In the modular THR, galvanic corrosion occurs between the coupling of the CoCrMo alloy with Ti-based alloy components. Some studies have noted galvanic corrosion's role in contributing to the degradation mechanism of the surfaces [152, 155]. However, the galvanic corrosion seems less destructive, and there was no prominent example of extensive corrosion damage. There were no significant galvanic corrosion traces in bearing couple studies, such as Co, Ti and SS-based alloys [156, 157]. The metallic implant will be protected from galvanic corrosion as long the passive film is stable, and no pitting or crevice corrosion is initiated [158-160].

2.5.5 Fundamentals of Corrosion Measurements

In this section, the relationship between EDL chemistry, the potential condition and the electrical current is explained. These aspects are essential for understanding the fundamental before conducting an electrochemical experiment and corrosion measurement. Furthermore, these explanations link the theories with the techniques and types of equipment used to measure corrosion behaviour.

2.5.5.1 Electrochemical Potential and Current

The Nernst equation can describe the correlation between the electrical potential of the metal with the EDL composition. Open Circuit Potential (OCP) is the potential of metal without any applied potential and where the anodic and cathodic rates are in equilibrium. The magnitude of the potential is determined by the chemical composition of the EDL; e.g., the concentration of metal ions and EAS. Thus, the OCP of metal will shift when changes occur in the bulk electrolyte and the EDL composition at the surface. An external power source or a couple of mixed metals can cause changes in the potential.

However, the Nernst equation will be unable to examine the rate of corrosion. Information about the net electrical current would be needed to calculate the rate of material degradation and its mass loss. The electrical potential changes can be related to calculating the current of a metal by using Equation (2.11), known as the Butler-Vormer equation [134].

$$i = i_{corr}\left\{\exp\left(\frac{\alpha_a nF\eta}{RT}\right) - \exp\left(-\frac{\alpha_c nF\eta}{RT}\right)\right\} \quad \textbf{(2.11)}$$

Where:

i : Current density as a result of the applied potential (Amps/cm^2)

i_{corr} : Corrosion current density at OCP (Amps/cm^2)

α_a : Anodic charge transfer coefficient

α_c : Cathodic charge transfer coefficient

n : Number of electrons in the half-cell reaction

η : Applied overpotential (V) = $E - E_{OCP}$

E : Electrode potential (V)

E_{OCP} : Open Circuit Potential (V)

The Butler-Vormer equation can be employed to generate Evans diagrams, as in Figure 2.10, with the electrical currents plotted over the potentials. In the Evans diagram, the anodic and cathodic directions are extrapolated from the linear parts of the measured values [161]. In a system where both are taking place at the metal surface, the measured values of OCP and i_{corr} will be a combination of both reactions. This combination is termed mixed potential theory and has been shown to occur where the anodic reaction of the iron intersects with the cathodic reaction of hydrogen. The mixed potential becomes complicated due to the various reactions occurring at the surface [134]. It is difficult for metal to reach the required potential for reduction reaction in an aqueous environment. Also, the metal is unlikely to deposit the released metal ions into the solution, since the hydrogen evolution

enhances the mixed potential of the sample, even above that required for the metal ions reduction.

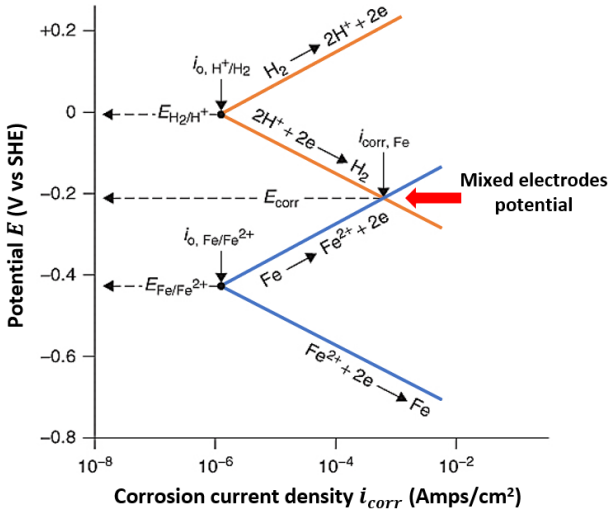

Figure 2.10 Example of an Evans diagram with anodic and cathodic half-reactions for iron (Fe) and hydrogen (H_2)

2.5.5.2 Three-Electrode and Potentiostat Setup

A standard experimental setup for measuring corrosion of a sample in an electrolyte uses a three-electrode cell with a potentiostat. Figure 2.11 illustrates the experimental setup in a standard three-electrode cell with a potentiostat. The cells consist of a Working Electrode (WE), a Reference Electrode (RE) and a Counter Electrode (CE), which are immersed in the electrolyte and connected to the potentiostat. The tested sample is the WE, whilst the RE is commonly a single cell with a metal submerged in such electrolyte. The RE is connected with the WE in the same electrolyte to afford a stable potential to determine the WE condition [134]. Thus, the potentiostat can measure the potential difference between the two connecting electrodes (OCP condition) simultaneously, or deliberately apply an external potential to the WE for any testing purposes (polarisation).

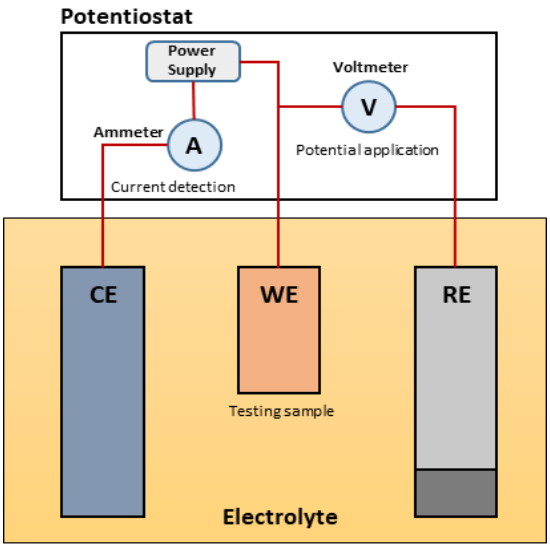

Figure 2.11 Standard experimental setup with a three-electrode cell (Working, Reference and Counter Electrodes)

2.5.5.3 Polarisation Techniques

In a polarisation test, the potentiostat can identify the overpotential by supplying or removing the current (electrons) between the WE and CE. Thus, the controlled currents will change the potential of the WE, and its direction will decide whether or not the sample is polarised anodically (by increasing the current and potential) or cathodically (by reducing them) [131]. The corrosion current of a sample can also be measured in a stable potential condition known as the potentiostatic test. Nevertheless, a sample is termed an OCP condition when there is an absence of net current between the WE and CE. The cyclic polarisation or potentiodynamic is known as one of the most common techniques used to characterise corrosion and performance. These polarisations can determine the sample response by shifting to any potential conditions, from the pure cathodic (low potential) to the full anodic (high potential). Figure 4.7 shows the corrosion current density as a response to the tested sample over the potential shifting ranges.

Anodic polarisation contains some typical regimes: between E_{corr} and the potential with the increasing current density (active-transitional regime); potential over constant current density (pseudo-passive regime); and potential after the current density started to increase again (transpassive regime). Cathodic polarisation consists of the expected regimes (ranging from E_{corr} to E= -1.0 V): the activation

polarisation (where the cathodic current increases over the potential) and the concentration polarisation (where the increasing current is limited due to diffusion-controlled transport) regimes. These variables and how they are estimated are stated in the methodology section.

2.5.5.4 Linear Polarisation Resistance (LPR)

Linear Polarisation Resistance (LPR) scans are useful for measuring the corrosion rate for long-term sample monitoring. The technique is non-destructive, due to the need to apply only the small polarisation range at the sample around the OCP [162]. The LPR scan is cathodically polarising the tested sample (WE) from a negative value and anodically sweeping it through the OCP towards a positive potential (typically from ±10 to ±25 mV OCP). Thus, the electrical current values between WE and CE can be measured at each potential step and are plotted onto the LPR curve, as shown in Figure 2.12.

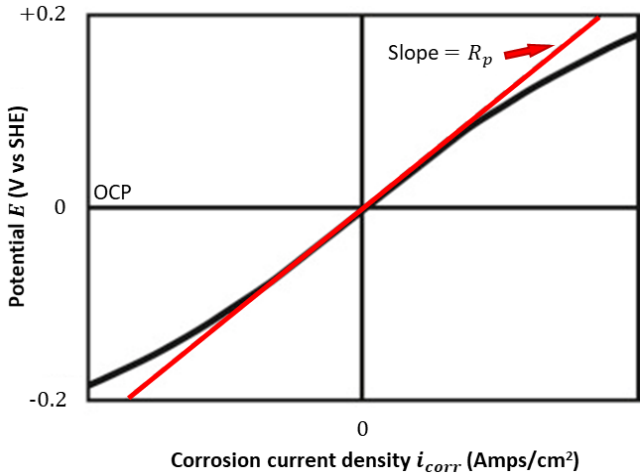

Figure 2.12 Example of a typical LPR curve

The corrosion current (i_{corr}) can eventually be calculated by using the Stern-Geary equation. As in Equation (2.12), the Stern-Geary formula uses the Tafel constants and the slope of the curve as the polarisation resistance (R_p), which approaches zero current. The sweep rate (mV/s) must be carefully selected since the EDL is too sensitive and must be left to adapt to each potential shifting step. Once the sweep

rate is too quick, the corrosion data might become invalid [134]. Nevertheless, the LPR scan will not determine whether it is a localised or general corrosion [134].

$$i_{corr} = \left[\frac{1}{2.303R_p}\right]\left[\frac{\beta_a\beta_c}{\beta_a+\beta_c}\right] \quad \textbf{(2.12)}$$

Where:

$\left[\frac{\beta_a\beta_c}{\beta_a+\beta_c}\right]$: Tafel constant

β_a : Anodic Tafel slope (V/decade)

β_c : Cathodic Tafel slope (V/decade)

2.5.5.5 Electrochemical Impedance Spectroscopy (EIS)

Electrochemical Impedance Spectroscopy (EIS) is a non-destructive technique used to determine the effect of applied electrochemical potential and environmental conditions (e.g., oxygen content, pH level and chemical composition in the electrolyte) on the surface films' electrochemical properties at the electrolyte-metal interface. The impedance technique allows the electrochemical systems to be characterised at the material surface, even in a medium with low conductivity [163].

EIS measures a metal electrode response to sinusoidal potential modulation with typically a 5-10 mV amplitude at various frequencies. The flow of alternative current (AC) tends to be resisted with respect to the impedance in the circuit. The relationship between the impedance, applied electrochemical potential and resulting current can be expressed systematically in Equation (2.13). The equation shows that the impedance is determined by the ratio of the amplitudes between the applied signal over the response signal, as well as the shifted phase within both signals [163, 164].

$$Z = \frac{E(t)}{I(t)} = \frac{E_0.\cos(\omega f)}{I_0.\cos(\omega f - \varphi)} = Z_0\frac{\cos(\omega t)}{\cos(\omega f - \varphi)} \quad \textbf{(2.13)}$$

Where:

Z : The electrochemical impedance (Ω)

$E(t)$: An excitation sinusoidal applied signal over a time function

$I(t)$: A sinusoidal current signal/response signal induced by potential

E_0 : The amplitude of the wave / applied signal (V)

I_0 : Amplitude (A)

$\omega = 2\pi f$: The radial frequency (rad/s)

f : Frequency (Hz)

φ : A shifted phase (°)

Using Euler's equation, these functions (the potential and current sinusoidal responses) can be represented as two vectors in the complex plane. Therefore, the vector sum between the impedance real (Z') and imaginary (Z'') parts represent the impedance Z, characterised by the modulus Z_0 (the impedance as a function of the magnitude) and the phase shift φ. Equation (2.14) describes Euler's relationship in understanding the impedance parameters [163, 164].

$$\exp(j\theta) = \cos\theta + j\sin\theta$$

$$Z = \frac{E_0\exp(j\omega t)}{I_0\exp(j\omega t - j\varphi)} = Z_0\exp(j\varphi) = Z_0(\cos\varphi + j\sin\varphi) \qquad \textbf{(2.14)}$$

$$Z = Z' + jZ''$$

Where:

$j^2 = -1$: The imaginary number

Z' : Impedance real part (Ω)

Z'' : Impedance imaginary part (Ω)

EIS produces two graphical results, i.e., the Nyquist diagram and Bode plot, representing the impedance spectra in Figure 2.13a and Figure 2.13b, respectively.

The Nyquist diagram consists of the electrochemical impedance real part Z′ on the x-axis and the imaginary part Z′′ on the y-axis. On the other hand, the Bode plot consists of the logarithmic scale of modulus |Z| (equals to $\sqrt{Z'^2 + Z''^2}$) and the phase shift φ (equals to arctan $\left(\frac{Z''}{Z'}\right)$) as a function of the frequency f on the logarithmic scale.

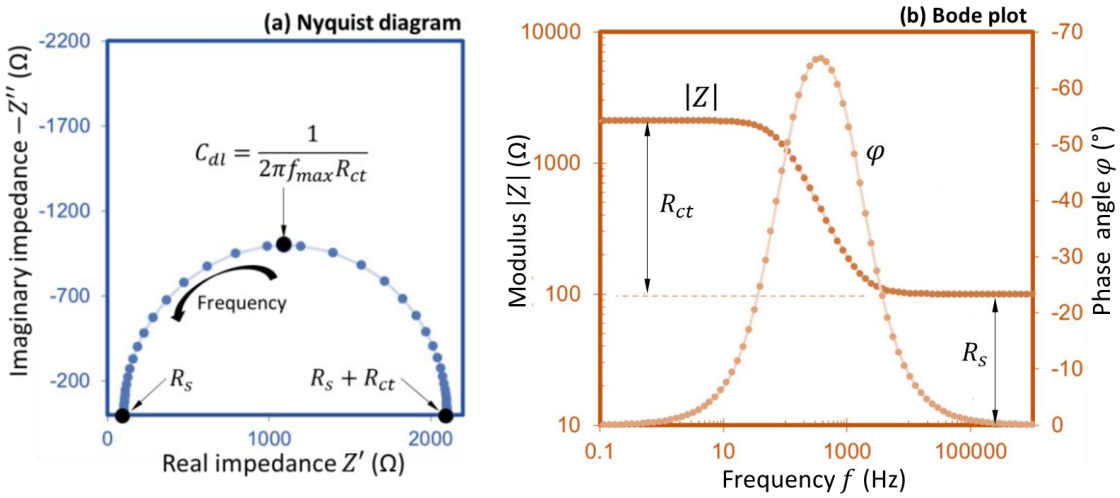

Figure 2.13 Examples of impedance data representing (a) a Nyquist diagram and (b) a Bode plot in a simple equivalent circuit

EIS data can be analysed qualitatively by comparing the obtained spectra. On the other hand, the EIS spectra are commonly interpreted using an equivalent circuit and electrical terms. A suitable Equivalent Electric Circuit (EEC) must be chosen and fitted with the experimental data. Table 2.6 shows the typical electrical elements used to interpret the impedance data. Metikos-Hukovic et al. [105] demonstrated that using fewer elements could lead to good data fitting. Also, it is suggested that the values of the chi-squared error ($\chi^2 < 10^{-4}$) and the individual elements error (< 5%) should be limited to obtain a valid interpretation.

Table 2.6 Typical electrical elements used to interpret the impedance data

Electrical Elements	Representation
Resistance (R)	Charge transfer at a certain interface (i.e. metal/electrolyte)
Capacitance (C)	Characteristic to store an electrical charge (EDL)
Inductance (L)	Resistance to oppose electrical current changes
Warburg (W)	Linear diffusion while subjected under semi-infinite conditions

Figure 2.14 shows an example of EEC at an electrolyte-metal interface, composed of elements of electrolyte resistance (R_s), double layer or EDL capacitance (C_{dl}) and charge transfer resistance (R_{ct}).

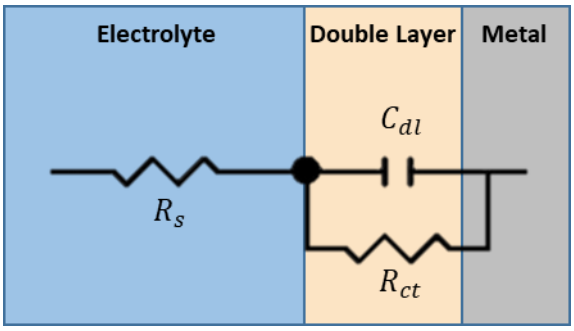

Figure 2.14 Schematic of a simple EEC (Randless circuit) at the electrolyte-metal interface

The impedance equation of the Randless system is shown in Equation (2.15). This simple circuit is used as a starter and more complicated configurations may be added, depending on the environmental and applied potential conditions [163, 165]. For instance, previous works added more parallel capacitance and resistance to characterise the inner and outer layers impedance in passive condition [163, 166, 167], whilst the Warburg element is applied for impedance in the cathodic state [163, 168].

$$Z(\omega) = R_s + \left[\frac{1}{\frac{1}{R_{ct}} + j\omega C_{dl}}\right] \quad \textbf{(2.15)}$$

However, a constant phase angle element (CPE) represents non-ideal behaviour due to various physical phenomena in the real systems, thus replacing the capacitance element during data fitting. Surface heterogeneity can be caused by the surface roughness, grain boundaries, and dislocations seen on a microscopic level at the metal-electrolyte interface [169]. Equation (2.16) defines the relation between capacitance element C and CPE in the impedance system [170], where Z_0 is the CPE constant. The exponent value (n) determines the representation of the CPE, whether as a resistance ($n = 0$; $Z_0 = R$), capacitance ($n = 1$; $Z_0 = C$), or Warburg impedance ($n = 0.5$; $Z_0 = W$). When $0.5 < n > 1$, the CPE describes the dielectric relaxation times distribution with respect to the frequency space.

$$Z(\omega) = Z_0(i\omega)^{-n}$$

$$CPE = R^{n-1}.C^n \quad \textbf{(2.16)}$$

Several studies [170-172] have demonstrated that the capacitance value C can be used to approximate the film thickness (d). Equation (2.17) involves the layer relative dielectric constant (ε), the vacuum permittivity (ε_0 = 8.85 x 10^{-14} F.cm^{-1}) and the exposed area (A), determining the dielectric behaviour between the passive oxide film and a capacitor in an anodic film growth. Namus et al. [167] observed passive film thickness between 0.7-0.9 nm at the CoCrMo surface under OCP conditions, which increases over the testing time via EIS measurement using Equation (2.17). The obtained thickness value is in good agreement with a study by Munoz et al. [95], which showed the CoCrMo film with 0.8-1.0 nm thickness under OCP conditions via AES depth profiling.

$$C = \varepsilon . \varepsilon_0 . \frac{A}{d} \quad \textbf{(2.17)}$$

Studies [95, 163, 169] have observed the typical passive behaviour at the CoCrMo surface under OCP or passive potential conditions, as defined by a semi-circle arc (capacitive behaviour) and high impedance values. The presence of biological species in electrolyte also affects the impedance behaviour at the CoCrMo alloy. Munoz et al. [95] demonstrated that phosphate in the electrolyte tended to increase corrosion resistance at CoCrMo under OCP and passive potential conditions. Also, bovine serum albumin was observed to reduce the outer layer resistance under OCP and move the phase angle towards a lower frequency under passive potential conditions. The impedance behaviour was, therefore, influenced by the biofilm formation and applied potential conditions.

2.6 Tribology in Hip Replacements

Tribology is a discipline in engineering that studies two contacting surfaces in a relative motion [173]. In general, tribology involves three major aspects: friction, wear, and lubrication [174, 175]. Friction is the resistance force of one contact surface when it moves in the opposite direction to another surface. Wear is a process of material loss that leads to the damaged surface due to that interacting movement. To reduce the friction and wear, lubrication takes a role as a separator of two contacting surfaces by creating a lubricant film between them. The lubricant used could be in the gas, liquid, or solid phase [176].

2.6.1 Contact of Solids

Contact mechanics is the study of how deformation occurs when two surfaces/bodies are brought into contact with an applied load. The contacting surfaces may deform both purely elastically or even through plastic deformation, in the static or dynamic loads [177]. The deformation is influenced by factors such as

the properties of the material and pressure at the contacting point. The conforming contact and non-conforming contact distinguish the configurations.

The contact conforms if the two surfaces are fitted precisely or even closely touch at some points before any deformation occurs. These two surfaces have a similar profile regarding direct contact. On the contrary, those surfaces are non-conforming if the two bodies have different profiles. Before any deformation occurs, the two surfaces would touch either at a point contact or a line contact [178]. The non-conforming contact mechanics generally consist of an average direction load (influenced by pressure and adhesion perpendicularly from the surface) and friction (tangentially working stress).

The deformation will occur at the contacting surfaces of the loaded sphere and the flat surface, as shown in Figure 2.15. The given load (W) towards such a direction will change the spherical radius (R) and its half-width length (a) at the contacting area [179]. The amount of the stress or pressure in this contact condition (point contact) can be measured using the Hertzian formula.

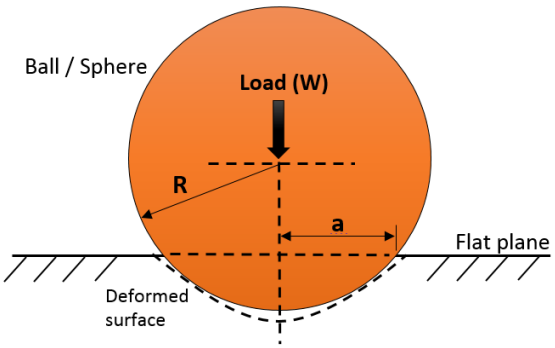

Figure 2.15 Deformation on the contact configuration of the ball/pin and flat surface (point contact)

Equations (2.18) to (2.22) in Table 2.7 demonstrate that the Hertzian contact pressure is also influenced by the elastic modulus and effective radius parameters [180].

Table 2.7 Equations for calculating the Hertzian contact pressure

The radius of the contact area, **a**	$\mathbf{a} = \left(\frac{\mathbf{3WR'}}{\mathbf{4E'}}\right)^{\frac{1}{3}}$	**(2.18)**
The relative radius of curvature, $\mathbf{R'}$	$R' = \left(\frac{1}{R_1} + \frac{1}{R_2}\right)^{-1}$	**(2.19)**
Effective elastic (Young's) modulus, $\mathbf{E'}$	$E' = \frac{2E_1E_2}{(1-v_1^2)E_2 + (1-v_2^2)E_1}$	**(2.20)**
Maximum Hertzian contact pressure, $\mathbf{P_{max}}$	$P_{max} = \frac{1}{2\pi}\left(\frac{3.W.E'^2}{R'^2}\right)^{\frac{1}{3}}$	**(2.21)**
Mean Hertzian contact pressure, $\mathbf{P_{mean}}$	$P_{mean} = \frac{2}{3}P_{max}$	**(2.22)**

W : Load (N)

R' : Effective radius

v_1, v_2 : Poisson's ratios of first and second bodies

E_1, E_2 : Elastic (Young's) modulus of first and second bodies

2.6.2 Friction

Friction is the resistant force of a surface that encounters another surface while rubbing over another [175]. Friction plays an essential role in a tribological condition, as it produces heat and wear that may damage the working surface. Figure 2.16 describes how dry friction works on two body surfaces.

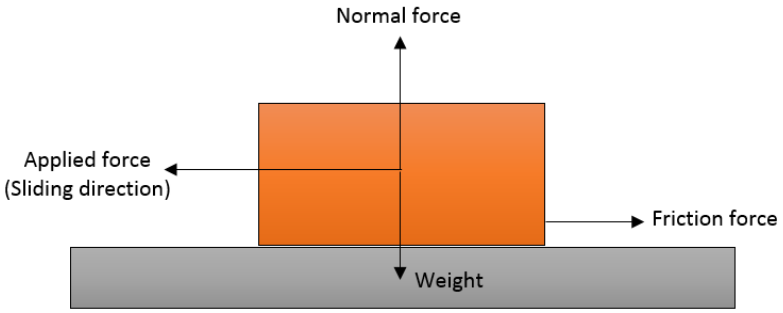

Figure 2.16 Dry friction during a sliding motion of two surfaces

2.6.2.1 Friction's Laws

Leonardo da Vinci initially introduced the laws of friction [181]. In 1699, Guillaume Amontons rediscovered those laws. Amontons' First Law stated that friction is proportional to the normal load. Hence, the resultant of friction (F) can be determined by the normal load (W) and the coefficient of friction/COF (μ), as shown in Equation (2.23). This condition is also known as static friction. Leonhard Euler was the first to use the term the coefficient of friction to represent the constant of proportionality.

$$F = W.\mu \tag{2.23}$$

Amontons' Second Law states that friction at the contacting surfaces in relative motion is independent of the apparent contact area [182]. The friction force is determined by the parameter of the true contact area (A) and the specific resistance to the shearing of the asperities (τ), as seen in Equation (2.24).

$$F = A.\tau \tag{2.24}$$

In 1781, Coulomb verified and analysed Amontons' Laws, even though facing scepticism at the time. Coulomb's Law stated that the magnitude of kinetic friction on two dry solid surfaces works independently of the sliding velocity [181]. The kinetic friction uses a coefficient of kinetic friction (μ_k) for the two moving bodies, which will almost always be less than the coefficient of the static friction (μ_s) while resting.

The equations for calculating the friction forces are compiled in Table 2.8, with an illustration in Figure 2.17. In short, static friction takes place before the two bodies move [183]. The friction force in this regime will be equal to the pushing force ($\mathbf{F_{push}}$) magnitude, as in Equation (2.25), but opposite in direction. The magnitude of the friction force rises as the pushing force increases, until the point where the bodies begin to slip. The point immediately before the surface slips is termed

impending motion, which has the maximum magnitude of static friction force before moving, as in Equation (2.26). After passing that point, the friction force drops down to and steadily works at the kinetic friction force. Kinetic friction occurs after the impending motion while the two bodies are rubbing. Equation (2.27) shows that kinetic friction is influenced by normal force (F_N) and the coefficient of kinetic friction (depending upon the contacting materials).

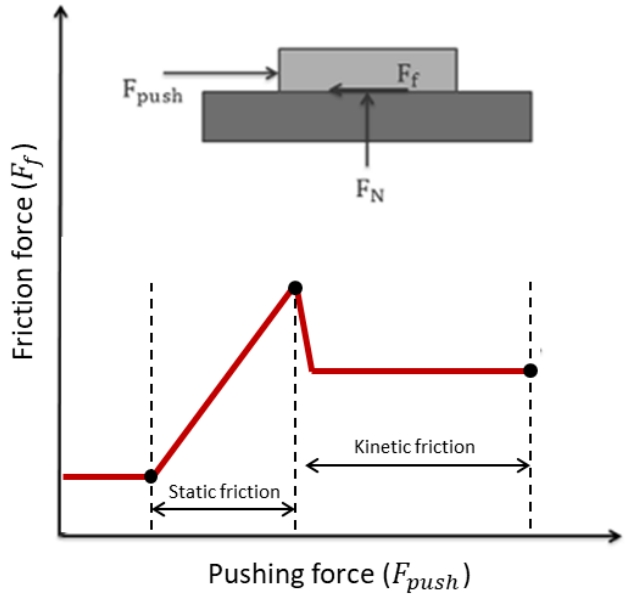

Figure 2.17 A model to illustrate the friction force in static and kinetic friction

Table 2.8 Equations for calculating the friction force in the static and kinetic stages between two solid surfaces

The static friction force	$\mathbf{F_f = F_{push}}$	(2.25)
Maximum static friction force (impending motion)	$F_f = \mu_s . F_N$	(2.26)
The kinetic friction force	$F_f = \mu_k . F_N$	(2.27)

2.6.2.2 Coefficient of Friction (COF)

The coefficient of friction (COF) is a dimensionless parameter value that examines the ratio between the friction force within two surfaces and the force pushing them together [184]. This parameter is usually symbolised by μ and has a value ($0 < \mu < 1$), depending on the materials employed. The lower the coefficient of friction, the more "slippery" will be the two contacting bodies "slippery" in terms of moving over each other. Based on Amontons' law of friction, the coefficient of static friction (μ_s) is used for bodies at rest relative to one another. The static coefficient of friction is influenced by the material deformation behaviour, surface roughness and asperities of the two surfaces, which have their chemical bonding characteristics between atoms in each material surface [185]. In the case of surfaces in relative motion, the coefficient of kinetic friction (μ_k) is employed.

This study mainly used a reciprocating pin-on-plate tribometer to measure the COF results. Similar to other modern tribometers, they apply a defined normal load by mass with a force transducer. The value of COF is generated after the reciprocating movement captures the loop of friction force and the velocity over the reciprocating cycles. The reciprocating tribometer measures the coefficient of friction by averaging the ratio of frictional forces in the load transducer to the loading force at the pin [186]. Studies have shown that implant failure can be caused by friction-induced moments during walking. A higher activity intensity will produce higher friction moment and wear. These will enhance the risk of aseptic loosening in an implant [187]. This fact indicates that it is critical to reduce the friction between the bearing surfaces in the implant [188].

2.6.3 Wear

Wear involves mechanical degradation and the removal of a material surface, resulting from an interaction between two surfaces in relative motion [189]. Wear can be caused by mechanical or chemical processes, which produce detached material from the surface (termed wear debris or particles of different sizes). The wear process can be categorised into four different types; i.e. abrasive wear, adhesive wear, corrosive wear and fatigue wear [175, 182].

2.6.3.1 Abrasive Wear

Abrasive wear occurs when a more ductile body encounters a material with a higher hardness [182]. The mechanisms of abrasive wear consist of ploughing, cutting and fragmentation. There are two modes of abrasive wear; i.e., two-body and three-body abrasion, as seen in Figure 2.18. The type of contact influences the abrasive mode. Two-body abrasion occurs when hard material or particles remove material from another surface. Three-body abrasion occurs when such particles are free to translate or rotate between the two rubbing surfaces. Those particles become third-body and contribute to the removal of one or both surfaces [182].

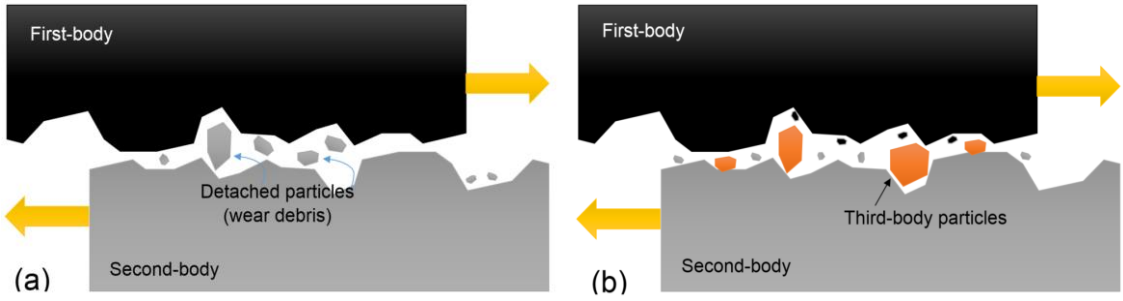

Figure 2.18 The mode of abrasive wear mechanisms: (a) two-body abrasion and (b) three-body abrasion

2.6.3.2 Adhesive Wear

Adhesive wear occurs if the atomic bonding forces in the two rubbing materials are stronger than the inherent material properties of the bodies. An illustration of adhesive wear can be seen in Figure 2.19. The shear initiates in the weaker material, and the detached wear particle is transferred to the other one. The transfer process is due to the high bonding strength and local pressure at the interface, which holds the transferred particle at the second surface or forms the wear debris [179, 190]. There is a chance that adhesive wear will increase the surface roughness, leading to the accelerating wear of the surface. Archard states that the adhesive wear volume is linear with the sliding distance and load [191].

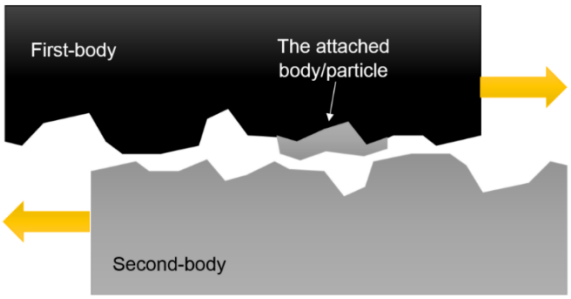

Figure 2.19 An illustration of the adhesive wear mechanism

2.6.3.3 Corrosive Wear

Corrosive wear occurs when rubbing surfaces work in a corrosive media, thus involving a chemical reaction and mechanical degradation in the process [192]. This reaction is usually influenced by the exposed material and the surrounding environment. The material can be uniformly removed from the surface or creep through the inter-granular path.

As shown in Figure 2.20, the pitting may appear on the worn area; therefore, it produces a rapid corrosion process [193]. The effect of corrosive wear tends to be more severe compared to when wear or a corrosion mechanism occur independently of each other.

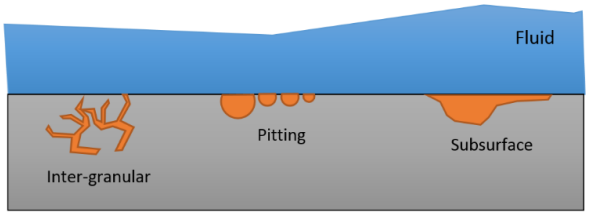

Figure 2.20 Material degradation caused by corrosive wear

2.6.3.4 Fretting Wear

Fretting mechanism is an oscillatory displacement at very low amplitude (micro-scale motion; when the displacement amplitude is lower than Hertzian contact radius) between two contacting bodies [194]. The fretting wear is described as fretting fatigue owing to the delamination mechanism in its wear process. The

displacement amplitude and applied load are two factors influencing the damage rates of the fretting wear. With the presence of metallic component, corrosive damage can be caused during the fretting mechanism; termed as fretting corrosion. In the total hip replacement, the fretting contacts between stem body and bone, as well as between stem neck and femoral head potentially produce the fretting wear and corrosion [195, 196].

2.6.3.5 Fatigue Wear

Fatigue wear occurs when the contacting surfaces work under sliding or rolling, which has a repetitive stress cycle in such a period. As in a typical fatigue process, fatigue wear is initiated by a crack on the material that grows to become a fracture [182]. The high stress caused by the repetitive loaded condition eventually produces a plastic deformation, removing the surface material. Figure 2.21 illustrates the crack growth within the loaded surface.

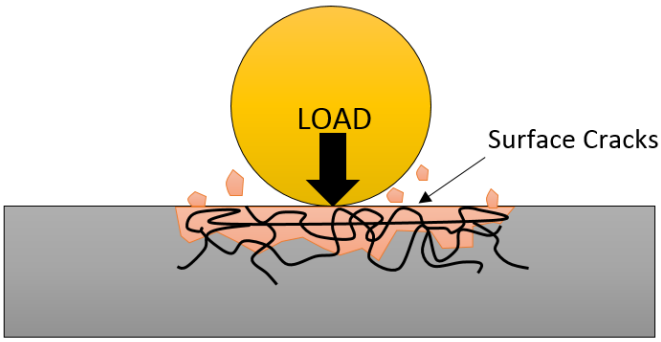

Figure 2.21 Crack propagation under a repetitive load cyclic in surface fatigue wear

2.6.4 Lubrication

Lubrication in a tribological condition occurs when a lubricant fluid is present between the two contacting surfaces and conveys a beneficial effect on both the wear and friction of the tribosystem [182, 192]. The lubricant used will generate a pressurised fluid film between the two surfaces, physically separating them. The lubrication performance may vary in terms of how the lubricant affects the

coefficient of friction and wear results, as well as how the applied load is supported at the surface. Therefore, there are lubrication regimes which can distinguish the lubrication performance.

Figure 2.22 presents the Stribeck diagram, commonly used to categorise lubrication regimes in a tribological condition [197]. This diagram is created by plotting the coefficient of friction (μ) on each lubrication parameter (Sommerfeld or Hersey number) that involves lubricant viscosity (η), sliding or rotational speed (v or ω) and contact pressure (P) [182]. The coefficient of friction itself is a ratio between the applied load (W) and the friction force (F).

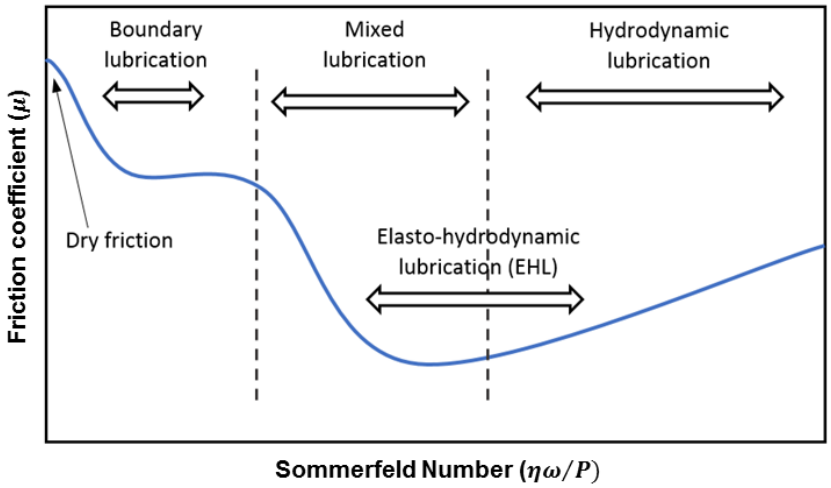

Figure 2.22 A Stribeck diagram representing the lubrication regimes

The lubrication regime can be represented by the lambda ratio (λ) or the specific film thickness [191]. The lambda ratio modifies the Stribeck curve by replacing the Sommerfeld number to describe the regimes in such a tribosystem [198]. As shown in Equation (2.28), the lambda ratio (λ) is influenced by the theoretical minimum film thickness (h_{min}) during sliding and the roughness of the two surfaces (R_{a1}, R_{a2}).

$$\lambda = \frac{h_{min}}{\sqrt{R_{a1}^2 + R_{a2}^2}} \quad \textbf{(2.28)}$$

In such a case of articulating implant surfaces, the h_{min} between the femoral head and acetabular cup can be theoretically calculated using Equation (2.29), known as the Hamrock-Dowson equation [199]. This equation can estimate the lubrication regime working in the bearing couple.

$$h_{min} = 2.8R'\left(\frac{\eta u}{E'R'}\right)^{0.65}\left(\frac{W}{E'R'^2}\right)^{-0.21} \quad \textbf{(2.29)}$$

Where:

h_{min} : Theoretical minimum film thickness (μm)

R' : Equivalent radius (m) = $\frac{r_1.r_2}{r_2-r_1}$

r_1 : Femoral head radius (m)

r_2 : Acetabular cup radius (m)

η : Lubricant viscosity (Pas)

u : Entraining velocity (m/s) = $\frac{\omega.r_1}{2}$

E' : Equivalent Elastic Modulus (Pa) = $2\left(\frac{1-v_1^2}{E_1}+\frac{1-v_2^2}{E_2}\right)$, v is Poisson's ratio

Figure 2.23 illustrates a schematic for an articulating femoral head in an acetabular cup.

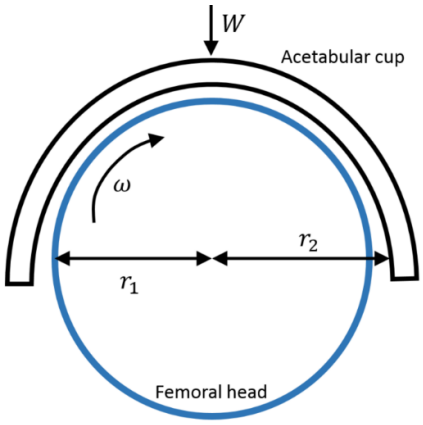

Figure 2.23 Schematic of an articulating femoral head in an acetabular cup

2.6.4.1 Boundary Lubrication

Boundary lubrication occurs when the roughness average of the articulating surfaces exceeds the minimum film thickness separating the bodies. Therefore, the lambda ratio is $0 < \lambda < 1$. Most of the load at the surface is supported by the contact of asperities. Furthermore, the coefficient of friction in the boundary lubrication would be higher compared to other regimes [192]. This regime commonly works under high load and low-speed conditions.

2.6.4.2 Mixed Lubrication

Mixed lubrication occurs when the lambda ratio is $1 < \lambda < 4$. In this regime, the asperities in such an area are divided by a lubricant film between two surfaces. However, asperity-asperity contact also occurs in another area. In other words, film formation is built up without fully separating the contacting surfaces. The mixed lubrication produces lower friction compared to the boundary lubrication, as in the Stribeck curve. Natural synovial joints in the human body tend to work in the boundary or mixed lubrication, where surface interaction mostly dominates the wear process [200]. Furthermore, the mixed lubrication was found at hard-on-hard interfaces (metal-on-metal and polyethylene-on-CoCrMo or ceramic heads) in the artificial hip under dynamic loading conditions [201, 202]. Lubrication regimes was stated to depend strongly on the loading and kinematics conditions, which mainly work under boundary or mixed regimes in the case of hip bearing contact.

2.6.4.3 Elastohydrodynamic and Hydrodynamic Lubrication

The elastohydrodynamic lubrication (EHL) regime works at $\lambda > 4$ when the lubricant film is fully separating the two contacting surfaces [203]. The lubricant film is thinner compared to the film in the hydrodynamic lubrication regime, so high pressure usually happens in the contact surfaces, creating the conditions for elastic deformation to occur. Therefore, this regime considerably affects the form and thickness of the lubricant film. The elastic deflection of the surfaces is essential to generate the total separating lubricant film.

The hydrodynamic lubrication regime happens at $\lambda > 10$ [203]. This regime behaves similarly to the EHL regime, where the lubricant film divides the contact

surfaces. The lubricant film is the thickest of all of the regimes. Thus, the film supports all of the load distribution.

2.7 The Role of Corrosion in Tribological Interfaces

As described earlier, biomedical devices commonly use passive-type metal alloys owing to their passive ability to reduce corrosion. The alloy surface has to react with oxidising species rapidly from the environment to form the passive oxide film [204]. However, the passive film can be removed mechanically under tribological conditions, leaving the bare surface exposed to the environment. Thus, the metal ion can be pulled out from the exposed surface due to the rapid oxidation process. This process is termed tribocorrosion.

2.7.1 Tribocorrosion Mechanisms

Tribocorrosion can be considered the irreversible degradation of surface materials from the simultaneous mechanical mechanism (i.e., friction, abrasion and erosion) and chemical/electrochemical interactions with an aqueous environment (i.e. corrosion reaction). The interaction involves tribological, electrochemical and chemical factors at the material surface within the mechanical contact and relative motion in a corrosive environment [205]. Tribocorrosion background combines two major areas discussed above; tribology and corrosion [204, 206-211].

Tribocorrosion describes a complex synergism between wear and corrosion; the rate of material removed when both mechanisms take place will be higher than when each is present individually [205-207, 209]. As summarised by Fuentes et al. [212], the typical synergism is schematically presented in Figure 2.24 and described as follows:

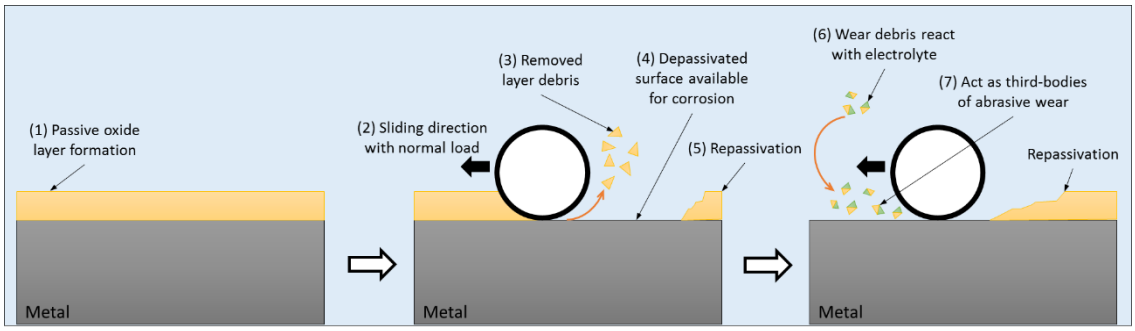

Figure 2.24 The schematics of the synergism in tribocorrosion

(1) In metal passivity, it has been explained that passive-type metal will form a passive oxide layer spontaneously to resist corrosion.

(2) Two articulating surfaces are rubbed with various normal load, velocity, and direction.

(3) The passive oxide layer and other wear debris are destroyed and removed from the surface (de-passivation).

(4) Fresh material at the de-passivated surface is exposed to the electrolyte and available for corrosion (wear-enhanced corrosion, or C_w henceforth). The corrosion roughens the surface and simultaneously causes corrosion-enhanced wear (or W_c henceforth).

(5) Meanwhile, the surface reforms the passive oxide film at some time after the removal (re-passivation).

(6) On the other hand, the removed wear debris (containing the oxide layer, metal ions, and the removed bulk surface) can oxidise, bind, and react with the electrolyte or biological species, if any.

(7) Studies [94, 212] stated that the metal debris-electrolyte products, such as hard oxides or other complex compounds, will accumulate and contribute as third-bodies of abrasive wear in the tribological contact, which increases the wear loss (corrosion-enhanced wear, or W_c henceforth).

Since the ions are released from the bulk metal, the worn surface would be an anodic area. Based on the findings of several studies, this condition forms a galvanic/electron connection that makes the area outside the worn path the cathode [210, 213]. Moreover, the re-passivation takes time and is not generated

directly. Therefore, the surface of the material can corrode. The material degradation depends on various factors during tribocorrosion, such as the surface and mechanical properties (surface roughness and load), electrochemical and environmental parameters (pH and temperature) and the physiological fluid as an electrolyte (biological species and proteins).

2.7.2 Tribocorrosion Approaches

Although studies have described the erosion-corrosion and abrasion-corrosion mechanisms of metals in the 1980s, the tribocorrosion mechanism was initially proposed in the 1990s, [207]. There are several approaches to evaluating the tribocorrosion mechanism, such as synergistic, mechanistic, third-body and nano-chemical wear [205, 214].

Watson et al. established the first standard approach to calculating wear-corrosion synergism in 1995, known as the synergistic approach [215]. This approach accumulates the total material loss as the sum of the material loss due to mechanical wear, electrochemical corrosion and a synergistic component (both wear and corrosion). A standardised method (in ASTM G119) has been proposed to evaluate tribocorrosion quantitatively. Watson et al. demonstrated that the overall material loss is also affected by a synergism factor (S), as in Equation (2.30) [208]. The mechanical wear mechanism not only produces a pure mechanical loss (W_0), but also changes the corrosion rate due to wear (ΔC_w) that coincides. The electrochemical process occurs as pure passive corrosion (C_0) outside the contact, as well as changes the wear due to corrosion (ΔW_c). As a result, all products can be accumulated as a total of degraded materials (V_{total}). This formula will be presented in detail in the methodology chapter. Equation (2.31) shows the synergistic components.

$$V_{total} = W_0 + C_0 + S \quad \textbf{(2.30)}$$

$$S = \Delta C_w + \Delta W_c \quad \textbf{(2.31)}$$

As stated in several studies [99, 207, 210, 216-219], the ASTM G119 standard has been relied upon to quantify the synergism of many materials in various environments. The interactions can be classified into antagonistic and synergistic [220]. An antagonistic interaction is identified when the corrosion and wear interplay decreases the total material loss, producing a beneficial effect, e.g. tribofilm formation in an MoM's hip joint due to sliding with protein presence [221]. On the contrary, a synergistic interaction is found when corrosion increases the wear and total material loss. Passive oxide film removal due to sliding or fretting can be an example of a synergistic behaviour [220].

The mechanistic approach was developed and standardised as a UNE 112086 standard in 2016 [222] to address several drawbacks from the synergistic approach. One of the first to introduce this tribocorrosion mechanism in fretting contact was Uhlig, by modelling the material loss due to the tribocorrosion process [204]. Uhlig described two main mechanisms that are at play during tribocorrosion; i.e., the mechanical removal and anodic dissolution/corrosion of material. As shown in Equation (2.32), the total volume loss (V_{total}) can be categorised into volume losses due to mechanical wear ($V_{mechanical}$ or V_W) and corrosion loss ($V_{chemical}$ or V_C) during intermittent de-passivation. However, this model had been developed due to its missing aspects in reality, i.e. pure passive corrosion outside the contact and corrosion-enhanced wear loss [223].

$$V_{total} = V_{mechanical} + V_{chemical} \qquad \textbf{(2.32)}$$

$$V_{total} = V_W + V_C$$

In order to address the drawbacks found in the earlier approaches, Mischler et al. [224] proposed a new method called the third-body approach in 2001, inspired by the third-body concept in a study by Godet [225] for dry sliding contact in 1984. This approach states that tribocorrosion generates the sum of the surface volume loss from three aspects; i.e., mechanically-detached material (adhesion or abrasion), chemically-removed material (metal ions released in the electrolyte) and the formation of a passive film by metal oxidation.

2.8 Protein's Role in Metallic Implants

Biological substances affect the mechanical wear (tribology) aspect and the electrochemical (corrosion) processes. All three aspects interact with each other in hip joint environments. The THRs system works inside the human body, making direct contact with the synovial joint fluid as the natural lubricant for the cartilage. The synovial joint fluid contains protein, glucose, uric acids and many other nutritional bio-substances that can directly affect the surface of the system. Furthermore, it is vital to understand the phenomenon of organic substances adsorption into the material. In this sub-chapter, the review will focus on the protein structure in synovial fluid and its interaction with the metallic implant surfaces.

2.8.1 Protein Structure

Proteins are a complex structure of amino acids with a long sequence and high molecular weight. Peptide bonds join and construct those amino acids so that the proteins have three-dimensional shapes. Protein types have their own specific structure and function. Protein can be categorised by its functional class, i.e. receptor, channel, transport, storage, enzyme, structural and immune response [226]. Figure 2.25 shows a basic structure of an amino acid.

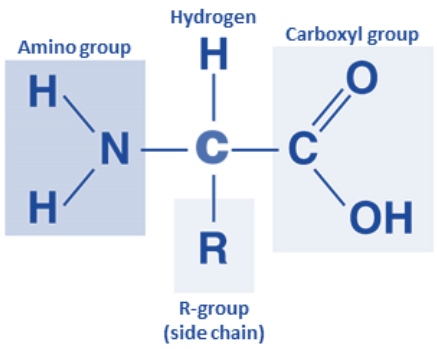

Figure 2.25 Basic structure of amino acids

Amino acids are bonded together by a covalent interaction through polymer formation into a building block of protein. Each amino acid is structured by a central

carbon (C), carboxyl group (COOH), amino group (-NH_2), hydrogen (H) and R-group as a side chain [227]. The R-group variant can be divided among amino acid types into the non-polar aliphatic, polar uncharged, aromatic, positively charged and negatively charged R groups.

An extensive sequence of amino acids creates a single protein molecule. The hydrogen bonds between the amino acids cause the unique structure of the protein, such as bending and curves. There are four distinct levels of protein structure, as follows:

- Primary structure; its sequence of amino acids forming its polypeptide chains.
- Secondary structure; the coiling or folding of its polypeptide chains. The coiling chains form a helical shape (alpha-helix) and the folding forms pleated sheets (beta-sheet). The processes depend on the formation of their hydrogen bonds.
- Tertiary structure; the three-dimensional shape of the polypeptide, composed of an alpha-helix and beta-sheet. The shape is caused by weak interactions between the R-groups and the environment.
- Quaternary structure; the final three-dimensional structure formed by all of the polypeptide chains contributing to the protein.

The protein molecules are stabilised by several interactions; i.e., covalent bonding (e.g., disulphide bonds) and non-covalent bonding (e.g., electrostatic forces, hydrogen bonding and hydrophobic interaction).

2.8.1.1 Protein Denaturation

Protein is described as being in its 'native state' if it is still in the natural folding structure. In this native state, the secondary structure of protein remains its functional form. On the other hand, the protein structure can be unfolded due to several factors; e.g., heat, acidity and chemical species concentration. An unstable intermolecular cross linking in a protein structure can increase the unfolding rate [228]. The unfolding process is known as denaturation, which produces an undefined formation of a secondary structure. Furthermore, the denaturation can

cause aggregation/agglomeration or degradation/fragmentation of the protein structure, as well as the loss of its biological activity. Figure 2.26 illustrates the structural changes between native and denatured protein.

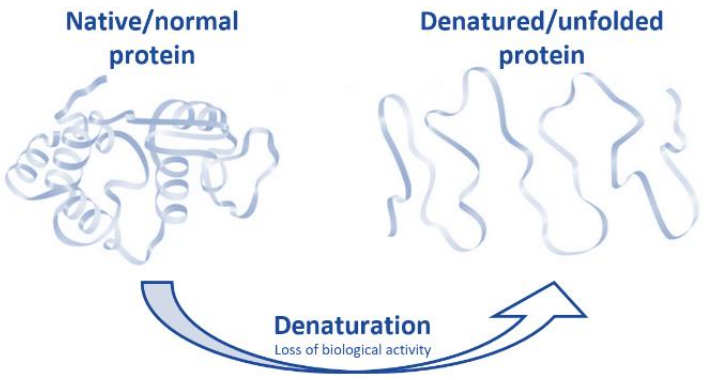

Figure 2.26 The structural changes between native and denatured protein

The protein can be denatured due to environmental factors, which affects the implant performance. Maskiewicz et al. [229] summarised that protein denaturation in serum-containing lubricant could be caused by physical and chemical factors during a hip implant *in vitro* test. The physical factor mainly involves a mechanical shear, provided through the tribological contact. The shear forces then disrupt the protein structure into an aggregation shape, and even fragment the protein with a higher force. The friction also can generate local heat in the contact area of the bearing surfaces. Therefore, thermal denaturation will occur in that zone to reduce the thermal stability of the protein, resulting in protein aggregation and precipitation.

On the other hand, the chemical factors include microbial contamination, interfacial denaturation, pH condition and reactive metal surfaces. The protein charges and pH level in the environment trigger a bonding between the proteins. The pH also affects the electrostatic force and ionic bonding between the amino acids within a protein structure. In an acidic environment, the positive charge is carried by the protein substances as the amino group changes from ($-NH_2$) to ($-NH_3^+$) of ions. On the other hand, the carboxyl group loses H^+ then changes the ions from (-COOH) to ($-COO^-$) in an alkaline environment. Therefore, the protein becomes negatively charged and has a weak electrostatic force to interact with the surface of the material [230].

Previous studies have successfully characterised the denaturation of proteins (by heat treatment [231, 232], conditioned pH [233-235], disease or chemical denaturation [236-239], etc.) using Raman spectroscopy. The denaturing of proteins can be characterised by changes in the Raman shift or intensity of certain de-convoluted bands. For instance, disulphide bonds, observed at a Raman shift ~500-550 cm^{-1}, represent the covalent bond of the sulphur units. Secondary structures (~1650 cm^{-1}) represent the protein backbone known as Amide I band, which can shift into ~1700 cm^{-1} during the denaturing process [231, 240]. Previous studies reported that the Raman bands of albumin in bovine serum at ~508, 523, and 545 cm^{-1} could represent the conformation of disulphide bridges (Gauche-Gauche-Gauche (GGG), Gauche-Gauche-Trans (GGT) and Trans-Gauche-Trans (TGT)), respectively. The Raman shifts were observed to increase after denaturing when compared to the albumin before treatment [236, 241, 242].

The tribocorrosion processes produce metallic ions and debris which have been shown to interact with protein species [11]. Therefore, it is useful to understand the interaction since the unfolded protein is hypothesised to affect the adsorption behaviour at the metal surface and act as a biological lubricant. In this case, the protein-metal interaction plays an essential role in implant performance, in which the interaction will affect the tribochemical reaction and surface film at the contacting surfaces.

2.8.2 Protein-Metal Interactions

As the predominant species in synovial fluid, proteins can interact with both the exposed metal surface and dissolved metal ions in the bulk solution. Protein can be competitive and affects the behaviour of passive oxide film at a metallic implant surface, causing less stable metal-oxide bonding and changing the corrosion reaction [243]. Albumin is the most abundant protein within the synovial fluid and has a high affinity with metal ions [244, 245]. For instance, albumin carboxylate and tyrosine structures can bind specific metal ions, such as cobalt, chromium, and ferrous and nickel ions [246-248].

2.8.2.1 Protein Adsorption

Proteins tend to absorb at the bulk solution-metal surface interfaces; termed protein adsorption [249, 250]. Protein adsorption onto a biomaterial surface is instantaneous and associated with the 'biocompatibility' of the material [251]. Also, the protein concentration in the bulk solution can influence the biomolecular adsorption [167, 251].

Adsorption is a mechanism whereby biological molecules interact then eventually absorb to a solid material surface. Some studies have proved that the protein was adsorbed in an instantaneous process with metallic surfaces, happening on its first contact immediately with biological tissues and fluids [252, 253]. Ithurbide et al. [254] mentioned that the complex nature of protein adsorption, including the amount of adsorbed protein within film formation, is influenced by the protein structure, electrochemical conditions, pH value, ionic strength of the environment, and material surface properties (e.g., surface potential, polar or ionic interaction, wettability, chemical structures and surfaces topography) [255]. It seems that the material properties are a critical factor in attracting the protein. Studies of protein adsorption have focused on many different parameters, such as adsorption kinetics and thermodynamics behaviour, micro- and spectroscopic studies of protein composition, as well as its structure and function [246, 256].

The adsorbed protein species have been shown to affect the corrosion/electrochemical processes of CoCrMo alloys [11]. Munoz and Mischler [95, 257, 258] investigated the roles of protein adsorption on the electrochemical properties of CoCrMo. It was observed that organic species, such as proteins, tend to increase the corrosion rate of the alloy. This was explained by the binding and transportation processes of protein and metal ion complexes away from the solution-material interface. Albumin is one of the most abundant types in the protein structures and attracted upon the metal surface [255, 257]. It seems that the bio-molecules are adsorbed onto the CoCrMo alloys surfaces, thereby decreasing the degree of oxygen reduction and affecting the passive oxide film's stability.

However, Yan et al. [259, 260] illustrated that protein adsorption considerably enhances the corrosion resistance of the articulating metal surfaces, as supported by several other studies [132, 261]. The rate of protein adsorption is affected by the

electrochemical potential condition of the surface; such as passive, transpassive and cathodic [255, 257, 262]. This shows that the reactivity of the organic molecules towards the surface are affected by the electrochemical potential and tribological condition.

2.8.2.2 Protein-Metal Interaction on Metal Degradation

Studies have reported the binding possibility between proteins and metal ions [263], in which the binding mechanism can be determined by the metal ion valence and charge of the proteins [264-266]. The metal-protein interactions are also essential to investigate since they are related to release of metallic materials. Figure 2.27 illustrates protein-metal interactions [186]. Hedberg [267] suggested that proteins can affect metal degradation as a consequence of their interaction via the following effects as a time function:

- Shielding effect; reduces material degradation initially by decreasing the cathodic reaction; however, increases the degradation via localised corrosion over time.
- Lubrication effect; initially can reduce friction and wear as well as with a tight packed protein film over time. However, it may increase friction after trapping wear particles in the protein film or protein aggregation.
- Attraction of counter-ions; may weaken the oxide or localised corrosion.
- Complexation effects; complexation between metal and protein, which can occur in an electrolyte, increases the dissolution/corrosion rates and detachments of metal-protein binds.
- Vroman effect; triggers an exchange of adsorbed proteins and thus enhances the corrosion/dissolution rate via the detachment of metal-bound proteins or a shielding effect.
- Protein-metal conjugates; by causing immunological and inflammatory reactions, protein-metal conjugates and large-sized protein aggregates can increase material degradation.

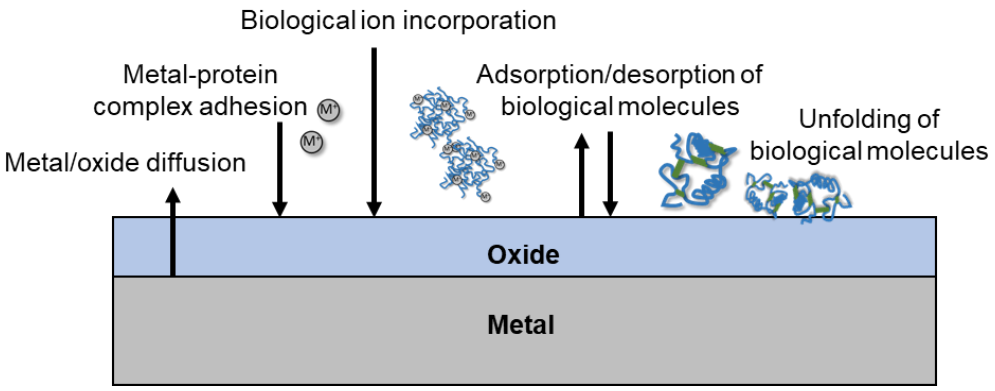

Figure 2.27 An illustration of protein-metal interactions

The protein-metal interactions affect the surface degradation and directly the health condition and protein-protein interactions. As mentioned earlier, metal-protein compounds can be an allergen in the human body, by causing a cell-mediated tissue reaction or sensitising the immune system [267]. Furthermore, the nano-sized metal-containing particles or ions can cause an interaction between proteins, resulting in structural aggregation [264, 268]. These aggregated protein particles can cause adverse effects in the body [269], as well as material degradation. The protein particles can increase the inflammatory (oxidative) conditions, which result in the increasing coefficient of friction and material wear [270].

Proteins are hypothesised to contribute to abrasive wear, despite being about to be deposited as film formation on the metal surface during sliding [271]. Based on the review, it seems that the protein can interact with the metal ions in the bulk solution. The interaction causes metal-induced protein denaturation [263]. Since the structure is unfolded, the proteins can easily complex the metal or aggregate with other proteins. These aggregation particles of the protein-metal complexation can remain as an abrasive particle and increase the material degradation rate. Therefore, protein-metal interaction is still the focus in some studies due to its complicated mechanism and effect on the metallic implant.

2.8.3 Temperature and Protein Concentration on Metallic Surfaces

Proteinaceous species are known to be sensitive to elevated temperatures [233] and shear, all of which are present within a tribological contact, leading to the re-arrangement of and damage to the protein structure [11]. A higher temperature than the normal human body condition can weaken and even break the disulphide chain, which results in an unstable secondary structure and reduced protein biological activity [237, 238, 272].

A study by Mishina and Kojima [273] found that protein denaturation begins to occur in temperatures ranging from 323 to 328 K. In another study, Wimmer et al. [274] estimated that the decomposition of protein occurs at temperature of or above 330 K. As reported by Bergmann et al. [275], the implant temperature could reach a range of 293-331 K, measured *in vivo* using an instrumented hip implant (at a sampling rate of 2-10 Hz and accuracy of 0.1˚C) with telemetric data transfer. Their study has proven that the artificial joint temperature can increase, depending on the walking cycles and speed, material combinations and surrounding environment temperature.

Lin et al. [240] reported that the conformational protein structure is reversible at temperatures below 323 K. However, it becomes irreversibly unfolded at temperatures 333 K. These unfolding processes (α-helices secondary structure and disulphide exchange aggregations) were indicated by the shifting Raman peaks and a reduction in signal intensity. After reaching 343 K, the proteins can be altered in their physical form into a gel-like structure, and grow darker in colour. Furthermore, previous studies have stated that the protein would be attracted to form a proteinaceous film at a metal surface [258, 276], which can lower the friction and wear, as well as suppress the rate of metallic ions release. It is hypothesised that the protein will more easily form a tribofilm when in a denaturing state.

Infections in the human body, such as arthritis and rheumatism, may increase the protein concentration in the synovial fluid [277]. Previous studies have successfully investigated the effect of protein concentration and temperature on the corrosion and tribocorrosion properties of CoCrMo alloys. Namus et al. [167] successfully employed Electrochemical Impedance Spectroscopy (EIS) to investigate the effect of protein (calf bovine serum) concentration and temperature on the CoCrMo

surface responses under cathodic polarisation to simulate the unworn area, that will be more cathodic. A significant reduction in oxide film resistivity was observed with the increasing concentration of protein and temperature up to 323 K. Atomic Force Microscope (AFM) confirmed that the protein concentration in the electrolyte influences the density of the surface adsorbed protein [278]. These findings indicate that the temperature could affect the protein adsorption and electrochemical processes on the metal surface. However, the study investigated a negative (cathodic) overpotential condition. Therefore, it is hypothesised that the temperature effect on protein adsorption will differ in the OCP condition due to the absence of forced electrochemical potential at the metal surface and there will be an anodic dissolution process.

Vidal et al. [251] also used electrochemical tests to observe the effect of temperatures ranging from 298 to 333 K and the protein concentration of bovine serum albumin on the adsorption process. The results clearly show that the higher temperatures will increase the passive film dissolution rate of CoCrMo alloys and reduce the transpassive (pitting) potential. During static immersion, the bulk protein concentration has been proven to accelerate the anodic reaction since the adsorbed protein can bind and transport the metal ions away from the solution-surface interfaces. This process seems to cause less protective passive/oxide film formation when compared to that without protein.

During sliding, the protein concentration's effect on the tribocorrosion of CoCrMo alloys has been investigated by Sun et al. [279]. The results show that the protein's increasing concentration can enhance the adsorbed protein density and thickness, reducing the polarisation resistance and increasing lubricity of the surfaces. However, the research on the effect of protein-metal interactions during tribocorrosion as a function of temperature remains limited. It is important to investigate the effect of elevated temperature and protein concentration on the tribocorrosive behaviour at the metallic surface in order to develop a clearer understanding about the failure mechanism of metal implant bearings in a complex physiological environment.

2.9 *In vitro* Studies of Metallic Implants

This sub-section will review and discuss several pre-clinical assessments associated with the conditions in a metallic implant. These involve *in vitro* studies of tribocorrosion of the implant in biological fluids and the effect of surface potential. Furthermore, the tribochemistry studies are also discussed, which can clarify the formation of tribochemical reaction films and their impact on the metallic implant.

2.9.1 Bio-Tribocorrosion

Recently, there has been an increasing number of tribocorrosion studies on biomedical areas, such as orthopaedic and dentistry. These tribocorrosion studies have been conducted with biological species in the electrolyte, termed bio-tribocorrosion [186, 199, 280]. Bio-tribocorrosion mainly expects to develop biomaterials with better biocompatibility and high resistance to both wear and corrosion in the human body. That aim eventually can be achieved by understanding the interaction between the biological species and material performance in wear and corrosion conditions. A study by Runa et al. [281] found that the effect of protein's presence can be either beneficial or undesired.

Therefore, the bio-tribocorrosion study is complicated, as it involves various influential parameters [205]. The interaction of physiological fluids containing proteins and other organic species with the tribology and corrosion of metallic implant leads to an even more complicated system.

2.9.1.1 Pre-Clinical Testing Procedures

Bio-tribocorrosion studies have been conducted using several methods for controlling the testing conditions to make them as close as possible to a real implant environment. In order to mimic these conditions, tribometer and hip simulators are usually employed with suitable sample materials, biological fluids and environmental settings. In our research group, the bio-tribocorrosion studies by Yan [186], Hesketh [280] and Beadling [199] used either a reciprocating pin-on-plate tribometer or hip simulator to re-create the sliding motion of the hip bearings.

Bryant [141] and Oladokun [196] also investigated the bio-tribocorrosive behaviour with the simulator and fretting tribometer for a fretting motion of cemented stem and modular taper, respectively. Those tools are instrumented with the three-electrode cells to assess or control the corrosion in the tribo-couples. The protein-containing serum was used as the lubricant to simulate the synovial joint fluid in the human body [9, 54]. Several surface analyses, including the wear volume, roughness and chemistry, are typically conducted following the bio-tribocorrosion (sliding) tests.

The reciprocating tribometer is one of the most popular types used to assess the tribocorrosion of biomaterials. This is due to its simple setup and ability to create a unidirectional sliding motion as in the joint. It only needs a small number of specimens and lubricants, which can be tested under a set of environmental parameters. However, the tribometer cannot simulate a more complex motion or angle as in the hip simulator that potentially occurs in the joint movement. Yan et al. [186] employed a reciprocating pin-on-plate tribometer instrumented with three-electrodes to investigate the lubricant effect on the corrosion behaviour of passive alloys under sliding. The specimens (316L stainless steel, HC- and LC-CoCrMo alloys) were tested in several electrolytes; i.e., 0.3% NaCl, 50% calf bovine serum and Dulbecco's Modified Eagle's Medium (DMEM) solutions. The tribocorrosion tests involved conditions of OCP and potentiostatic polarization, comparing all specimens and lubricants. The results showed that the organic species in the sliding condition behaved differently compared with the static condition. In the static condition, there was an indication of increasing corrosive damage in the presence of proteins. The proteins seemed to reduce the electrical potential required for passive film breakdown. In sliding, the corrosion-related damage in the contacting materials contributed to the total volume loss. However, the trend was different for each alloy material. In the end, the surface chemistry was analysed by XPS and showed a film formation.

Hesketh et al. [280] conducted an observation to study how the structure and chemical nature of tribofilm formed in the cobalt-based biomaterial. Using the reciprocating tribometer, a sliding speed of 1 Hz was set, as it is equal to 20 mm/s. The pin horizontally pushed the plate with a 5 kg hanging weight as the starting load, then reciprocated for 144 m sliding distances. This configuration obtained a

210 MPa of Initial Hertzian Contact Pressure. Furthermore, the hip simulator was also employed for MoM bearings investigation. The study successfully correlates with the repeating patterns in anodic currents of MoM bearings with the severity factor. This factor demonstrates that, since the interface becomes severe, it causes an increase in the material surface's de-passivation, indicated by the measured anodic current over time. The conditions of increasing load or reduced film thickness could be the factor associated with severing the surface.

Beadling et al. [199] used the tribometer and hip simulators with an electrochemical instrument to investigate the corrosive degradation of MoM and CoM bearings under adverse loading conditions. The results showed that increasing load pressure enhances the material degradation rate in the tribometer. In the simulator, the micro-separation was found to increase the corrosive volume loss compared to the standard gait condition as one of the adverse loading scenarios. The change in the acetabular inclination angle was found to affect the anodic current transient under potentiostatic polarisation. These findings indicate that the corrosion in the THR components was the primary source of the metal ion release, which can be sensitive under different articulating positions.

Those studies show that an electrochemical surface potential can influence the wear rate of biomaterials under tribocorrosion systems. This behaviour is also in close alignment with the previous study [94], but still debatable depending on the passive film characteristics under different surface potentials and the tribological condition. This effect was also crucial in bio-tribocorrosion, where the metal ions release due to wear and corrosion depends on the potential of the working electrode. The role of the surface potential will be discussed in the next section.

2.9.1.2 Effect of the Electrochemical Potential Condition

Electrochemical dissolution (corrosion) is one of the key factors of bio-tribocorrosion. The corrosion process is driven by the difference in the electrochemical potential on the surface, which can affect the material passivity and the formation of the surface film. Metal implants inside the human body have actual electrode potentials, although these are inconsistent over the whole surface [282]. The galvanic coupling experiences both lower and higher potentials near to the

reversible potential of the implant material [213]. These phenomena can be shown on removing passive oxide film while rubbing, resulting in a potential drop compared to the remaining area [110]. The change in the electrode potential can also be influenced by the surface pH [283], metal ion release [284], materials used and biological fluid [259, 285]. These indicate that the actual value of the surface potential in the body can vary greatly and even differ at different implant area sites.

The potential change seems to affect the properties of an exposed surface. In terms of surface microstructure, Wang et al. [282] reported that applied potentials (comparing at +0.2 $V_{Ag/AgCl}$, Open Circuit Polarisation (OCP) and -0.8 $V_{Ag/AgCl}$) affect the subsurface deformation. The result indicates that the surface potential modified the passivity and protein adsorption rate on the CoCrMo surface.

A study by Kerwell et al. [262] evaluated tribofilms formed on CoCrMo alloy at various anodic potentials (-0.4, +0.6, +0.7 and +0.8 $V_{Ag/AgCl}$). The results showed that electrochemically-induced surface films at the specific potential condition can affect corrosion resistance. Thus, these results indicate that electrochemical conditions can be sensitive, even with a small potential difference, in changing the protein adsorption on a metallic implant.

Munoz et al. [257] highlighted that the protein adsorption rate is higher at cathodic -1 $V_{Ag/AgCl}$ than observed at the more passive potentials. It turns out that this behaviour of protein adsorption in a cathodic environment occurs not only in a static immersion test, but also a tribological condition. Yan et al. [186] attempted to decrease the total volume loss of cobalt-based alloy under sliding at -0.8 $V_{Ag/AgCl}$. The cathodic reaction on the surface generates a protein film and protects the material from the tribocorrosion process. Nevertheless, the specific role of the surface potential of a cobalt-based alloy in a biological fluid is still poorly understood. Therefore, it is essential to investigate the effect on film formation in the organic-containing lubricant under tribological and applied potential conditions.

The surface potential, along with the contact pressure and normal load in the articulating surfaces, can affect the lubricating ability of the protein films, as found by several studies by Sadiq et al. [286], Mathew et al. [221] and Liao et al. [13]. The applied potential also affects the level of metal ion release, which determines the denatured protein and chemistry of the film [107, 108, 255, 262, 279]. Under a

particular condition, proteins were reported to form a biofilm on the articulating surface, which deposited a complex structure of inorganic and organic compounds and enhanced the lubricity [13]. Hence, it is useful to discuss the protein effects on the behaviour of tribocorrosion and tribochemistry of implant materials.

2.9.2 Tribochemistry

Tribochemistry can be referred to as the reactions that chemically occur at a tribo-contact activated by friction, shear stress and wear mechanism [287] [288]. Tribochemistry is a branch of mechanochemistry; a chemistry study that involves physical and chemical changes in matter caused by a mechanical force [289]. This reaction is crucial in the boundary lubrication regime, since there is an asperity-asperity interaction. Tribochemistry studies mainly focus on the automotive application, such as for oil additives [203, 290-292]. The aim is for the addition of a chemical agent to oil to be effectively activated and achieve the optimum lubrication during the mechanical rubbing of the components. The tribological condition can also accelerate the rate of additives' decomposition, generating tribochemical film formation as friction and wear protection on the surfaces. The growth of the film formation, physically and chemically, is usually conducted by Atomic Force Microscopy (AFM) and Raman spectroscopy.

Generally, the reaction generates a tribochemical film (tribofilm or tribomaterial) that is influenced by many parameters. The affecting factors are contact pressure [276, 293], sliding speed [54, 276, 294], sliding distance [294], lubricant constituents [259, 295], rubbing cycle [296] and surface materials [259, 264, 293], as reviewed in Table 2.9. It seems that the origin and exact mechanism of the chemical reaction are challenging to understand due to the involvement of a moving system on a tiny scale. However, the compiled information below should be adapted in the same way to understand the tribochemistry in implant devices. Thus, the tribofilms in implant surface seem to form due to high pressure between the bearing couple's contacting zones. The reaction would also give the various chemical components of the film, depending on the type of materials.

Table 2.9 The influential parameters of the tribochemical mechanisms

Parameters	Behaviour	References
Contact pressure	Reducing the contact pressure to increase the lubrication tribofilm thickness	[45, 276, 293]
Sliding speed	Lower speed to have the thicker tribofilm	[54, 276, 294]
Sliding distance	Adding the sliding distance to form more tribofilms	[294]
Lubricant contents	Lubricant constituents affect the chemical reactions and structure of tribofilm	[259, 295]
Rubbing cycle	The tribofilm thickness tends to increase with sliding duration	[296]
Surface materials	The different tribofilm formations are found in different material surfaces	[259, 264, 293]

Tribochemistry studies are still relatively young but very important in biomedical applications, especially in the boundary lubrication regime, such as in hip bearing contact. The tribochemical reactions in the THRs occur when the biological species in the synovial fluid interact either with the articulating implant surfaces or the other species in the body fluid, which eventually produce such deposited or precipitated compounds. Studies have found that the tribochemistry in the hip-bearing surfaces can also generate an organic tribofilm that helps to reduce the friction and degradation at the contacting bodies [297]. These results demonstrate that tribochemical reactions undoubtedly take place in THRs, such as between the acetabular cup and femoral head due to the sliding motion. It also shows that the tribofilm structure is complicated since it involves the organic species, material particles from the surface and even passive oxide film in the metallic implants. The next section will summarise several pieces of evidence of the tribofilm formation found on the tested CoCrMo alloys in simulated body fluid.

2.9.2.1 Tribochemical Film on a Metallic Implant

This section provides several pieces of evidence of tribochemical film formation and its effects on the surface friction and corrosion found on the tested CoCrMo alloy surfaces in simulated body fluid. Espallargas et al. [11] categorised the possibility

of tribofilm specifications in a metallic implant based on published results. Three different surface depositions can be summarised (Figure 2.28) as follows:

- Case (a) : A pure and thick passive oxide film on the metal surface.
- Case (b) : A layer of organic species covering the metal surface without a transitional oxide film.
- Case (c) : A thinner oxide film covering the metal surface with a high organic species formation concentration.

These categories are for metallic implant since an oxide film automatically reacts when the passive-type metal surface is in contact with the environment. However, the bi-layer surface reaction film might be the closest formation to the real condition. It seems that the formation of organic species must compete with the bonding of metal-oxide in the passive film during the deposition process.

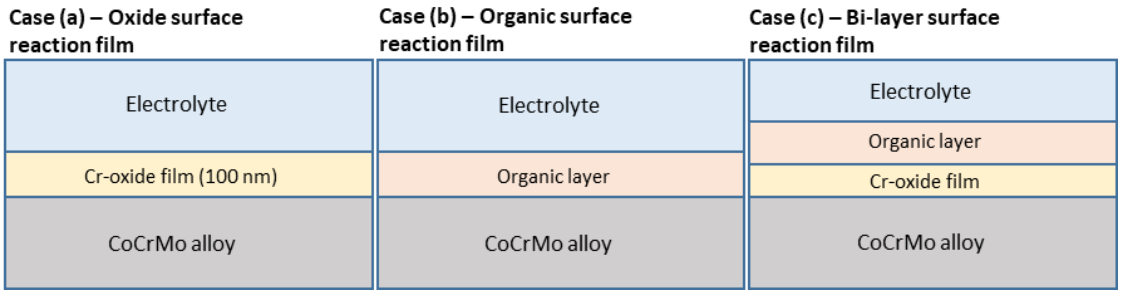

Figure 2.28 Schematic cross-section of the cases of surface reaction film

Wimmer et al. [298] attempted to assess the surface chemistry of *in vivo* MoM specimens retrieved from 42 users of McKee-Farrar prostheses and compared the results with *in vitro* specimens from the simulator test. The results showed a complex nano-structured film found in both the *in vivo* and *in vitro* specimens. SEM and EDS detected the elements of C, Na, Cl, K, Cr, Co, Mo, N, O, P and Ca on the self-mated ISO 5832-12 wrought CoCrMo alloys *in vitro*. The *in vivo* specimens with self-mated ASTM F75 CoCrMo alloys were covered by a thick oxide film in the worn area and a thin passive film in the unworn area. Tribofilms were also associated with the wear behaviour, which can protect from the adhesion and abrasion in both sample sets [12, 259, 276, 298].

Hesketh et al. [280] conducted tribocorrosion study with a hip simulator to assess the structure of tribofilm in MoM THRs. The tested surface was analysed by TEM (Transmission Electron Microscopy) along with EDS and EELS for the chemical properties. The morphology of the particles in the film is small and smooth, which dominantly contains cobalt sulphide and is rich in carbon and oxygen [10]. Yan et al. [259] found that the film formed in the MoM configuration was also a complex nano-scale structured layer. The films consisted of depositions of embedded organic particles [9, 10]. Hence, the protein adsorption played an essential role in the generation of the surface film, which is related to tribochemical film formation [246]. Yan et al. [8] explained that proteins can affect the tribological response of hip components either by combining with released metal ions or working as their native/denatured states to produce a tribofilm. By conducting experiments on bovine serum containing electrolyte, a tribofilm with a ~20 nm thickness containing denatured proteins and organometallic mixture (a complexation between organic and Co species) was observed on the CoCrMo surface, in which the study did not find any traces of organic species via XPS at the sample surface tested in NaCl solution The organometallic tribofilm was observed to reduce the total material loss and ion dissolution during a hip simulator test. The thickness and composition of this tribofilm after the hip simulator test was claimed to be similar to that found on a retreived hip implant. Furthermore, Yan's findings are in close alignment with a study of friction and film thickness using simulated synovial fluid by Mavraki et al. [54].

Pourzal et al. [299] used a hip simulator with self-mated ASTM F1537 CoCrMo alloys in bovine serum solution to simulate the joint condition. The EDS and TEM showed a carbonaceous layer with a 50 nm thickness on the CoCrMo surface after the simulator test. The tribofilm also contained particles that were mechanically mixed with the alloy surface. In another study, Pourzal et al. [300] characterised the wear particle from self-mated HC wrought CoCrMo alloys in calf serum with a hip simulator. It found some nanocrystalline subsurface areas after the test. Moreover, particles of non-oxidised metal (length 300-800 nm, width 100-300 nm and HCP structure) and oxidised metal (amorphous: O, Co, Cr; crystalline: only Cr and O; and Cr_2O_3 particles with 5-15 nm size) were detected on the alloy surfaces. Zeng et al. [301] attempted *in vitro* testing using a pin-on-disc tribometer with HC-CoCrMo

against alumina in bovine serum. The EELS detected a thick carbonaceous layer of 0-50 nm thickness and a nanocrystalline layer on the worn surface of 0-60 nm thickness.

Fan et al. [9] found that this proteinaceous layer build-up occurs in the boundary lubrication regime. As a result, the protein film can affect the tribological responses; e.g., by reducing friction and wear loss on the metallic surfaces. Mathew et al. [302] observed that protein resulted in a 23% decrease of the total volume loss from the CoCrMo surfaces when tested under boundary lubrication conditions. Liao et al. [12] observed the tribological layer in the hip resurfacing MoM with self-mated CoCrMo alloys. Using EELS and Raman spectroscopy, the signal indicated clear evidence of the presence of graphitic carbon as the main structure of tribofilm. The graphitic carbon deposition was also claimed to reduce friction and protect the surfaces from wear as well as corrosion. However, it still needs to be clarified how the protein can degrade into those complexes under the sliding condition, which produces the solid lubricant and protective effect associated with the denaturing state of the protein structure.

The presence of the proteinaceous film on the metal surfaces is still debatable with regard to their effect on corrosion. Some previous studies observed that the protein film tends to accelerate the metal ion dissolution rate, which can cause an adverse tissue reaction [259, 303]. However, recently, the nature of protein interaction has shown the different mechanisms and roles in the tribological contact surfaces. The protein tribofilm has been shown to reduce the corrosion processes on CoCrMo alloys by limiting the oxygen transported from the bulk environment to the metal bearings [259-261]; consequently, it alters the anodic and cathodic reactions at the metal-electrolyte interface. The metal ion dissolution rate and friction and wear degradation were also affected by the presence of protein-tribofilm [9, 274, 298].

Those findings show that spectroscopies can trace the complex metal-protein reactions from the deposition of proteinaceous constituents on the metal surface, degradation products, or detached compounds in the bulk electrolyte [139]. The *in vivo* and *in vitro* studies consistently found the presence of carbonaceous element, oxide (bound with metal ion as a passive oxide film) and several organic/proteinaceous elements (e.g., sulphur and phosphorus), whilst most of the film formation has a nanometre scale of thickness. The tribochemical reaction

seems to produce the surface tribofilms, metallurgical transformations and particle precipitations. The biological substances in the body fluid, such as protein and other species, were known to be mechanically mixed on the articulating surfaces, due to the shear stress, and eventually form a tribochemical film. However, the detailed mechanisms and chemical reaction kinetics of the tribofilms are still fragmented, with several variables (e.g., the effects of the surface potential changes, denaturing of the protein structure and protein-metal ion interaction on tribofilm formation) in the system remaining unexplored. The effect of the proteinaceous tribofilm on the corrosion behaviour of the CoCrMo alloys still need to be systematically investigated in light of such environmental variables. Therefore, further investigations are needed in order to obtain a full understanding of the nature of tribofilm formation, its effect on the surface degradation and the influential factors in the system while the metallic bearings are articulating.

2.10 Summary of the Literature Review

The risk of elevated metal ion levels in the bloodstream, associated with an adverse tissue reaction in a metallic implant user, became the major reason why MoM implants were recalled and taken out of use. Thus, understanding the fundamental mechanisms of wear and corrosion has been recognised as one way to solve the 'lack-of-longevity' problem plaguing orthopaedic implants. Tribochemistry, an interaction between electrolyte species and a metal surface during the articulation of surfaces resulting from shear stress and/or chemical interactions, is also shown to affect surface degradation [139]. Ultimately, the effect of this incredibly complex synovial fluid on the joint replacement materials is the primary concern. However, due to the complex nature of the environment engineers are still striving to create the optimal system [11, 304].

Under articulating conditions, the adsorbed protein film from a complex chemical reaction was affected by the tribological aspects and organic-metal interaction on the implant surface [8]. Those tribofilm compositions, in which the denatured protein and organometallic species were found, have been assessed in previous studies on worn CoCrMo surfaces. Researchers were able to conclude that such

compositions could enhance both lubricity and corrosion protection [1, 8, 247, 259]. Protein-metal interaction worked differently in various electrochemical potential conditions, influencing tribochemistry and tribocorrosive behaviour [186, 262, 282]. In addition, the total protein content [167, 305] and the dissolved metal ions, e.g. the Mo ion in protein-containing electrolyte [107], were observed to affect the tribocorrosion and surface film behaviour of CoCrMo alloys. Based on this current understanding, the following knowledge gaps are identified:

- The understanding of the tribocorrosive behaviour and tribochemical film processes of the CoCrMo surface in several organic-containing electrolytes and electrochemical potential conditions remains limited.
- The mechanisms pertaining to the formation of the tribofilms, when subjected to various protein conformations and concentrations, still requires further investigation.
- Besides the biological tissue reaction, the role and effect of released metal ions, e.g. Co, Cr and Mo ions, from the CoCrMo alloy surface in the physiological fluid, on the surface tribochemical film and tribocorrosive degradation, remain largely unknown.

Therefore, this study was designed to assess the hypothesis that several unexplored variables in the system, such as: (a) organic species-containing electrolyte, (b) the electrochemical potential condition, (c) the denatured protein and (d) dissolved metal ions, could play an important role in the tribocorrosive degradation and tribochemical processes of CoCrMo alloys, with either beneficial or destructive outcomes.

Chapter 3
Research Aim and Objectives

3.1 Research Aim

The aim of this thesis is to clarify the role of the system variables, such as: (a) organic species, (b) surface potential, (c) protein conformation and (d) dissolved metal ions, on the bio-tribocorrosion and bio-tribochemical processes of CoCrMo alloys under boundary lubrication sliding conditions. Throughout this thesis, a framework consisting of *in situ* tribocorrosion assessment and advanced surface analysis has been adopted.

3.2 Research Objectives

In order to meet the aims of this project, the following objectives were set:

- To observe the role of organic-containing electrolytes' and surface electrochemical potentials' effect on the tribochemical processes and film formation, as well as the tribocorrosion synergistic and mechanistic behaviour at the CoCrMo surface. These objectives are addressed in **Chapter 5** and **Chapter 6**.
- To investigate the effect of the denaturing structure of protein and its concentration in simulated electrolyte on the tribofilm build-up and tribocorrosion mechanism at the CoCrMo surface. This objective is addressed in **Chapter 7**.
- To observe the role of dissolved Co, Cr and Mo ions in the simulated serum protein-containing electrolyte on the tribochemical processes and tribocorrosion mechanism at the CoCrMo surface. This objective is addressed in **Chapter 8**.

Chapter 4
Experimental Methodology

4.1 Chapter Introduction

This chapter describes the experimental methodology and analytical instruments used in this study. It also provides the detailed procedures and rationale for the material preparation, bio-tribocorrosion experiments and surface analysis conducted in this study. The fundamental protocols related to handling and processing the data taken from each sample are explained in this chapter.

4.2 Material Preparation

4.2.1 CoCrMo Sample

Wrought low-carbon Cobalt-Chromium-Molybdenum (later abbreviated to Co-28Cr-6Mo or CoCrMo) alloy was used as a flat sample, according to the specification in ISO 5832-12 standard [36]. The alloy was supplied (Peter Brehm GmbH, Germany) as a 22 mm diameter rod, cut into a flat component with 6 mm thickness. The samples were ground by silicon carbide paper (grit sizes 600 to 1200) then mirror-polished by a 3 μm and ¼ μm diamond paste and polishing paper (Bruker Corporations, UK) to achieve an approximate surface R_a ~5 nm. After polishing, the CoCrMo samples were thoroughly cleaned under a stream of deionised water.

4.2.2 Testing Electrolytes

Foetal Bovine Serum (FBS) (Sera Laboratories International, UK), triple 0.1 μM sterile filtered and European grade, was used as the testing electrolyte in this study. Bovine serum is a typical electrolyte used to simulate the synovial fluid proteins

with such concentrations [306-308]. The chemical composition of the FBS solution can be seen in the Appendix section, with the following information [186, 309]:

- pH = 7.4
- viscosity < 0.001 Pa.s

Analytical laboratory grade sodium chloride (NaCl) was purchased from Sigma, UK, and used as received salts ion in this study. In the present study, the experiments used different mixtures of electrolyte.

Chapters 5 and 6 compare the four testing electrolytes, i.e. 0.9% NaCl (saline electrolyte), 25% FBS + PBS, DMEM and 25% FBS + DMEM. The tests were carried out in all electrolytes (n=3). Four different electrolytes were used, i.e.:

- **Saline electrolyte** – organic species-free; 0.9% w/v NaCl solution
- **25% FBS + PBS** – protein-containing buffered saline
- **DMEM** – protein-free cell culture medium
- **25% FBS + DMEM** – to identify the mixed composition influence

The FBS concentration was based on the version of ISO 14243-3 standard for hip simulation, which required a 25% (v/v) concentration of serum or a minimum 17 g/L total protein content [100, 308, 310]. In this present study, the FBS was diluted either in Phosphate Buffered Saline (PBS) or pure saline. The saline dilution aimed to increase the conductivity in the electrolyte during electrochemistry tests. The composition of a Dulbecco's PBS tablet (Oxoid Ltd., UK) can be seen in the Appendix, which contained phosphate and saline. The pure saline electrolyte consisted of 0.9% w/v sodium chloride (NaCl) in deionised water and had a viscosity of 0.000885 Pa.s [311].

A high-glucose Dulbecco's Modified Eagle's medium (Gibco's DMEM) solution (Life Technologies Corporation, UK) was used as one of the organic-containing electrolytes but without protein, lipids, or any growth factors. The composition of DMEM can be seen in the Appendix. It contained Mg ions from magnesium sulfate ($MgSO_4$-$7H_2O$), which FBS and NaCl solutions do not. However, this solution contained a high glucose level of 4.5 mg/mL as well as a high concentration of amino acids, vitamins and inorganic salts. This solution also had a pH of 7.2 and conductivity of 0.68 mS/cm, and was commonly used for cell culture processing

applications. DMEM had the same amount of chloride as in the FBS, which influences the corrosion behaviour. Table 4.1 shows the general characteristics of all electrolytes given by the suppliers.

Table 4.1 Characteristics of the electrolytes

	Saline	25% FBS + PBS	DMEM	25% FBS + DMEM
pH	6.9	7.4	7.2	7.2
Conductivity (mS/cm)	3.8	3.8	0.68	0.68
Viscosity (mPa s)	0.88	<1	1.07	1.07
Lambda ratio λ	0.019	0.021	0.022	0.022
Protein (albumin, globulins)	0 g/L	17 g/L	0 g/L	17 g/L

Chapter 7 is focused on the saline electrolyte (0.9% NaCl) and 25% FBS in saline electrolyte with several pre-treatments and protein concentrations. The heat treatment processes for FBS were conducted prior to dilution for tribocorrosion testing. A digitally-controlled hotplate was used to heat the as-received FBS (as-FBS) at several temperatures (40°C, 50°C, 60˚C and 70°C) for 1 h. The heating temperatures were expected to denature the protein in previous studies [229, 258, 276]. Following these tests, all of the heated FBS were taken (30 mL by syringe) and moved to Petri dishes for Raman spectroscopy purposes. This stage aimed to confirm the change in FBS structure after pre-heating, as represented by the Raman spectra.

Figure 4.1 shows the testing electrolytes used in this study. A digitally-controlled hotplate was used to heat the as-received FBS (as-FBS) at 70°C for 1 h to produce pre-heated FBS (de-FBS). This heating temperature was chosen since this is the highest temperature that can be achieved in a realistic condition and expect to denature the protein, as in previous studies [229, 258, 276]. Both as-FBS and de-FBS were diluted with DI water to 25% and 75% (v/v), or a minimum of 17 g/L and 51 g/L total protein content, respectively. Saline was then added to the FBS electrolytes to a concentration of 0.9% w/v NaCl. The 0.9% w/v NaCl without FBS

(pure saline electrolyte) was also used. FBS concentration was based on the version of ISO 14243-3 standard for hip simulation, which required a 25% (v/v) concentration of serum. The 75% (v/v) aimed to be a comparative variable regarding the concentration effect [100, 308, 310]. In addition, the dilution process was conducted after the pre-heating process to avoid any concentration reduction and to maintain the FBS in a similar condition to the untreated one.

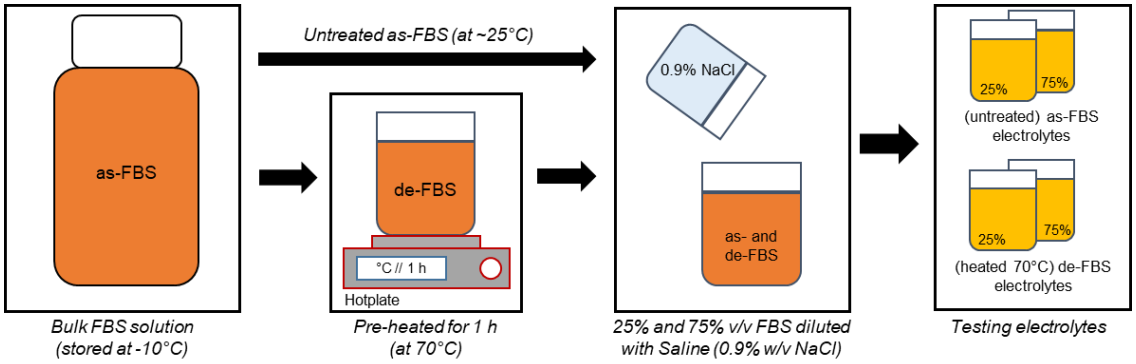

Figure 4.1 Preparation of FBS containing electrolyte: (a) pre-heating process at 70°C for 1 h and (b) saline dilution for the FBS with different concentrations (25% and 75%)

The objective was to investigate the effect of protein structure and concentration on the tribocorrosive behaviour at the CoCrMo surfaces. Thus, five different electrolytes were used in the tribocorrosion tests as follows:

- **Saline electrolyte** – 0.9% w/v NaCl
- **25% as-FBS** – total protein content 17 g/L untreated FBS diluted saline
- **75% as-FBS** – total protein content 51 g/L untreated FBS diluted saline
- **25% de-FBS** – 17 g/L pre-heated FBS diluted saline
- **75% de-FBS** – 51 g/L pre-heated FBS diluted saline

Chapter 8 is focused on the saline electrolyte (0.9% NaCl) and 25% FBS diluted saline with additional metal ions. Metal ion compounds, i.e., cobalt chloride, chromium chloride, and sodium molybdate powders consisting of Co, Cr and Mo ions, respectively, were added into the control electrolytes (saline electrolyte and

with 25% as-FBS electrolyte). The pH level was adjusted to a range 6.7-7.2 to obtain a valid comparison. The concentration was set to contain ~250 ppm (parts per million) or equal to mg/L unit of each specific metal ion (the Co, Cr and Mo ions), which were locally higher than normal concentration (in ppb). This concentration represented the amount of Co ion in bovine serum electrolyte after ~4 million cycles from an *in vitro* tribocorrosion test by Espallargas [94]. Therefore, the weight unit (gram) had to be adjusted according to each element's stoichiometry. The electrolytes used in the tribocorrosion tests are listed as follow:

- **Saline electrolyte** – 0.9% w/v NaCl
- **25% as-FBS** – total protein content 17 g/L untreated FBS diluted saline
- **Saline electrolyte +Co** and **25%FBS +Co** – One gram of Cobalt (II) chloride hexahydrate ($CoCl_2.6H_2O$) in 1L of control electrolytes to obtain 250 ppm of Co ions
- **Saline electrolyte +Cr** and **25%FBS +Cr** – 1.28 gram of Chromium (III) chloride hexahydrate ($CrCl_3.6H_2O$) in 1L of control electrolytes to obtain 250 ppm of Cr ions
- **Saline electrolyte +Mo** and **25%FBS +Mo** – 0.63 gram of Sodium molybdate dihydrate ($Na_2MoO_4.2H_2O$) in 1L of control electrolytes to obtain 250 ppm of Mo ions

4.2.3 Raman Spectroscopy

InVia Raman spectroscopy (Renishaw, UK) was utilised to confirm the bovine serum's protein structural changes after the heat treatment process for the electrolyte preparation in Chapter 7. The protein structural changes were represented by some typical signals, such as amide I and disulphide bands. The parameter was set at frequency 100%, which used laser power 785 nm and three times accumulative scanning feature. The raw signals were processed by using WiRE 3.4 software (Renishaw, UK) to subtract the entire spectrum baseline and truncate several expected band intervals.

The interval regimes of 500-570 cm^{-1} and 1500-1800 cm^{-1} were observed as representing the covalent bond of the sulphur unit and the amide I band,

respectively [231, 240]. The signals were then convoluted and fitted into sub-peaks using Origin 2019b software (OriginLab Corporation, USA), especially to calculate the percentage areas of the ordered and disordered α-helix backbone of the protein secondary structure in the amide I band [240]. Figure 4.2 shows an example of the Raman signal obtained. In the high-resolution analysis, the peaks can be convoluted and fitted by some expected sub-peaks, representing ordered and disordered states of the α-helix. The objectives were to confirm the effect of pre-thermal heating and deliberately denaturing the protein structures before using them in tribocorrosion tests.

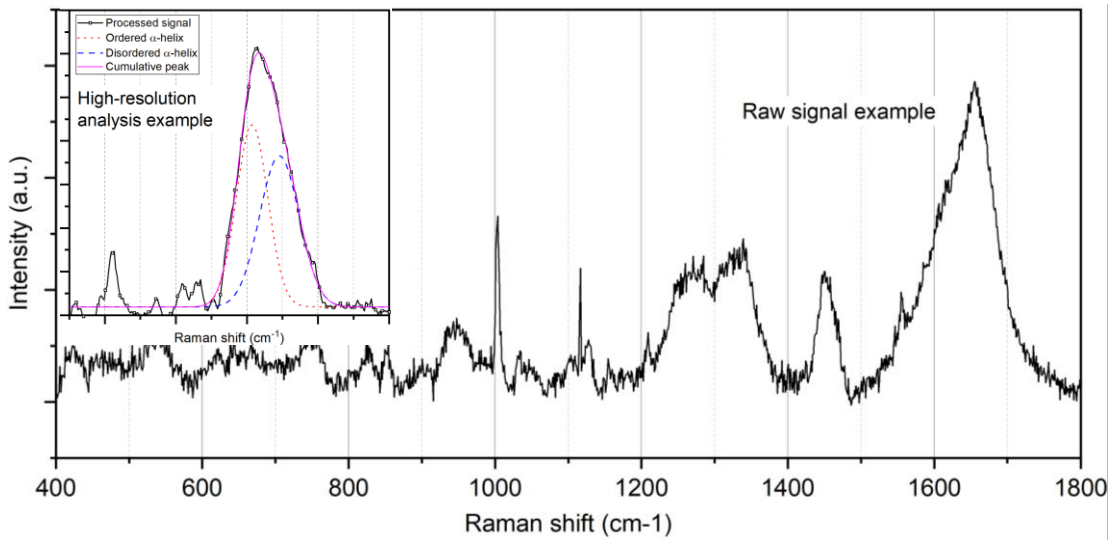

Figure 4.2 An example of the Raman signal obtained

4.3 Tribocorrosion Tests

This section describes all measurement techniques used for tribology and electrochemistry tests. Tribocorrosion was simulated using a reciprocating tribometer integrated with a 3-electrode electrochemical cell. The fundamentals of each method were explained in Chapter 2. At the end, the worn samples were stored in a desiccator.

4.3.1 Reciprocating Tribometer

A reciprocating pin-on-plate tribometer (BICERI, UK) was employed to mimic the sliding condition in a hip implant acetabular cup against the femoral head. The sliding test configuration involved a reciprocating alumina (Al_2O_3) ceramic ball, with Ø = 12 mm ± 0.76 µm (Atlas Ball and Bearing Company, UK), directly in contact with a flat CoCrMo sample.

The contact between the alumina-CoCrMo was modelled as a spherical shape against a flat surface. Hence, it causes an unequal pressure distribution over a circular contact area. The contact pressure was calculated using the Hertzian equation, as described in the previous chapter. Although the Hertzian analysis is commonly used to approach dry contact, it can be employed with rational efficacy for a contact working in the boundary lubrication regime [280]. Figure 4.3 illustrates a schematic of the reciprocating pin-on-plate setup.

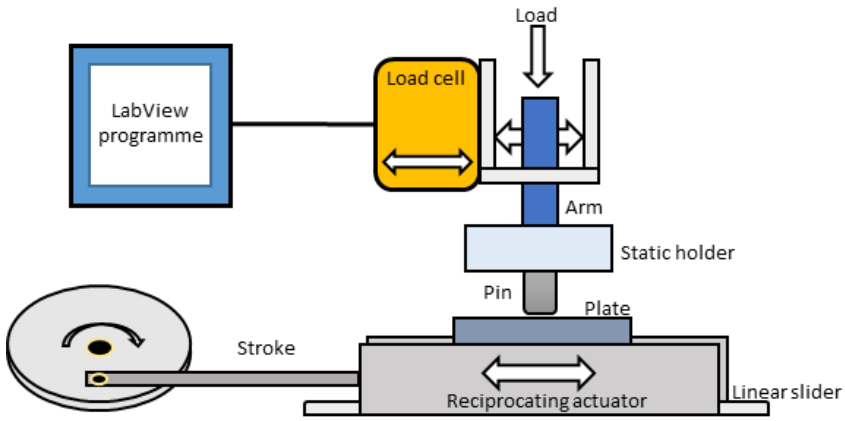

Figure 4.3 Schematic of the reciprocating pin-on-plate tribometer setup

The CoCrMo flat sample and electrolyte bath are driven by a stroke/crank mechanism over a slider track, causing them to reciprocate in a linear sliding motion. This mechanism resulted in a sliding velocity and constant normal load which operated sinusoidally against each cycle, as shown in Figure 4.4. The friction force at the contacting surfaces was conveyed through the cantilever arm, measured by a load cell. The oscillatory force between the arm and the load cell allowed the calculation of the friction between the contacting bodies. The measured data were converted using a LabView software (National Instrument, UK)

programme, producing a coefficient of friction (COF) of the static alumina ball and reciprocating CoCrMo sample.

In this study, the applied contact pressure was higher than in the normal standard gait condition in order to shorten the sliding test duration. The initial mean Hertzian and maximum contact pressures (P_{mean} and P_{max}) are 815 MPa and 1223 MPa, respectively, as the normal load of 30 N was applied continuously over time to the Al_2O_3 ball for Chapters 5 and 6. However, the tribocorrosion tests in Chapters 7 and 8 used a lower normal load, in which the P_{mean} and P_{max} are 565 MPa and 848 MPa, respectively, as the normal load of 10 N was applied continuously during the sliding test. The applied normal loads of 30 N and 10 N produce average final contact pressures of 59 MPa and 26 MPa, respectively, after 2 h sliding tests. Furthermore, all of the tribocorrosion tests were conducted with a 1 Hz frequency, a sliding amplitude of 10 mm at 20 mm/s (1 s is equal to 1 sliding cycle) and set at room temperature (~25°C). Room temperature was utilised due to the fact that it is lower than body temperature. The purpose was to maintain the bovine serum condition before and during the test. In addition, a 20 mL electrolyte was used in each static or tribocorrosion test.

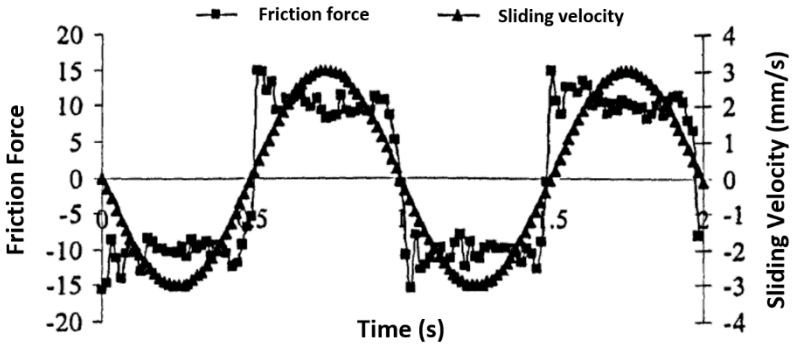

Figure 4.4 The friction force and sliding velocity over time of reciprocating motion

4.3.2 Three-Electrode Cell Setup

Figure 4.5 shows that the reciprocating tribometer was instrumented with a PGSTAT101 potentiostat (Metrohm Autolab, Netherlands). The 3-electrode electrochemical cell consists of the CoCrMo sample as the working electrode, whilst

the reference and counter electrodes were silver/silver chloride (Ag/AgCl) and platinum (Pt) discs, respectively. The equipment integration enabled the measurement or control of the corrosion at the CoCrMo sample simultaneously during the sliding test.

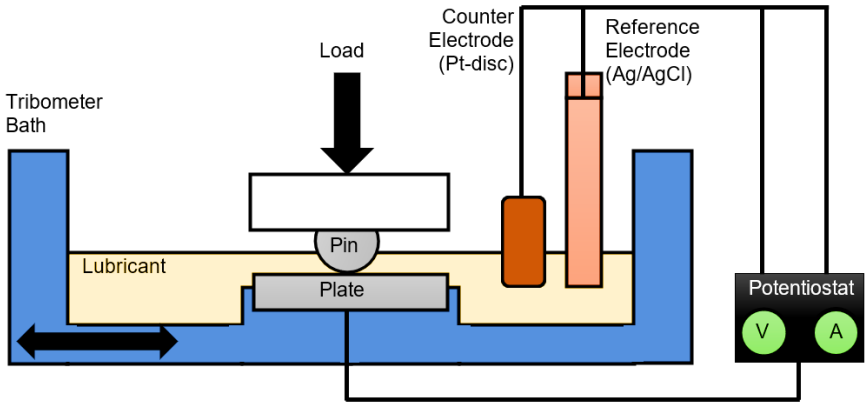

Figure 4.5 Schematic of the reciprocating tribometer instrumented with a potentiostat

4.3.3 Open Circuit Potential (OCP)

The open circuit potential (OCP) measurement was used to observe the state of passivity of a sample. Therefore, a metal surface's corrosion regime can be indicated semi-quantitatively, either in an active or passive state. OCP is the potential difference measured between the working and reference electrodes. In the tribocorrosion test, the OCP value indicates a galvanic coupling between the unworn/passive and worn/de-passivated site at the contacting metal interfaces [204]. The unworn/passive site is dominated by cathodic reactions whilst anodic reactions occur mainly at the de-passivated site. However, the OCP measurement does not provide the reaction kinetics information. The characteristic corrosion potential, ratio and position of the worn and unworn site and kinetics of the electrochemical reactions are parameters that theoretically affect the measured OCP in a tribocorrosion condition [312].

4.3.4 Linear Polarisation Resistance (LPR)

Intermittent Linear Polarisation Resistance (LPR) measurements were taken to assess the corrosion currents close to OCP. The LPR technique is considered non-destructive because it operates near the OCP value of a sample. The LPR measurements are conducted at periodic intervals between each scan to avoid a change in the system.

Figure 4.6 shows a plot of the current vs potential obtained from an LPR test under (a) static and (b) sliding conditions. The gradient of the line through the zero current is known as the resistance to polarisation (R_p). Noisy data were commonly observed in the LPR scan during sliding when compared to the static condition owing to transient de-/re-passivation processes. The fitting process of the LPR data was crucial to obtain the right R_p of the system. Indeed, the cathodic tail has to be omitted as much as possible from the curve. Therefore, the slope is fitted in the linear regimes of the data. The spread and noise data in the sliding condition are also involved while fitting the slope.

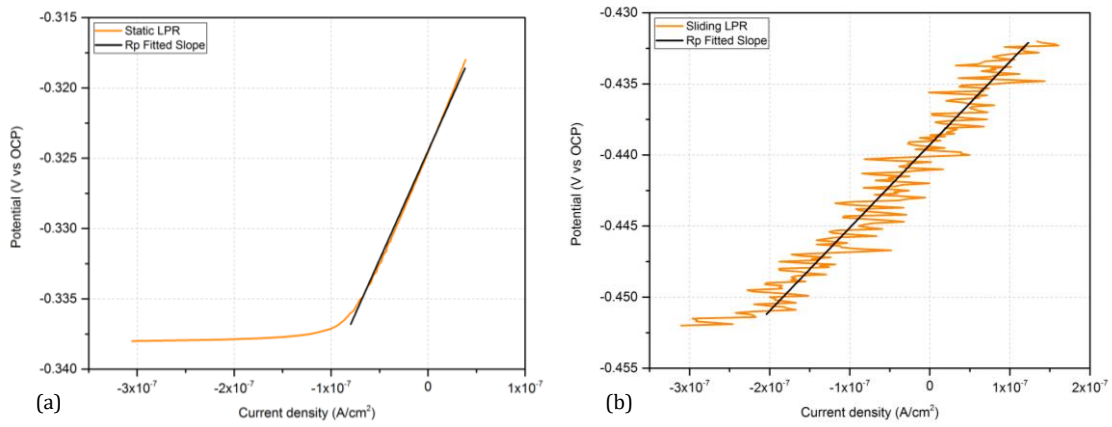

Figure 4.6 Example of polarisations during the LPR scan under (a) static and (b) sliding conditions

The obtained R_p can be converted into a corrosion current (I_{corr}) or corrosion current density using the Stern-Geary equation (Equation (2.12)) and a set value of Tafel constants (β_a and β_c in mV/decade unit) obtained from the polarisation curves data.

In this study, the LPR measurements were employed in each tribocorrosion test under the OCP condition. The potential was shifted from -10 mV to +10 mV, with a scan rate of 0.25 mV/s vs OCP in the present study. Intermittent LPR measurements were taken at 500 s after immersion, at 1.5 h intervals during the sliding and at 500 s after the test stopped quantifying the corrosion currents.

4.3.5 Potentiodynamic Scans

This present study performed potentiodynamic scans on the CoCrMo samples in various electrolytes, during both static and tribocorrosion/sliding conditions. For a potentiodynamic polarisation under static conditions, the tribometer bath was still employed to immerse the sample and associated electrodes, except without the pin and sliding motion.

The potentiodynamic scans in this study began with the OCP condition to monitor the E_{corr}. The potential was polarised in the anodic or cathodic direction to a vertex potential of +/- 1 V at a scan rate of 0.25 mV/second. Anodic and cathodic polarisations were conducted on fresh samples each time to avoid any changes occurring in the surface chemistry owing to the application of potential in either the anodic or cathodic domain following OCP stabilisation. Potentiodynamic tests were conducted for the Results Chapter 6 (both anodic/cathodic polarisations) and Chapter 8 (starting from -50 mV vs the stable OCP value, anodically shifted to +1 V).

Figure 4.7 shows the corrosion current density as a response to the tested sample over the potential shifting ranges. There are several variables and regimes of anodic potential in a passive-type material, as follows:

- Corrosion potential (E_{corr}) and corrosion current (I_{corr}); where the cathodic and anodic curves intersect between the cathodic and active/transitional regimes.
- Critical point of the potential (E_{cp}) and current (I_{cp}); where the current stops increasing after transitional regime and starts to reduce drastically.
- Passive potential (E_p) and passive current (I_p); where the current starts to have a constant current density over a passive regime after the reduction.

- Pseudo-passive potential (E_{pp}) and pseudo-passive current (I_{pp}); where the current starts to have a constant current density without a reduction over some potentials (termed as pseudo-passive regime).
- Transpassive/pitting/breakdown potential (E_b); where the current starts to re-increase after passing the passive (or pseudo-passive) regime.

On the other hand, the cathodic polarisation curve consists of typical regimes [130, 134]:

- Activation polarisation regime; where the cathodic current increases as a function of the applied cathodic potential, starting from E_{corr}. In this regime, the reduction reaction is controlled by activation energy (ion charge transfer), where the O_2 reduction or water reduction (in lower potential) take place.
- Concentration polarisation regime; where the increasing current slope is saturating at a limited value due to the diffusion-controlled mass transport. The limited reduction reaction is determined by the transport rate at which the O_2 may diffuse in the electrolyte.

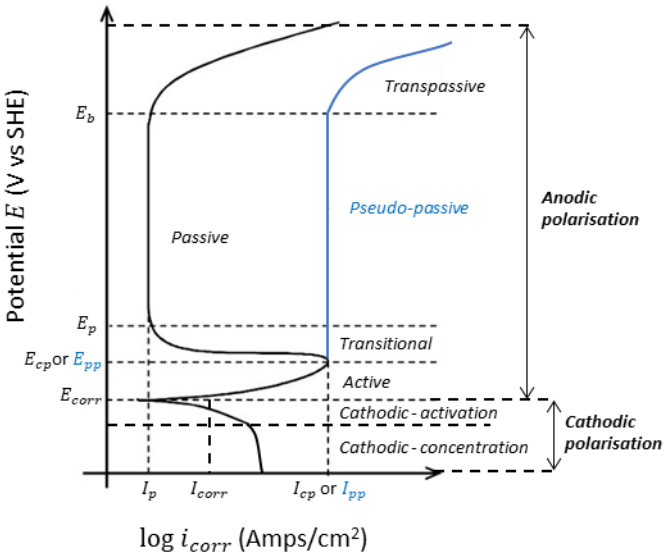

Figure 4.7 A typical plot of polarisation measurement with its potential regimes over the current density from ASTM G3-89 [313, 314]

4.3.6 Corrosion Volumetric Loss

The corrosion volumetric loss can be calculated using Faraday's Law. Firstly, the corrosion current I_{corr} (Ampere), resulting from LPR at OCP (or a net current from the potentiostatic test at the anodic potential), was integrated over the tribocorrosion test time t (s) to obtain the total charge transfer of ions removal, Q (Coulomb) in Equation (4.1), which passed through a substance [199].

$$Q = \int_0^t I_{corr}\, dt \qquad \textbf{(4.1)}$$

Figure 4.8 illustrates a transient corrosion current (Current vs Time plot), obtained from the LPR scan during a tribocorrosion test. In terms of the synergistic approach, the area shaded in green corresponds to the ion charge transfer due to pure corrosion (C_0). On the other hand, the area shaded in blue represents the increase in charge transfer due to the wear-enhanced corrosion (ΔC_w). However, the method also works for any corrosion current from LPR or net current from the anodic potentiostatic conditions.

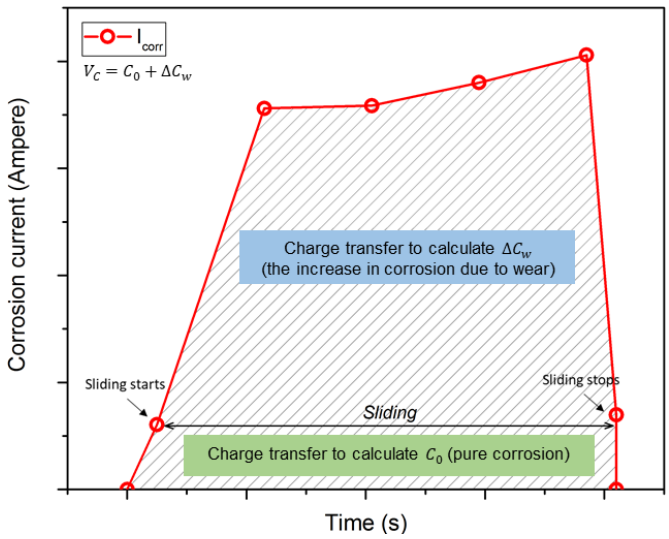

Figure 4.8 LPR plot integration to calculate the total charge transfer

After obtaining the charge transfer from the corrosion current, Faraday's Law was used to estimate a mass loss (m) of metallic surface resulting from corrosion components as in Equation (4.2). The Faraday's constant was 96,500 C/mol and the molar mass (M) was 55.7 g/mol, obtained from the stoichiometric average of the CoCrMo alloys' composition. Therefore, the valence number (n) was 2.4 and density (ρ) was 8.29 g/cm^3. These values were similar to those used in previous studies with the CoCrMo sample [141, 196, 199]. The estimated mass loss was divided by the value of material density, as in Equation (4.3), to estimate the corrosion loss in volumetric unit (V).

$$m = \frac{M.Q}{n.F} \tag{4.2}$$

$$V = \frac{m}{\rho} \tag{4.3}$$

4.3.7 Potentiostatic Tests

Potentiostatic polarisation aimed to monitor the transient anodic or cathodic net current behaviour with a fixed (static) potential established between the WE and RE. The sample can be either a net anode or a cathode, depending on the overpotential applied. The potentiostat keeps the fixed potential of the working electrode, maintained by the reference electrode. The current flows between the working electrode and counter electrode, which is measured for the duration of the tribology test. The data could be plotted as a transient anodic or cathodic net current change over time.

Potentiostatic tests have been widely used to investigate tribocorrosion and the de-passivation mechanism of materials [204, 315, 316]. The anodic net current from a potentiostatic test can be only indicative of oxidation at the sample surface. Therefore, the metal ionic release from the surface might be more significant into the electrolyte than into the OCP or cathodic condition. On the contrary, the potentiostatic in a fixed cathodic potential was considered to inhibit the metal surface's oxidation. By applying more cathodic potential during sliding, the

corrosion damage can be avoided and the pure mechanical wear loss (W_0) can be measured at the surface. Potentiostatic tests, under both static and sliding conditions, were employed for the Results Chapter 6. The application of the potentiostatic technique in this study is explained at the end of the chapter. Figure 4.9 shows a schematic of the tribocorrosion test protocol under an applied potential (potentiostatic). Samples (n=3) were immersed in OCP to stabilise the surface passivation for 500 s, and then a constant potential was applied. The tribological condition was applied at 60 s potentiostatic. The potentiostatic tests remained in a sliding condition for 2 h.

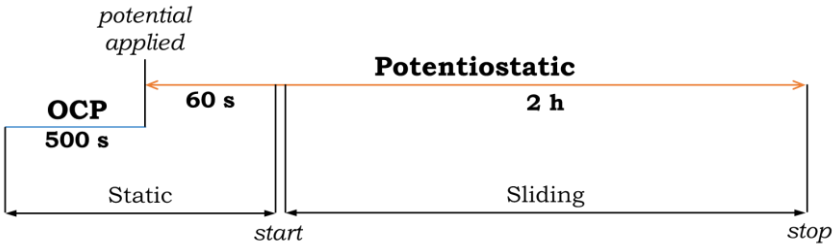

Figure 4.9 Schematic of the tribocorrosion test protocol under the applied potential (potentiostatic)

4.3.8 Electrochemical Impedance Spectroscopy (EIS)

The EIS technique is utilised to characterise the change in the electrochemical properties at a metallic surface with respect to the impedance behaviour under specific conditions. The equivalent electrical circuit (EEC) utilised for impedance data fitting at the passive alloy under the OCP condition is similar to the passive potential condition. This similarity is due to the fact that a passive film can be formed under both the OCP and passive conditions. Figure 4.10 shows a schematic of the EEC used for impedance under OCP/passive conditions at the electrolyte-CoCrMo interface in this study. Since the condition used (Chapter 8) is OCP, therefore, this type of EEC circuit can fit all samples in this study.

The equivalent circuit shows electrolyte resistance (R_s), followed by the time constants attributed for the charge transfer resistance of the outer layer R_{out}/CPE_{out} (representing an inhomogeneous passive film or biofilm if there are any biological species in the electrolyte) and inner layer R_{in}/CPE_{in} (passive oxide

resistance). The EIS spectra at the passive condition typically produces a high impedance value with a capacitive behaviour due to a superposition between the two semi-circle arc/time constants. This method has shown a good fit to data for the CoCrMo alloy, utilised in previous studies [95, 163, 166, 317].

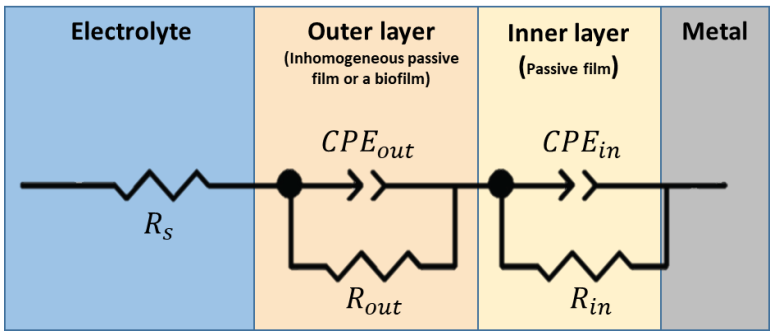

Figure 4.10 Schematic of the EEC for impedance under OCP/passive conditions at the electrolyte-metal interface

Therefore, this study (Chapter 8) used EIS to investigate the effect of dissolved metal ions in the control electrolytes (saline electrolyte and bovine serum) on the electrochemical behaviour at the electrolyte-CoCrMo interface. The impedance tests were also observed before and after the sliding tests. The CoCrMo samples were constantly polarised at a stable OCP value from 10^5 Hz to 10^{-3} Hz with 10 data cycles/decade and an AC amplitude of ±10 mV, as utilised in several studies [163, 167]. The obtained data were analysed using Autolab NOVA 2.1 software (Metrohm Autolab B.V., Netherlands) and fitted to the corresponding EEC for the OCP condition.

4.4 Post-Test Wear Analysis

Surface analysis in this study was only conducted for the worn CoCrMo alloy surfaces, subjected to tribocorrosion. The measurements consist of film formation analysis after the tribocorrosion tests, utilising Scanning Electron Microscopy (SEM), Energy Dispersive X-Ray Spectroscopy (EDS), X-Ray Photoelectron Spectroscopy (XPS) and Atomic Force Microscopy (AFM). The samples were then

cleaned extensively before the surface profiling to measure the total volume loss using Vertical Scanning Interferometry (VSI). The methodologies used are described in the following sub-sections.

4.4.1 Scanning Electron Microscopy (SEM)

Scanning Electron Microscopy (SEM) was used to observe the worn surface morphology and film depositions at the surface. SEM was operated to obtain the surface characteristics of worn CoCrMo surfaces in a high resolution to the nanometre (nm) scale. The magnitude of the electron wavelengths that bombarded the surface sample can be several orders smaller than conventional light microscopes. Moreover, SEM was instrumented with Secondary Electron (SE) and Back-Scattered Electron (BSE) detectors. These detectors can support SEM to take a contracted image that indicates elements with a different molecular weight of compounds at the surface. Figure 4.11 shows an EVO MA 15 SEM (Carl Zeiss, Germany) employed in this study, with an accelerating voltage of 10 kV.

Figure 4.11 Carl Zeiss EVO MA15 Scanning Electron Microscope

4.4.2 Energy Dispersive X-ray Spectroscopy (EDS)

Energy Dispersive X-ray Spectroscopy (EDS), enabled the observation of the chemical elements on the sample surface. The electron beam is used to excite the emission, allowing electron transfer through the inner shell electron to the outer

shell. The x-ray beam is sensitive to the level of elemental energy, therefore EDS can identify the chemical elements that appear on the surface, represented by the brightness and contrast parameter, to describe the characteristics and distribution of an element signal.

The present study predominantly used the map scanning method by EDS. The map results were analysed using licensed software, Aztec (Oxford Instruments, UK) by applying the 'TruMap' feature to obtain a more accurate data quantification [196]. Previous studies [1, 318] characterised that typical elements; e.g. carbon, nitrogen, sulphur, oxygen and metallic traces, were found on the retrieved implant surface. EDS is employed in all result chapters in this study. The atomic weight percentage (at%) was taken from two spots inside the wear scar in each sample by EDS, as illustrated in Figure 4.12.

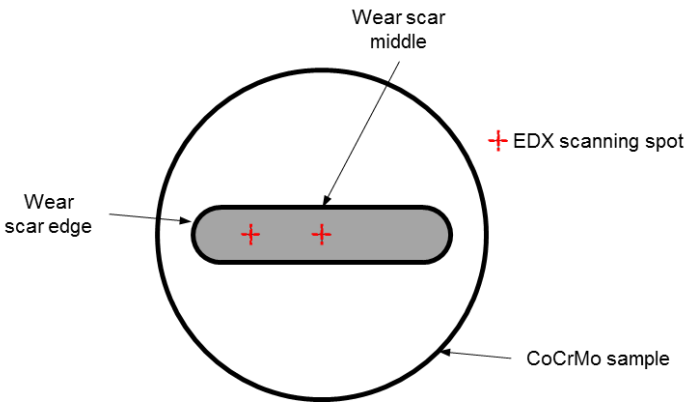

Figure 4.12 An illustration of EDS scanning spots on a worn CoCrMo surface

4.4.3 X-ray Photoelectron Spectroscopy (XPS)

X-ray Photoelectron Spectroscopy (XPS) was utilised to investigate further the deposited film chemistry. XPS is capable of observing chemical compounds in more detail at the surface. The x-ray photons (hv) can ionise the atoms within bulk material or compounds by ejecting the inner core electrons. Therefore, the required energy to eject these electrons is equivalent to the electron's Binding Energy (BE).

This study used a K-Alpha™ + XPS (Thermo Fisher Scientific, USA), which offered a better quantification of the detected elements while using high-resolution scanning when compared to the general scanning feature. Instead of analysing several

nanometres of the sample sub-surface, the x-ray photoelectrons penetrated to a micrometre's depth in high resolution. In this state, it is possible to characterise the passive film with nanometres thickness and the bulk materials. The etching process allowed the atomic composition of detected elements to be assessed in depth from the outer surface. By using a Ta_2O_5 standard, the XPS etched 9 nm of the surface depth per 10 s.

The XPS produced element peaks that observe the chemical bonding reactions as a result of tribocorrosion tests. Licensed CasaXPS software was utilised for the fitting processes before the peaks were interpreted in the proper regime of binding energy (eV). A background removal feature named 'Shirley' was chosen during the fittings. Also, a charge correction using the Aliphatic C 1s was conducted in every fitting process at 284.8 eV as a calibration point. Several parameters, e.g. the Full-Width Half Maximum (FWHM), peak shapes and BE, were referred from valid webpage repositories and previous literature studies [30, 95, 319-321]. XPS would appear to characterise only the film formation in Chapter 5 of this study.

4.4.4 Atomic Force Microscopy (AFM)

Atomic Force Microscopy (AFM) (Bruker, USA) was employed to observe the surface roughness and high resolution of the topography images of deposited films at the worn samples. The AFM was operated by moving a measurement probe on a cantilever over the expected surface with an atomic force and mechanism. The probe tip can sense surface properties, causing a deflection of the cantilever while moving. The cantilever simultaneously deflected a laser from the diode to a position-sensitive photodetector. The photodetector was able to produce a signal with a feedback loop. In the end, the signal was processed by a piezoelectric scanner which generated positions (x,y,z) with equal accuracy to the output.

The higher resolution of the topography and data processing in this study was obtained by using licensed NanoScope Analysis software (Bruker, USA). The peak-force tapping mode was used to generate the mapping inside the wear scar on the samples after the tribocorrosion tests. This method was relatively easy to operate and able to minimise any damage and lateral forces inflicted on the sample compared with the intermittent contact mode. The cantilever was made of silicon

nitride, with a 0.977 Hz resonance frequency and 40 N/m spring constant. The scans were taken of a 5x5 μm area, at different spots (n=3). In the present study, AFM was employed in Chapters 7 and 8.

4.4.5 Vertical Scanning Interferometry (VSI)

Vertical Scanning Interferometry (VSI) (NPFlex, Bruker, USA) was conducted to obtain sample surface profiles as three-dimensional topography and measure the total volume loss of the samples after sliding. VSI used white light and surface reflection to generate fringes with a magnification lens of 10x. The results were proceeded by the Vision64 software (Bruker, USA) to generate three-dimensional images. The topography images allow the wear scar contour and volume to be calculated after the appropriate removal of the surface form and filter functions. The total volume loss was measured by adjusting the layer height to calculate all points below the plane.

White light from the source passes through the beam splitter, which is diffracted in different directions. Light is reflected towards the reference mirror and the second to the sample surface. Then the two lights are recombined and captured using the camera, which eventually produces the visual image. The principle is to calculate the difference in the phases between the two waves that result from the interference as fringes. The fringes indicate the surface's vertical height and depth variation and generate the surface mapping by a piezoelectric actuator [322]. An example of the measurement results can be seen in Figure 4.13.

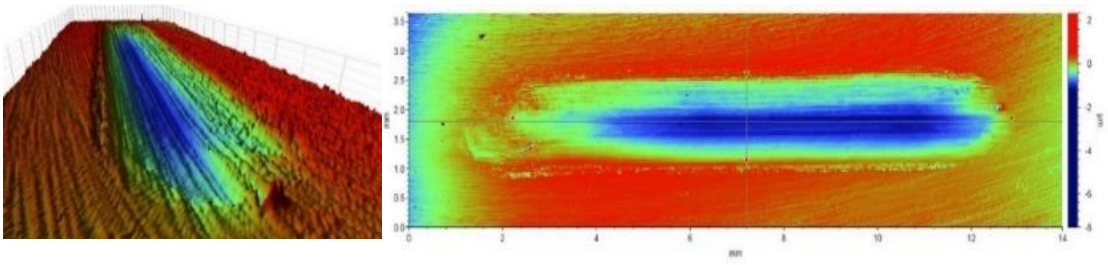

Figure 4.13 The 3D mapping of a wear scar on a sample surface

This present study used SWRs as a result, which were calculated according to Archard's Law (1953) [323] as utilised in previous studies [324, 325]. Equation (4.4) [326] shows that the specific wear rate (SWR) (μm^3/N.m) is calculated using the total volume loss V_{total} (μm^3) divided by the constant normal load W (N) and sliding run distance ΔS (m). The sliding run distance can be calculated by multiplying a sliding velocity (m/s) with running time (s). Thus, this present study used 144 m, 216 m, 432 m and 648 m for 2 h, 3 h, 6 h and 9 h sliding, respectively. The SWRs approach would be attributed to compare the sample volume loss in all of the results chapters throughout this study.

$$V_{total} = SWR \times W \times \Delta S \quad \textbf{(4.4)}$$

4.5 Tribocorrosion Analysis

As mentioned in Chapter 2, the mechanical wear mechanism will accelerate the corrosion process that coincides between two bodies under tribological process. In addition, the electrochemical process at the contacting surface will increase the mechanical wear rate. As a result, all of the components can be accumulated as a total of the degraded materials. In this study, both synergistic and mechanistic approaches were used to analyse the tribocorrosive behaviour under such testing conditions.

4.5.1 The Tribocorrosion Synergistic Approach

In this study, the ASTM G119 standard [215] was used to calculate the material loss of the CoCrMo samples after the tribocorrosion test. The ASTM standard consists of four contributors: pure mechanical wear (W_0), pure corrosion (C_0), and the wear and corrosion combinations (S), based on a formula by Watson et al. (Equation (4.5)) [205]. The synergistic component S can be subdivided into the increase in wear loss due to corrosion dissolution (corrosion-enhanced wear; ΔW_c) and the increase in corrosion loss due to mechanical wear (wear-enhanced corrosion; ΔC_w).

$$V_{total} = W_0 + C_0 + S$$

$$V_{total} = W_0 + C_0 + (\Delta W_c + \Delta C_w) \quad \textbf{(4.5)}$$

Where:

V_{total} : Total of material loss

W_0 : Rate of material loss without corrosion presence

C_0 : Electrochemical corrosion rate without mechanical wear

ΔW_c : The increase in wear loss due to corrosion dissolution (corrosion-enhanced wear)

ΔC_w : The increase in corrosion loss due to mechanical wear (wear-enhanced corrosion)

S : Synergetic component (both wear and corrosion) of material loss

In this study, all material loss contributors were converted into 'volume loss' with the volumetric unit of micrometre-cubic (μm^3) and obtained by referring to the ASTM G119 standard as follows:

- V_{total} was measured by VSI and further termed 'total volume loss'. The definition was an accumulation of the material loss after a tribocorrosion test.
- C_0 and ΔC_w were estimated from the corrosion current measured by LPR scans around OCP during static immersion and the tribocorrosion process, respectively. Faraday's Law was used to convert electrochemical currents into volume loss.
- W_0, further termed 'pure mechanical wear loss', was measured by VSI after the potentiostatic sliding test at the cathodic potential (at -0.8 V in Chapter 6 result).
- ΔW_c was calculated by subtracting the V_{total} with W_0, C_0 and ΔC_w.

The synergistic behaviour of corrosion and wear can be estimated by the ratio between corrosion-enhanced wear (ΔW_c) over the wear-enhanced corrosion (ΔC_w).

The interactions were classified into: antagonistic, antagonistic-synergistic and synergistic [220], as follows:

- Antagonistic : $\Delta W_c/\Delta C_w < 0.1$
- Antagonistic-synergistic : $1 > \Delta W_c/\Delta C_w \geq 0.1$
- Synergistic : $\Delta W_c/\Delta C_w > 1$

4.5.2 The Tribocorrosion Mechanistic Approach

A dominant mechanism, either electrochemical corrosion or mechanical wear processes upon the total material degradation, can be estimated using a mechanistic approach by Uhlig's formula [204]. Based on the studies by Stack et al. [327, 328], the total volume loss (V_{total}) can be categorised into V_W and V_C for the volume loss due to mechanical wear and electrochemical corrosion components, respectively (Equation (4.6)). Since the total volume loss (V_{total}) has been measured by VSI and the corrosion volume loss (V_C) was estimated via Faraday's Law, resulting from either the LPR at OCP or a net current from the potentiostatic test at anodic potential, therefore, the wear volume loss (V_W) can be subtracted.

$$V_{total} = V_W + V_C \quad \textbf{(4.6)}$$

Where:

V_W : Volume loss due to mechanical wear components

V_C : Volume loss due to electrochemical corrosion components

The mechanism of tribocorrosion can be determined by the ratio between the corrosion loss (V_C) and the wear loss (V_W) [327, 328]. Therefore, the relation between the total material loss with electrochemical corrosion and mechanical wear loss can be estimated under such tribological conditions. The following criteria identify the dominating tribocorrosion mechanisms:

- Wear : $V_C/V_W \leq 0.1$
- Wear-corrosion : $0.1 < V_C/V_W \leq 1$

- Corrosion-wear : $1 < V_C/V_W \leq 10$
- Corrosion : $V_C/V_W > 10$

4.6 Statistical Analysis

All of the results are presented as an average attributed with the error bar (standard deviation/SD). A statistical analysis was conducted using a one-way analysis of variance (ANOVA). The number of tested samples (n) was categorised into specific variables (e+.g., potential condition, electrolyte and test duration) as comparative groups. An ANOVA test can determine whether or not the electrolytes significantly affected the charge transfer during tribocorrosion, volume loss and roughness average. The level of significance used $\alpha = 0.05$ for comparison with a P-value in all of the mentioned comparisons. The compared results that are significantly different ($p < 0.05$) are marked by an asterisk (*).

4.7 Overall Experimental Protocol

Figure 4.14 shows a flow diagram summarising the overall experimental protocol followed throughout this study. This chapter explains the underpinning experimental techniques employed to address the research question. Each Result Chapter had a different aim and objectives; therefore, a specific setup, condition and protocol were applied for each experiment.

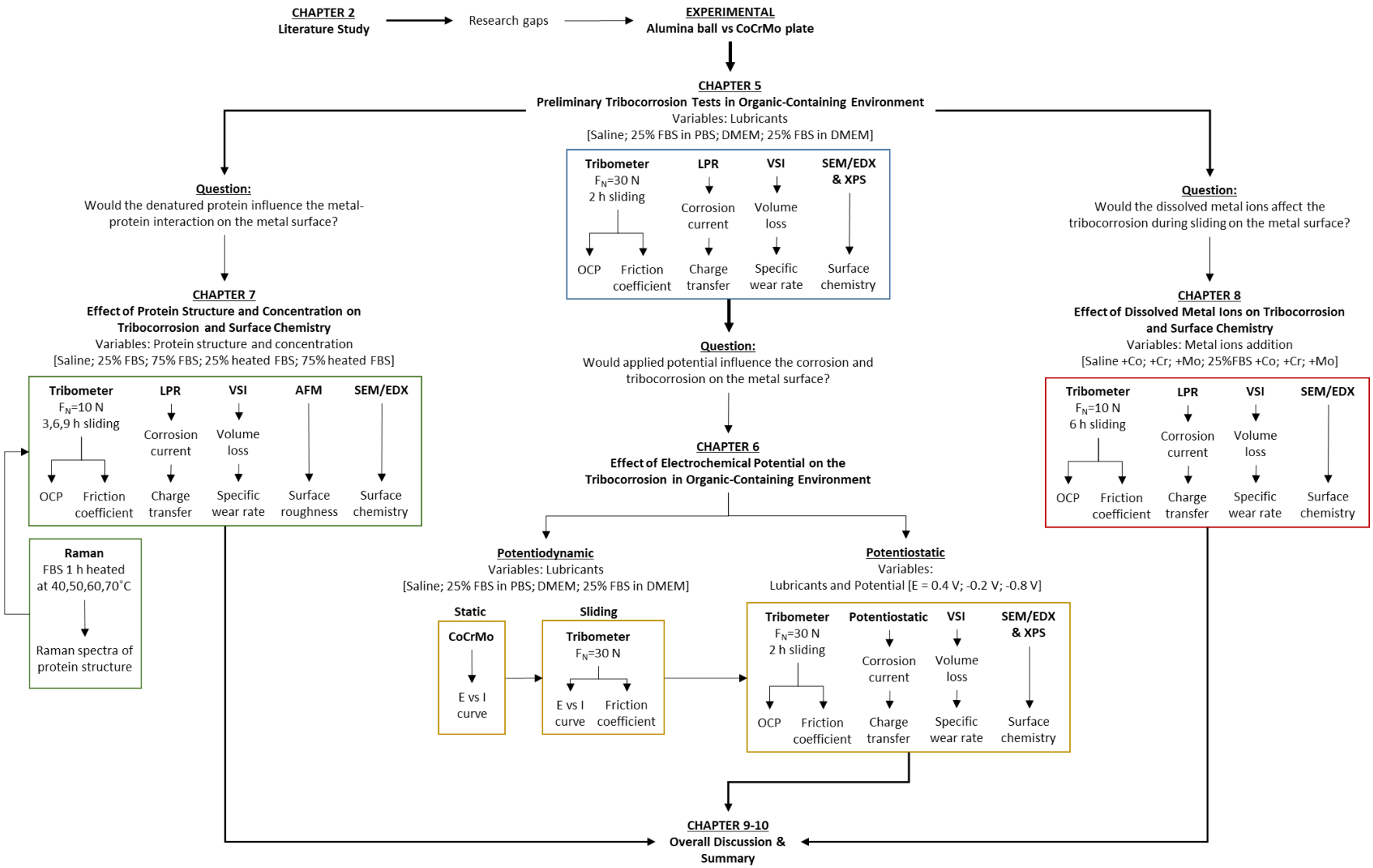

Figure 4.14 Overall experimental workflow

Chapter 5
The Effect of Organic-Containing Electrolytes on Tribochemistry and Tribocorrosive Behaviour at the CoCrMo Alloy

5.1 Chapter Introduction

The fundamental mechanisms of wear and corrosion are recognised as primary factors in overcoming orthopaedic implants' 'lack-of-longevity' problem. However, studies have struggled to achieve a last-longer implant (>20 years lifespan) due to the current lack of a complete understanding of the complex nature of the implant's working environment [11, 304]. The tribochemistry aspect in the hip bearing system is known to affect tribocorrosive behaviour at the material surfaces. The tribochemical reactions, e.g. corrosion and film formation, can be generated by a reaction between the materials and biological fluids [329]. Although biotribology in hip bearings is a growing research field, aspects such as the role of the electrolyte constituents on tribochemistry and tribocorrosion synergism on metallic surfaces, remain largely unknown. Across the literature and ISO/ASTM standards, a number of lubricants and electrolytes are described, with evident appreciation of the tribochemical/tribocorrosion processes.

Therefore, Chapter 5 reports the efforts to investigate the tribochemical and tribocorrosion interactions between organic-containing electrolytes and CoCrMo alloy surfaces at OCP. The research questions to be answered in this chapter are:

- What is the role of electrolyte on the tribocorrosion mechanisms and material loss synergies? This aspect of the investigation will consider commonly-used simulated biological fluids.
- What are the tribochemical films' characteristics on CoCrMo alloys tested at OCP under tribocorrosion, with and without the presence of organic species?
- What is the effect of the aforementioned tribofilms' formation on surface friction, wear and corrosion behaviour?

Detailed information about the tests and post-test analysis can be found in the methodology chapter (Chapter 4). The tribofilms' formation and its effect on the tribocorrosion were discussed. Figure 5.1 shows an overview of the experimental protocol and the outcomes discussed in this chapter. The 2 h sliding test results were discussed to analyse the effect of the organic-containing electrolyte on friction and tribocorrosion loss, as well as the wear scar characteristics by SEM, XPS and VSI. Also, 2 h potentiostatic-sliding tests (Figure 4.9) at cathodical protection (E=-0.8 $V_{Ag/AgCl}$) were conducted to obtain the pure mechanical wear loss (W_0). Therefore, the tribocorrosive behaviour in each electrolyte could be investigated by adopting the synergistic approach.

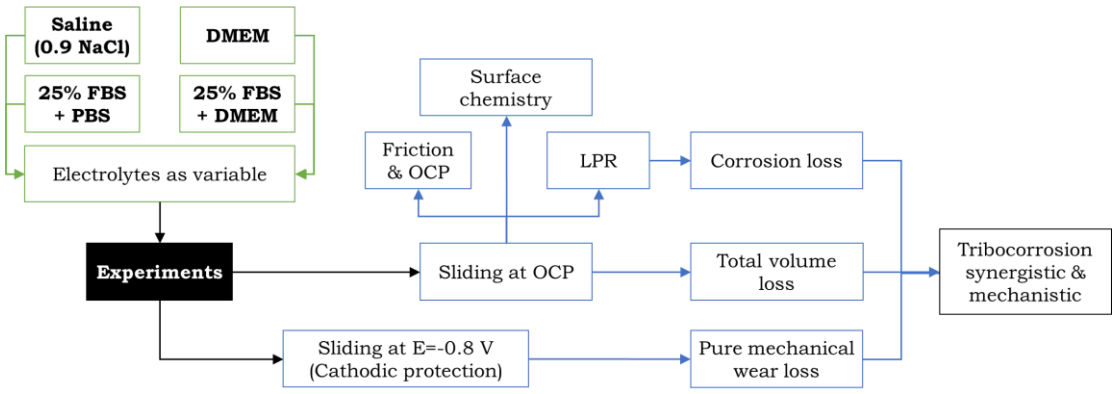

Figure 5.1 Schematic diagram of the experiments in Chapter 5, including the preliminary results of the tribocorrosion test at OCP and characterisation of surface chemistry

5.2 Tribocorrosion Tests

The tribocorrosion tests (n=3) were conducted at the Open Circuit Potential (OCP). Figure 5.2 illustrates the tribocorrosion test protocol.

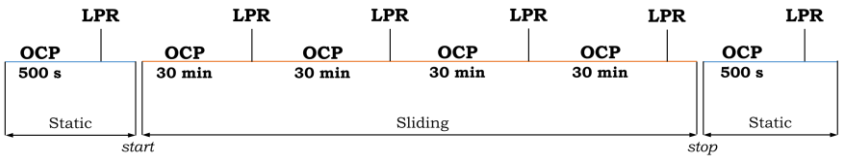

Figure 5.2 Schematic of the tribocorrosion tests' protocol

OCP was measured in static conditions for 500 s to ensure that the passivation became stable. A 2 h sliding test was applied while simultaneously measuring the transient coefficient of friction and OCP. To monitor the corrosion behaviour, LPR was taken at 500 s after the initial immersion, at 30 min intervals during the sliding and at 500 s after the sliding stopped.

5.2.1 Coefficient of Friction (COF)

Figure 5.3a shows the transient coefficient of friction/COF (μ) over the 2 h tribocorrosion test at the OCP condition. The COF in saline electrolyte was the highest when compared with organic-containing electrolytes, starting at μ~0.35 ± 0.02 then gradually increasing over time to μ~0.37 ± 0.02 at the end of the sliding. The friction in the organic-containing electrolytes had a high initial coefficient, reaching a maximum of μ~0.27 ± 0.05 within the running-in stage, then spontaneously decreasing into a steady-state of μ~0.14 ± 0.01.

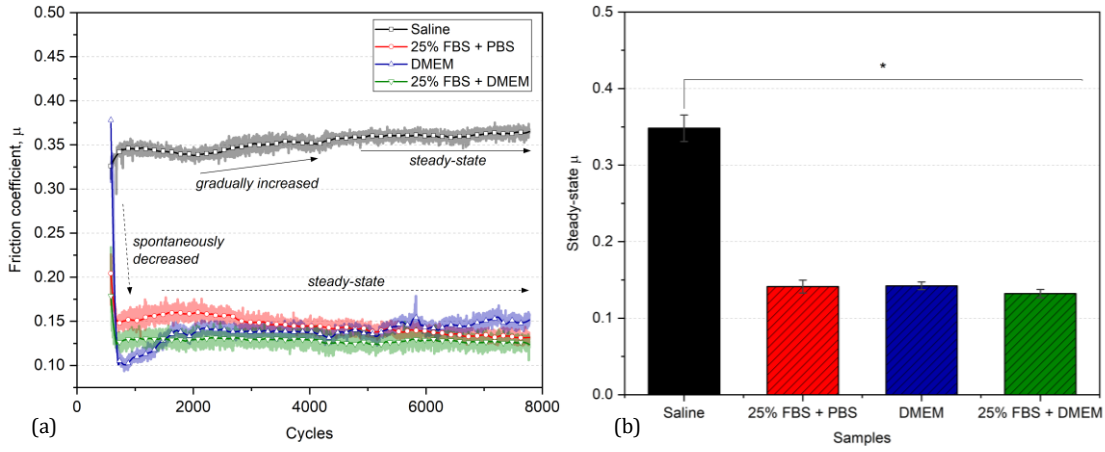

Figure 5.3 (a) The evolution of the transient COF over 2 h of sliding cycles and (b) the average of the steady-state COF in all electrolytes under OCP conditions (n=3; SD bar; *p<0.05)

Figure 5.3b shows the steady-state COF (μ) (average steady-state during the final 60 cycles in the sliding test; sample (n) = 3) with standard deviation (error bar). Significantly higher friction was observed in saline electrolyte when compared to organic-containing electrolytes. No significant difference in the steady-state μ

average was observed between 25% FBS and DMEM-containing electrolytes, within an interval of μ∼0.13 to 0.14 ± 0.01.

5.2.2 OCP Measurements

Figure 5.4 shows the transient OCP evolution during early immersion (pre-sliding), tribocorrosion testing and after the test (post-sliding) in all electrolytes. The OCP value in all electrolytes was observed to increase gradually over time under static immersion conditions. During sliding, the transient OCP signals tended to fluctuate more compared to static and post-sliding due to the reciprocating motion. The de-passivation of the CoCrMo was observed upon the start of sliding after the tests were conducted in saline electrolyte [8], i.e., less noble OCP when compared to the static condition and steadily reduced during sliding. For samples tested in organic-containing electrolytes, the de-passivation of the CoCrMo was also seen upon the start of sliding, except when followed by the re-passivation process (restoring the OCP towards the value in the static condition). The OCP value in DMEM was stable/time independent during the sliding condition. However, for 25% FBS + PBS and 25% FBS + DMEM, the OCP of CoCrMo was observed gradually to reduce (after being re-passivated) over time during sliding, then entered a steady-state after ∼5,000 cycles until the end of sliding. The OCP spontaneously increased (the re-passivation process) immediately after the sliding stopped in all electrolytes, and was even higher than the OCP in the pre-sliding condition.

In the pre-sliding stage, CoCrMo in saline electrolyte had a higher (more noble) OCP at -0.29 V when compared to 25% FBS + PBS at -0.40 V. No difference in the OCP was observed between: saline electrolyte and 25% FBS + PBS in the sliding and post-sliding stages, as well as the 25% FBS + PBS and 25% FBS + DMEM samples in all test stages. The OCP for DMEM was higher (more noble) when compared to saline electrolyte and 25% FBS + PBS in the static immersion and sliding stages. Furthermore, the 25% FBS + DMEM decreased (less noble) the OCP when compared to the as-received DMEM in all stages.

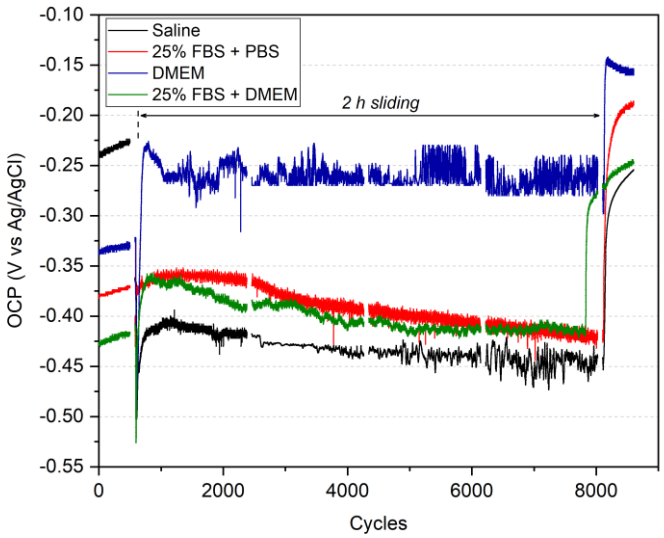

Figure 5.4 The evolution of transient OCP per the stages over static and tribocorrosion tests in all electrolytes (n=3)

5.2.3 Corrosion Volume Loss

Figure 5.5a shows the evolution of the current density, measured by LPR during 2 h tribocorrosion tests. In all cases, lower current densities were observed during the static corrosion stages (pre- and post-sliding) when compared to the sliding stage. During sliding, the saline electrolyte sample tended to result in higher current densities when compared to the organic-containing electrolytes. The use of 25% FBS content was observed to reduce the current densities when compared to samples tested in saline and DMEM electrolytes.

Figure 5.5b shows the average total charge transfer from all tribocorrosion test durations. The volume loss owing to corrosion (V_C) after the 2 h tribocorrosion test can be estimated and attributed via the total charge transfer and application of Faraday's Law (Equation (4.2) and Equation (4.3)). CoCrMo surfaces tested in saline electrolyte had a significantly higher total charge transfer when compared to CoCrMo surfaces tested in organic-containing electrolytes. A significant decrease in the charge transfers was seen with the use of 25% FBS-containing electrolytes when compared to CoCrMo tested in saline electrolyte and as-DMEM. No significant difference in the total charge transfer after 2 h of sliding was observed between the 25% FBS + PBS and 25% in DMEM samples. Table 5.1 shows the conversion of the

total charge transfer to the corrosion volume loss (V_C) during the tribocorrosion tests.

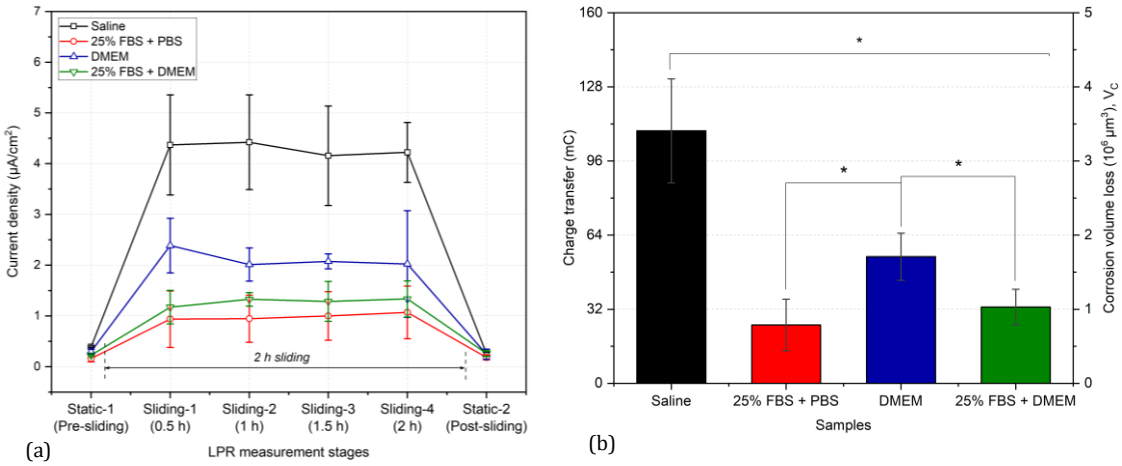

Figure 5.5 (a) The evolution of the corrosion current density, measured under static and tribocorrosion conditions; (b) the total charge transfer and corrosion volume loss during tribocorrosion in all electrolytes (n=3; SD bar; *p<0.05)

Table 5.1 The total charge transfer and corrosion volume loss (V_C) during tribocorrosion at OCP in all electrolytes (n=3; ±SD)

Electrolytes	Charge transfer, Q (mC)	Corrosion volume loss, V_C (x 10^6 μm³)
Saline	109.00 ± 22.49	3.42 ± 0.71
25% FBS in PBS	25.20 ± 11.17	0.79 ± 0.35
DMEM	54.70 ± 10.13	1.72 ± 0.32
25% FBS in DMEM	32.96 ± 7.65	1.04 ± 0.24

5.3 Post-Test Wear Analysis

The wear analysis of the CoCrMo samples tested in all electrolytes involved SEM and chemical analysis (XPS) and total volume loss (VSI) alongside the SWR calculation.

5.3.1 Electron Microscope Analysis

Figure 5.6 shows SEM images of the CoCrMo wear scars after the tribocorrosion tests in all electrolytes. The wear scar on the sample tested in saline electrolyte was observed to have a greater width (~509.73 μm), with traces of abrasive grooves, than the organic-containing electrolytes (~367.67 μm measured for 25% FBS-containing electrolyte). The layers dominated the tip corner and outside of the wear track, indicating the removed passive film during sliding and its reformation. A clear indication of the layers covering the wear scar's inside and edges were observed on the sample tested in 25% FBS and DMEM-containing electrolytes. Organic species originating from the bovine serum and oxide traces from passive reformation were hypothesised to present on the wear scar of the samples tested in organic-containing electrolytes.

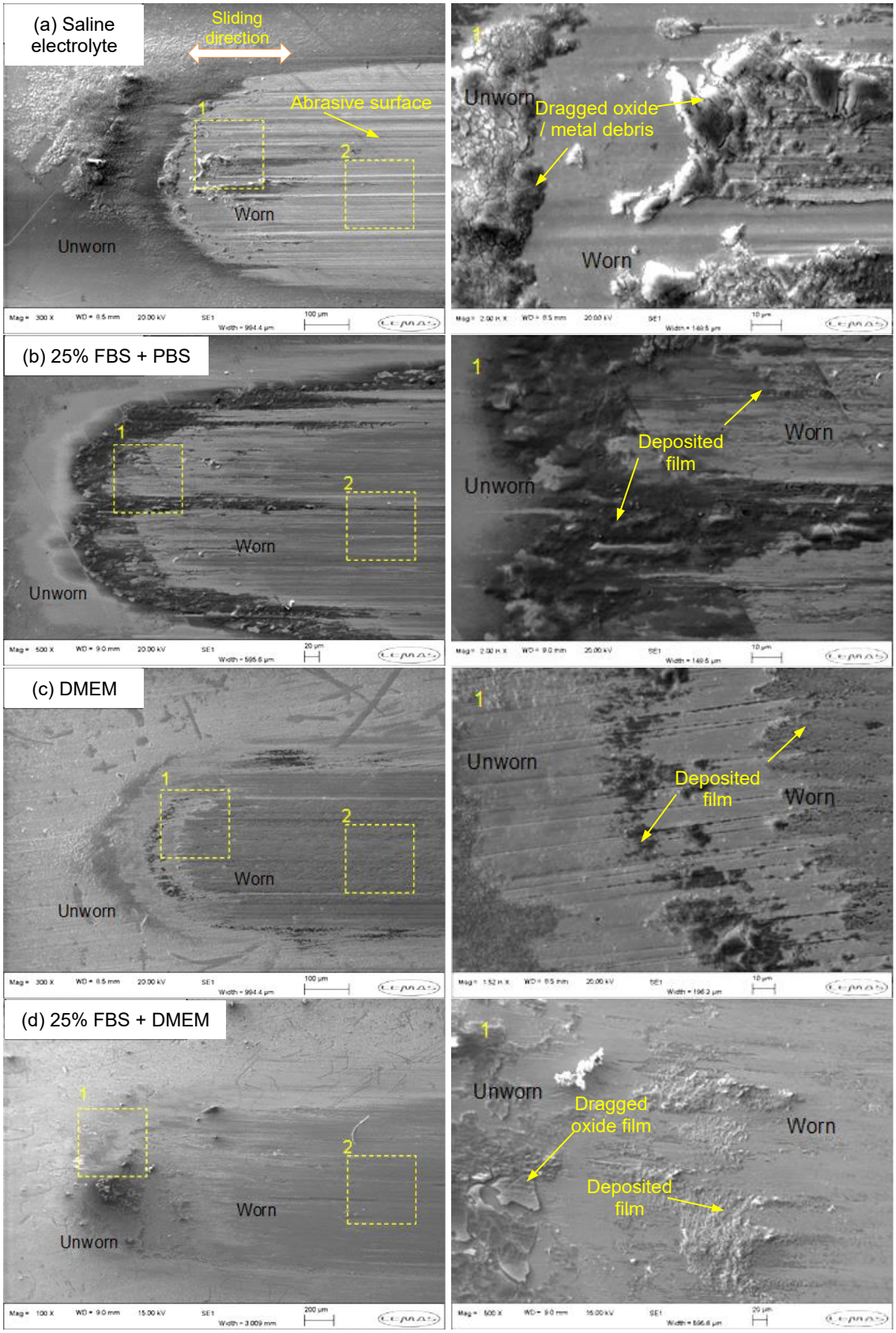

Figure 5.6 SEM on the wear track of CoCrMo alloys after 2 h sliding test at OCP in (a) saline electrolyte, (b) 25% FBS + PBS, (c) DMEM and (d) 25% FBS + DMEM

5.3.2 Chemical Analysis of the Surface Films

Figure 5.7 shows the elemental composition (as an atomic percentage or at%) as a function of depth, determined by XPS analysis, for both inside and outside the wear scars. The graphs present cross-sectional views of the film's composition, from the very top to approximately 90 nm in depth.

The cobalt (Co 2p peaks), chromium (Cr 2p peaks) and molybdenum (Mo 3d peaks) increased with increasing etching time, suggesting the formation of a surface film [330, 331]. An oxide element (O 1p peak) at the wear scar of the saline electrolyte samples was observed at a profiling depth of ~27 nm, which was higher at% when compared to the outside of the wear scar. There was no carbon or proteinaceous species deposited on the saline electrolyte samples, as expected.

A proteinaceous film with a thickness of ~45 nm was deposited inside the wear scar of the 25% FBS samples, dominated by the carbon and phosphorus signals. Sulphur was a dominant element inside the wear scar on the DMEM sample. In the 25% FBS-containing electrolytes, high carbon, nitrogen, and phosphorus concentrations were observed at the CoCrMo surfaces, indicating the precipitation of bovine serum species.

The presence of 25% FBS + DMEM seemed to reduce the carbon percentages when compared to the as-received DMEM sample. In the DMEM, the carbon percentage was observed to be lower than the sulphur, phosphorus and calcium. Magnesium can be seen in the DMEM-containing electrolytes, since DMEM comprises magnesium sulfate ($MgSO_4$-$7H_2O$) as one of its inorganic salts.

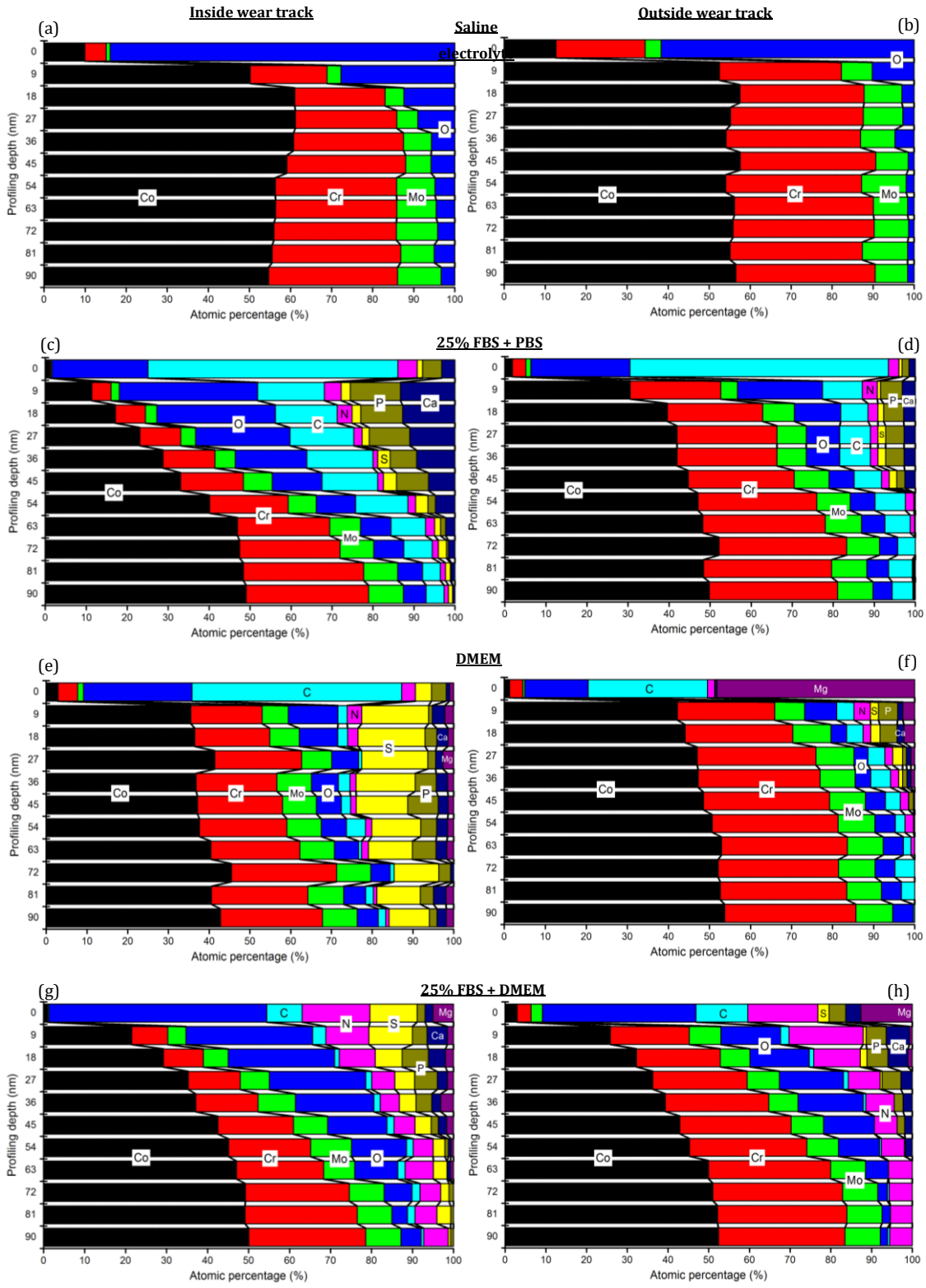

Figure 5.7 XPS atomic concentration from the top surface to a 90 nm depth profiling on both inside (left-hand side row) and outside the wear scar (right-hand side row) on the tested samples in (a and b) saline electrolyte, (c and d) 25% FBS + PBS, (e and f) DMEM and (g and h) 25% FBS + DMEM at the OCP condition

5.3.3 Total Volume Loss

5.3.3.1 At the OCP Condition

Figure 5.8a compares the total volume loss at the OCP condition (V_{total}) on the CoCrMo after 2 h tribocorrosion tests in all electrolytes. Table 5.2 shows the conversion of total volume loss (V_{total}) to SWR during tribocorrosion. The V_{total} in saline electrolyte (6.77 ± 0.91) x 10^6 μm^3 was the highest after 2 h of sliding when compared to the samples tested in organic-containing electrolytes. An increasing V_{total} was observed in 25% FBS + PBS after 2 h of sliding when compared to the DMEM sample. No significant difference in the V_{total} was observed between samples tested in 25% FBS + PBS and 25% FBS + DMEM.

Figure 5.8b shows cross-sectional profiles of the wear scar after 2 h of sliding in all electrolytes. A lower point in wear depth and a more significant lateral width were seen in samples tested in saline electrolyte, reaching ~ -5 µm and <5 mm respectively, when compared to organic-containing electrolytes. The sample tested in 25% FBS + PBS showed deeper wear (~ -2.9 µm) when compared to samples tested in the DMEM-containing electrolytes.

Table 5.2 Total volume loss at OCP (V_{total}) and the SWR of the wear scar on CoCrMo in all electrolytes over 2 h sliding tests (n=3; ±SD)

Condition	Electrolytes	Total volume loss, V_{total} (x 10^6 μm^3)	SWR (x 10^3 μm^3/N.m)
OCP	Saline	6.77 ± 0.91	1.57 ± 0.21
	25% FBS in PBS	4.25 ± 0.55	0.98 ± 0.13
	DMEM	3.04 ± 0.39	0.70 ± 0.09
	25% FBS in DMEM	3.10 ± 0.63	0.72 ± 0.15

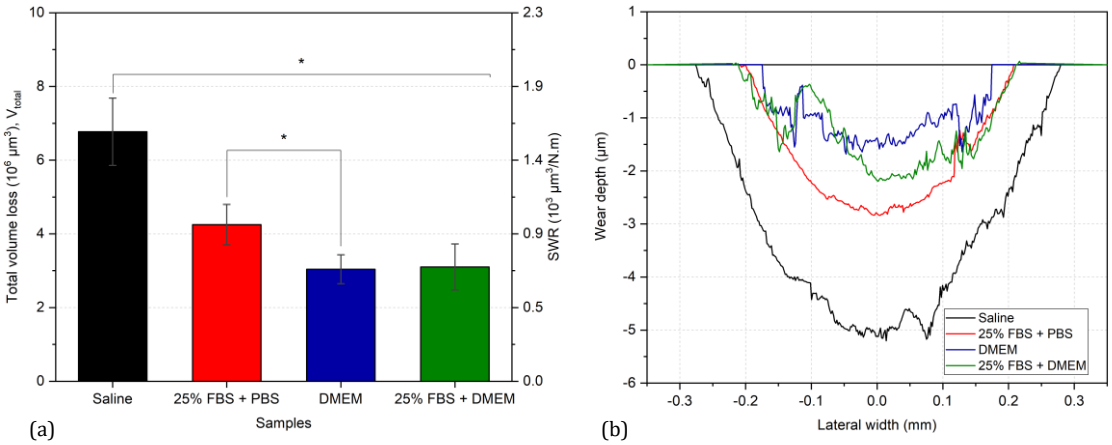

Figure 5.8 (a) Total volume loss (V_{total}) and SWR (n=3; SD bar; *p<0.05) and (b) a cross-sectional view of the wear scar on CoCrMo in all electrolytes over the 2 h tribocorrosion tests at OCP

5.3.3.2 At the E=-0.8 V Condition

In Figure 5.9a, the evolution of the transient net current during 2 h sliding at E = -0.8 V (vs RE Ag/AgCl) potentiostatic was observed to have negative values, owing to the cathodic protection. Therefore, the electrochemical degradation owing to corrosion can be neglected on the CoCrMo surface and the total material loss obtained was purely due to mechanical wear degradation. Figure 5.9b shows the total volume loss at E = -0.8 $V_{Ag/AgCl}$ (or pure wear volume loss, W_0) at the CoCrMo after 2 h sliding in all electrolytes. The W_0 in saline electrolyte (2.36 ± 0.20) x 10^6 µm^3 was observed to be significantly higher when compared to samples tested in the organic-containing electrolytes. No significant difference in W_0 was observed between the 25% FBS + PBS, DMEM and 25% FBS + DMEM samples during 2 h of sliding. Table 5.3 shows the conversion of W_0 to SWR after 2 h sliding. The surface analysis (SEM) for all samples tested at E=-0.8 V is presented in Chapter 6.

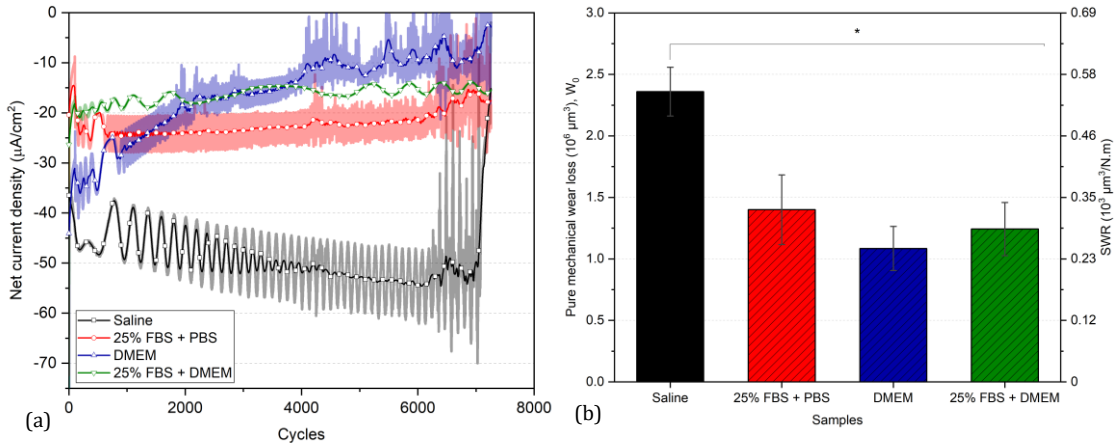

Figure 5.9 (a) Transient net current during 2 h sliding and (b) total volume loss and SWR on CoCrMo after the 2 h sliding tests at potentiostatic E=-0.8 V (cathodic protection) in all electrolytes (n=3; SD bar; *p<0.05)

Table 5.3 Total volume loss at E=-0.8 V (W_0) and the SWR of the wear scar on CoCrMo in all electrolytes over the 2 h sliding tests (n=3; ±SD)

Condition	Electrolytes	Total volume loss, (W_0) (x 10^6 μm³)	SWR (x 10^3 μm³/N.m)
E = -0.8 V	Saline	2.36 ± 0.20	0.55 ± 0.05
	25% FBS + PBS	1.40 ± 0.28	0.32 ± 0.07
	DMEM	1.09 ± 0.18	0.25 ± 0.04
	25% FBS + DMEM	1.24 ± 0.22	0.29 ± 0.05

5.4 Chapter Discussion

This present study aimed to investigate the tribochemical interactions between electrolytes containing organic matter and their interactions with a CoCrMo alloy under tribocorrosion conditions. Based on the results obtained, this sub-section discussed the effects of organic species on the tribochemistry and tribocorrosive behaviour at the CoCrMo surface after 2 h of sliding.

5.4.1 Tribochemistry of Metal-Proteinaceous Interaction

The XPS signals determined the tribochemical behaviour at the CoCrMo surface, showing the interaction between metal and protein species during the tribocorrosion test. Figure 5.10 shows that the Ca 2p peak inside the wear track had a higher concentration when compared to the outside. The signals of C 1s, O 1s and proteinaceous constituents are higher inside the wear track than outside it. The comparison of the atomic percentage, inside and outside the wear scar, indicated that proteinaceous-metal interactions are tribology-induced [332, 333]. In other words, the sliding condition causes the proteinaceous species to react. The FBS electrolyte contains calcium, albumin and alpha, beta and gamma-globulin, which have a native protein structure [334]. The native protein is predominantly constructed of carbon, nitrogen, oxygen, hydrogen, phosphorus and disulphide chains. Furthermore, the unfolded protein can adsorb at the metal surface and more easily react with the oxide and metal ions. A larger ratio between the Ca 2p inside and outside wear suggested that the DMEM is more reactive than the FBS since it already contains sulphur, amino acids and other minerals while being protein-free.

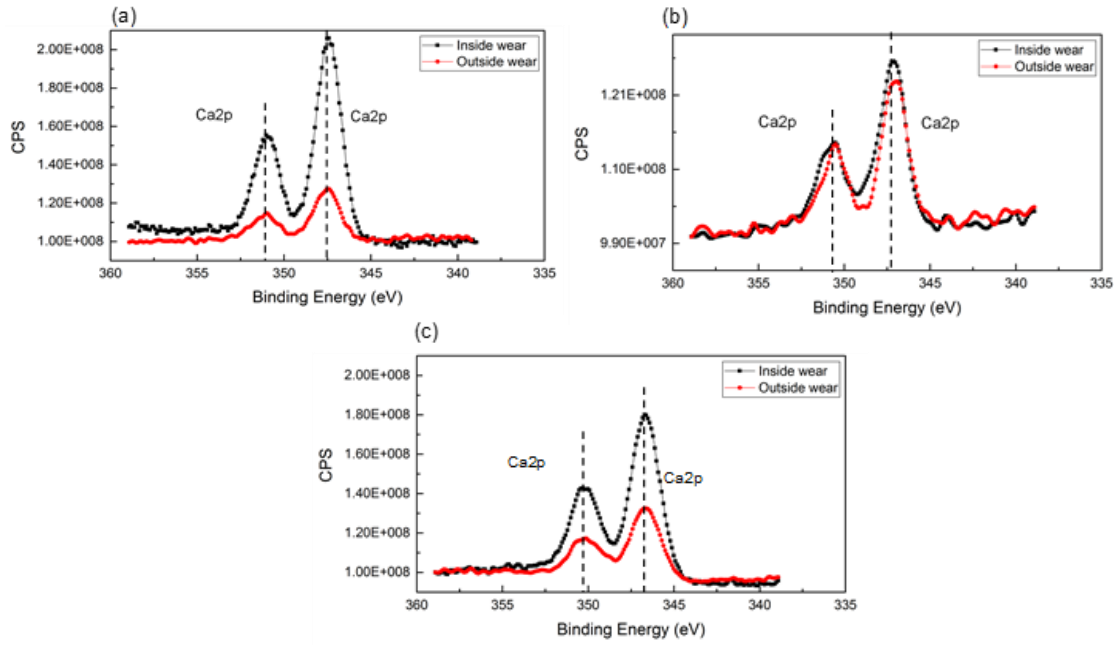

Figure 5.10. An XPS comparison of the calcium (Ca 2p) peaks inside and outside the wear scar in (a) 25% FBS + PBS, (b) DMEM and (c) 25% FBS + DMEM

The Ca 2p on both the FBS and DMEM samples had two different peaks, as the orbital split with the Ca 2p 3/2 binding energy of ~347.30 eV [335]. It was suggested that the calcium binds the other elements, such as calcium oxide (CaO), calcium hydroxide ($Ca(OH)_2$) and calcium carbonate ($CaCO_3$), with the binding energy of O 1s and C 1s are ~531.50 eV [336] and ~289.20 eV [337], respectively. The calcium hydrogen phosphate ($CaHPO_4$) also appeared in the XPS peaks interpretation, as the P 2p 3/2 has a binding energy of ~133.30 eV [337].

A strong phosphorus (P 2p) signal was detected within the wear scar tested in 25% FBS diluted PBS compared to the outside. Chromium phosphate ($CrPO_4$) appears on the CoCrMo specimens generated in both FBS and DMEM-containing electrolytes. The P 2p 3/2 shows a binding energy of ~133.40 eV [338] along with the Cr 2p 3/2 at ~577.80 eV [339]. $CrPO_4$ was found in a previous study to be a corrosion product on MoM bearing [340]. Cooper et al. [321] observed that chromium phosphate particles were observed within fibrin and tissue covering the joint surface.

Several tribochemical pathways are known to determine the formations of tribofilm and passive oxide reformation. However, without a thorough understanding of the chemical speciation of the tribofilms formed, the route to formation cannot be investigated. Figure 5.11 shows the carbon peaks' deconvolution (C 1s) obtained at the binding energy range ~280-292 eV. These could be fitted into five different peaks (~282.4 eV, 284.5 eV, 286.3 eV, 288.2 eV and 289.2 eV). Some organic compounds were bond metal ions and hydro-oxide elements [341].

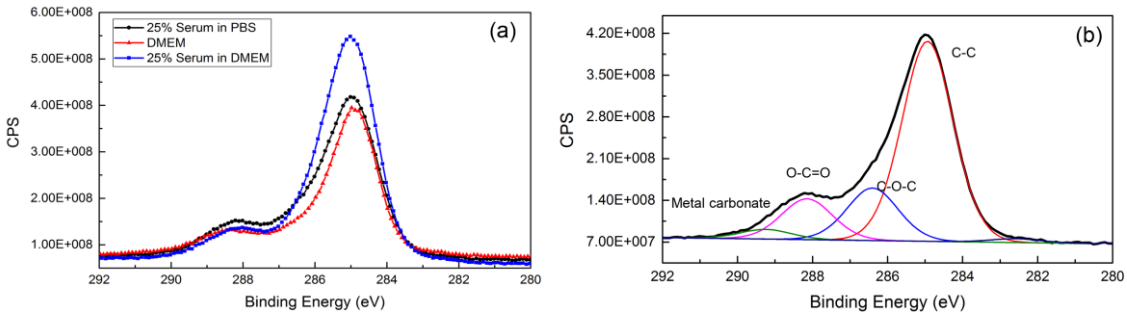

Figure 5.11. Carbon C1s signals (a) comparison and (b) each peak's interpretation

Figure 5.12 shows an XPS comparison of the Co 2p, Cr 2p and Mo 3d peaks inside the wear scar in all electrolytes. The Co 2p signal indicated peaks rising at 781.18 eV and 788.00 eV, indicating CoO and Co-satellite's existence, respectively [30, 139]. The areas of CoO and Co-satellite spectra significantly increased with the presence of FBS. The signal at the DMEM sample tended to be similar to the pre-tested sample. The traces of oxide (O 1s) represented the passive films formation (metal-oxide binding) after the reformation process [140, 330, 342]. The Cr 2p signal indicated the debris of $Cr(OH)_3$ and Cr_2O_3, with peaks at 577.50 eV and 576.28 eV, respectively [30, 103, 139, 320]. A higher ratio of oxide in the Cr 2p peaks was found in FBS-containing electrolytes.

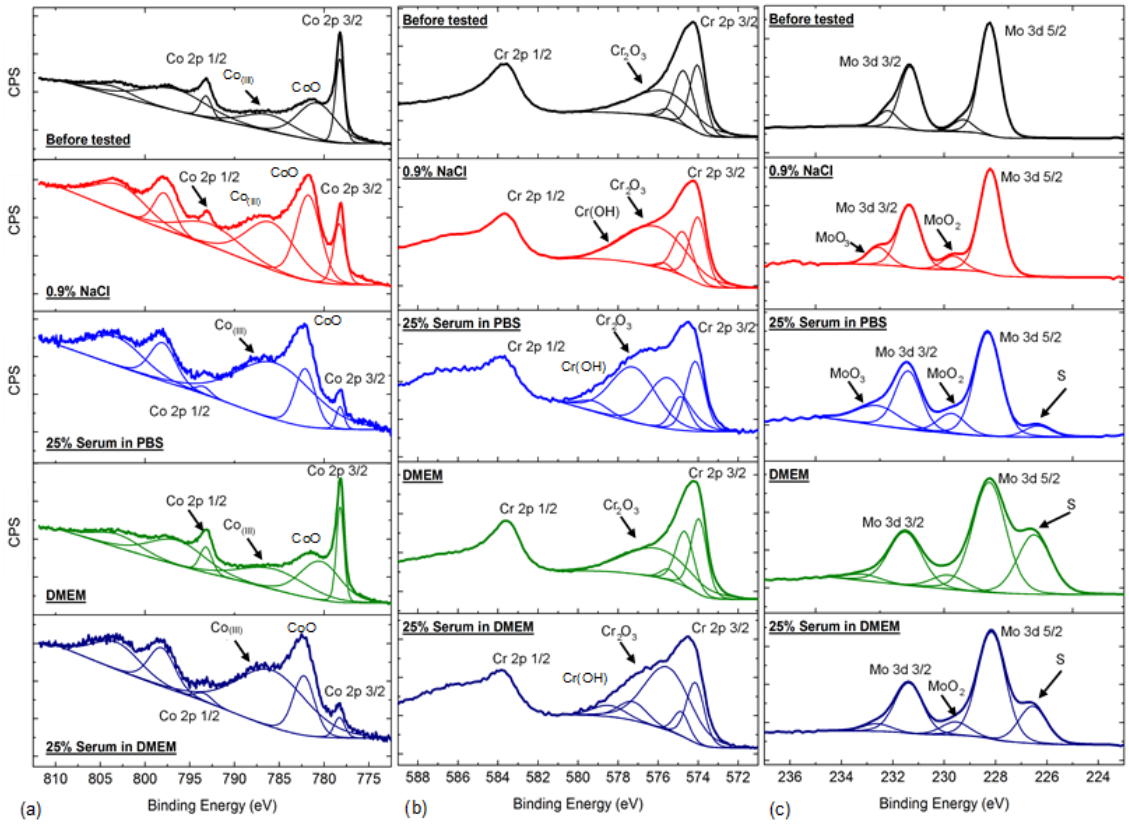

Figure 5.12 XPS comparison of (a) Co 2p, (b) Cr 2p and (c) Mo 3d peaks inside the wear scar in all electrolytes

The Mo 3d spectra show that the sulphur was identified at ~227.00 eV at the sample tested in organic-containing electrolytes. DMEM had a higher concentration of sulphur bond with molybdenum compared to 25% FBS + PBS. The MoO_2 and MoO_3

were resolved at 29.50 eV and 233.10 eV, respectively [30, 139]. The peaks showed that the MoO_2 and MoO_3 had stronger concentrations in the presence of FBS compared to the other electrolytes. All of the comparisons suggested that the FBS-containing electrolytes can enhance the rate of oxide-metal bonding reactions in the tribocorrosion condition.

5.4.2 Tribocorrosion in Different Electrolyte Species

Since this study employed sliding tests under cathodical protection, all of the tribocorrosive degradation contributors therefore can be estimated. Table 5.4 shows all of the obtained tribocorrosion contributors based on synergistic (C_0, W_0, ΔC_W and ΔW_C) and mechanistic (V_C and V_W) approaches.

Table 5.4 The volume loss of each contributors when using the synergistic and mechanistic approaches over the 2 h tribocorrosion tests (n=3; ±SD)

Electrolytes	Volume losses contributors (x 10^6 µm^3)						
	V_{total}	Synergistic				Mechanistic	
		C_0	W_0	ΔC_W	ΔW_C	V_C	V_W
Saline	**6.77 ± 0.91**	0.30 ± 0.05	2.36 ± 0.20	3.12 ± 0.31	0.99 ± 0.04	3.42 ± 0.71	3.35 ± 0.23
25% FBS in PBS	**4.25 ± 0.55**	0.16 ± 0.06	1.40 ± 0.28	0.63 ± 0.15	2.06 ± 0.11	0.79 ± 0.35	3.46 ± 0.23
DMEM	**3.04 ± 0.39**	0.26 ± 0.01	1.09 ± 0.18	1.46 ± 0.31	0.23 ± 0.14	1.72 ± 0.32	1.32 ± 0.10
25% FBS in DMEM	**3.10 ± 0.63**	0.23 ± 0.03	1.24 ± 0.22	0.81 ± 0.21	0.82 ± 0.20	1.04 ± 0.24	2.06 ± 0.42

Figure 5.13 shows (a) the %-contributions ratio and (b) the volumetric loss of each contributor in the tribocorrosive degradation using the synergistic approach over the 2 h sliding tests in all electrolytes. In Figure 5.13a, the total volume loss for the saline electrolyte and DMEM were dominated by %-ΔC_W with more than ~45%, followed by %-W_0 ~35% of their V_{total}. Furthermore, the %-C_0 and %-ΔW_C only

contributed below ~15% each in saline electrolyte and DMEM. The opposite behaviour is observed for the %-contributions in 25% FBS-containing electrolytes. The total volume loss for the 25% FBS + PBS was dominated by %-ΔC_W ~48% of the V_{total}, followed by %-W_0~36%, %-ΔC_W and %-C_0. For the CoCrMo tested in 25% FBS + DMEM, the contributions of %-ΔW_C and %-ΔC_W were similar, at ~26% of the V_{total} each. Therefore, the total volume loss in the 25 FBS + DMEM was dominated by %-W_0 ~40%, while the %-C_0 was only ~4% of the V_{total}.

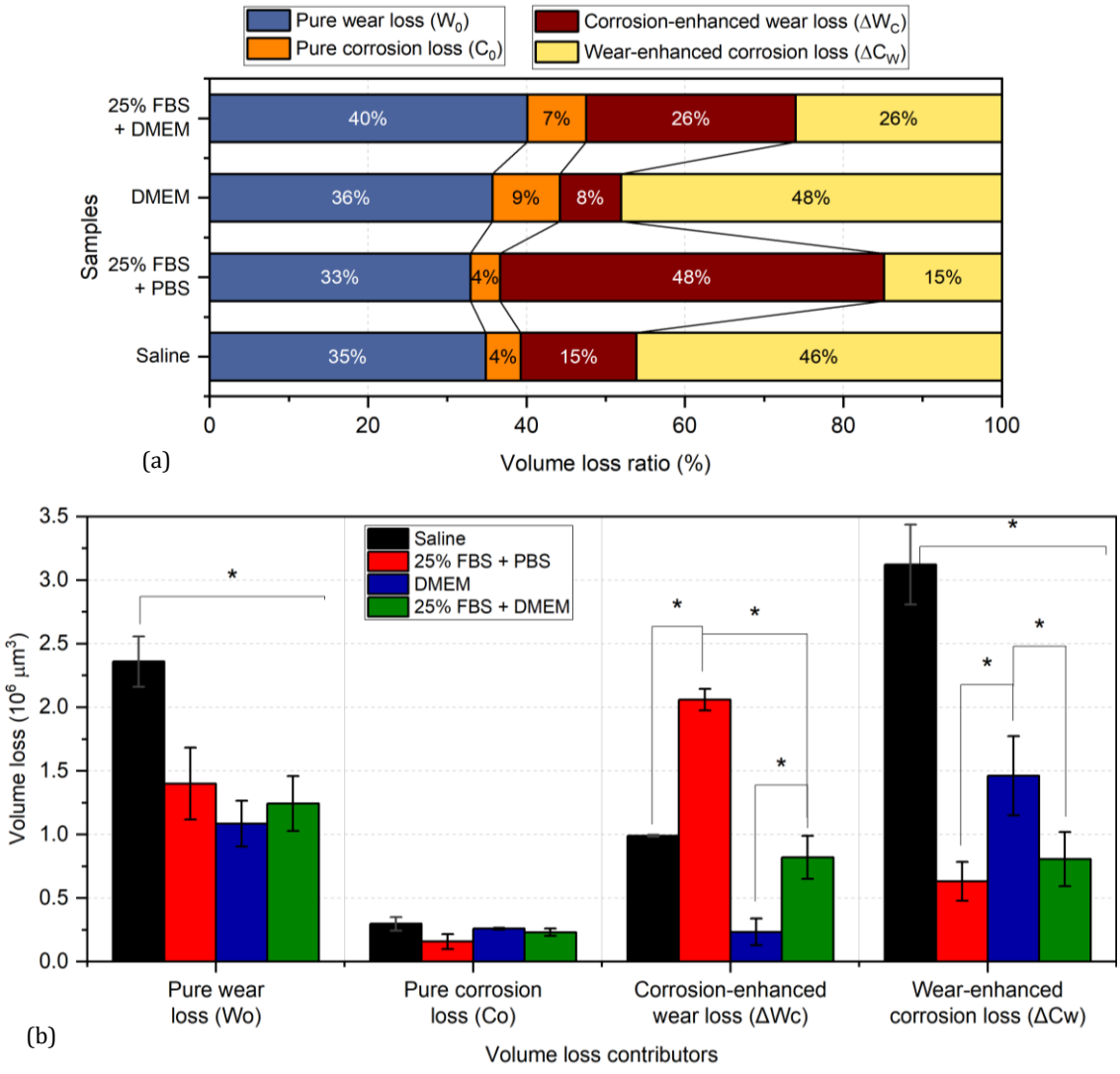

Figure 5.13 Ratio and (b) volume loss of each contributor when using the synergistic approach over the 2 h tribocorrosion tests (n=3; SD bar; *p<0.05)

Figure 5.13b shows that the C_0 was significantly lower when compared to the other volume loss contributors in all electrolytes. No significant difference was observed

in the C_0 between the samples in all electrolytes. As explained in Figure 5.9b, the W_0 in saline electrolyte was observed to be significantly higher when compared to samples tested in the organic-containing electrolytes. No significant difference in W_0 was observed between the 25% FBS + PBS, DMEM and 25% FBS + DMEM samples during the 2 h of sliding. The CoCrMo tested in 25% FBS + PBS had the highest ΔW_C, whilst the DMEM was the lowest when compared to the remaining electrolytes. The ΔW_C in saline electrolyte was seen to be higher when compared to the 25% FBS + DMEM after the 2 h sliding tests but was not statistically different. However, the 25% FBS + DMEM was seen significantly to decrease the volume loss of ΔW_C when compared to the sample tested in 25% FBS + PBS, suggesting an effect of DMEM content. On the other hand, the 25% FBS + PBS and 25% FBS + DMEM were observed significantly to reduce the ΔC_W when compared to the DMEM. The CoCrMo in saline electrolyte had the highest volume loss of ΔC_W when compared to the samples tested in organic-containing electrolytes. These trends indicate that the protein content in the FBS electrolyte tends to increase the corrosion-enhanced wear loss ΔW_C but can reduce the wear-enhanced corrosion loss ΔC_W contributor during tribocorrosion on the CoCrMo surface when compared to the protein-free electrolytes (saline electrolyte and DMEM, in this case).

Figure 5.14 shows the effect of electrolyte species on the tribocorrosive behaviour, which was compiled from all volume loss contributors. The interaction behaviour between the corrosion and wear processes ($\Delta W_C/\Delta C_W$) using the tribocorrosion synergistic approach [220] in all electrolytes were investigated in this study (Figure 5.14a). The synergistic interaction ($\Delta W_c/\Delta C_w > 1$) was observed for the 25% FBS + PBS, whilst the samples tested in saline electrolyte and DMEM indicated an antagonistic-synergistic interaction ($1 > \Delta W_c/\Delta C_w \geq 0.1$). The CoCrMo tested in 25% FBS + DMEM was seen to lie between the synergistic and antagonistic-synergistic regimes, suggesting the opposite role between the protein content in FBS and protein-free organic species in DMEM.

In Figure 5.14b, the tribocorrosion mechanistic maps [327, 328] were also determined to analyse the ratios between the respective volume loss owing to electrochemical corrosion (V_C) and mechanical wear (V_W). The tribocorrosion mechanism in the 25% FBS-containing electrolytes was observed to be dominated by the wear-corrosion mechanism within the ratio of $0.1 < V_C/V_W \leq 1$. The reason

for the wear-corrosion being dominant in the 25% FBS electrolytes is probably the distinctive effect of the protein content in reducing the corrosion process but increasing the mechanical damage on the CoCrMo surface during the sliding condition. The mechanistic behaviour is in good agreement with a study by Mathew et al. [221], showing that wear-corrosion dominated the tribocorrosive degradation at alumina-CoCrMo interfaces in bovine calf serum electrolyte. The study also explained that the wear-corrosion mechanism can be driven by the increasing mechanical degradation on the surface as a function of the increasing contact pressure. However, the corrosion-wear mechanism was seen to dominate the tribocorrosion process in saline electrolyte and DMEM. In this case, the reason for the corrosion-wear behaviour is the fact that the saline electrolyte and DMEM are protein-free electrolytes, which can lead to their increased role in the corrosion process.

As observed in Figure 5.8a, the total volume loss (V_{total}) of the CoCrMo after the 2 h tribocorrosion tests in saline electrolyte was the highest when compared to the samples tested in organic-containing electrolytes. No significant difference was observed between the wear and corrosion volume loss contributing to the total material degradation for saline electrolyte. Therefore, the role of organic species in FBS and DMEM electrolytes is significantly to reduce the total material loss during sliding when compared to saline electrolyte. An increase in the V_{total} was observed in the 25% FBS + PBS after the 2 h of sliding when compared to DMEM and the 25% FBS + DMEM samples. The material degradation with the presence of FBS was suggested to be more dominated by the volume loss owing to mechanical wear. This behaviour was indicated by the comparison between V_W in the 25% FBS + PBS and saline electrolyte (despite no significant difference), as well as the higher V_W in 25% FBS + DMEM when compared to the DMEM samples (refer to Figure 5.14b). However, the V_C in 25% FBS-containing electrolytes was lower when compared to saline electrolyte and DMEM in this study. Hence, the role of protein content in FBS was suggested to decrease the total material loss owing to corrosion's contribution during the tribocorrosion process. Mathew et al. [221] showed an inline result, suggesting that the protein content in bovine serum contributes to the protective film generation against the corrosive process during sliding.

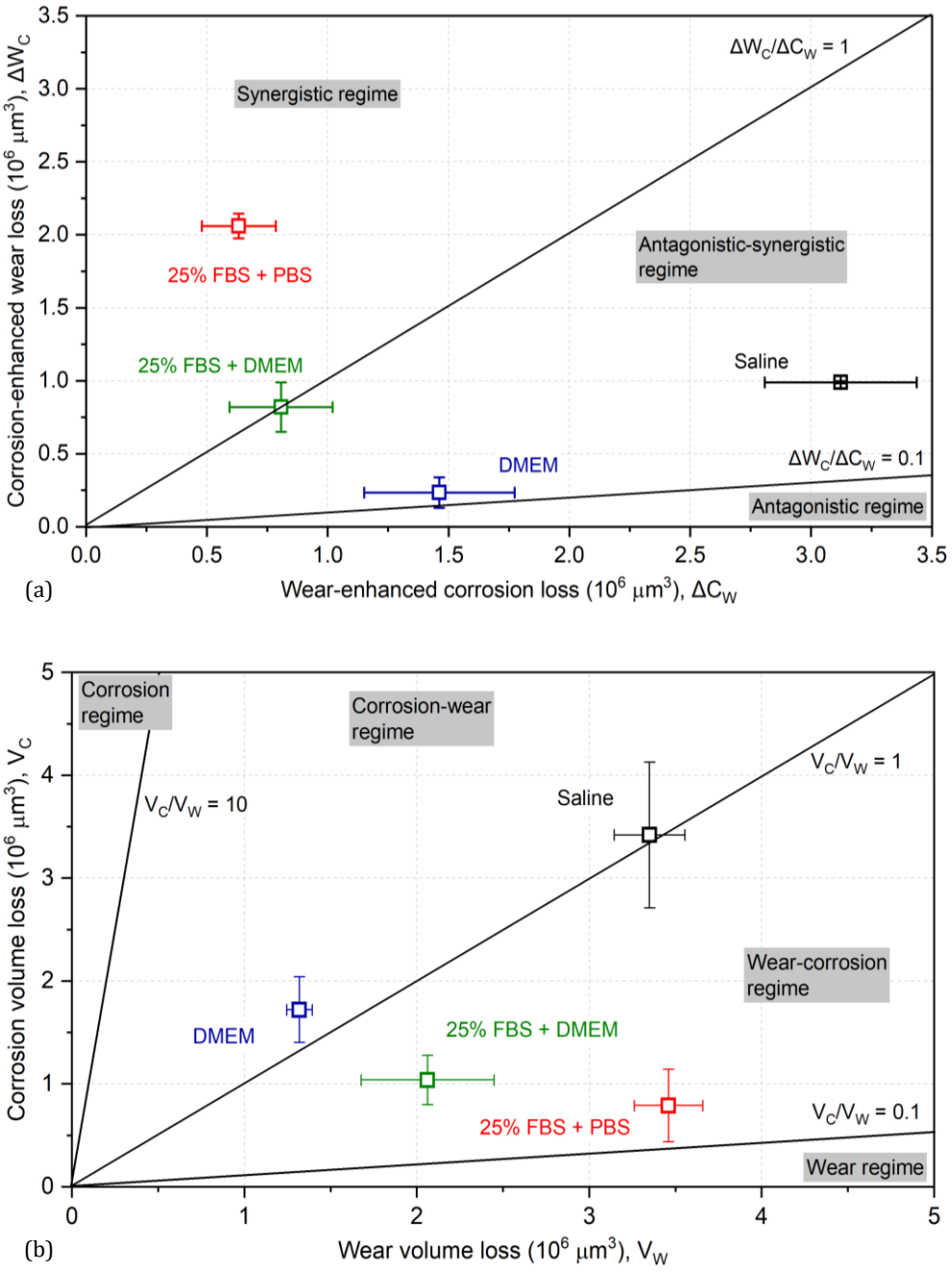

Figure 5.14 The role of the electrolytes on tribocorrosive behaviour using (a) synergistic and (b) mechanistic approaches after the 2 h sliding tests (n=3; SD bar)

5.4.3 Effects of the Tribochemistry on the Tribocorrosive behaviour

The COF was significantly lower in the presence of organic-containing electrolytes than when tested in saline electrolyte. The saline electrolyte sample showed the passive oxide film covering the metal surface as protection. The passive film was removed and reformed during the sliding condition. Although the re-passivation

process can reform the film, it takes time to oxidise the metal ion and become stable at the surfaces [343]. In the organic-containing electrolytes, proteinaceous constituents play a critical role in constructing the tribofilm. Proteins bind the metal ions which precipitate on the surface as a biofilm.

The total material loss significantly decreased for the DMEM sample when compared to samples tested in FBS-containing electrolytes. Amino acids and proteinaceous species in DMEM were suggested to act as a more reactive species at the CoCrMo surface. DMEM showed a lower SWR and wear volume loss, and a sulphur-rich layer was deposited on the substrate surface when compared to the FBS sample. There was an indication of the effect of sulphur concentrations in the Mo3d peak with wear resistance. The presence of sulphur on the surface tended to reduce the wear volume loss shown in several studies [344, 345]. This tribochemistry interaction is hypothesised to play an essential role in tribology behaviour, specifically with high sulphur content containing electrolyte.

The samples in FBS-containing electrolytes showed higher wear loss but a significantly lower corrosion loss contribution than the samples in saline electrolyte and DMEM. The higher mechanical wear process at the surface material was indicated in FBS-containing electrolytes due to the dominant abrasive wear. The wear scar at the FBS electrolytes showed several grooves found in SEM analysis (Figure 5.6), indicating that an abrasive removal had occurred. The aggregated proteins' content was hypothesised to act as the third-body within the sliding interfaces, contributing to the abrasion mechanism. The abrasive can also relate to the traces of oxide concentration in the Co 2p, Cr 2p and Mo 3d peaks. The XPS analysis showed that the presence of FBS tended to increase the ratios of CoO, $Cr(OH)_3$, MoO_2 and MoO_3. The debris of these metal-oxide formations was hypothesised to enhance the abrasive wear in the FBS and saline electrolyte.

The results outlined above are in line with the findings of previous studies [43, 346-348]. Catelas et al. [346] stated that abrasive wear played the main role in MoM THRs' failure and surgical revision. The mechanism can be hypothesised as ensuring that the debris produced from the surface removal will act as a third-body in FBS-containing electrolyte, describing the abrasive wear mechanism. The aggregated proteins became the third-body within the configuration. Proteinaceous species formed a barrier to reduce the material removal rate during sliding by

interacting with the metal surface. As a boundary electrolyte, the layers cover large surface areas, affecting the adhesive and abrasive wear [298]. Mathew et al. [302] observed that the presence of protein content from FBS resulted in a 23% decrease in the total volume loss in a CoCrMo disc. This indicated that the total volume loss follows a similar trend to the COF average. However, this study's friction only significantly differs between non-organic and organic-containing electrolytes, suggested to be due to the relatively higher contact pressure used during the test.

In this case, corrosion behaviour was linked to the total material loss's role but independent of the COF. The conductivity changes in each electrolyte might potentially affect the corrosion process during the tribocorrosion test. However, the protein adsorption was known to inhibit the oxidation reaction in the tribological condition. Thus, the oxidation of metal ions and the total charge transfer can be reduced due to the protein content from FBS. Lyvers et al. [129] showed good agreement in electrochemical behaviour at the CoCrMo surfaces with the results obtained in this study. The protein content suppressed the charge transfer and corrosion reaction at the exposed metal surface under mechanical wear, thus increasing the corrosion resistance of CoCrMo surface during sliding. Therefore, DMEM samples would fare better in terms of mechanical wear resistance but be more susceptible to corrosion during sliding. This is because the DMEM contains reactive species, such as high sulphur concentration and protein-free.

Furthermore, the constituents from serum protein and DMEM electrolytes play a role in the tribochemistry. The trace of $CaHPO_4$ was suggested to play an important role related to friction and wear reduction. The formation was caused by organic substances being affected by the shear stress, heat and pH conditions [349, 350]. Zhang et al. [351] used calcium phosphate as a coating on metal alloys or biomaterial implants and osseous defect treatments. Those tribofilms produce a robust lubrication effect during the tribological condition between two surfaces. The tribofilm behaviour will eventually be changed by the tribochemical reactions with the metal-organic interactions. Understanding the detailed mechanisms of electrolyte-metal interaction in building the film is very important in developing biomaterial design.

5.5 Chapter Summary

In this chapter, the role of organic species in electrolytes on tribochemistry and the formations of films at the CoCrMo alloy surface, tested in the tribocorrosion condition, were successfully investigated. Since the sliding tests were also conducted in the absence of corrosion (under cathodical protection), the organic species' effects on the tribocorrosive behaviour, via synergistic and mechanistic approaches, were also observed. The following points are offered to conclude this chapter:

- The presence of organic species in electrolytes significantly reduced the COF and material degradation rate when compared to CoCrMo tested in saline electrolyte. No significant difference was observed in the steady-state friction between the FBS and DMEM-containing electrolytes.
- Increasing carbon, nitrogen and phosphorus concentrations were observed at the CoCrMo surface in FBS-containing electrolytes, indicating the bovine serum species precipitated during sliding. Higher concentrations of sulphur, phosphorus and calcium were seen with the DMEM sample via XPS.
- The total material loss was significantly lower for the DMEM-containing electrolytes, when compared to the FBS samples. The high sulphur concentration from the DMEM, indicated in the Mo 3d XPS surface signal, was hypothesised to increase the mechanical wear resistance. Abrasive grooves were seen via SEM at the wear scar in the saline electrolyte and FBS-containing electrolytes.
- The protein content in the FBS significantly decreased the total charge transfer and volume loss owing to corrosion but increased the mechanical wear loss in the tribocorrosion process, when compared to the protein-free electrolytes. The sample in DMEM indicated an increase in mechanical wear resistance but was more susceptible to corrosion during sliding, due to its protein-free composition.
- The tribocorrosion mechanism in the FBS-containing electrolytes was dominated by the wear-corrosion mechanism with a synergistic interaction. However, the corrosion-wear mechanism and antagonistic-synergistic

interaction was observed to dominate the tribocorrosion process in the saline electrolyte and DMEM samples employed in this study.

Chapter 6
The Effect of Electrochemical Potentials on Tribocorrosion at the CoCrMo Alloy in Organic-Containing Environments

6.1 Chapter Introduction

Although the tribocorrosion synergisms have been detailed in the previous chapter, the effect of their electrochemical potential nature on the tribocorrosion mechanisms of a CoCrMo surface in different biological fluids is largely unknown. Therefore, it is essential to investigate the surface chemistry and tribocorrosive behaviour of CoCrMo surfaces when tested in organic-containing electrolytes under different electrochemical potential conditions.

Chapter 6 reports this investigation into the influence of electrochemical potential conditions on the tribochemistry and tribocorrosion of the CoCrMo alloys in organic-containing electrolytes. The research questions to be answered in this chapter are:

- What are the effects of applied electrochemical conditions on the resultant surface morphology and chemistry after tribocorrosion tests?
- What are the effects of applied electrochemical conditions on the corrosion and tribocorrosion mechanisms in various simulated biological fluids?

Figure 6.1 shows the experimental flow diagram for this chapter. The friction, corrosion, volume loss and tribocorrosive behaviour, using the mechanistic approach from potentiostatic tests under sliding, are directly compared to the tribocorrosion results at OCP and cathodical protection wear tests addressed in Chapter 5. The interaction of the metal-organic species at the applied potentials (anodic, OCP and cathodic *in vitro* sliding tests) are also discussed.

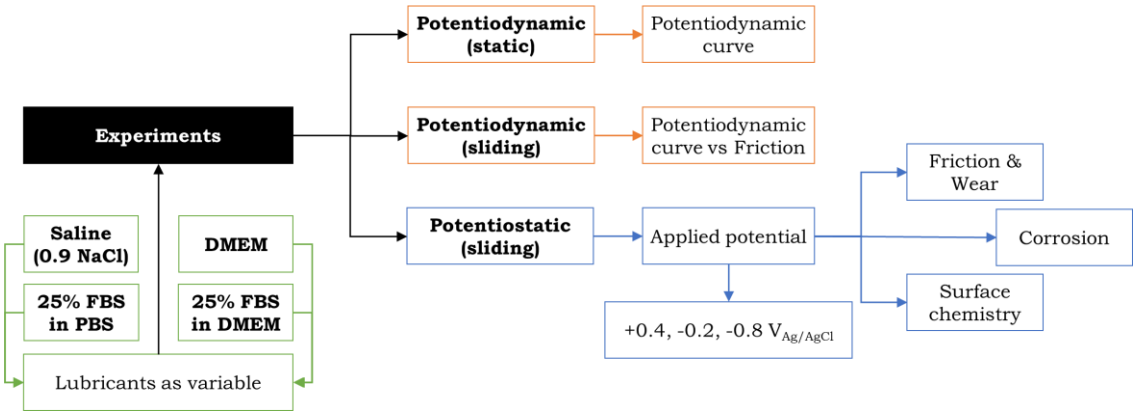

Figure 6.1 Schematic of potentiodynamic experiments under static and sliding conditions, tribocorrosion tests and analysis protocols throughout Chapter 6

6.2 Potentiodynamic Scans

Cyclic polarisation (potentiodynamic) was conducted to characterise the electrochemical behaviour of the CoCrMo alloy when subjected to the electrolytes in a static condition. The samples were immersed for 500 s at the OCP condition before each test to stabilise the passivation. In each electrolyte, polarisation was started from E_{corr} (a stable OCP at 500 s immersion) and constantly shifted toward two different directions: anodic polarisation (n=2) from E_{corr} to +1.4 V (vs RE Ag/AgCl) and cathodic polarisation (n=2) from E_{corr} to -1 V (vs RE Ag/AgCl), as shown in Figure 6.2. The scanning rate was 0.25 mV/s. Both the anodic and cathodic polarisation results would intersect at E_{corr} as the starting point. Thus, the results showed the evolution of the corrosion current density vs the shifting potential.

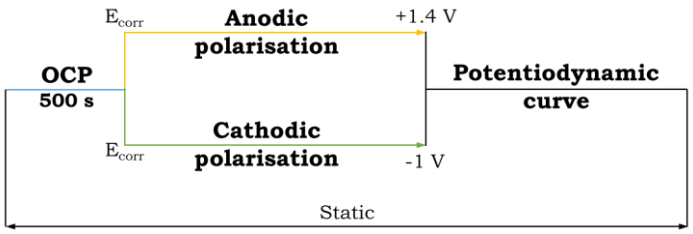

Figure 6.2 Potentiodynamic test protocol

In the next phase, the tribological aspect was added during the cyclic polarisation measurement. The interfaces of the alumina pin and CoCrMo samples were directly rubbed with the aforementioned testing condition. As described in Figure 6.3, the CoCrMo samples were immersed in the electrolyte for 500 s, then tested at the OCP condition for 10 min to stabilise the passivation. After that, the potential was polarised in the anodic or cathodic direction to a vertex potential of +1.4 V/-1 V, with a similar protocol to the static condition. The results simultaneously observed the effect of the shifting potential vs the evolution of the coefficient of friction and corrosion current density in each electrolyte.

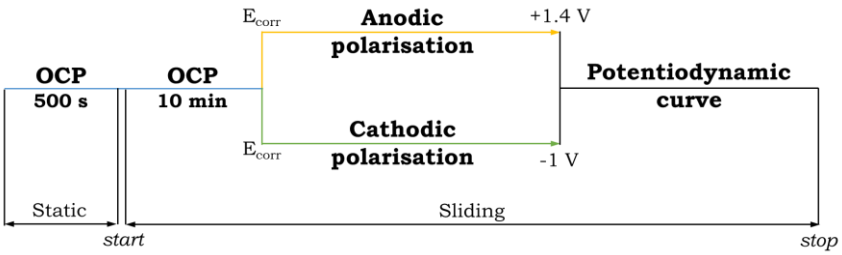

Figure 6.3 Potentiodynamic test protocol under the tribological condition

6.2.1 Polarisation Curves

Figure 6.4 shows the potentiodynamic polarisation curves of the CoCrMo tested in saline, 25% FBS and DMEM electrolytes under a static condition. All of the potentiodynamic curves consist of cathodic, active, pseudo-passive and transpassive regimes, as explained earlier in Figure 4.7. Table 6.1 shows that the E_{corr} of 25% FBS + PBS was the lowest, followed by saline electrolyte and DMEM. CoCrMo in 25% FBS + PBS was observed to have a higher corrosion current density (I_{corr}) of 0.11 ± 0.06 µA/cm^2 when compared to the samples immersed in saline electrolyte and DMEM. The pseudo-passive potential (E_{pp}) was seen to be higher in 25% FBS + PBS when compared to saline electrolyte. A constant current density during the pseudo-passive regime (I_{pp} ~0.83 ± 0.18 µA/cm^2) was observed in the saline electrolyte, 25% FBS + PBS and DMEM. Furthermore, a lower breakdown potential (E_b = 0.38 ± 0.05 V) was seen for the 25% FBS + PBS when compared to the samples tested in saline electrolyte and DMEM. The polarisation curves for the cathodic reaction were also seen to change with different electrolytes. CoCrMo

immersed in 25% FBS + PBS had the highest current density trend during cathodic polarisation, followed by DMEM and saline electrolyte.

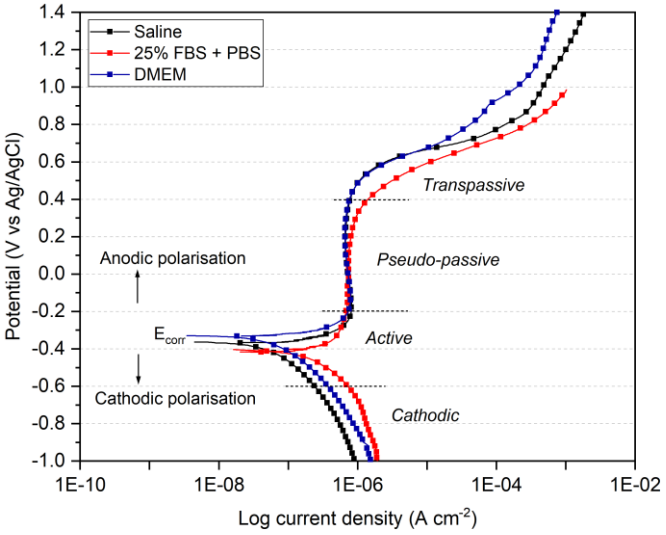

Figure 6.4 The potentiodynamic curves of CoCrMo in various electrolytes under a static condition

Table 6.1 Extracted values, E_{corr} with the corresponding current (I_{corr}), pseudo-passive potential (E_{pp}) with its stable current (I_{pp}) and breakdown potential (E_b) from polarisation curves during static immersion (n=2; ±SD)

Electrolytes	E_{corr} (V)	I_{corr} (μA/cm²)	E_{pp} (V)	I_{pp} (μA/cm²)	E_b (V)
Saline	-0.35 ± 0.02	0.05 ± 0.02	-0.07 ± 0.02	0.84 ± 0.09	0.44 ± 0.09
25% FBS + PBS	-0.43 ± 0.05	0.11 ± 0.06	-0.10 ± 0.05	0.83 ± 0.18	0.38 ± 0.05
DMEM	-0.29 ± 0.08	0.02 ± 0.01	-0.06 ± 0.02	0.84 ± 0.10	0.44 ± 0.06

Figure 6.5 shows the potentiodynamic polarisation behaviour of CoCrMo during the sliding condition in all electrolytes (saline electrolyte, 25% FBS + PBS, DMEM and 25% FBS + DMEM). Due to the sliding contact, the polarisation curves showed increased current densities, shifting the whole curves towards the right when compared to samples tested in the static condition (Figure 6.4). The sliding also

slightly increased the current densities during the pseudo-passive regime when compared to the static corrosion trend.

The addition of 25% FBS + DMEM was observed to less noble E_{corr} when compared to as-received DMEM, also shown in Table 6.2. In all cases, the E_{corr} trend is in strong agreement with the OCP during sliding in the previous chapter; however, the opposite to the E_{corr} trend during static immersion. In the active-passive transitional regime, where the current densities constantly increase, CoCrMo in saline electrolyte was observed to follow the higher current density trend when compared to organic-containing electrolytes. Table 6.2 also shows that the saline electrolyte sample had a higher I_{corr} when compared to the organic-containing electrolytes. In addition, the current densities trend during this transitional regime was seen to be lower for the DMEM and 25% FBS + DMEM when compared to the CoCrMo tested in 25% FBS + PBS. The DMEM and 25% FBS + DMEM tended to increase (more noble) pseudo-passive potential (E_{pp}) when compared to the saline electrolyte and 25% FBS + PBS. A higher increase in the I_{pp} values was observed in the DMEM and saline electrolyte than in the samples tested in 25% FBS-containing electrolytes. Interestingly, the DMEM and 25% FBS + DMEM had a higher breakdown potential (E_b) when compared to the saline electrolyte and 25% FBS + PBS samples. This was suggested to be due to a current reduction at E ~+0.75 V observed for DMEM-containing electrolytes before the transpassive regime.

Changes in the cathodic polarisation curves were observed in Figure 6.5. CoCrMo in saline electrolyte had the highest cathodic current trend when compared to all organic-containing electrolytes, which contradicts the trend during static immersion. Furthermore, the cathodic curve for saline electrolyte was seen constantly to increase and be predominantly controlled by the activation polarisation towards E=-1.0 V. In organic-containing electrolytes, the activation slopes were continued by concentration polarisation, in which the increasing cathodic current value was limited. This behaviour indicated that the organic species in electrolyte change the cathodic/reduction reactions with a consideration of diffusion-controlled mass transport at the electrolyte-CoCrMo interface. In addition, these cathodic current densities were re-increased by the activation polarisation at E ~0.7 V, immediately after the concentration polarisation regime.

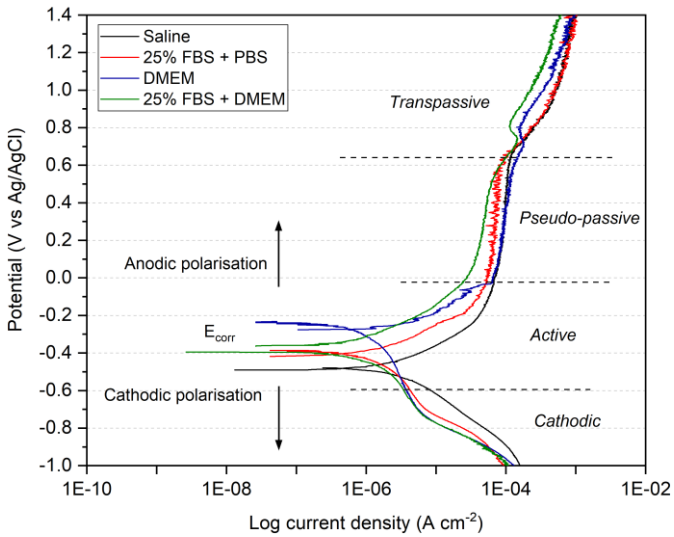

Figure 6.5 Potentiodynamic curves of the CoCrMo in various electrolytes under the sliding condition

Table 6.2 Extracted values from the polarisation curves under sliding; containing open-circuit potential (E_{corr}) with the corresponded current (I_{corr}), pseudo-passive potential (E_{pp}) with its stable current (I_{pp}) and breakdown potential (E_b) (n=2; ±SD)

Electrolytes	E_{corr} (V)	I_{corr} (μA/cm²)	E_{pp} (V)	I_{pp} (μA/cm²)	E_b (V)
Saline	-0.49 ± 0.04	2.02 ± 0.46	-0.16 ± 0.02	98.68 ± 3.46	0.64 ± 0.09
25% FBS + PBS	-0.43 ± 0.08	1.77 ± 0.59	-0.12 ± 0.01	64.47 ± 2.72	0.62 ± 0.11
DMEM	-0.28 ± 0.05	1.76 ± 0.33	-0.03 ± 0.03	101.32 ± 2.31	0.79 ± 0.08
25% FBS + DMEM	-0.39 ± 0.08	1.62 ± 0.52	0.05 ± 0.03	48.15 ± 4.64	0.80 ± 0.10

6.2.2 Coefficient of Friction during the Potentiodynamic Scans

Figure 6.6 and Figure 6.7 show the evolution of the coefficient of friction (μ) during anodic and cathodic polarisations (starting from the E_{corr} potential), respectively. Saline electrolyte (Figure 6.6a) showed a higher coefficient of friction since the beginning (E_{corr}) when compared to organic-containing electrolytes (Figure 6.6b to

Figure 6.6d). A reduction in friction was seen for the saline electrolyte in the transitional domain between the active and pseudo-passive regimes, but continued gradually to increase in the pseudo-passive regime, with the increasing voltage. During the active regime, the 25% FBS + PBS showed a decreasing trend for the coefficient of friction, whilst an increasing trend was seen in both of the DMEM-containing electrolytes. Interestingly, a drastic increase in the coefficient of friction was observed in all organic-containing electrolytes after reaching the transitional regime when compared to the results for the active regime potential. CoCrMo tested in saline electrolyte and DMEM steadily increased the transient coefficient of friction as a function of anodic overpotential after passing the pseudo-passive potential. On the contrary, the 25% FBS-containing electrolytes tended to stabilise the friction during the pseudo-passive regime, then showed a trend of reduction from the potential E ~+0.5 V during the transpassive regime.

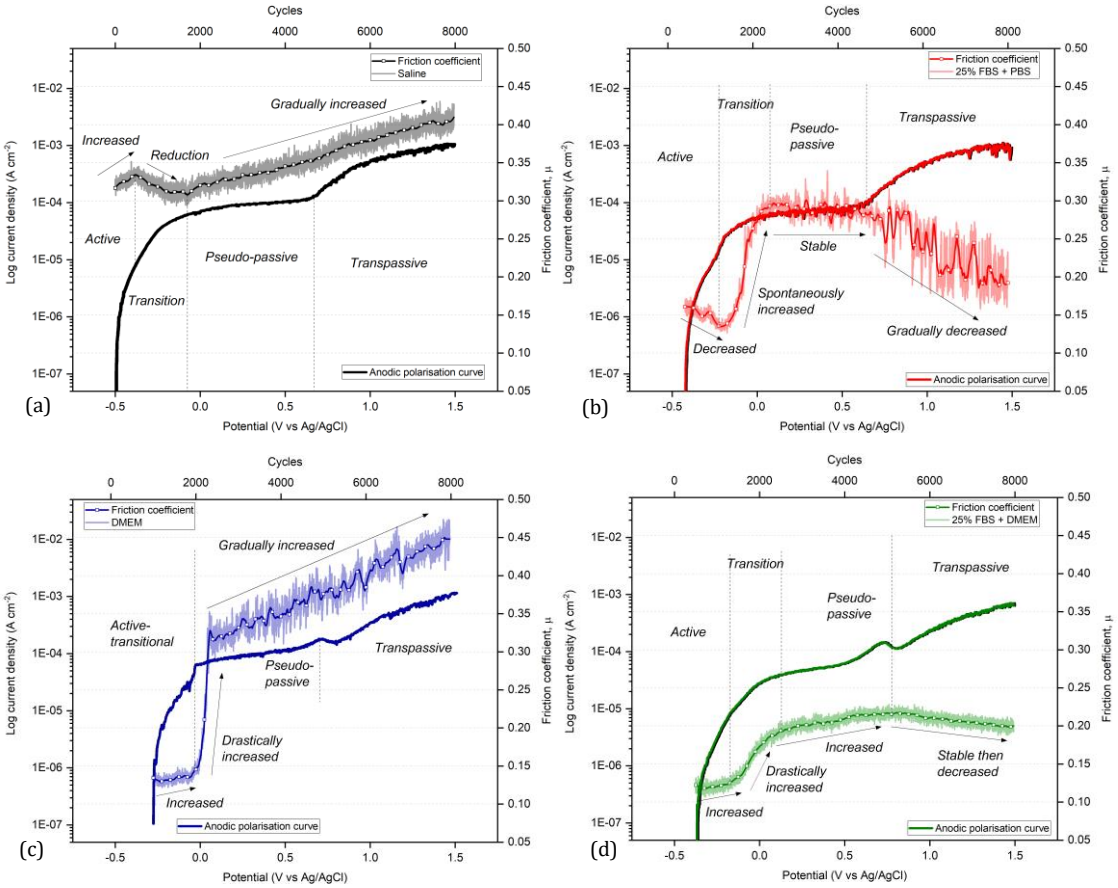

Figure 6.6 The transient coefficient of friction as a function of sliding cycle and potential during anodic polarisation tested in (a) saline electrolyte, (b) 25% FBS + PBS, (c) DMEM and (d) 25% FBS + DMEM

During cathodic polarisation, the coefficient of friction could be manipulated, as shown in Figure 6.7. The coefficient of friction in saline electrolyte μ ~0.33 (Figure 6.7a) was higher when compared to CoCrMo tested in organic-containing electrolytes (below μ~0.17 in Figure 6.7b to Figure 6.7d) over the cathodic polarisation. In saline electrolyte, the coefficient of friction was seen gradually to reduce as a function of cathodic polarisation. The hypothesis for this constant reduction in friction is due to the absence of a concentration polarisation regime observed on the cathodic current curve over the cathodic polarisation in saline electrolyte.

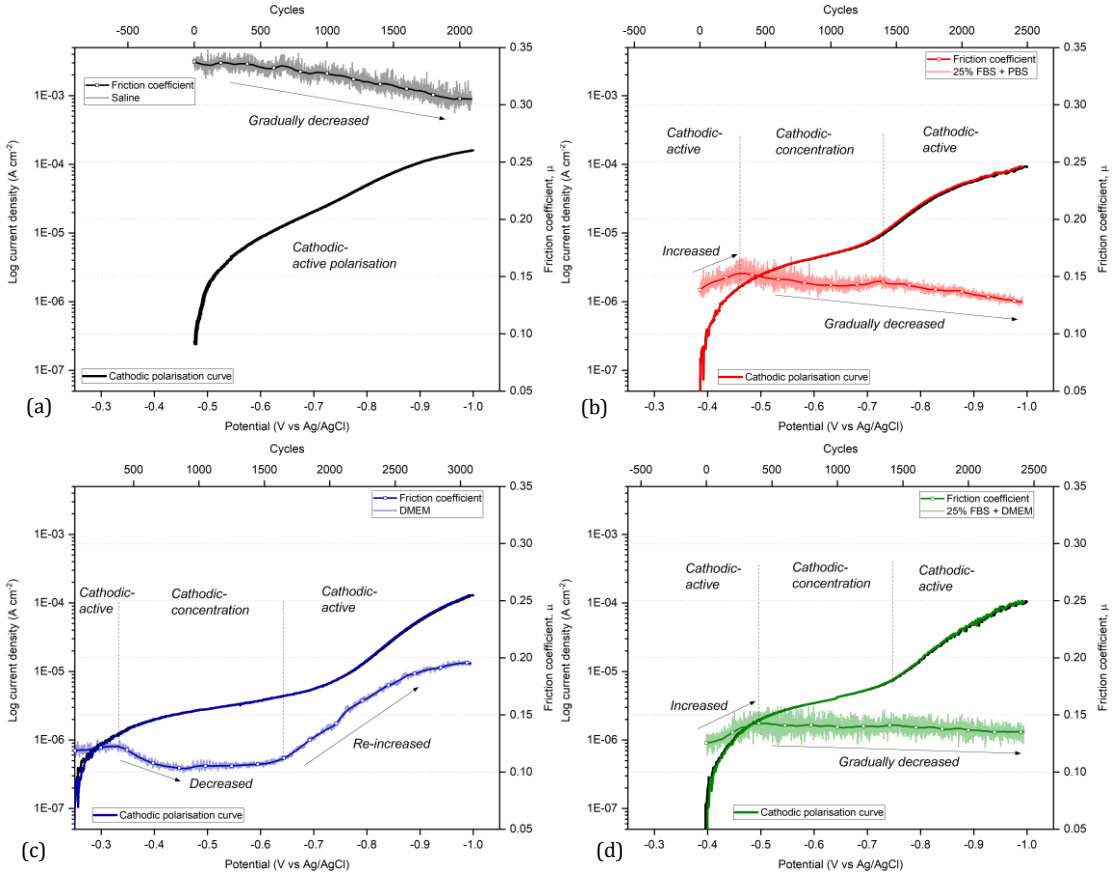

Figure 6.7 The transient coefficient of friction as a function of the sliding cycle and potential during cathodic polarisation tested in (a) saline electrolyte, (b) 25% FBS + PBS, (c) DMEM and (d) 25% FBS + DMEM

In both of the 25% FBS-containing electrolytes, the coefficient of friction was seen to increase during the cathodic activation regime, then gradually decrease after

passing the concentration regime with a reducing applied potential. In the DMEM, the friction behaviour was seen to depend on the cathodic current regimes, showing a lower friction observed during the concentration regime when compared to the activation regimes. In addition, the coefficient of friction gradually increased during the second activation regime. Since the concentration polarisation regime is caused by diffusion-controlled mass transport at the electrolyte-surface interface, it can be hypothesised that there was a change in the surface film during this regime which limited the cathodic current and reduced the friction. Therefore, the cathodic current-friction interaction is suggested to correlate with the changes in electrochemical reactions, ion and mass transport behaviour at the electrolyte-CoCrMo interface. Despite the fact that the three cathodic regimes were also observed in the 25% FBS-containing electrolytes, the coefficient of friction was independent of the cathodic current changes. It can be hypothesised that the protein content in FBS has an effect of stabilising and reducing the surface friction during the cathodic activation regime.

Figure 6.8 shows the compiled coefficient of friction data measured under anodic and cathodic conditions in all electrolytes. Overall, the saline electrolyte showed a higher coefficient of friction of $\mu \sim 0.33$, which even increased with the increasing potentials, when compared to the organic-containing electrolytes. The coefficient of friction observed was below $\mu \sim 0.15$ during the active regime, with the reducing applied voltages (cathodic) in organic-containing electrolytes. However, the coefficient of friction for the DMEM was seen to increase spontaneously to $\mu \sim 0.30$ after reaching the transitional regime, which therefore was in line with the high friction in saline electrolyte over the pseudo-passive and transpassive regimes. Despite the drastic increase in the coefficient of friction at the transitional regime also observed for the 25% FBS + PBS and 25% FBS + DMEM, however, the friction trend eventually stabilised and then reduced with the increasing overpotential. This drastic increase in the friction can be hypothesised as being due to a change in the electrochemical reaction at the electrolyte-surface interface at the transition between the active (ion transfer control) and pseudo-passive (mixed with the mass transport control) regimes. It therefore leaves the CoCrMo surface unprotected, without a stable tribochemical film formation, and the coefficient of friction independent from the electrolyte species. It is also hypothesised that the protein

content in FBS still plays a protective role against surface friction which is independent of the electrochemical potential condition on the CoCrMo sample. This behaviour can also be indicated by the increasing friction observed for the DMEM (protein-free organic electrolyte) at a high overpotential condition.

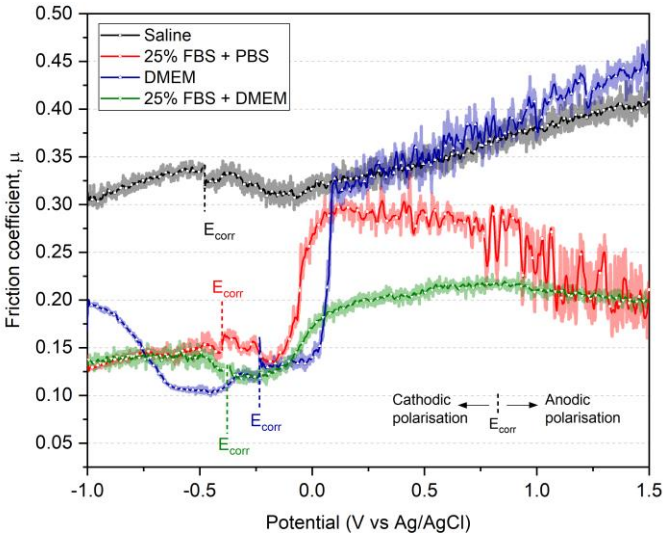

Figure 6.8 The evolutions of the coefficient of friction over the electrochemical potentiodynamic started at E_{corr} (dashes) in all electrolytes

6.3 Tribocorrosion Tests under Potentiostatic Conditions

Tribocorrosion tests were conducted under constant applied electrochemical potentials (potentiostatic as in Figure 4.9) at pseudo-passive +0.4 V (vs RE Ag/AgCl) and active -0.2 V (vs RE Ag/AgCl), chosen from the potentiodynamic curve behaviour. The results were expected to obtain the transient evolution of the coefficient of friction and net current density vs applied potentials and sliding cycles. The cathodical protection test at E= -0.8 V (vs RE Ag/AgCl) was employed with this protocol during the discussion in Chapter 5.

The SEM and EDS results were analysed for the wear characteristics. These results were also compared with the sliding-OCP and cathodical protection (E=-0.8 $V_{Ag/AgCl}$) tests discussed in Chapter 5. The current density and total volume loss at E= +0.4, -0.2 V and OCP in all electrolytes were analysed to observe the effect of surface potentials on the tribocorrosion mechanism.

6.3.1 Coefficient of Friction (COF)

Figure 6.9 shows the transient coefficient of friction/COF (μ) at the CoCrMo samples tested in all electrolytes. At E=+0.4 V (Figure 6.9a), the COF of the saline electrolyte and DMEM were observed to increase and stabilise at μ ~0.36 and 0.43, respectively, after ~6,000 cycles during 2 h sliding. On the other hand, the CoCrMo tested in 25% FBS-containing electrolytes showed a reduction in the COF during the tests and stabilise at μ~0.22 after 3,000 cycles. A similar comparison order of the COF as a function of the sliding cycle was shown between the overpotentials at E=-0.2 V (Figure 6.9b) and -0.8 V (Figure 6.9c). The order showed that the saline electrolyte had the highest COF at μ~0.32, when compared to the organic-containing electrolytes (μ~0.14). Nevertheless, an increase in the COF was observed for the CoCrMo tested in saline electrolyte at E=-0.2 V before stabilising at 6,000 cycles.

Figure 6.9d shows the average steady-state COF (μ) (averaged over the last 60 cycles in sliding test) from all tests under applied potentials and the OCP condition (from Figure 5.3b) in all electrolytes. In all organic-containing electrolytes, a significant increase in the steady-state μ was observed at E=+0.4 V when compared to the CoCrMo tested at E=-0.2, -0.8 V and OCP condition. On the other hand, the steady-state μ for the CoCrMo tested in saline electrolyte was seen to be independent of the electrochemical potential, showing no statistical difference between all of the applied potential conditions. At E=+0.4 V, both of the 25% FBS-containing electrolytes significantly decreased in terms of their steady-state μ when compared to the samples tested in the saline electrolyte and DMEM. No significant differences were observed for the steady-state μ between the saline electrolyte and DMEM, as well as between the 25% FBS + PBS and 25% FBS + DMEM at E=+0.4 V. For E=-0.2, E=-0.8 V and OCP conditions, and an increased steady-state μ was observed for CoCrMo tested in saline electrolyte when compared to the organic-containing electrolytes. In addition, no significant difference was seen between the steady-state μ for the CoCrMo tested at E=-0.2 V, E=-0.8 V and OCP conditions in organic-containing electrolytes.

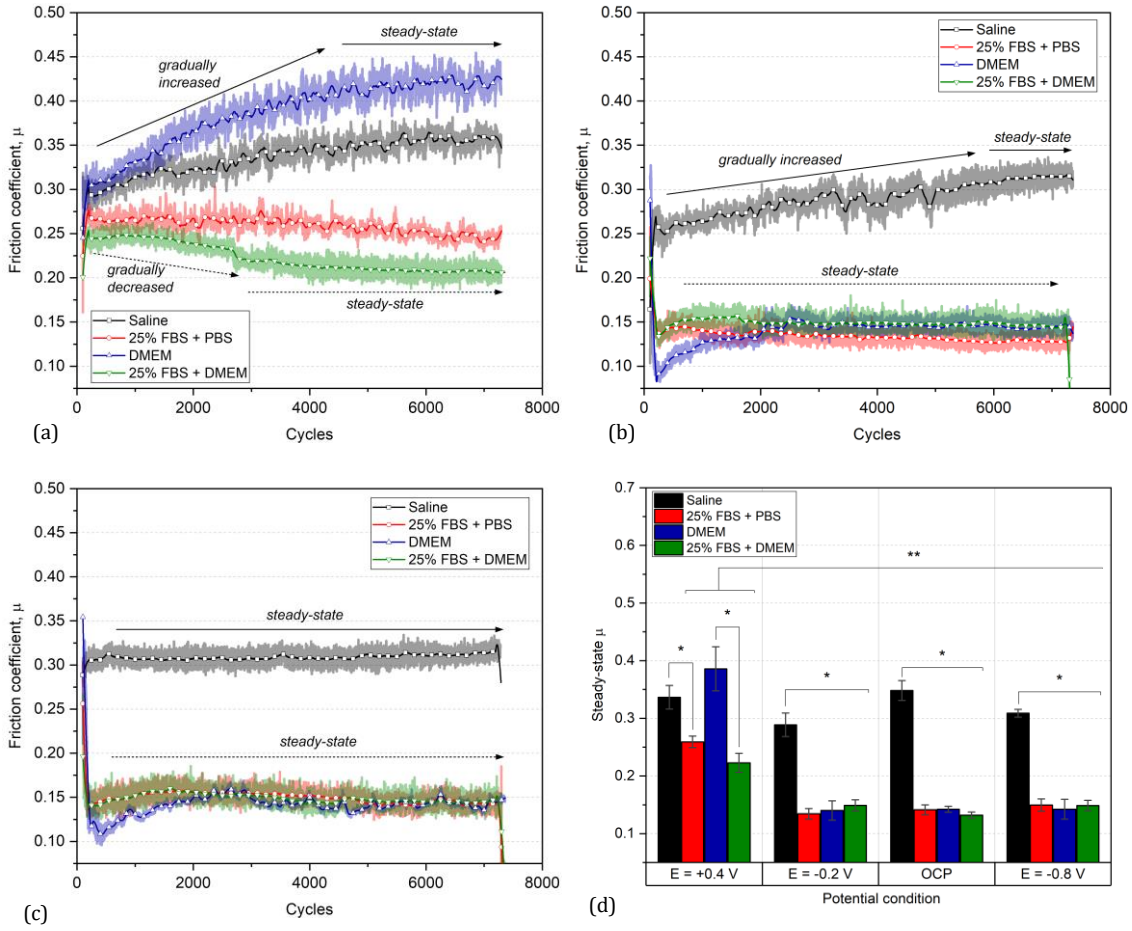

Figure 6.9 The transient COF over 2 h sliding cycles at (a) E=+0.4 V, (b) E=-0.2 V (c) E=-0.8 V and (d) steady-state μ averages when compared to OCP (n=3; SD bar; p<0.05 for ANOVA as a function of (*)electrolyte and (**)potential condition)

6.3.2 Corrosion Volume Loss

Figure 6.10a and Figure 6.10b show the net current density transients over 2 h tribocorrosion at E=+0.4 V and -0.2 V (vs RE Ag/AgCl), respectively. Referring to Figure 5.9a, the evolution of the transient net current during 2 h sliding at E = -0.8 V (vs RE Ag/AgCl) was observed to have negative values, owing to the cathodical protection condition. Therefore, the electrochemical corrosion loss can be neglected on the CoCrMo surface. At E=+0.4 V, the net current densities in the saline electrolyte and DMEM were seen gradually to increase during the 2 h sliding. On the contrary, both of the 25% FBS-containing electrolytes tended to have a stable, reducing transient net current during the sliding tests.

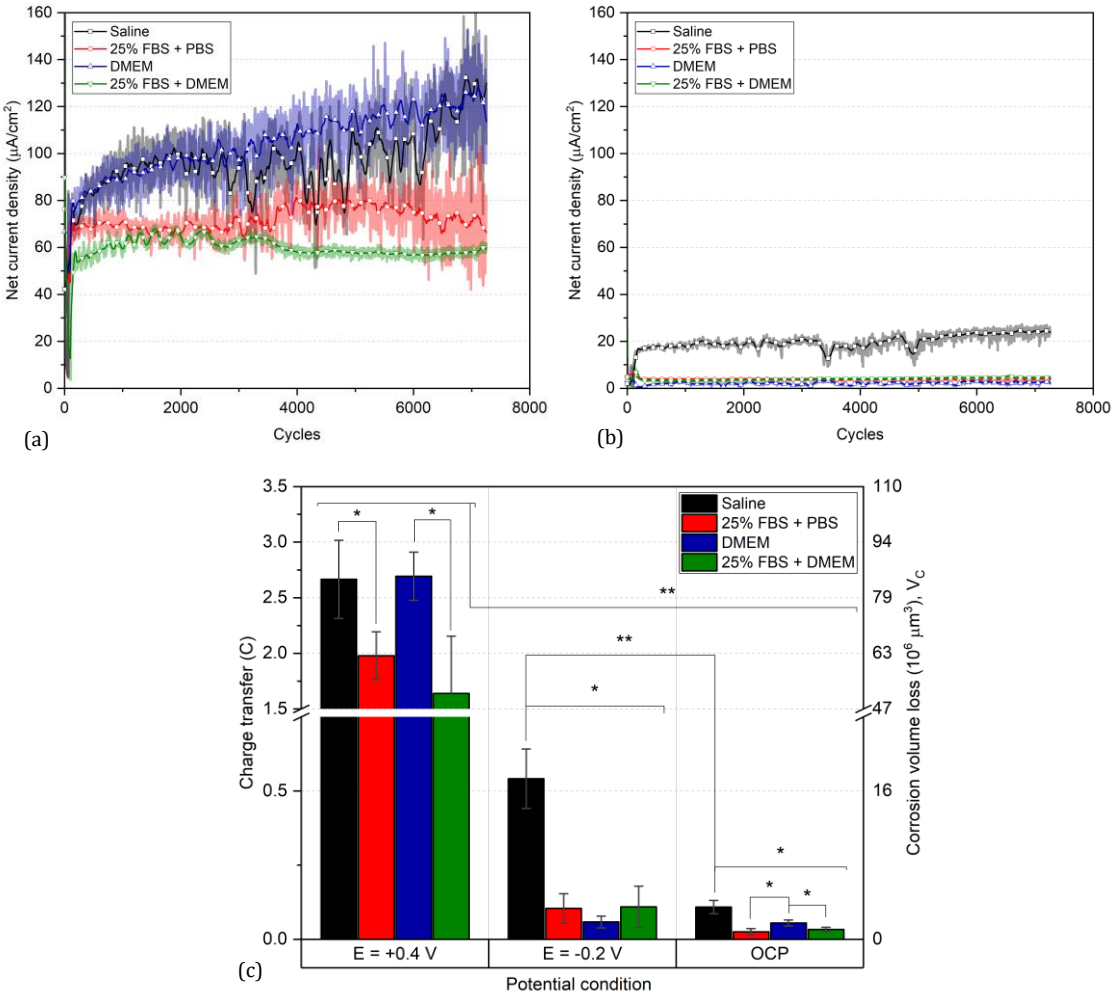

Figure 6.10 The transient current density over 2 h tribocorrosion at (a) E=+0.4 V (b) E=-0.2 V (vs RE Ag/AgCl) and (c) Total charge transfer and corrosion volume loss in all electrolytes when compared to the OCP condition (n=3; SD bar; p<0.05 for ANOVA as a function of (*)electrolyte and (**)the potential condition)

Figure 6.10c and Table 6.3 show the average comparisons of the total charge transfer (Q) and corrosion volume loss (V_C) at E=+0.4, -0.2 V and OCP condition (refer to Table 5.1) over 2 h sliding. In all electrolytes, the total charge transfer for E=+0.4 V was observed to be significantly higher when compared to the E=-0.2 V and OCP condition. At E=+0.4 V, the 25% FBS + DMEM significantly reduced the charge transfer when compared to the sample tested in the DMEM. No significant differences were observed for the charge transfer and corrosion volume loss between samples tested in saline electrolyte and DMEM, as well as between the 25% FBS + PBS and 25% FBS + DMEM at E=+0.4 V. At E=-0.2 V, the charge transfer

in saline electrolyte was observed to be significantly higher when compared to the samples tested in organic-containing electrolytes and the OCP's saline electrolyte. No statistical differences were shown for the total charge transfer and corrosion volume loss between all organic-containing electrolytes at E=-0.2 V. A reduction was observed for the charge transfer of the CoCrMo tested in the 25% FBS-containing electrolytes at the OCP condition when compared to the potentiostatic E=-0.2 V.

Table 6.3 The total charge transfer (Q) and corrosion volume loss (V_C) during tribocorrosion at E=+0.4 and -0.2 V in all electrolytes (n=3; ±SD)

Electrolytes	Charge transfer, Q (C)		Corrosion volume loss, V_C (x 10^6 µm^3)	
	E=+0.4 V	E=-0.2 V	E=+0.4 V	E=-0.2 V
Saline	2.67 ± 0.35	0.54 ± 0.10	83.05 ± 11.07	17.05 ± 3.15
25% FBS in PBS	1.98 ± 0.21	0.10 ± 0.05	61.71 ± 6.74	3.28 ± 1.57
DMEM	2.69 ± 0.22	0.06 ± 0.02	84.83 ± 6.82	1.84 ± 0.63
25% FBS in DMEM	1.64 ± 0.52	0.11 ± 0.07	51.25 ± 16.26	3.45 ± 2.20

6.3.3 Electron Microscope Analysis

Figure 6.11 and Figure 6.12 show SEM images of the CoCrMo wear scars after 2 h of sliding tests in all electrolytes at E=+0.4 V and E=-0.8 V, respectively. The characteristics of the wear scar after being tested at E=-0.2 V were similar to the OCP condition (SEM images in Figure 5.6). Therefore, this chapter only presents the SEM images of the CoCrMo tested at E=+0.4 V and E=-0.8 V. The SEM images confirmed that the wear scar width on all samples tested at E=+0.4 V was two to three-folded greater when compared to the E=-0.8 V. The wear track edges and abrasion characteristic at E=+0.4 V surface were relatively more apparent when compared to the E=-0.8 V samples.

Figure 6.11a and Figure 6.11c show the wear scar at E=+0.4 V for saline electrolyte and DMEM. A greater wear scar width of more than ~1002.67 µm and an absence of surface film/precipitates was observed in these electrolytes when compared to

the 25% FBS-containing electrolytes of less than ~863.71 μm (Figure 6.11b and Figure 6.11d). This trend is in strong agreement with the total volume loss for all samples (Figure 6.13). Pits due to electrochemical pitting corrosion and grooves due to abrasive wear were observed to scatter on the wear scar in the saline electrolyte and DMEM samples. Severe grooves due to mechanical wear damage and traces of wear debris were also seen at the corner of the wear track. SEM images for the DMEM at E=+0.4 V indicated that oxide and wear debris were dragged to the corner during the sliding condition at the intersection of the wear scar. Interestingly, darker layers were seen at the outside of the wear edges. The wear scar at E=+0.4 V in the 25% FBS-containing electrolytes showed no traces of severe pits and less abrasion damage when compared to the saline electrolyte and DMEM samples, but grooves were seen at the corner of the wear area. A few layers were also observed covering the wear edges and grooves. Thus, the protein content from the FBS can be hypothesised to reduce the wear width, electrochemical pits and abrasion damage when compared to the sample tested in saline electrolyte and the as-received DMEM at E=+0.4 V.

Figure 6.12a shows that the saline electrolyte E=-0.8 V sample had a greater wear width of ~419.79 μm when compared to the E=-0.8 V in the organic-containing electrolytes of ~<355.62 μm. Wear debris and particles were seen inside the abrasive grooves within the wear scar of the CoCrMo tested in the saline electrolyte. The layers indicating a tribofilm formation were dominated within the wear scar and corner of the CoCrMo tested in organic-containing electrolytes. SEM images of the wear scar obtained after sliding at E=-0.8 V in 25% the FBS-containing electrolytes (Figure 6.12b and Figure 6.12d) indicated a few pits and grooves filled by deposited organic species. Also, wear debris and particles were seen at the corner of the wear due to sliding. However, the wear scar in the DMEM (Figure 6.12c) had fewer grooves inside the wear track and more precipitated particles outside the wear edges when compared to the 25% FBS-containing electrolytes. The wear characteristics can be hypothesised to be the reason for the lower friction observed in the organic-containing electrolytes =-0.2 V when compared to the CoCrMo tested in saline electrolyte and all electrolytes at E=+0.4 V.

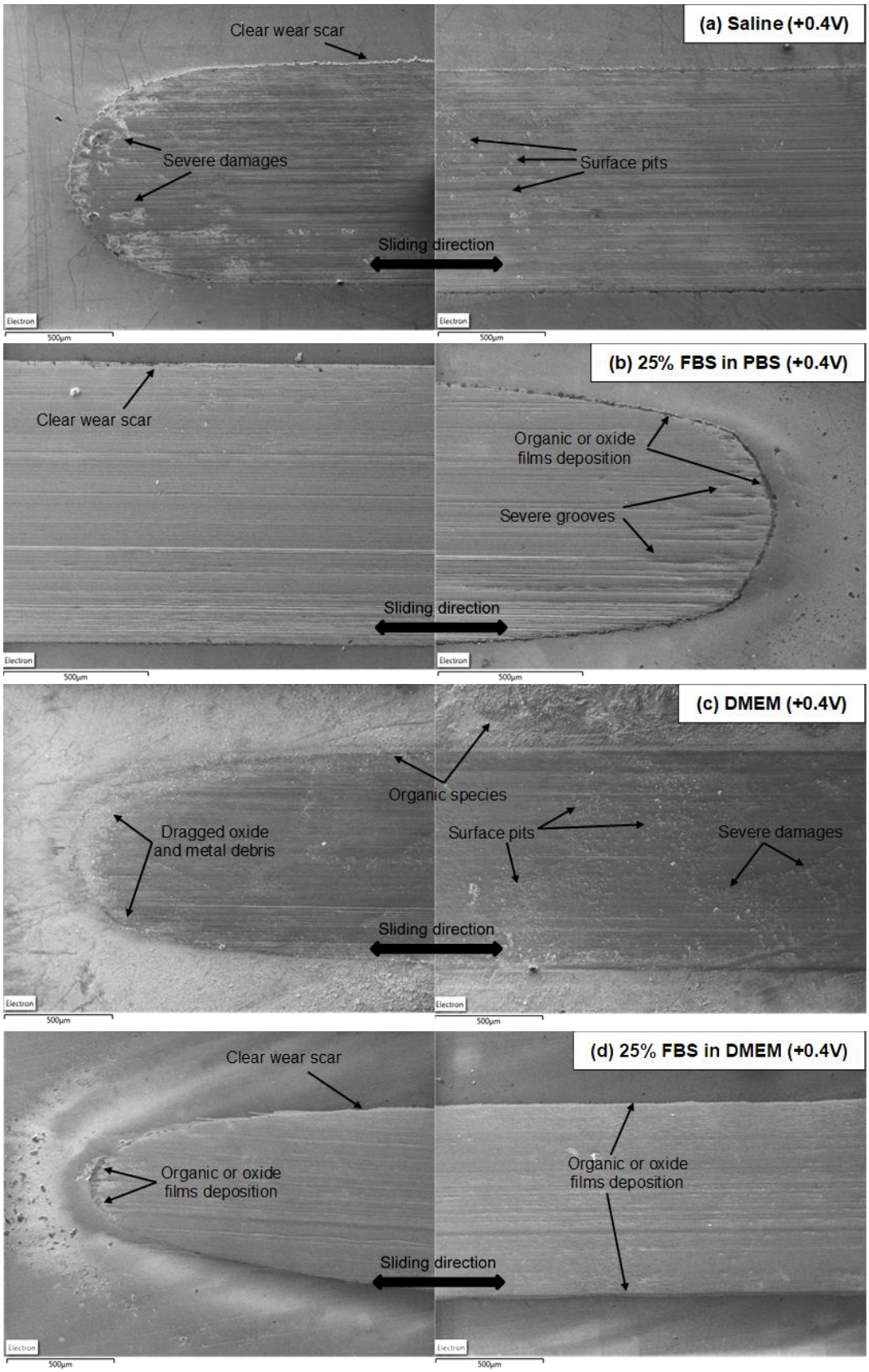

Figure 6.11 SEM images on the wear track of the CoCrMo alloys after 2 h sliding test at the potentiostatic E=+0.4 V in (a) saline electrolyte, (b) 25% FBS + PBS, (c) DMEM and (d) 25% FBS + DMEM

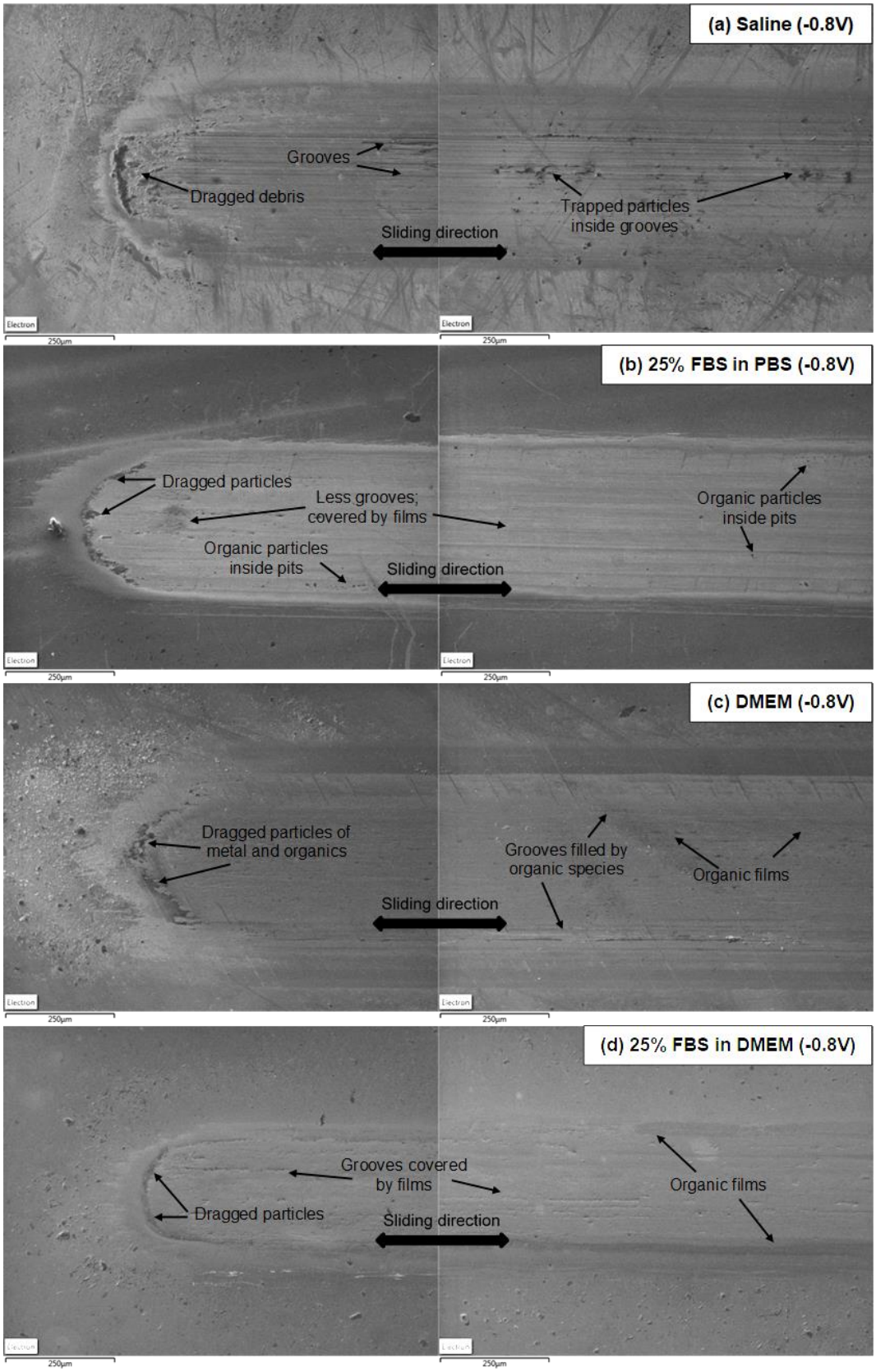

Figure 6.12 SEM images on the wear track of the CoCrMo alloys after 2 h sliding test at the potentiostatic E=-0.8 V in (a) saline electrolyte, (b) 25% FBS + PBS, (c) DMEM and (d) 25% FBS + DMEM

6.3.4 Chemical Analysis

Table 6.4 shows the atomic percentages (at%) of the elements observed by the EDS on the CoCrMo wear scar after the sliding test at potentiostatics (E=+0.4, -0.2 and -0.8 V). Several species, i.e., carbon (C), oxygen (O), and proteinaceous elements (nitrogen (N), sulphur (S), calcium (Ca) and phosphorus (P) from FBS and DMEM), appeared, along with metal elements (Co, Cr and Mo).

Table 6.4 EDS atomic percentage (at%) of the deposited elements within the wear scar on the CoCrMo surfaces tested in the organic-containing electrolytes, comparing at E = +0.4 V, -0.2 V and -0.8 V

Elements	Atomic percentages (at%)								
	25% FBS + PBS			DMEM			25% FBS + DMEM		
	+0.4 V	-0.2 V	-0.8 V	+0.4 V	-0.2 V	-0.8 V	+0.4 V	-0.2 V	-0.8 V
Co	48.5	40.1	32.1	50.6	37.8	31.3	45.4	37.5	32.8
Cr	21.5	19.2	18.4	25.2	21.6	20.8	23.3	15.5	19.5
Mo	6.4	6.8	4.5	7.4	8.6	5.3	8.6	9.5	5.3
O	8.4	9.6	0.6	4.7	6.4	0.4	6.5	19.5	0.6
C	7.7	12.8	17.7	6.6	4.8	16.5	6.6	1.9	18.6
N	2.2	1.8	5.5	1.1	1.7	6.2	2.2	5.1	6.6
S	1.1	3.0	5.6	2.1	12.2	7.9	3.1	4.4	8.4
Ca	1.1	1.8	7.3	1.1	2.8	5.9	1.1	2.5	3.6
P	3.1	4.8	8.3	1.2	4.1	5.7	3.2	4.2	4.6

The atomic percentage of metal elements were relatively higher on the CoCrMo surfaces tested at E=+0.4 V when compared to E=-0.2 V and E=-0.8 V for all electrolytes. On the other hand, the total percentage of proteinaceous species elements was higher at the E-0.8 V samples when compared to the E=+0.4 V and E=-0.2 V samples. These results are in strong agreement with the indications from the SEM images, showing fewer layers in the wear scar at E=+0.4 V when compared to E=-0.8 V. The calcium and phosphate were seen to increase for the CoCrMo tested

in FBS-containing electrolytes. On the other hand, sulphur and nitrogen were higher for the samples tested in DMEM-containing electrolytes. SEM/EDS indicated that the calcium and phosphorus dominated the wear scar edges and corner area, while sulphur was observed inside the wear scar. The presence of carbon and proteinaceous species containing tribofilm can be correlated as the reason for the reduced friction on the CoCrMo interface.

6.3.5 Total Volume Loss

Figure 6.13 compares the total volume loss (V_{total}) and SWR of the CoCrMo alloys during the 2 h sliding tests at applied potentials E = +0.4, -0.2 (refer to Table 6.3), OCP condition (refer to Table 5.2) and E=-0.8 V (refer to Table 5.3). In all electrolytes, the V_{total} and SWR significantly increased for the samples tested at E=+0.4 V when compared to the other potential conditions. On the other hand, the samples tested in all electrolytes at E=-0.8 V showed a significant reduction in the V_{total} when compared to the anodic potential and OCP conditions due to the absence of a corrosion process (cathodical protection). All of the CoCrMo tested in saline electrolyte showed an increase of V_{total} with the increasing applied potential conditions, and a statistical difference was observed with an order from E=-0.8 V, OCP, E=-0.2 V and E=+0.4 V in this case.

At E=+0.4 V, the V_{total} was significantly reduced for the 25% FBS + PBS when compared to the samples tested in saline electrolyte and DMEM electrolytes. No significant differences were observed in the V_{total} between the saline electrolyte and DMEM, nor between the 25% FBS + PBS and 25% FBS + DMEM at E=+0.4 V. On the other hand, at the E=-0.2 V and OCP conditions, an increasing V_{total} was seen for the 25% FBS + PBS when compared to the CoCrMo tested in DMEM. Furthermore, the V_{total} for all organic-containing electrolytes was seen to increase at E=-0.2 V when compared to the OCP condition, although this difference was not statistically significant.

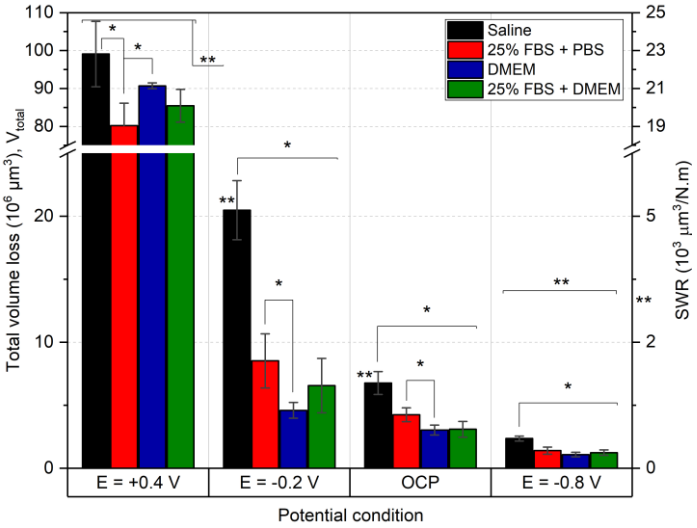

Figure 6.13 Total volume loss and SWR at the CoCrMo after 2 h of sliding at all potentiostatics and the OCP condition in all electrolytes (n=3; SD bar; p<0.05 for ANOVA as function of (*)electrolyte and (**)potential condition)

Table 6.5 Total volume loss at OCP (V_{total}) and the SWR of the wear scar after tribocorrosion at E=+0.4 and -0.2 V in all electrolytes (n=3; ±SD)

Electrolytes	Total volume loss, V_{total} (x 10^6 µm^3)		SWR (x 10^3 µm^3/N.m)	
	E=+0.4 V	E=-0.2 V	E=+0.4 V	E=-0.2 V
Saline	99.08 ± 8.64	20.48 ± 2.34	22.94 ± 2.00	4.74 ± 0.54
25% FBS in PBS	80.23 ± 5.92	8.53 ± 2.15	18.57 ± 1.37	1.97 ± 0.50
DMEM	90.70 ± 0.78	4.60 ± 0.63	20.99 ± 0.18	1.06 ± 0.15
25% FBS in DMEM	85.46 ± 4.32	6.57 ± 2.16	19.78 ± 1.00	1.52 ± 0.50

6.4 Chapter Discussion

In this chapter, the applied electrochemical potential was shown to affect the friction, corrosion current density and wear behaviour of the CoCrMo surface. The surface chemistry was also seen to vary at applied potentials affecting the tribological processes. This chapter aimed to investigate the influence of electrochemical potentials on the behaviour of tribochemistry and tribocorrosion.

Hence, the interactions between the electrolyte species and the CoCrMo surfaces tested in saline electrolyte and organic-containing electrolytes under applied potentials were discussed, with reference to related studies. The specific roles of protein content at the different potential conditions were also highlighted on the tribocorrosion mechanism as an essential finding of this study.

6.4.1 Tribochemistry and Friction at Various Potential Conditions

In this study, SEM/EDS showed the wear scar characteristic and trace of chemical elements percentage to analyse the tribochemical reaction on the CoCrMo sample tested at different potential conditions in the organic environment. A study by Wang et al. [282] showed that the electrochemical potential nature affected the electrochemical reaction at the electrolyte-surface interface. Interestingly, this study also demonstrated the changes in the COF of the CoCrMo as a function of the shifting electrochemical potentials during the potentiodynamic polarisation tests. Therefore, changes in protein adsorption, oxide passivation, the COF and sub-surface behaviour at the metallic surface were anticipated due to the different electrochemical reactions.

In this study, the proteinaceous species found on the worn CoCrMo surfaces originated from the organic-containing electrolytes used; i.e., FBS and DMEM. These species can also be termed tribochemistry products due to their mixing process with the metal surface suggested through the sliding condition. The EDS showed that the total atomic percentage of proteinaceous elements (carbon, nitrogen, sulphur, calcium and phosphorus) at the wear scar after being tested at E=-0.8 V in organic-containing electrolytes was constantly higher when compared to the samples tested at E=+0.4 V and -0.2 V. More proteins adsorbed at the CoCrMo surface was indicated at the cathodic condition than the anodic one. This finding is in strong agreement with previous studies [186, 257]. A study by Munoz et al. [257] showed an increase in protein adsorption rate at the CoCrMo surface under cathodic polarisation (a static condition) by weighing the samples with deposited protein. In the sliding condition, a study by Yan et al. [186] demonstrated decreased CoCrMo material loss in FBS at the cathodic E=-0.8 V due to the proteinaceous tribofilms' protection and the absence of corrosion.

The reduction reactions, i.e. atomic reduction of hydrogen, water and proteins, were suggested to occur at the electrolyte-surface interface under the cathodic condition [257]. Figure 6.14 shows the pathways of the reaction between the reduced hydrogen atoms and protein structure at a CoCrMo surface [282]. Shin et al. [352] found that the adsorbed hydrogen atom at the cathodic surface can be produced via two reactions, i.e. hydrogen (proton) ion reduction or water molecule reduction from the electrolyte. In a study of protein electrochemistry in bovine serum, Stankovich and Bard [353] demonstrated that the adsorbed hydrogen atoms contributed to the protein structure reduction with the disulphide chain (RSSR). Thus, the insoluble proteinaceous can be deposited as a tribofilm formation at the metallic surface after several cycles or at lower potentials [353]. Furthermore, the absence of hydrogen gas (no bubble) is typically seen in the electrolyte during this process [282].

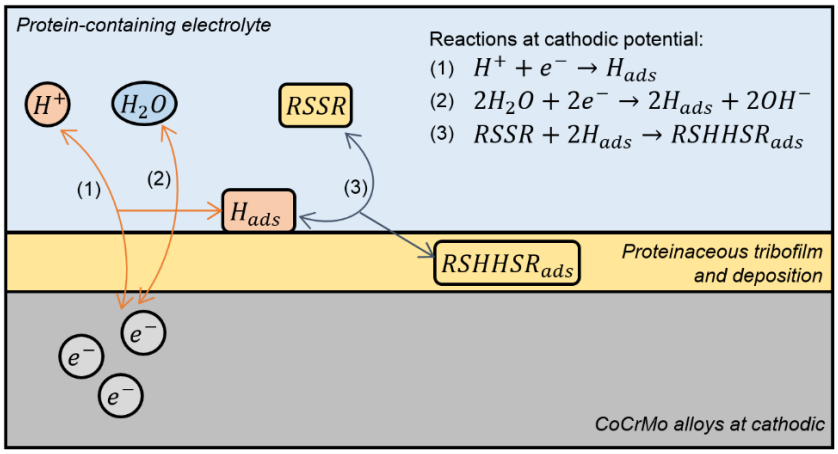

Figure 6.14 A schematic for the electrochemical reactions at the CoCrMo surface in a protein-containing environment at the cathodic potential

On the contrary, the atomic percentages of the metallic elements (cobalt, chromium and molybdenum) were higher on the CoCrMo tested at E=+0.4 V samples when compared to the E=-0.2 V and -0.8 V samples. Fewer deposited layers but more debris and severe damage were also seen via SEM images at the wear scar in this potential. Kojichan et al. [354] explained that the anodic potential condition increased in the oxidation (passive reformation) process and decreased during the cathodic reaction. The less cathodic state reduced the adsorbed protein and film

formation at the metal surface due to an inhibition in protein structure reduction. Therefore, the tribochemistry was dominated by a passive oxide film and sub-surface mechanisms at the anodic potential (E=+0.4 V, in this case).

Figure 6.15 shows schematic film formations after the tribocorrosion test at the applied potentials and under the OCP condition. The passive film coverage was suggested to be greater at the OCP when compared to E=+0.4 V, a indicated by the deposition of metal and oxide elements via EDS, in line with the previous study [282]. This behaviour is due to the fact that the passive oxide at OCP was protected by the proteinaceous film during the mechanical removal process. On the other hand, the thickness and coverage of the proteinaceous films decreased at E=+0.4 V, so less protective tribofilm and thus passive films were mechanically removed. Despite there being an inhibition of anodic reaction under cathodic polarisation E=-0.8 V, the oxide signal can still be observed on the tested CoCrMo surface but only at a small percentage. It can be hypothesised that the oxide and protein layers are integral on the CoCrMo surface. The tribofilm formation can be linked to the variations in friction seen at lower and higher applied potentials during sliding in this study. For the potentiostatic sliding test, a constant COF was found at OCP, E=-0.2 V and -0.8 V, which was significantly lower when compared to E=+0.4 V. In this case, the changes in the electrochemical potential and resultant friction can be clearly seen at low voltages and near the E_{corr}, suggesting the role of proteinaceous tribofilm.

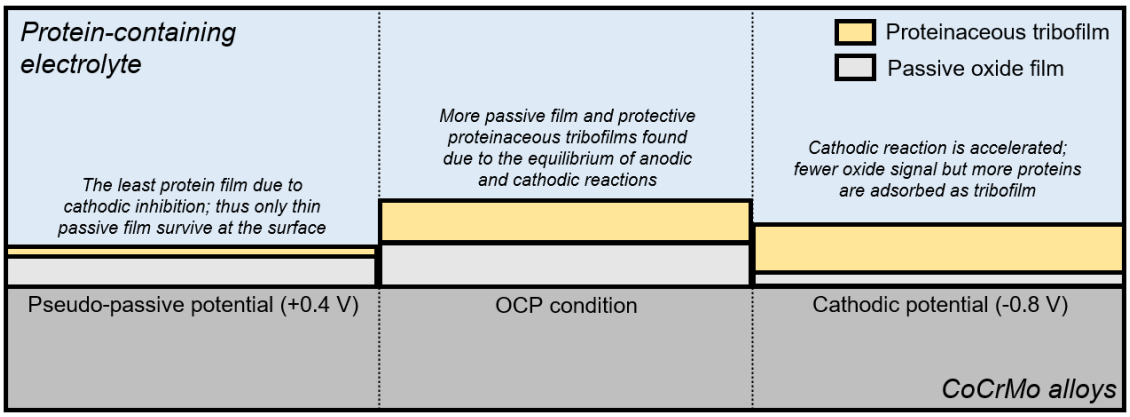

Figure 6.15 A schematic of the tribofilm formations at the CoCrMo surfaces after testing in the protein-containing environment under potentiostatic and OCP

However, the transient friction as a function of electrochemical potentials was observed to be segmented by the changes in the ionic and concentration transport controls, as well as governed by different electrolyte species (refer to Figure 6.8). Thus, the oxidation and reduction reactions on the metal surface could not be generalised to occur similarly throughout the anodic and cathodic polarisations potential conditions.

During the anodic polarisation, a drastic change in the friction of CoCrMo was always observed at the transitional regime (between the active and pseudo-passive regimes) for all electrolytes. In other words, this regime is where the ionic transport control at the electrolyte-surface interface is shifted into mass transport, starting to limit the charge transfer by diffusion control [134]. A sudden reduction in the friction was observed in the saline electrolyte, whilst a drastic increase was seen in all organic-containing electrolytes at this transition regime. Interestingly, all friction moved towards and stopped at a similar range of ~0.30-0.35, except at ~0.25 in the case of the 25% FBS + DMEM. It can be suggested that the protective role of tribofilm is omitted, and also the electrochemical reaction on the surface works independently and is unaffected by different electrolyte species at this transitional regime. Then, the friction gradually increases during the pseudo-passive regime although in the organic-containing electrolytes. The reason for this increasing friction is hypothesised as being due to the fact that there exist a stable but high corrosion current density and lack of tribofilm during this regime. This means that, despite the fact that the charge transfer is stable and limited by diffusion control, however, the cathodic reaction becomes more inhibited and the protein tribofilm therefore cannot be formed. At the same time, the accelerated oxidation reaction can also deform the surface via the corrosion process and change asperities of the contacting surfaces. This study also indicates that the protein content in FBS tends to reduce the COF at the transpassive regime, where the ionic charge transfer begins to dominate the electrolyte-surface interface after the mass transport control during the pseudo-passive regime. This can be related to the friction in DMEM, which still gradually increases during transpassive despite containing organic species (except the protein structure) and has a similar transient friction with the sample tested in saline electrolyte.

The COF was also transient within the cathodic polarisation test in all organic-containing electrolytes, whilst steadily reduced with the decreasing potentials in the saline electrolyte. This is clearly influenced by different electrolyte species and surface conditions due to the change in the electrochemical reactions at the electrolyte-surface interface. The evidence for this difference can be spotted when the frictions were transiently changed with the shifting cathodic polarisation regimes. As shown in Figure 6.7, the cathodic current in the organic-containing electrolytes is segmented into three regimes from E_{corr} to E=-1.0 V: cathodic-active, concentration and the second active polarisation regimes. The friction was observed to increase transiently during the cathodic-active polarisation regime when compared to E_{corr}, where the cathodic current increased as a function of the reducing potential. Then, the friction transiently decreased during the cathodic concentration regime. This regime is where the increasing cathodic current is limited and becomes constant over the lower potentials. Therefore, it can be hypothesised that the reduction reaction is driven by the electrochemical potential, which affects the surface condition. During the cathodic-active regime, the interface is dominated by an activation/ionic charge control of the oxygen reduction process [134]. The current is, therefore, increasing due to the ionic transfer when producing the hydroxide ion without the adsorbed hydrogen atoms. In this case, the insoluble proteinaceous cannot be deposited as a tribofilm formation at the metallic surface during this regime and the surface asperities are thus changed. On the other hand, the cathodic reaction is limited by how fast the oxygen may diffuse in electrolyte [134] due to the mass transport-controlling organic species during the cathodic-concentration regime. Hence, the current tends to be constant as a function of polarisation and the organic tribofilm can be formed at the metal surface. This process may explain the decreasing transient friction during the concentration regime when compared to the active regime in all organic-containing electrolyte. Lastly, the second active polarisation regime, after the concentration regime, was observed in the organic-containing electrolytes. This regime is dominated by the reactions of water reduction and hydrogen evolution. Since there is a product of adsorbed hydrogen evolution, the protein structure with a disulphide chain (RSSR) can be reduced. Hence, the insoluble proteinaceous can be deposited as a tribofilm formation at the metallic surface at this regime [353]. However, increasing friction

was instead observed in DMEM due to the absence of a protein structure in the electrolyte.

6.4.2 Electrochemical Potentials' Effect on the Tribocorrosion mechanism

Electrochemical potential conditions were observed to influence the tribocorrosive loss behaviour of the CoCrMo surface, based on the results obtained in this study. Figure 6.16 shows the volume loss of corrosive and mechanical processes toward total tribocorrosive volume loss after 2 h sliding at E=+0.4 V, -0.2 V, OCP condition and E=-0.8 V in all electrolytes. Subtracting the corrosion volume loss (V_C) and the total volume loss (V_{total}) made it possible to estimate the wear volume loss (V_W) at the E=+0.4 V, -0.2 V and OCP conditions, while the V_C is neglected at E=-0.8 V and V_{total} is thus equal to V_W. Overall, the V_W for each electrolyte at E=+0.4 V was higher when compared to samples tested at the E=-0.2 V, OCP condition and E=-0.8 V (Table 6.6).

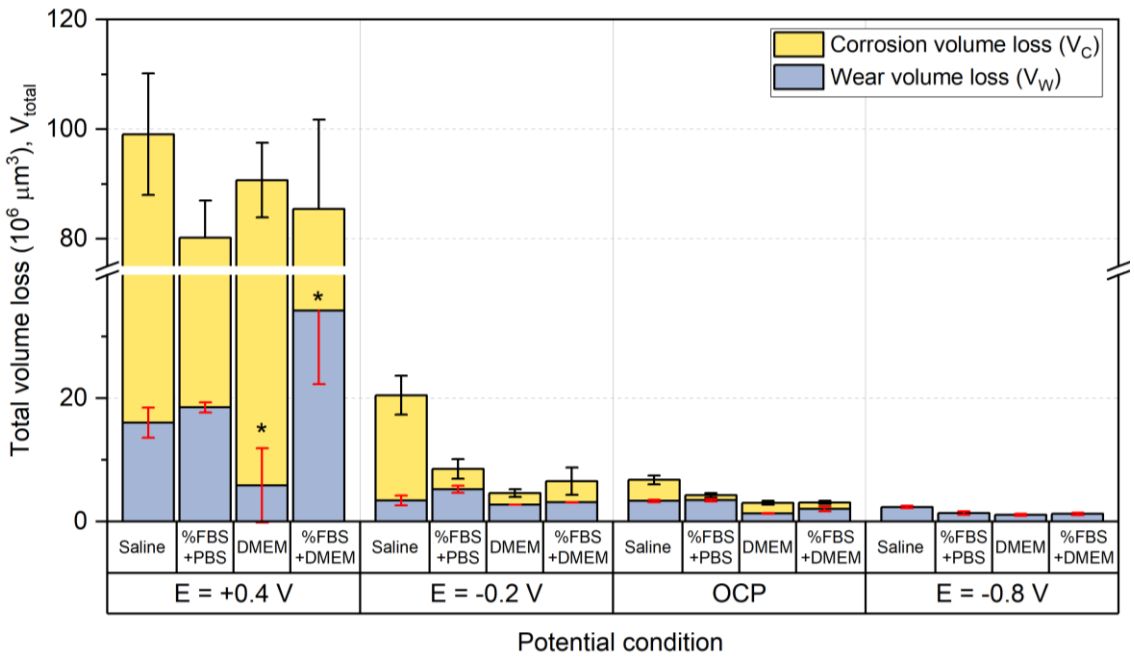

Figure 6.16 The contributors to total volume loss after 2 h sliding at E=+0.4 V, -0.2 V, OCP condition and E=-0.8 V in all electrolytes (n=3; SD bar)

Table 6.6 The volume loss of each contributor using the tribocorrosion mechanistic approach after 2 h sliding tests (n=3; ±SD)

Conditions	Electrolytes	Tribocorrosion mechanistic contributors (x 10^6 µm^3)		
		Total vol. loss, V_{total}	Corr vol. loss, V_C	Wear vol. loss, V_W
E=+0.4 V	**Saline**	**99.08 ± 8.64**	83.05 ± 11.07	16.03 ± 2.46
	25% FBS in PBS	**80.23 ± 5.92**	61.71 ± 6.74	18.51 ± 0.85
	DMEM	**90.70 ± 0.78**	84.83 ± 6.82	5.87 ± 6.06
	25% FBS in DMEM	**85.46 ± 4.32**	51.25 ± 16.26	34.21 ± 11.97
E=-0.2 V	**Saline**	**20.48 ± 2.34**	17.05 ± 3.15	3.43 ± 0.84
	25% FBS in PBS	**8.53 ± 2.15**	3.28 ± 1.57	5.25 ± 0.60
	DMEM	**4.60 ± 0.63**	1.84 ± 0.63	2.76 ± 0.06
	25% FBS in DMEM	**6.57 ± 2.16**	3.45 ± 2.20	3.12 ± 0.07
OCP	**Saline**	**6.77 ± 0.91**	3.42 ± 0.71	3.35 ± 0.23
	25% FBS in PBS	**4.25 ± 0.55**	0.79 ± 0.35	3.46 ± 0.23
	DMEM	**3.04 ± 0.39**	1.72 ± 0.32	1.32 ± 0.10
	25% FBS in DMEM	**3.10 ± 0.63**	1.04 ± 0.24	2.06 ± 0.42
E = -0.8 V	**Saline**	**2.36 ± 0.20**	-	2.36 ± 0.20
	25% FBS + PBS	**1.40 ± 0.28**	-	1.40 ± 0.28
	DMEM	**1.09 ± 0.18**	-	1.09 ± 0.18
	25% FBS + DMEM	**1.24 ± 0.22**	-	1.24 ± 0.22

At E=+0.4 V, the DMEM showed a significant reduction in V_W when compared to the saline electrolyte and FBS-containing electrolytes. No significant difference in the V_W between the saline electrolyte and 25% FBS + PBS was observed. At E=-0.2 V, the V_W was observed to increase for the 25% FBS + PBS when compared to the saline electrolyte and DMEM-containing electrolytes. An increasing V_W was also observed for the 25% FBS + DMEM when compared to the sample tested in the DMEM. Furthermore, the V_W trend at E=-0.2 V was in strong agreement with the OCP condition, showing that the DMEM had the lowest V_W when compared to the

saline electrolyte and FBS-containing electrolytes. Also, at the OCP condition, the 25% FBS + PBS had the highest V_W, although this was not statistically significant when compared to the saline electrolyte. From these differences in all potential conditions, it can be hypothesised that the protein content in the FBS tends to increase the volume loss owing to mechanical wear (V_W) when compared to the protein-free electrolytes. It can even be observed that the 25% FBS-containing electrolytes had a higher volume loss at E=-0.8 V when compared to the DMEM, although it was not statistically different and was purely mechanical wear without any corrosion-enhanced wear loss.

This section investigates the effect of electrochemical potential conditions on the tribocorrosion of the CoCrMo surface when using the mechanistic approach. As explained in the previous section, the friction behaviour is changed by the polarisation regime and electrolytes species due to the effect of the electrochemical reaction influencing the tribofilm formation. Hence, the tribocorrosive loss is hypothesised to correlate with the change in surface friction behaviour. Figure 6.17 shows the relationships between V_C, V_W and the steady-state friction (μ) after 2 h sliding at the E=+0.4 V, E=-0.2 V and OCP conditions in all electrolytes. The mapping of the tribocorrosion mechanisms using a ratio of V_C over V_W at each condition can also be observed. Nevertheless, the mechanistic map for the samples tested at E=-0.8 V cannot be investigated since there was only a pure mechanical wear process during the sliding test.

At E=+0.4 V (Figure 6.17a), the tribocorrosive loss on the CoCrMo tested in the DMEM was dominated by the corrosion mechanism. It was shown that the V_C predominantly contributed to the total volume loss (V_{total}) of the samples in the DMEM and saline electrolyte (except for the lower V_W in saline electrolyte when compared to the DMEM). On the other hand, the corrosion-wear mechanism was seen to dominate the tribocorrosion process for the CoCrMo tested in saline electrolyte, 25% FBS + PBS and 25% FBS + DMEM. It is clear that the CoCrMo in the DMEM tends to be susceptible to corrosion but can resist the mechanical wear process, whilst the opposite is true for the sample tested in the 25% FBS-containing electrolytes. Furthermore, the comparison order of steady-state μ in all electrolytes is in line with the volume loss owing to corrosion (V_C). The CoCrMo tested in the

DMEM and saline electrolyte was observed to have a higher V_C and steady-state μ when compared to both of the 25% FBS-containing electrolytes.

At E=-0.2 V (Figure 6.17b), the tribocorrosion process of the CoCrMo tested in the saline electrolyte and 25% FBS + DMEM was dominated by the corrosion-wear mechanism. The sample in the 25% FBS + PBS and DMEM were seen to be dominated by the wear-corrosion mechanism during the 2 h sliding. Interestingly, the tribocorrosion mechanisms for the DMEM and 25% FBS + DMEM were seen to be inconsistent between the corrosion-wear and wear-corrosion regimes. This is an indication that the DMEM content tends to be more susceptible to corrosion when compared to the role of protein in FBS. In this case, the V_W was clearly shown to contribute predominantly to the V_{total} of the 25% FBS + PBS sample. However, the difference in the V_C for the 25% FBS + PBS, DMEM and 25% FBS + DMEM was not statistically significant. Furthermore, the CoCrMo tested in the saline electrolyte was observed to have a significantly higher V_C and steady-state μ when compared to all of the organic-containing electrolytes. The sample in the 25% FBS + DMEM showed a higher V_C and steady-state μ when compared to the 25% FBS + PBS and DMEM, although this difference was not significant.

Figure 6.17c shows the relationships between the tribocorrosion mechanism and the steady-state μ at the OCP condition, in a modification of Figure 5.14b. As explained, the tribocorrosion mechanism in the 25% FBS-containing electrolytes was observed to be dominated by the wear-corrosion mechanism. The corrosion-wear mechanism was seen to dominate the tribocorrosion process in the saline electrolyte and DMEM. Furthermore, the sample in the saline electrolyte showed a massive V_{total} when compared to the organic-containing electrolytes. This is due to both of the tribocorrosion contributors, V_C and V_W, increasing with the mechanistic ratio close to ~1 during the 2 h sliding in the saline electrolyte. On the other hand, the V_W was clearly shown to contribute predominantly to the V_{total} of the 25% FBS + PBS sample, which is in strong agreement with the trend at E=-0.2 V. Nevertheless, the saline electrolyte sample had the highest V_C and steady-state μ when compared to the organic-containing electrolytes. The DMEM tended to increase the V_C and steady-state μ when compared to the 25% FBS-containing-electrolytes.

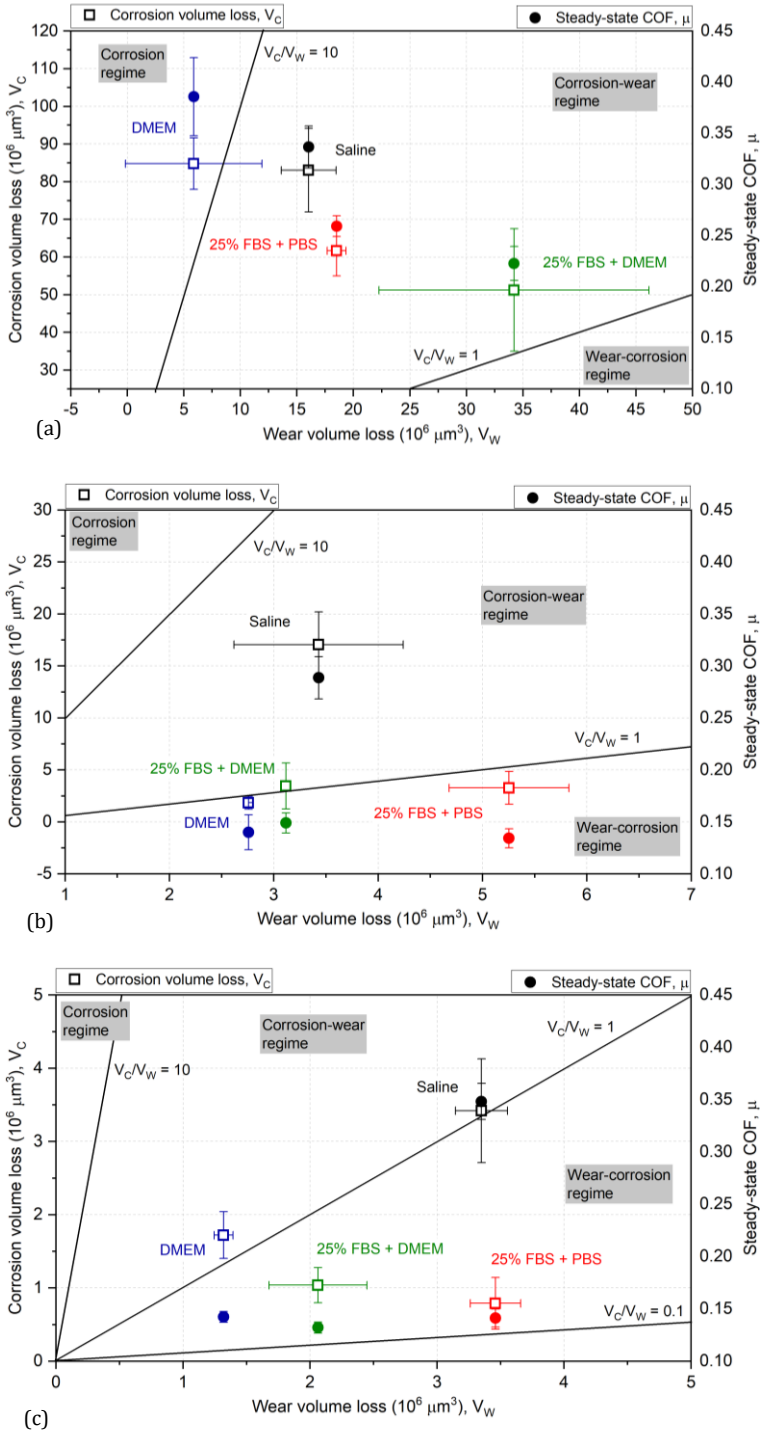

Figure 6.17 The relationships between the corrosion volume loss (V_C), wear volume loss (V_W) and steady-state friction (μ) after 2 h sliding at (a) E=+0.4 V, (b) E=-0.2 V and (c) the OCP condition in all electrolytes (n=3; SD bar)

This study showed significant increases in the COF and tribocorrosive volume loss observed in samples tested at E=+0.4 V in the saline electrolyte and organic-containing electrolytes when compared to the lower potential conditions. This

behaviour was also indicated by the obtained potentiodynamic curve at the pseudo-passive regime. In the literature [86], a typical passive regime in the polarisation or galvanostatic condition at passive alloys usually shows a significant reduction in the corrosion current. The corrosion reduction typically stabilises during this regime, indicating that a stable formation of passive film inhibits the corrosion reaction. However, this study instead showed a significant increase in the corrosion current during the pseudo-passive potential regime, which agrees with studies using the CoCrMo alloy [94, 96, 355]. The corrosion current was significantly higher and stable during this regime, indicating the passive protective film at the alloy surface. Therefore, severe damage and tribocorrosive material loss were seen at the wear scar after potentiostatic E=+0.4 V in this study and were dominated by the corrosive mechanism when compared to the samples tested at the E=-0.2 V and OCP conditions. Also, since the proteinaceous or organic film coverage decreased at E=+0.4 V, the tribocorrosive loss therefore increased, although tested in the organic-containing environments. This is one of reasons why the organic matter's functions become less effective at E=+0.4 V.

The increasing friction and tribocorrosive loss for the CoCrMo tested at E=+0.4 V was also hypothesised to be related to the change in the material sub-surface during tribocorrosion at the anodic condition. Wang et al. [282] theoretically calculated that the shear stress in the sub-surface depth increased at higher applied potentials, owing to the increased COF and contact stress. The wear mechanism caused surface dislocations at the sliding condition; e.g., pushing in the sub-surface structures toward the bulk material, pulling out the structure and forming debris due to the dislocations piled up at the interface [282, 356]. Bidiville et al. [357] demonstrated that the flux of the dislocated surface towards the bulk material was increased due to the covering passive film. The stacking fault density and strain accumulation at the sub-surface were hypothesised to increase since the anodic potential allows more oxidation and a passive film formed. The strain accumulation might cause sub-grains and nanocrystal formation, so a massive material loss in the wear scar and high COF during sliding at E=+0.4 V occurred. Although very few traces of tribofilm were found at the CoCrMo tested in the 25% FBS-containing electrolyte, the protein content in the FBS was hypothesised to affect the sub-surface behaviour at E=+0.4 V due to protein adsorption [358]. As a result, the 25% FBS-containing

electrolytes tended to decrease the average COF and corrosive volume loss when compared to samples tested in protein-free electrolytes (the saline electrolyte and DMEM) at E=+0.4 V. However, the protein content in the FBS and organic matter in the DMEM are still less effective in surviving the CoCrMo surface, with significantly higher friction and volume loss when compared to the lower applied potential. The higher ion flux due to the accelerated oxidation is hypothesised to change the interactions between the metal-proteinaceous species. Consequently, this might also change the sub-surface of the CoCrMo, after which a high material loss and COF at the pseudo-passive potential tend to occur. This study did not provide any sub-surface evidence. However, the linked results of potentiodynamic polarisation, the COF and the increasing loss in both contributors, V_C and V_W (Figure 6.17a), when compared to the lower potentials, can represent the explained theory.

6.4.3 Concluding Remarks

It has been suggested that the electrolyte species is sensitive to electrochemical potential. The organic matter's functions are hypothesised to become less effective regarding the protective role regarding material loss at E=+0.4 V, when compared to the lower potential and OCP conditions. In organic-containing electrolytes, the tribocorrosion mechanism at E=-0.2 V and OCP conditions was seen to shift at least one regime towards the wear regime from their mechanism at E=+0.4 V. Samples tested in saline electrolyte at all potential conditions showed a consistent corrosion-wear mechanism dominating the tribocorrosive degradation, while the 25% FBS + PBS in all conditions were dominated by the wear-corrosion mechanism. Based on these maps, the comparison order of V_C in all electrolytes under applied potential conditions are in line with the trend of COF. Hence, the change in the surface friction behaviour is shown to correlate not only with tribochemistry (see previous section) but also with the tribocorrosive loss via the corrosion process (V_C). The corrosion process is governed by the nature of the electrochemical potential and also the species in the electrolytes. These factors can deform the surface condition and asperity of the contacting surfaces due to oxidation and wear-enhanced corrosion degradation. By correlating with the tribochemical behaviour in the previous section, the surface deformation mechanism can explain why corrosion loss influences the surface friction behaviour of the CoCrMo alloy.

In the non-organic containing electrolyte (saline electrolyte, in this study), a high COF was observed throughout the changes of potential when compared to organic-containing electrolytes. This behaviour is due to the absence of organic matter in the electrolyte, and therefore the tribofilm can only rely on passive oxide formation to survive the surface friction. The friction in saline electrolyte was even observed to increase transiently with the increasing potentials during anodic polarisation (except at the transitional regime) and reduce with the decreasing potentials during cathodic polarisation. The change in friction indicates a correlation between the accelerated oxidation reaction due to the increasing potential with the asperity of the contacting surfaces, suggesting a deformation at the metal surface due to the corrosion process. Based on all of the comparisons, the interaction between the electrochemical potential condition and electrolyte species affects the change in the electrochemical reactions at the electrolyte-surface interface. Then, these reactions manipulate the tribofilm formation and eventually drive the friction behaviour on the contacting surfaces.

6.5 Chapter Summary

This chapter has presented details of the successful investigation into the effects of electrochemical potentials on tribochemistry at the CoCrMo alloy surface, tested in organic-containing environments. The tribocorrosion mechanism was also observed in the presence of organic matter at the potentiostatic via a sliding test. The results were analysed and compared to the findings outlined in the previous chapter. The following points are offered to conclude this chapter:

- A steady increase in the transient COF as a function of the anodic potentials, via potentiodynamic, was observed in the saline electrolyte and DMEM samples, whilst the FBS-containing electrolytes showed a friction reduction at E~0.5V.
- The total atomic percentage of the proteinaceous elements was higher via EDS in organic-containing electrolytes at the E=-0.8 V wear scar compared to the E=+0.4 V and E=-0.2 V, indicating greater protein adsorption at the CoCrMo surface tested at the cathodic potential.

- The total tribocorrosive loss significantly increased in all electrolytes for potentiostatic at E=+0.4 V when compared to the E=-0.2 V and OCP conditions.
- More significant reductions in the corrosion volume loss, total volume loss and steady-state COF were observed at the potentiostatic E=+0.4 V in FBS-containing electrolytes, compared to the samples tested in the saline electrolyte and DMEM.
- The tribocorrosion mechanism in the saline electrolyte was dominated by the corrosion-wear interaction at all potential conditions, whilst the wear-corrosion mechanism was primary in the FBS-containing electrolytes at this potential. The tribocorrosion process in the sample tested in the DMEM electrolytes was also dominated by a wear-corrosion mechanism at the E=-0.2 V and OCP conditions, except for the corrosion mechanism at E=+0.4 V.
- The change in the surface friction behaviour is indicated to correlate with the tribocorrosive loss via the corrosion process (V_C) at various electrochemical potential conditions.
- The electrochemical potential condition and electrolyte species interaction affect the electrochemical reactions at the electrolyte-surface interface. These reactions manipulate the tribofilm formation and eventually drive the friction behaviour and tribocorrosive degradation on the contacting surfaces.

Chapter 7
The Effect of Protein Structure and Concentration on the Surface Chemistry and Tribocorrosion at the CoCrMo Alloy

7.1 Chapter Introduction

Elevations in temperature owing to the frictional shear of the asperity at the contacting interfaces, known as 'flash temperatures', are extensively described in the field of tribology [233]. However, the temperature parameter has received little attention in the area of biotribology, despite the sensitive nature of the lubricating environment [11]. The native protein structure is known to be sensitive to temperature, leading to the protein denaturation process [228]. It is therefore logical that the tribochemistry at the contacting surfaces is also affected, since the protein structures in synovial fluid can be degraded due to the increased flash temperature. Therefore, it is essential to understand the underlying degradation mechanisms of metallic bearings when subjected to various protein conditions in biological fluid.

Previous studies have investigated protein and metal alloy interactions at several temperatures and protein concentrations, as explained above in the literature review. However, no study used deliberately denatured protein structures as the testing electrolyte during tribocorrosion. Although several studies have also employed external heat and Raman spectroscopy to examine the protein structure in the biochemistry field, the subsequent effect of this on the tribology and corrosion remains largely unknown. Therefore, Chapter 7 aims to present an understanding of the role of protein structures and concentration on tribocorrosion and surface tribofilms formed on CoCrMo alloys during boundary regime sliding. The experiments in this chapter were performed in order to address the following questions:

- What is the influence of simulated flash temperatures on the denaturation of serum proteins?

- What is the role of protein structure and concentration on the deposited chemical elements within the wear scar at the CoCrMo surface?
- What is the role of protein structure and concentration on the tribocorrosion mechanism at the CoCrMo surface?

The flow diagram in Figure 7.1 shows the general experimental methods and surface analysis conducted in this chapter. One of the novelties of this study is the use of heat intentionally to break down the protein structure and simulate the possibility of temperature changes occurring inside the human body via tribology at hard surfaces.

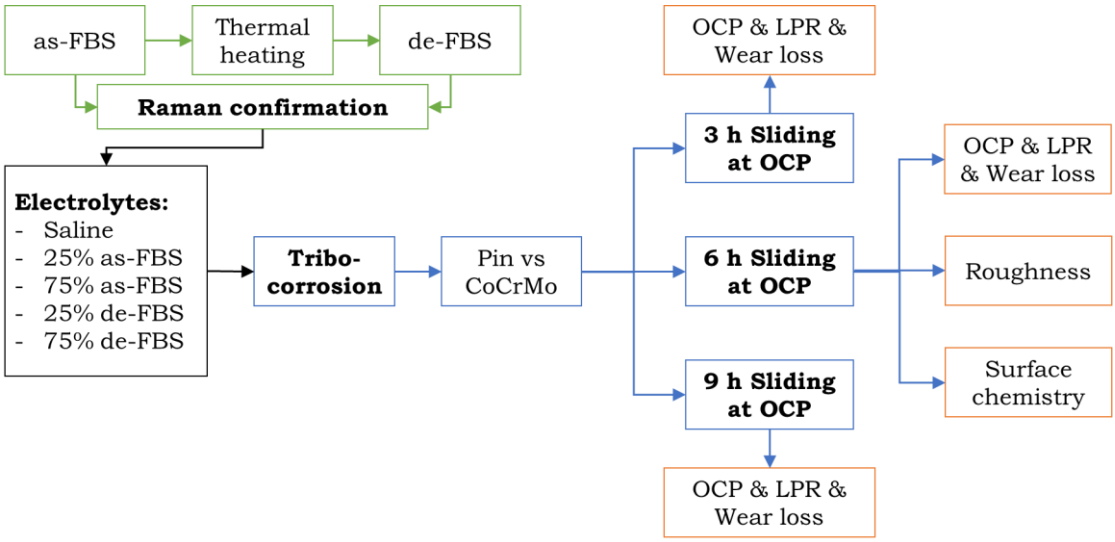

Figure 7.1 Schematic of the tribocorrosion tests and analysis protocols throughout Chapter 7

Raman spectroscopy was used to characterise the effect of pre-heated bovine serum on changes in protein structure, by determining the denaturation of FBS after an hour being heated at various simulated flash temperatures, prior to dilution for tribocorrosion testing. The untreated (as-FBS) and heated (de-FBS) FBS were then diluted in saline electrolyte (0.9% NaCl) at different concentrations (25% and 75% v/v) for the tribocorrosion tests.

7.2 Raman Confirmation

Figure 7.2a shows the Raman spectra of the secondary structure (amide I) and disulphide bonding chain bands between 1500-1800 cm^{-1}. An amide I peak of as-FBS, characterised at ~1654 cm^{-1}, was observed. The shift in the amide I peak was seen to reach ~1667 cm^{-1} with increasing temperature (after heating at 70°C). Figure 7.2b shows the ratio between the Raman peaks intensity at heated FBS over the as-FBS (I_T/I_0) to identify the changes as a function of temperature. A critical reduction, with a steep slope in the intensity ratio, was observed at temperature 50°C after polynomial fitting. Moreover, an extensive reduction was observed at 70°C, showing half of the as-FBS intensity ratio.

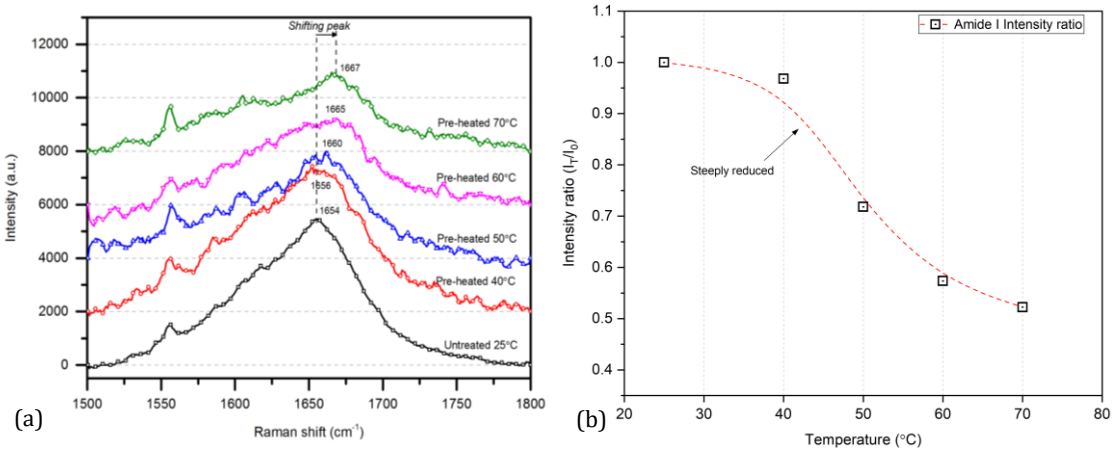

Figure 7.2 (a) Raman spectra and (b) intensity ratio (I_T/I_0) of the amide I band of the secondary structure in as-FBS and 1 h heated FBS at various simulated temperatures

Figure 7.3 shows the Raman spectra for FBS before (as-FBS) and after heat treatment at 70°C. Figure 7.4 shows that the percentage of ordered α-helix decreased with heat treatment and enhanced the disordered α-helix percentage. This indicates that the native structure became denatured. A significant decrease in the amide I peak intensity was seen for the de-FBS after being subjected to heat-treatment at 70°C for 1 h. Therefore, the pre-heated FBS at 70°C for 1 h was used as content for the tribocorrosion electrolyte, further termed as 'de-FBS'.

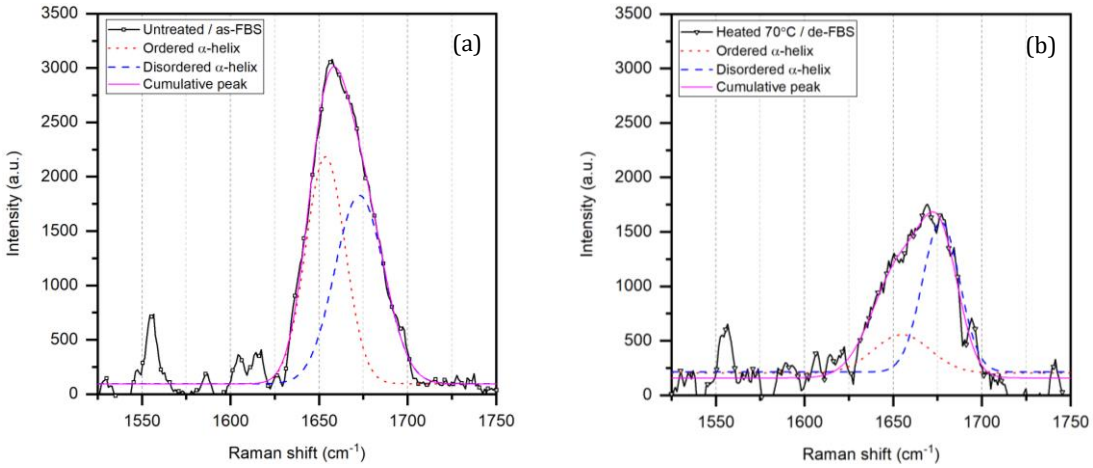

Figure 7.3 Deconvolution samples of the amide I Raman band to fit the sub-peaks of an α-helix structure for (a) the untreated / as-FBS and (b) after 1 h being heated at 70°C / de-FBS

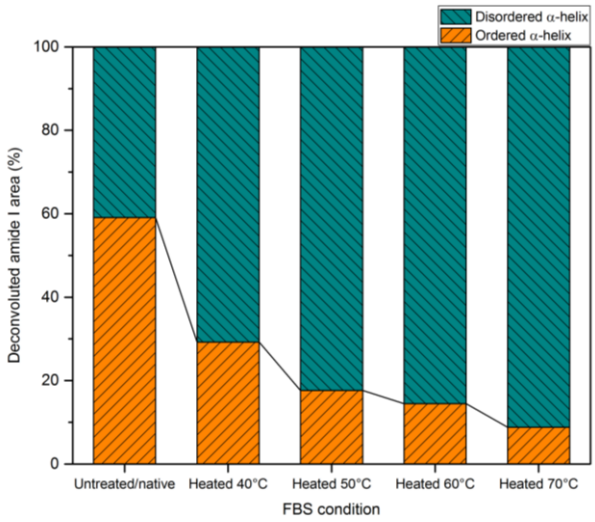

Figure 7.4 The deconvoluted area percentage of α-helix structures in each peak, comparing the as-FBS and all heated FBS protein structures

The characterisation of the changes in pre-heated FBS was conducted in this study via Raman analysis. A change in the amide I peak intensity, showing a decrease in the ordered α-helix and an increase in the disordered α-helix deconvoluted area percentages, was seen for the de-FBS after being thermally treated at 70°C for 1 h. A past study [240] demonstrated that the protein conformational structure is reversible at temperatures below 50°C. However, protein becomes irreversibly unfolded after heat treatment higher than 60°C. After reaching 70°C, the physical

form of the proteins can be altered into a gel-like structure along with a change in colour. That study also showed that the critical temperature range for protein denaturing was 50-60°C. Similar to this study, the unfolding processes (the α-helices secondary structure) were indicated by the shifting of the Raman peaks and a reduction in signal intensity. Therefore, the protein structure in the de-FBS electrolyte used in this study was suggested to be fully denatured since the pre-heating treatment has passed the unfolding critical temperature.

7.3 Tribocorrosion Tests

Tribocorrosion tests produced simultaneous results for the coefficient of friction and OCP evolutions. The result of the intermittent LPR measurement was also processed to obtain a charge transfer and corrosion volume loss. The CoCrMo samples (n=3) were immersed in the electrolyte for 500 s to stabilise the static OCP (vs RE Ag/AgCl). The 9 h sliding tests were conducted to measure OCP simultaneously during friction (Figure 7.5). After sliding, the static OCP was still measured for 500 s.

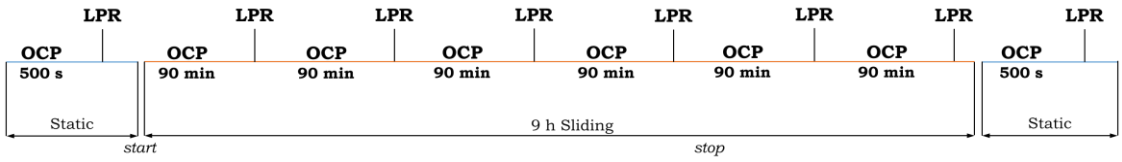

Figure 7.5 Schematic of the 9 h tribocorrosion test at the OCP condition

7.3.1 Coefficient of Friction (COF)

Figure 7.6a shows the transient coefficient of friction /COF (μ) over 9 h of sliding. A typical trend was demonstrated with the highest friction in saline electrolyte when compared to the FBS-containing electrolytes. An increase in the transient friction was observed during the first 2,500 cycles of sliding in saline electrolyte then became steady. All FBS containing electrolytes displayed a similar, steady state μ.

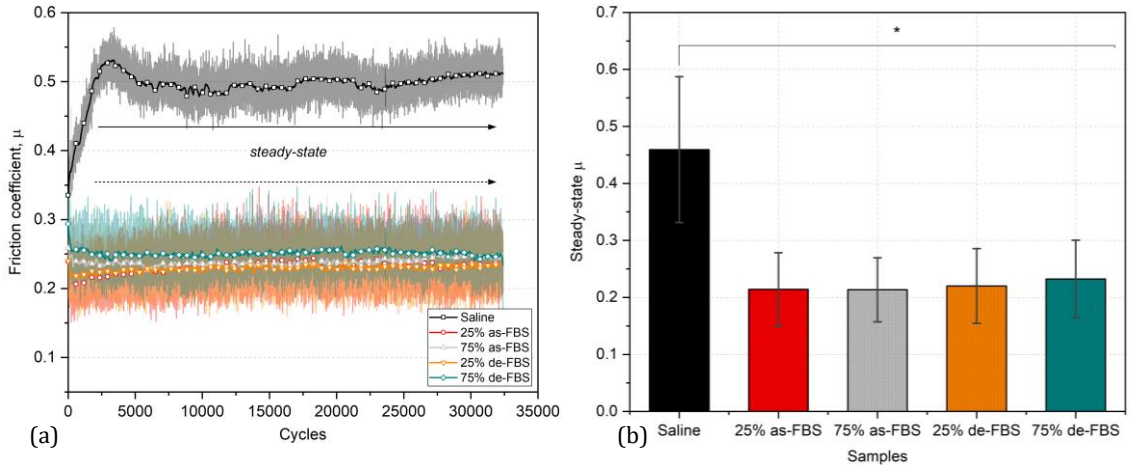

Figure 7.6 (a) The evolution of the transient COF over 9 h sliding cycles and (b) the average steady-state COF in the saline electrolyte and FBS-containing electrolytes (n=3; SD bar; *p<0.05)

Figure 7.6b shows the average steady-state COF (averaged over the final 1 min of the sliding test) with a standard deviation (error bar). The COF significantly decreased in the FBS electrolytes when compared to the saline electrolyte of μ ~0.46 ± 0.13. No significant difference in the steady-state μ ~0.23 ± 0.07 was observed for the as-FBS or de-FBS.

7.3.2 OCP Measurement

Figure 7.7a and Figure 7.7b show the transient OCP evolution during the early immersion (pre-sliding), tribocorrosion test and after the test (post-sliding) in all electrolytes. A typical de/re-passivation behaviour upon the start of sliding was seen in the tests conducted using saline electrolyte [8]. The addition of the FBS modified this behaviour and an increase in OCP was seen when the sliding ceased, indicating an ennoblement of the surfaces. Interestingly, although the OCP reduction occurred when sliding was initiated, the transient OCP in all of the FBS electrolytes steadily increased over the test duration. After sliding, the OCP in all of the electrolytes recovered to values greater than those recorded in the initial static immersion stage.

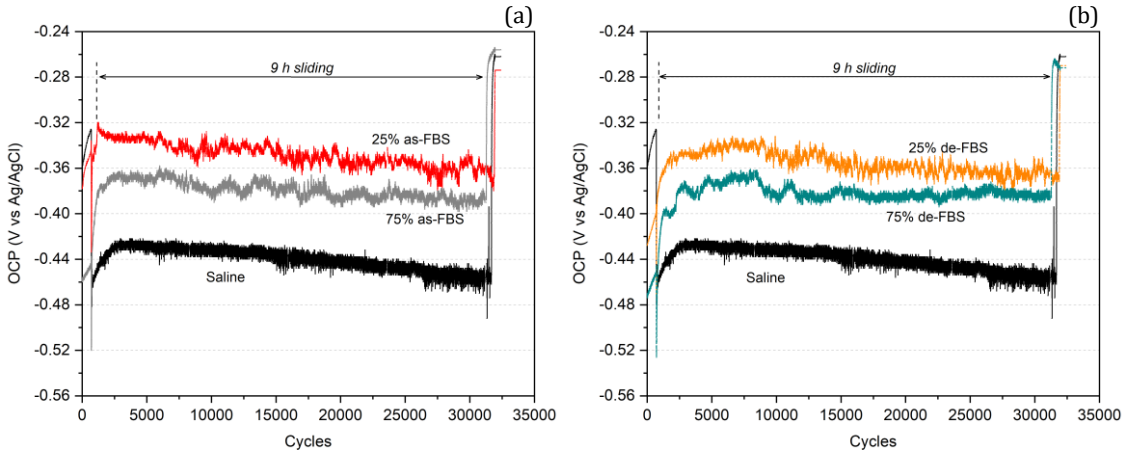

Figure 7.7 The evolution of the transient OCP in (a) as-FBS and (b) de-FBS measured over early immersion (pre-sliding), tribocorrosion test and after the test stopped (post-sliding) to compare saline electrolyte and different FBS concentrations (n=3)

In the static immersion stage (pre-sliding), the CoCrMo sample in the saline electrolyte had a more noble OCP ~ -0.37 V when compared to the 75% FBS-containing electrolytes and 25% de-FBS. During this test stage, the OCP for the 25% de-FBS was seen to be more noble when compared to the sample immersed in the 75% de-FBS. During sliding, the OCP in the saline electrolyte ~ -0.45 V was more negative when compared to all of the FBS electrolytes. Similarly to the pre-sliding stage, the OCP for the 25% de-FBS during the sliding stage was seen to be more noble when compared to the sample tested in the 75% de-FBS. In the post-sliding stage, all of the electrolytes had a more noble OCP when compared to their pre-sliding stage. No difference was observed for the post-sliding OCP between the saline electrolyte and FBS-containing electrolytes. Furthermore, the 75% as-FBS had a more positive OCP when compared to the 25% de-FBS sample.

7.3.3 Corrosion Volume Loss

Figure 7.8a shows the evolution of the current density, measured by LPR, during the 9 h tribocorrosion tests. All of the samples tended to have a lower current density in the absence of sliding, both before and after sliding, when compared to the sliding stage (Table 7.1). Furthermore, the current densities tended gradually

to increase as a function of time during the sliding stage. Overall, for all of the tests conducted in the 25% FBS-containing electrolytes, the current densities were lower than for the tests conducted in the 75% FBS and saline electrolytes. In sliding, the de-FBS tended to result in lower current densities when compared to the as-FBS electrolytes.

Figure 7.8b shows the average total charge transfer for all of the tribocorrosion tests. For all test durations, the use of the 25% FBS and 75% FBS was seen significantly to decrease and increase the total charge transfer, respectively, when compared to the saline electrolyte. Furthermore, an increase in the charge transfer was observed for all of the 75% FBS-containing electrolytes when compared to all of the samples tested in the 25% FBS-containing electrolytes. No significant difference in the total charge transfer was observed between the CoCrMo tested in as-FBS or de-FBS.

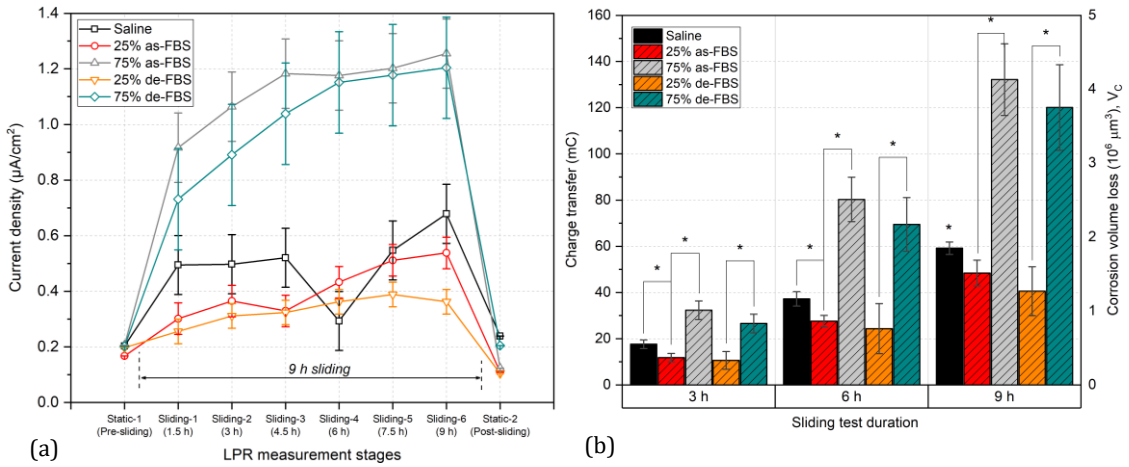

Figure 7.8 (a) The evolution of the corrosion current density measured during the 9 h tribocorrosion and (b) a comparison of the total charge transfer and corrosion volume loss with a split of test durations (n=3; SD bar; *p<0.05)

Table 7.1 The total charge transfer and corrosion volume loss (V_C) at OCP in all electrolytes with a split of sliding durations (n=3; ±SD)

Electrolytes	Charge transfer, Q (mC)			Corrosion volume loss, V_C (x 10^6 µm^3)		
	3 h	6 h	9 h	3 h	6 h	9 h
Saline	17.60 ± 1.85	37.26 ± 3.12	59.19 ± 1.69	0.55 ± 0.06	1.17 ± 0.10	1.86 ± 0.05
25% as-FBS	11.82 ± 0.85	27.58 ± 2.48	48.45 ± 5.59	0.37 ± 0.03	0.87 ± 0.08	1.53 ± 0.18
75% as-FBS	32.32 ± 4.04	80.28 ± 7.63	132.15 ± 8.53	1.02 ± 0.13	2.53 ± 0.24	4.16 ± 0.27
25% de-FBS	10.62 ± 0.85	24.38 ± 1.84	40.54 ± 5.59	0.33 ± 0.03	0.77 ± 0.06	1.28 ± 0.18
75% de-FBS	26.60 ± 4.04	69.49 ± 7.63	120.09 ± 8.53	0.84 ± 0.13	2.19 ± 0.24	3.78 ± 0.27

7.4 Post-Test Wear Analysis

The wear analysis involved chemical analysis (SEM/EDS), surface topography (AFM) and total volume loss (VSI), along with the SWR calculation.

7.4.1 SEM and Chemical Analysis

Figure 7.9 and Figure 7.10 show the SEM and EDS analysis of the wear scars (two different spots) for the CoCrMo surfaces after being tested for 9 h in the as-FBS and de-FBS electrolytes, respectively. These SEM images were supported by EDS mapping to observe the distribution of the elements within the wear scar. Several species, i.e., carbon (C) and sulphur (S), appeared, along with metal elements (Co, Cr and Mo) and oxygen (O). The EDS analysis at the wear scar edges and corner indicated signs of carbon and oxygen. Sulphur and traces of carbon were also observed within the wear scar. The darker layers dominated the tip corner of the wear and inside wear track and along the wear borders. The EDS confirmed carbon

and sulphur from bovine serum and also oxide from the passive reformation. The wear scar at the 25% FBS showed a smaller width (via the SEM image scale) and more oxide films were visible at the corner when compared to the 75% FBS.

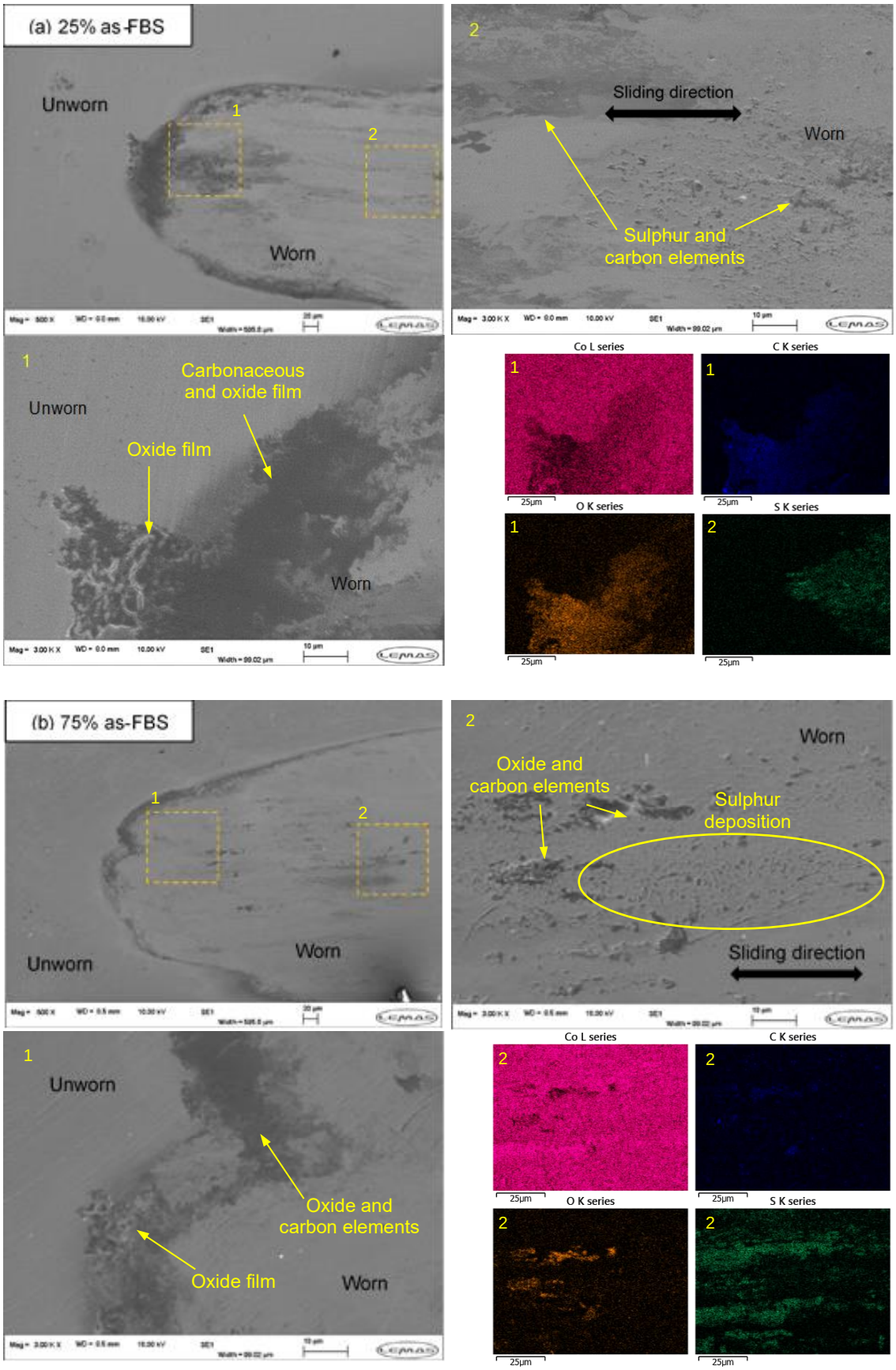

Figure 7.9 SEM/EDS in the wear scar of the CoCrMo alloys after being tested in (a) 25% as-FBS and (b) 75% as-FBS

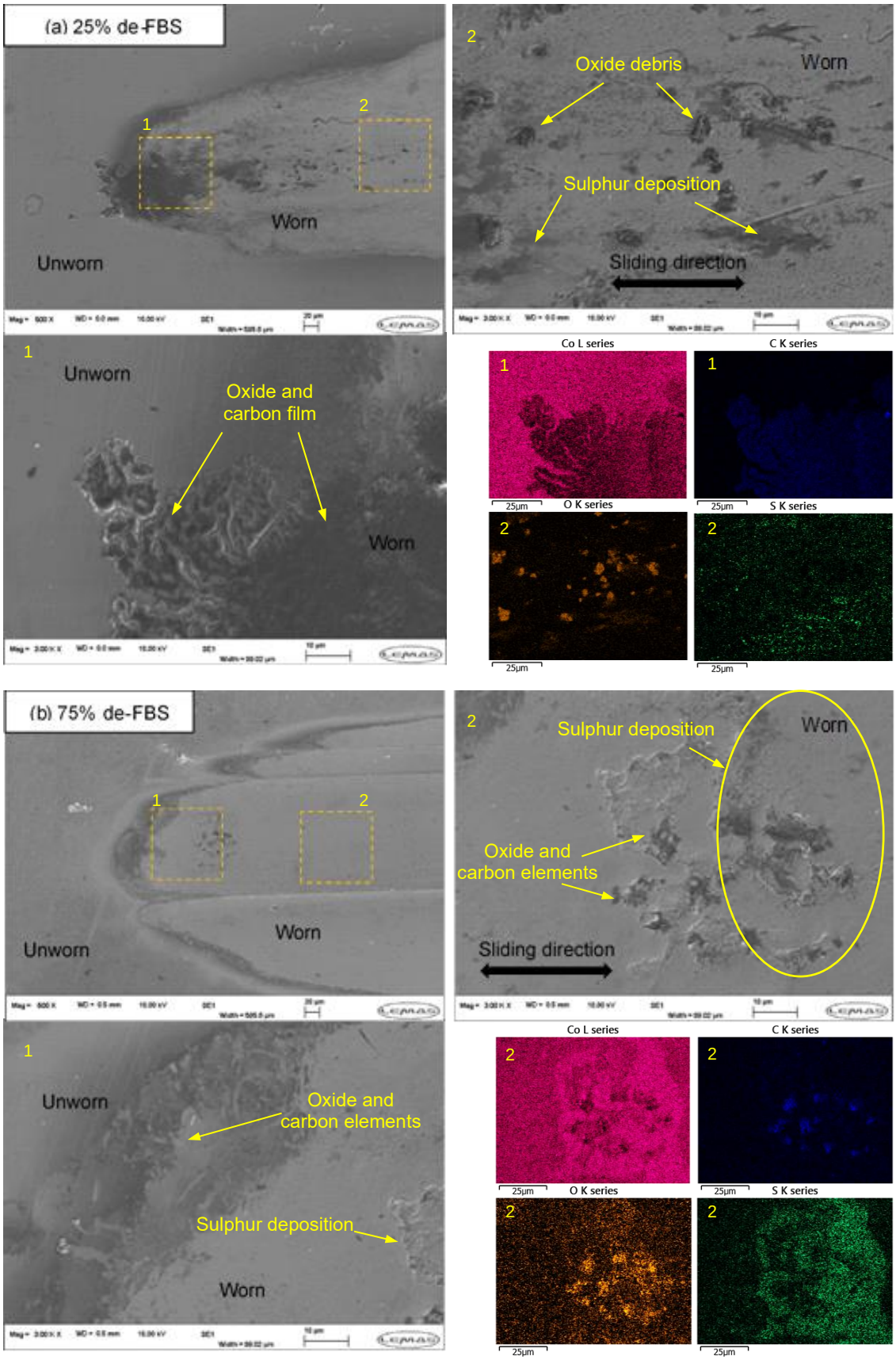

Figure 7.10 SEM/EDS in the wear scar of the CoCrMo alloys after being tested in (a) 25% de-FBS and (b) 75% de-FBS

Table 7.2 shows the average atomic percentages of the elements (n = two different spots) found on the CoCrMo surfaces after the 9 h tribocorrosion test. The atomic percentages of the carbon, oxygen and nitrogen were relatively lower on the surfaces tested in the 75% FBS samples when compared to the 25% FBS samples. On the contrary, the sulphur element percentage was higher on the 25% FBS samples when compared to the 75% FBS samples. Carbon and oxygen were found to increase in the wear scar of the denatured FBS samples. The sulphur was observed to be higher on samples tested in the 75% FBS-containing electrolytes when compared to the 25% FBS electrolytes.

Table 7.2. EDS atomic percentage of the deposited elements at CoCrMo surfaces tested in saline electrolyte and FBS-containing electrolytes (n=2; ±SD)

Elements	Atomic percentages (at%)				
	Saline	25% as-FBS	75% as-FBS	25% de-FBS	75% de-FBS
Co	50.19 ± 0.95	41.11 ± 0.91	43.76 ± 0.47	29.91 ± 0.96	44.03 ± 0.39
Cr	18.72 ± 0.48	12.80 ± 0.20	11.99 ± 0.49	8.99 ± 0.23	10.29 ± 0.53
Mo	3.36 ± 0.16	6.58 ± 0.07	6.89 ± 0.08	5.02 ± 0.11	7.02 ± 0.08
O	27.73 ± 0.83	13.52 ± 0.95	8.51 ± 0.25	25.64 ± 0.60	9.46 ± 0.06
C	-	19.71 ± 0.74	15.53 ± 0.23	24.29 ± 1.09	19.26 ± 0.25
N	-	2.17 ± 0.07	1.82 ± 0.05	2.67 ± 0.11	1.20 ± 0.02
S	-	4.13 ± 0.58	11.52 ± 0.16	3.50 ± 0.47	8.75 ± 0.83

7.4.2 Surface Topography

Figure 7.11 shows representative images of the surface topography of samples tested in the different electrolytes, as measured by AFM. Signs of abrasion (characterised by grooves/scratches) was observed in the wear scar of the CoCrMo samples tested in a saline electrolyte. The AFM analysis of the CoCrMo surfaces tested in FBS electrolytes displayed evidence of film formation and localised build-up, arranged in the direction of sliding. The CoCrMo surfaces tested in as-FBS showed a smoother texture compared to those tested in de-FBS. The film deposition

for the CoCrMo surface tested in the de-FBS was seen to be more scattered when compared to surfaces tested in the as-FBS. The samples tested in the de-FBS demonstrated an increased amount of localised build-up of material on the surface when compared to surfaces tested in the as-FBS.

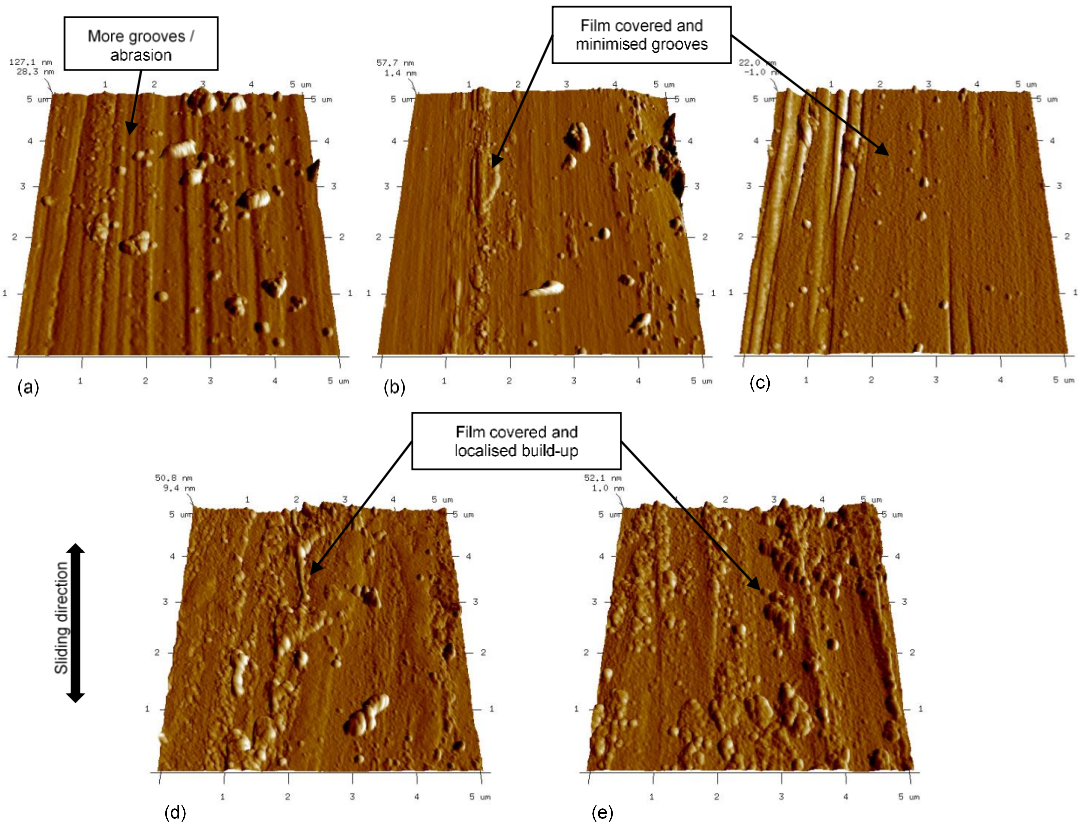

Figure 7.11 AFM 5x5 µm images of wear scar after being tested in (a) saline electrolyte, untreated (b) 25% FBS and (c) 75% FBS, as well as denatured (d) 25% FBS and (e) 75% FBS

7.4.3 Total Volume Loss

Figure 7.12a shows the V_{total} measured by VSI with respect to the tribocorrosion test duration in all electrolytes. The V_{total} was significantly higher for the CoCrMo tested in the saline electrolyte when compared to all of the FBS electrolytes for all test durations (Table 7.3). After the 3 h sliding tests, the V_{total} was higher for all of the 75% FBS-containing electrolytes when compared to the 25% FBS-containing electrolytes. The CoCrMo tested in the 75% de-FBS was observed significantly to decrease the V_{total} when compared to the 75% as-FBS, indicating the role of

denaturing protein in FBS. No significant difference was observed between all of the FBS electrolytes after the 6 h sliding tests. Furthermore, after the 9 h sliding tests, the V_{total} for the 25% de-FBS was significantly lower when compared to the CoCrMo tested in the 25% as-FBS and the 75% de-FBS.

Figure 7.12b shows the SWRs for each time duration of the tribocorrosion test. The purpose of the SWR comparison was to interrogate any degradation mechanism change within each test interval (every three hours during the 9 h tribocorrosion test). During the 3 h sliding tests, the SWR was suggested to change due to the protein concentration in the FBS, showing a higher average SWR for all of the 75% FBS-containing electrolytes when compared to the 25% FBS-containing electrolytes. Furthermore, the CoCrMo tested in the 75% de-FBS was observed significantly to decrease the SWR when compared with the 75% as-FBS, indicating the role of the denaturing protein in the FBS. No significant difference was observed between the FBS electrolytes during the 6 h sliding tests. After the 9 h sliding test, the SWR for the 25% de-FBS was seen to be significantly lower when compared to the CoCrMo tested in the 25% as-FBS and 75% de-FBS.

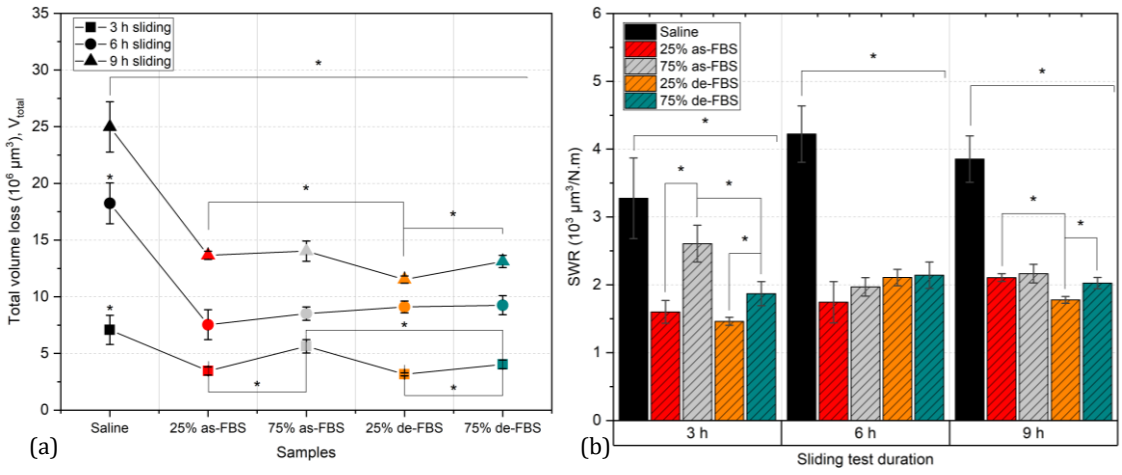

Figure 7.12 Comparison (a) total volume loss measured by VSI and (b) SWR with a split of test durations of 3, 6 and 9 h tribocorrosion tests in all electrolytes (n=3; SD bar; *p<0.05)

Table 7.3 Total volume loss at the OCP (V_{total}) and the SWR of the wear scar on the CoCrMo in all electrolytes, with a split of sliding test durations (n=3; ±SD)

Electrolyte	Total volume loss, V_{total} (x 10^6 µm^3)			SWR (x 10^3 µm^3/N.m)		
	3 h	6 h	9 h	3 h	6 h	9 h
Saline	7.07 ± 1.29	18.24 ± 1.79	24.98 ± 2.22	3.28 ± 0.60	4.22 ± 0.42	3.85 ± 0.34
25% as-FBS	3.46 ± 0.36	7.53 ± 1.32	13.65 ± 0.37	1.60 ± 0.17	1.74 ± 0.30	2.11 ± 0.06
75% as-FBS	5.63 ± 0.59	8.51 ± 0.58	14.03 ± 0.89	2.61 ± 0.27	1.97 ± 0.14	2.16 ± 0.14
25% de-FBS	3.16 ± 0.13	9.11 ± 0.52	11.52 ± 0.32	1.46 ± 0.06	2.11 ± 0.12	1.78 ± 0.05
75% de-FBS	4.04 ± 0.38	9.25 ± 0.84	13.12 ± 0.54	1.87 ± 0.18	2.14 ± 0.20	2.02 ± 0.08

7.5 Chapter Discussion

There are a limited number of studies which used the treated serum protein as electrolyte during tribocorrosion. For the first time, the tribocorrosion tests were conducted in the pre-heated FBS-containing electrolyte. This study aimed to understand the role of the pre-heated FBS and its concentration in the electrolyte on the tribocorrosive behaviour and surface tribofilms of CoCrMo alloys. Hence, the relationship between the FBS electrolytes and tribocorrosion mechanism, based on the obtained results, is discussed in this section.

7.5.1 Tribocorrosion mechanism in Various Protein Conditions

Figure 7.13 shows the contribution of volume loss due to corrosive (V_C) and mechanical (V_W) processes to the total tribocorrosive volume loss (V_{total}) as a function of test duration and electrolyte. The V_C was estimated using Faraday's Law, allowing subtraction of V_{total} to obtain V_W (Table 7.4). For all test durations, saline

electrolyte had the highest V_W when compared with all FBS-containing electrolytes. Following a 3 h sliding test, the V_W for 25% as-FBS and 75% de-FBS were significantly lower when compared to 75% as-FBS. After 6 h sliding tests, a significant difference in V_W was observed for 25% de-FBS, which was higher when compared to 75% de-FBS. After 9 h sliding tests, CoCrMo tested in 25% as-FBS was seen to have a significantly higher V_W when compared to 75% as-FBS and 25% de-FBS. Furthermore, the V_W for 25% de-FBS was significantly higher when compared to 75% de-FBS.

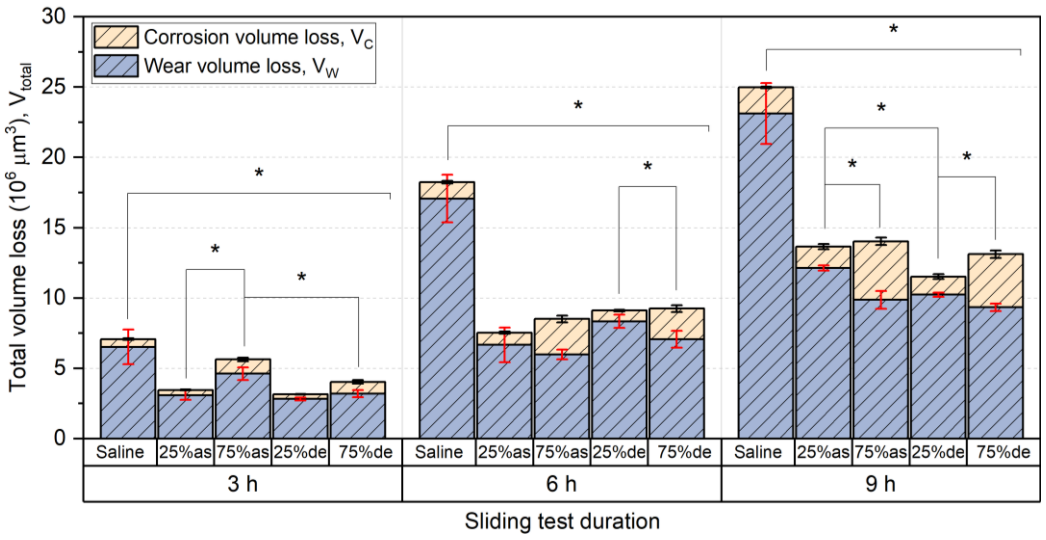

Figure 7.13 The contributors to total volume loss as a function of the tribocorrosion test duration for all electrolytes (n=3; SD bar; *p<0.05 for V_W as a function of electrolyte)

Table 7.4 The volume losses of each contributors from tribocorrosion mechanistic approach with a split of sliding test durations (n=3; ±SD)

Electrolyte	Tribocorrosion mechanistic contributors (x 10^6 µm^3)					
	Corrosion volume loss, V_C			Wear volume loss, V_W		
	3 h	6 h	9 h	3 h	6 h	9 h
Saline	0.55 ± 0.06	1.17 ± 0.10	1.86 ± 0.05	6.52 ± 1.26	17.07 ± 1.73	23.11 ± 2.20
25% as-FBS	0.37 ± 0.03	0.87 ± 0.08	1.53 ± 0.18	3.09 ± 0.37	6.66 ± 1.27	12.13 ± 0.22
75% as-FBS	1.02 ± 0.13	2.53 ± 0.24	4.16 ± 0.27	4.61 ± 0.49	5.98 ± 0.37	9.86 ± 0.65
25% de-FBS	0.33 ± 0.03	0.77 ± 0.06	1.28 ± 0.18	2.82 ± 0.13	8.34 ± 0.50	10.24 ± 0.18
75% de-FBS	0.84 ± 0.13	2.19 ± 0.24	3.78 ± 0.27	3.20 ± 0.29	7.06 ± 0.63	9.33 ± 0.30

Figure 7.14 shows the volume loss ratio (%-contribution) as a function of the test duration and electrolyte. In all cases, the %-V_W was seen to contribute to more than 70% of the V_{total}. In the case of CoCrMo tested in 75% de-FBS, the %-V_c was seen to increase with increased sliding time, accounting for ~30% of the total material loss. This trend is hypothesised to be influenced by a change in tribochemical behaviour on the CoCrMo surface as a function of the sliding duration and different protein concentrations in FBS electrolytes. FBS with a 75% concentration is hypothesised to form a tribofilm on the CoCrMo surface over the sliding cycles, improving the lubricity to minimise the incremental rate of mechanical wear degradation based on the results of this study. However, this particular concentration of protein in electrolyte increased the rate of corrosion. There was no evidence of the effect of protein structure on the incremental rate of volume loss contributors over all test durations.

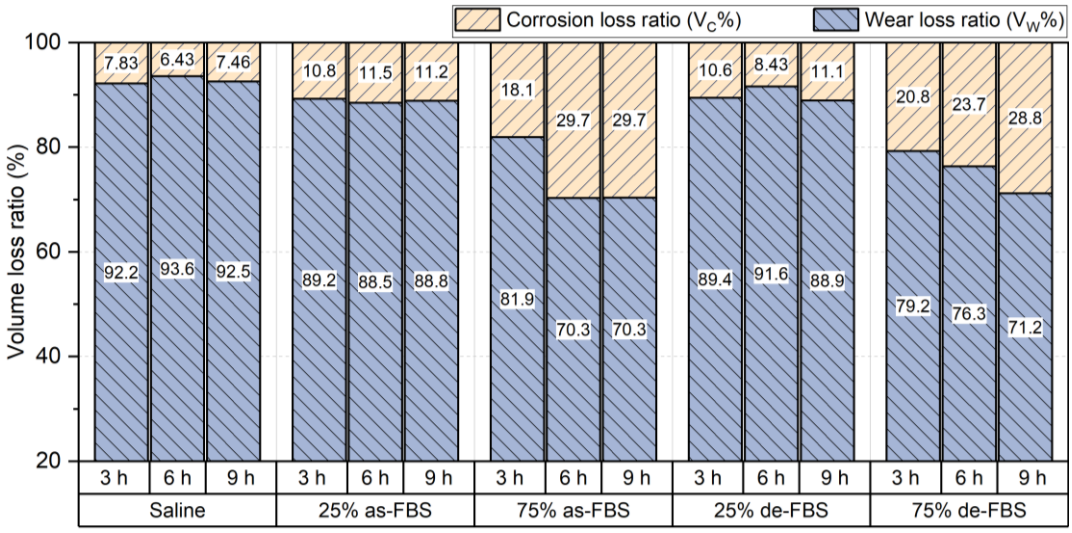

Figure 7.14 The ratio of the contributing volume loss components as a function of tribocorrosion test duration for all electrolytes

To investigate the link between protein structure and concentration effects, the V_C and V_W can be used to indicate tribocorrosive behaviour via the mechanistic approach [223] after 3, 6 and 9 h sliding tests in various FBS-containing electrolytes (Figure 7.15). The tribocorrosion process on CoCrMo tested in saline electrolyte was constantly dominated by the mechanical wear mechanism during the 3, 6 and 9 h sliding tests. On the other hand, all of the FBS-containing electrolytes consistently showed that the wear-corrosion mechanism was dominating the tribocorrosive degradation for all sliding test durations, except for 25% de-FBS after 6 h sliding in, which represented a wear dominated regime. However the total volume loss was not significantly different when compared to the 25% as-FBS in the wear-corrosion regime. Furthermore, the tribocorrosion mechanism was shifted back onto the wear-corrosion mechanism after 9 h sliding.

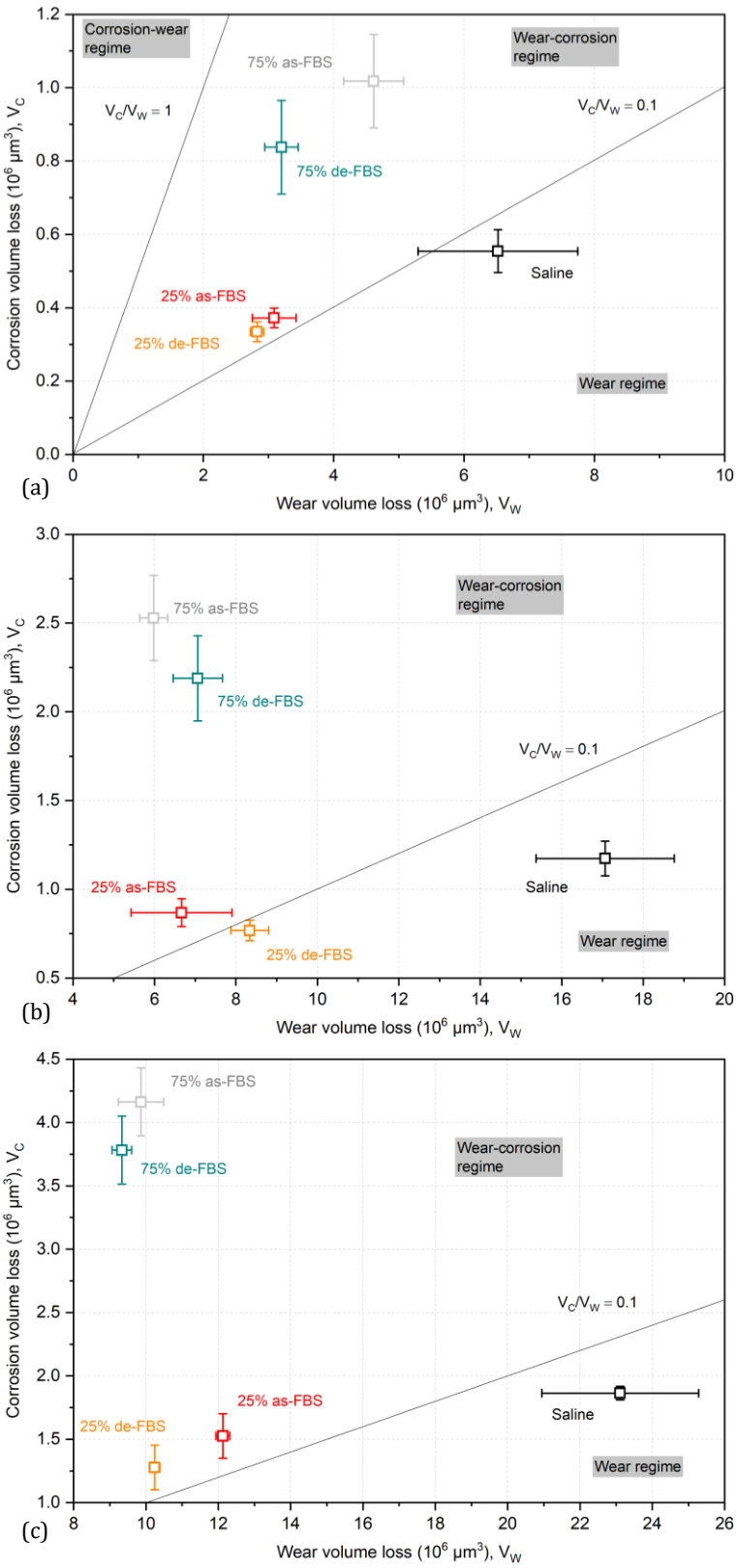

Figure 7.15 The tribocorrosive behaviour of CoCrMo using a mechanistic approach after (a) 3 h, (b) 6 h and (c) 9 h sliding tests in all electrolytes (n=3; SD bar)

These observations suggest that the tribocorrosion mechanism of CoCrMo is independent of sliding duration. Whilst there is also no effect of protein structure and concentration observed on the overall tribocorrosion mechanism during the sliding test, the contribution of wear and corrosion did vary with time (i.e. ratio varies). The reason for a wear-corrosion dominated mechanism in all FBS electrolytes is hypothesised as being due to the distinctive effect of protein concentration in reducing mechanical damage but increasing the corrosion process on the CoCrMo surface during the sliding condition. This mechanistic behaviour is in strong agreement with a study by Mathew et al. [221], showing that wear-corrosion dominated the tribocorrosive degradation at alumina-CoCrMo interfaces in bovine calf serum electrolyte. The study also explained that the wear-corrosion mechanism can be driven by the increasing material degradation on the surface as a function of increasing contact pressure. However, the wear mechanism was seen to dominate the tribocorrosion process in saline electrolyte. In this case, the reason for wear behaviour is because the saline electrolyte is protein-free electrolyte, which can lead to an increased role in the degradation process. However, it is clear that the electrolyte with a lower protein concentration (25% FBS, in this case) tends to shift the plot towards the wear regime by reducing V_C when compared to the 75% FBS-electrolytes. In addition, the denatured FBS tends to lower the material degradation by reducing both V_C and V_W without changing the V_C/V_W ratio when compared to as-FBS electrolytes. These results indicate that the role of protein concentration is unaffected by the protein structure.

7.5.2 Protein Denaturation Effect on Surface Chemistry Behaviour

In this study, the effect of denatured protein structure in de-FBS electrolytes on the volume loss was not consistent over the sliding test duration. A reducing trend in total volumetric loss (V_{total}) was observed during the tribocorrosion test in de-FBS electrolytes at 3 h and 9 h sliding tests when compared to as-FBS electrolytes (refer to Figure 7.12a). However, these differences are only significant for the 75% concentration at the 3 h sliding test and 25% concentration at 9 h sliding. Nevertheless, the denatured protein structure in de-FBS electrolytes tends to reduce the volume loss owing to mechanical wear (V_W) on the CoCrMo samples when compared to as-received, FBS-containing electrolyte. Moreover, the

denatured protein structure in de-FBS electrolytes is also indicated to decrease the volume loss owing to corrosive degradation (V_C) on the CoCrMo samples when compared to as-FBS electrolytes. This is hypothesised as being due to the change in tribochemical and oxidation reactions on the articulating surface. After being pre-heated at 70°C, the physical form of the proteins can be altered into a gel-like structure along with a change in colour, which is in line with a study by Lin et al. [240]. The denaturing processes also raises interesting questions concerning the rheology of the electrolyte at the interface. If a gel-type electrolyte were to form as a result of denaturation of the protein, it is plausible that a decrease in mechanical degradation processes may arise through enhanced electrolyte. It has also been observed in this study that the de-FBS incurred a lower total charge transfer, which indicated a reduction in volume loss due to corrosion, further highlighting the need to gain a clearer understanding of the complex interfacial degradation mechanisms. The denatured protein in FBS was observed to be attracted to form a proteinaceous tribofilm, which tends to interact with metal ions, suppress the metal ions release and reduce material loss owing to mechanical wear [258, 276].

The reason for this decreasing behaviour can be linked with the denaturing effect on protein-metal interaction and film deposition. The change in film formation due to denatured protein adsorption behaviour has been shown via AFM data on a CoCrMo slide for a 9 h tribocorrosion test (refer to Figure 7.11). Mishina and Kojima [273] investigated serum albumin changes due to friction in the combinations of CoCrMo, polyethylene (UHMWPE) and alumina samples. The study showed that protein denaturation occurs in the temperature range of 50-55°C, affecting the absorption behaviour and decreasing friction and wear. The effect of protein denaturation on wear reduction obtained in that study can be linked with the finding of this study, which is influenced by the change in protein adsorption on the CoCrMo surface. Proteins with an unfolded structure were observed to have a higher kinetic rate to be adsorbed on the CoCrMo surfaces [229].

Firstly, the thermal heating can be hypothesised to modify the disulphide bridges in this study along with amide I band in the Raman spectra. This hypothesis is based on previous studies [236, 241, 242], which reported that the Raman bands of albumin in bovine serum could represent disulphide bridge bonding. The signal peak was demonstrated to change for denatured protein when compared to the

native one, indicating disulphide structure aggregation. This study does not show the conformation of disulphide bridges via Raman spectra within the electrolyte. However, this study provides evidence of cobalt, molybdenum and sulphur on the surfaces via EDS after tribocorrosion, the concentration of which is affected by the FBS concentration and protein structure. Furthermore, the authors have identified Mo-S speciation via XPS in a previous study which was hypothesised to influence the wear and friction during tribocorrosion [1]. The presence of sulphur in the form of cobalt sulphide was also observed via XPS and SAED images within the tribofilm on the CoCrMo surface tested in bovine serum by Hesketh et al. [10]. The presence of sulphur on the surface and its tendency to reduce volume loss due to mechanical wear have been demonstrated in several studies [344, 345]. However, the effect of the sulphur element on volume loss due to corrosion has not been observed yet.

Secondly, a higher carbon signal was detected on CoCrMo tested in de-FBS electrolytes when compared to as-FBS samples. The carbonaceous film deposition can reduce the corrosion process on CoCrMo alloy in the tribological condition [260, 261]. The film was formed under the articulating condition due to a complex electro-tribochemical reaction that was affected by tribological aspects and organic-metal interaction on the implants surface [8]. The tribofilm compositions assessed in the previous study (indicated by C and N elements) on the worn CoCrMo surfaces were observed to enhance its lubricity and corrosion protection [1, 259]. Furthermore, Wimmer et al. [274, 359] investigated the protein species on CoCrMo alloy after being tested *in vitro* in hip simulator and retrieved implants. The study demonstrated that the protective tribofilm formation on the retrieved samples were formed by the mechanism of shear stress on the contacting surfaces. The shear stress was observed to induce the denaturation process of protein structure in biological fluids. Thus, it can be hypothesised that the denaturing protein affects the properties of the tribofilm and its protective effect on the material degradation. Also, the carbonaceous film obtained via EDS on samples tested in de-FBS plays an essential role in reducing volume loss. A bigger localised build-up width, measured from 0.2-0.5 μm, was also seen on de-FBS samples by AFM when compared to as-FBS. AFM could not confirm that those were protein species. However, the SEM/EDS mapping scans can observe the carbon element on the worn surfaces.

Based on this study, the protein structure in FBS electrolytes appears to reduce the tribocorrosive degradation of the CoCrMo surface. These effects are caused by the change in tribochemical behaviour on the sample during sliding. This behaviour can also indicate the mechanism of how denaturing FBS changes the protein adsorption, tribofilm formation and material degradation of the tested CoCrMo surface. The denatured protein conformation is hypothesised to be important in the protein adsorption process, that contributes to the protective tribofilm formation at the contacting interfaces. The denaturing protein in electrolyte can therefore reduce the volume loss owing to the corrosion and wear processes of the CoCrMo surface slide since the beginning of the 3 h sliding test. This is because the denatured protein structure has a higher rate of adsorption on the CoCrMo surface [229], in which the de-FBS will more readily form a protective tribofilm due to fast kinetics compared to the as-FBS electrolyte.

7.5.3 Serum Concentration Effect on Surface Chemistry Behaviour

The higher FBS concentration was observed to increase the volume loss due to corrosion. As expected from the charge transfer data, the V_C in as-FBS and de-FBS at 75% concentration were significantly higher than at a 25% concentration. On the other hand, the V_W were significantly lower at a 75% concentration than 25% FBS electrolytes. Thus, the V_C at a 75% concentration were responsible for increasing the V_{total}. This behaviour indicates that a higher FBS concentration is hypothesised to enhance the synergism between wear and corrosion during sliding. Also, the corrosion process is suggested to promote material degradation during sliding at 75% FBS electrolytes. In line with the observations by Thornley et al. [319] it can be hypothesised that the increased FBS concentration will inhibit oxygen-reduction reactions and delay passive film formation, hence resulting in a higher/sustained dissolution process.

The behaviour of protein aggregation had a higher protein concentration when compared to the lower concentration compliments observations made by

Sun et al. [360] observed the protein aggregation behaviour originating from the simulated electrolytes containing bovine serum at different protein concentrations. The study reported that misfolded protein aggregates were found on the worn

CoCrMo surfaces with various dimensions. The proteins seemed to be aggregated and bonded with metal debris and ions, forming agglomeration bodies trapped within the contact surface. The extent of agglomeration might be affected by protein concentration since it would be easier to bind the metal debris/ions in electrolyte. In this study, the aggregated proteins in high concentration coincided with increased corrosion loss (Figure 7.8b). These proteins also tended to produce a typical abrasive mechanism, indicated in the AFM (Figure 7.11) and SEM results (Figure 7.9 and Figure 7.10). Nevertheless, the higher protein concentration is indicated to have an positive effect on reducing the volume loss owing to mechanical wear. The FBS with a 75% concentration tends to reduce the V_W when compared to the 25% FBS concentration for CoCrMo after being tested for 6 h and 9 h. In the present study, higher sulphur and lower oxygen percentages were observed by EDS on the wear scar after testing in 75% FBS. The mechanism is hypothesised to relate to the protein film's deposition, which was catalysed by the protein concentration.

In the present study, 75% FBS-containing electrolytes reduced the OCP and increased corrosion during static immersion and sliding when compared to 25% FBS. This observation was complimented by evidence of less oxygen in the wear scar as confirmed by EDS. The 75% FBS also increased the total charge transfer in the tribocorrosion test. The protein concentration effect on the tribocorrosion performance of CoCrMo alloys was investigated by Sun et al. [279]. It shows that the increasing protein concentration was observed to reduce CoCrMo resistance to polarisation (and increase corrosion) due to competitive behaviour. The concentration also affected the potential at the CoCrMo surface in a static condition [167]. This behaviour is in strong agreement with a study by Vidal and Munoz [361] that characterised the electrochemical behaviour on CoCrMo alloys in simulated body fluid. Albumin has been shown to reduce the polarisation resistance and inhibit the oxide film formation in a static test. The protein concentration accelerated the anodic reaction since the adsorbed protein can bind and transport the metal ions away from the electrolyte/metal interfaces. Thus, protein content causes less protective passive/oxide film formation compared with that without protein. However, the protein behaviour remains debatable since the biological species have complex reactions on the corrosion mechanisms in biomedical alloys.

A study by Thornley et al. [319] showed different electrochemical processes of CoCrMo in simulated body fluid. The passive film reformation was quickest in a phosphate-buffered saline (PBS), whilst delayed with bovine serum albumin (BSA) content. It was explained that the albumin inhibits the oxygen-reduction reaction as it obstructs the CoCrMo exposed sites when adsorbed onto the surface. Moreover, BSA content affected the passive film chemistry, e.g. reducing molybdenum quantity from the film composition.

7.5.4 Concluding Remarks

Based on the observations made in this study, the protein structure and concentration in FBS electrolyte have various effects on the tribocorrosive degradation of the CoCrMo surface. These effects are driven by the change in tribochemical behaviour of the sample during sliding. The denatured protein structure and higher protein concentration in electrolyte tend to reduce the volume loss owing to mechanical wear (V_W) on the CoCrMo samples. This result is due to the fact that the denatured protein conformation has a higher rate of adsorption on the CoCrMo surface, building a protective tribofilm formation.

The higher protein concentration also promotes the organic-metal interaction to build the tribofilm formation. This behaviour can be seen after testing at least for 9 h sliding cycles. The denatured protein structure was also observed to decrease the volume loss owing to corrosive degradation (V_C) due to the change in tribochemical and oxidation reactions on the contacting surface. In this current study the 25% FBS concentration has reduced V_C when compared to the CoCrMo tested in protein-free saline electrolyte. However, the 75% FBS concentration instead increases V_C when compared to 25% FBS concentration. It is hypothesised that the effect of protein content on V_C has a dependency on its concentration in electrolyte. Therefore, the CoCrMo tested in 25% de-FBS is observed to have the lowest total volume loss (V_{total}) instead of the 75% de-FBS. This outcome is because the latter tends to affect the tribochemical reaction and oxidation rate on the contacting surface, which promotes the total material loss via corrosive degradation. This behaviour also indicates the independency between the effects of protein structure and concentration on the tribocorrosion mechanism.

7.6 Chapter Summary

The effect of the denaturing of FBS (via heat treatment) with different concentrations on tribocorrosion and tribochemistry on a CoCrMo alloy surface was successfully investigated. The following points are drawn from the obtained results as conclusions:

- The increased protein concentration of FBS electrolytes was seen to reduce the transient OCP and promote charge transfer significantly. However, de-FBS was seen to decrease the corrosion current density when compared to as-FBS electrolytes during sliding.
- The film deposits were seen on the de-FBS samples by AFM without confirming that those were protein species. A bigger localised build-up width, measured from 0.2-0.5 μm, was observed for de-FBS via AFM compared to as-FBS.
- SEM/EDS mapping scans observed higher carbon percentages at the wear scar of the de-FBS samples, when compared to the as-FBS at both concentrations. An increase in sulphur elements was traced for both samples with a concentration of 75% FBS.
- The effects of protein structure and concentration in FBS electrolytes on the tribocorrosive degradation of CoCrMo surface is time-dependent during the tribological condition.
- The denatured protein in the FBS electrolyte can reduce the volume loss due to the corrosion and wear processes of the CoCrMo surface after being tested for 9 h.
- A higher protein concentration is indicated to have a positive effect in reducing the volume loss owing to mechanical wear after 6 h and 9 h sliding tests.
- However, the 75% FBS concentration increases the corrosion volume loss when compared to the 25% FBS concentration. It is hypothesised that the effect of protein content on corrosion volume loss is dependent on its concentration in electrolyte.

Chapter 8
The Effect of Dissolved Metal Ions on the Surface Chemistry and Tribocorrosion at the CoCrMo Alloy

8.1 Chapter Introduction

The role of metallic ions originating from biomedical alloys is well described in the field of biochemistry; e.g., causing an adverse tissue reaction [116-120]. Investigations into the role of metal ions upon static corrosion and protein adsorption behaviour have also been conducted in several *in vitro* studies [107, 108]. However, the roles of dissolved metal ions in friction, wear, corrosion and tribochemistry remain largely unknown.

Thus, Chapter 8 presents details of the investigation into the effect of dissolved metal ions (Co, Cr and Mo ions) in simulated physiological electrolytes on surface chemistry and tribocorrosive behaviour at the CoCrMo surface. The experiments reported in this chapter were expected to address the following questions:

- If the released metal ions in the physiological fluid were found to affect the biological tissue, is there any effect of locally high concentrations of metal ions on surface tribochemical film behaviour?
- What is the role of dissolved metal ions on the material degradation and tribocorrosion mechanism at the CoCrMo surface?

The flow diagram in Figure 8.1 shows the overall experimental methods and surface analysis used in this chapter. A novelty is that the metal ion contents dissolved in simulated electrolytes were used in the tribocorrosion test to replicate the metal ions present in synovial or other biological fluids inside the human body. The interaction between the dissolved metal ions with the tribocorrosive behaviour of the CoCrMo alloy, via the *in vitro* reciprocating tribometer test, was also investigated.

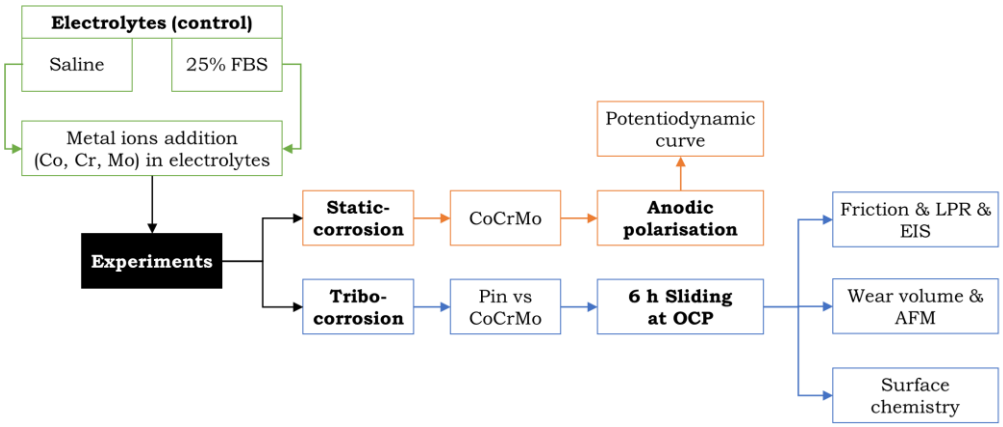

Figure 8.1 Schematic of the tribocorrosion tests and analysis protocols throughout Chapter 8

8.2 Anodic Polarisation

Potentiodynamic scans were conducted to characterise the corrosion properties (shifting potential vs current density) of the CoCrMo immersed in the saline electrolyte and 25% FBS, with and without metal ions. In this case, the potential was shifted anodically, facilitating the corrosion process at higher potentials than E_{corr}. Figure 8.2 shows the anodic polarisation protocol. The flat CoCrMo sample was immersed in the electrolyte for 500 s at the OCP condition to stabilise the passivation. The anodic polarisation started from -50 mV vs the stable OCP value, then shifted to +1 $V_{Ag/AgCl}$ (scanning rate 0.25 mV/s) and simultaneously measured the corrosion current.

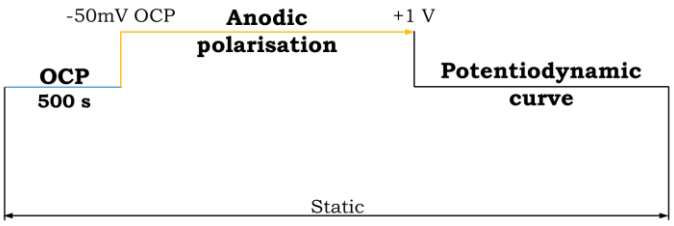

Figure 8.2 Anodic polarisation test protocol

Figure 8.3 shows the anodic polarisation curves at the CoCrMo surface in the saline electrolyte and 25% FBS electrolytes with the addition of metal ions. In saline

electrolyte (Figure 8.3a), the addition of Co and Cr ions tended to increase the corrosion potential and current during the activation-controlled regime (refer to Figure 4.7), but reduce the current density during the transpassive regime of the polarisation curve when compared to the as-saline electrolyte and saline electrolyte +Mo ion. Furthermore, the current densities were observed to increase during the active-transitional regime as a function of the applied potential for the saline electrolyte +Mo when compared to the as-saline electrolyte, saline electrolyte +Co and +Cr ions.

In the 25% FBS electrolyte (Figure 8.3b), the addition of Co and Cr ions tended to reduce the current density slope during the active-transitional and transpassive regimes as a function of the applied potential when compared to the 25% as-FBS and 25% FBS +Mo ion. The addition of the Co and Cr ions to the 25% FBS had a similar characteristic in the current slope during the transpassive regime when compared to the saline electrolyte +Co and +Cr ions.

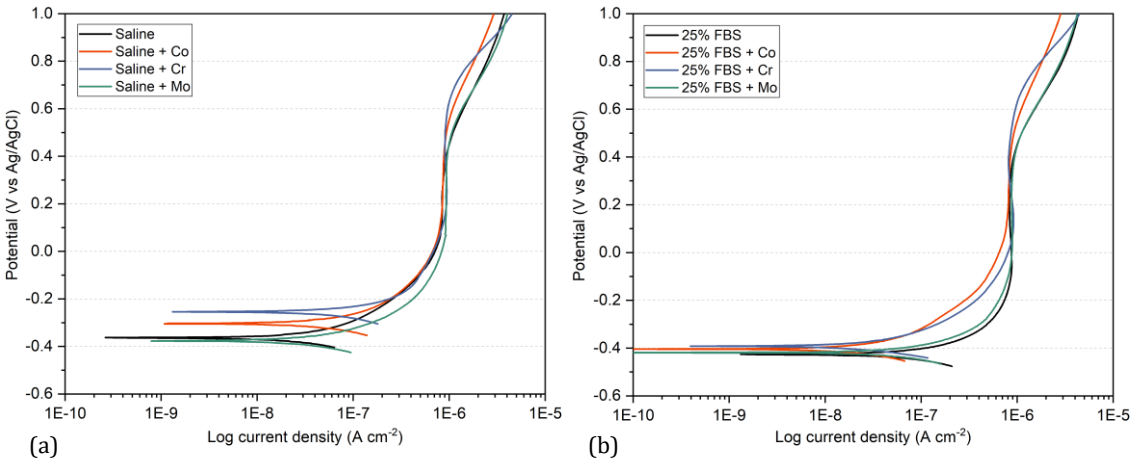

Figure 8.3 Anodic polarisation curves at the CoCrMo surface in (a) saline electrolyte and (b) 25% FBS electrolytes

Table 8.1 summarises the values extracted from the polarisation curves under the static condition. The E_{corr} in the 25% as-FBS was lower when compared to the as-saline electrolyte sample, showing a strong agreement with the trend between saline electrolyte and the 25% FBS + PBS under static condition in Chapter 6. The use of the Co and Cr in saline electrolyte was seen to increase the E_{corr}, I_{corr} and E_{pp}

when compared to the as-saline electrolyte and saline electrolyte +Mo ion. All of the metal ions tended to increase the values of the I_{pp} and E_b in the saline electrolyte. On the other hand, the Co and Cr ions in the 25% FBS were observed to reduce the I_{corr} and increase all of the potential values when compared to samples in the 25% as-FBS and 25% FBS +Mo ion. Furthermore, the addition of the Mo ion to the 25% FBS was seen to increase the E_{pp} and I_{pp} when compared to the 25% as-FBS. However, a potentiodynamic scan was only conducted once for each electrolyte and the statistical standard deviation thus could not be identified.

Table 8.1. Extracted values, E_{corr} with the corresponding current (I_{corr}), pseudo-passive potential (E_{pp}) with its stable current (I_{pp}) and breakdown potential (E_b) from the polarisation curves under static condition in the electrolytes

Electrolytes	E_{corr} (V)	I_{corr} (μA/cm²)	E_{pp} (V)	I_{pp} (μA/cm²)	E_b (V)
Saline	-0.35	0.05	0.07	0.84	0.45
Saline + Co	-0.30	0.07	0.16	0.86	0.52
Saline + Cr	-0.26	0.11	0.18	0.90	0.66
Saline + Mo	-0.38	0.05	0.06	0.93	0.65
25% FBS	-0.43	0.11	-0.10	0.83	0.41
25% FBS + Co	-0.40	0.03	0.13	0.81	0.49
25% FBS + Cr	-0.39	0.04	0.13	0.81	0.63
25% FBS + Mo	-0.42	0.09	-0.02	0.88	0.42

8.3 Tribocorrosion Tests

The tribocorrosion tests produced simultaneous results for the coefficient of friction and OCP evolutions in all electrolytes. The intermittent LPR measurement was also processed to obtain the charge transfer and corrosion volume loss in different electrolyte contents. The CoCrMo samples (n=3) were immersed in the electrolyte for 500 s to stabilise the static OCP (vs Ag/AgCl electrode). After sliding,

the static OCP was still measured for 500 s. The 6 h sliding tests also simultaneously measured the OCP during friction. Furthermore, the EIS measurements were conducted before and after the 6 h sliding tests to observe the change in impedance behaviour (Figure 8.4).

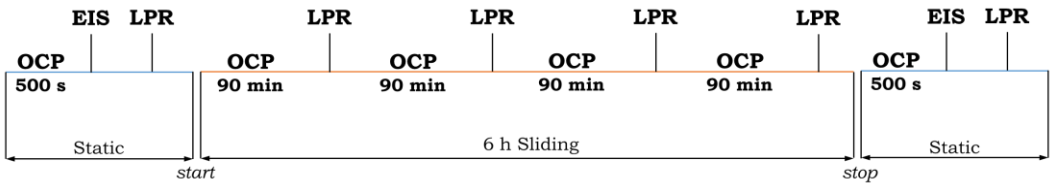

Figure 8.4 Schematic of the 6 h tribocorrosion with EIS for Chapter 8

8.3.1 Coefficient of Friction (COF)

Figure 8.5 shows the transient coefficient of friction/COF (μ) over 6 h of sliding. A typical trend was demonstrated by the higher transient μ of the CoCrMo in saline electrolyte when compared to the FBS-containing electrolytes (Figure 8.5a). A similar characteristic of the transient μ as a function of the sliding cycle was observed between the as-saline electrolyte and saline electrolyte +Cr, showing a high level of friction at the beginning of the test then becoming stable after 2,500 cycles of sliding. However, an increasing trend of the transient μ over the sliding cycle was shown for the CoCrMo tested in the saline electrolyte +Co and +Mo ions, showing a steady-state after 20,000 cycles of sliding. On the other hand, the transient μ for all of the FBS-containing electrolytes was steady throughout the 6 h sliding cycle.

Figure 8.5b shows the steady-state COF (μ) averaged over the final 1 min in the sliding test, with standard deviation. The steady-state μ significantly decreased in all FBS electrolytes (the highest μ ~0.25 ± 0.03 with Cr ion addition) when compared to in all saline electrolyte (the highest μ ~0.50 ± 0.05 with Mo ion addition). No significant difference in the steady-state μ was observed after the metal ions addition in both of the control electrolytes.

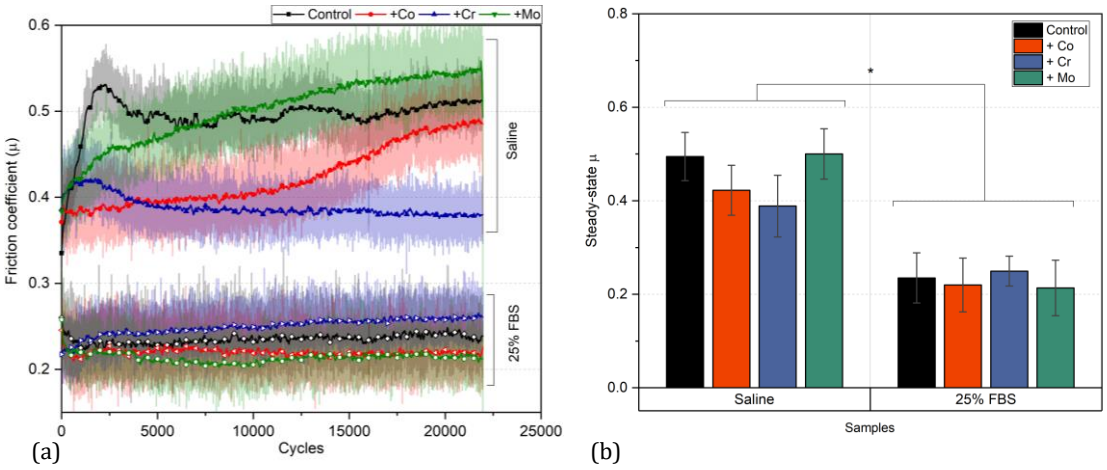

Figure 8.5 (a) The evolution of the transient COF over the 6 h sliding cycles and (b) the average steady-state COF in the saline electrolyte, 25% FBS and with metal ions addition (n=3; SD bar; *p<0.05)

8.3.2 OCP Measurements

Figure 8.6 shows the evolutions of the transient OCP over early immersion (pre-sliding), the tribocorrosion test and after the test (post-sliding) for all electrolytes. Typical OCP behaviour in the saline electrolyte and 25% as-FBS was observed in the previous chapter; i.e., de-/re-passivation behaviour upon the start of sliding in the saline electrolyte [8] and the ennoblement of the surfaces were indicated when the sliding ceased with the addition of the FBS. The transient OCP for all of the saline electrolytes steadily decreased over the sliding cycle, which became steady after 20,000 sliding cycles (Figure 8.6a). The addition of the Co and Cr to the saline electrolyte tended to have a more noble transient OCP when compared to the CoCrMo tested in the as-saline electrolyte and saline electrolyte +Mo ion. For all of the 25% FBS-containing electrolytes, the transient OCP was steady throughout the sliding cycle (Figure 8.6b).

Generally, all of the saline electrolytes tended to have a more negative average OCP during sliding when compared to the static immersion stages. In all stages, the addition of Co and Cr ions resulted in an increased (more noble) OCP when compared to both of the control electrolytes. In saline electrolyte, Mo ion addition did not have any effect on the OCP for-saline electrolyte in all stages. Nevertheless, the use of the Mo ion in the 25% FBS tended to have a more negative (i.e., less noble)

OCP when compared to the CoCrMo tested in the 25% as-FBS during the sliding and post-sliding stages.

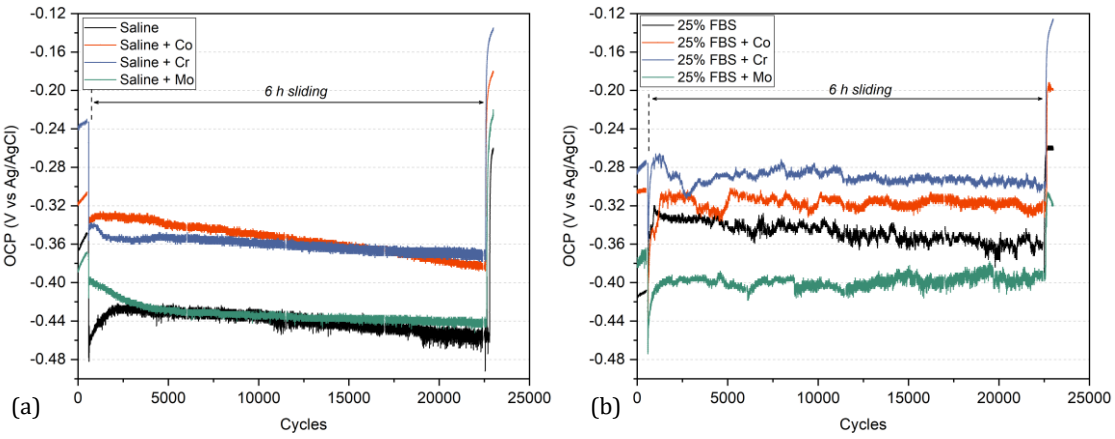

Figure 8.6 (a)(b) The evolution of the transient OCP per stages over the static and tribocorrosion tests in the saline and 25% FBS electrolytes, respectively (n=3)

8.3.3 Corrosion Volume Loss

Figure 8.7 shows the evolution of the current density, calculated from the LPR measurements during the 6 h tribocorrosion tests in the saline electrolyte and 25% FBS electrolytes. In all cases, the samples tended to have lower current densities at the static corrosion stages, both before and after sliding, when compared to the sliding stage. During sliding, the saline electrolytes (Figure 8.7a) tended to result in higher current densities when compared to the FBS-containing electrolytes (Figure 8.7b). In the saline electrolyte, the addition of the Cr ion was observed to increase the current densities when compared to the as-saline electrolyte and saline electrolyte +Co and +Mo ions during sliding. The current densities in the 25% FBS with +Cr and +Mo ions were more elevated compared to the sample tested in the 25% as-FBS; however, these differences were not statistically significant.

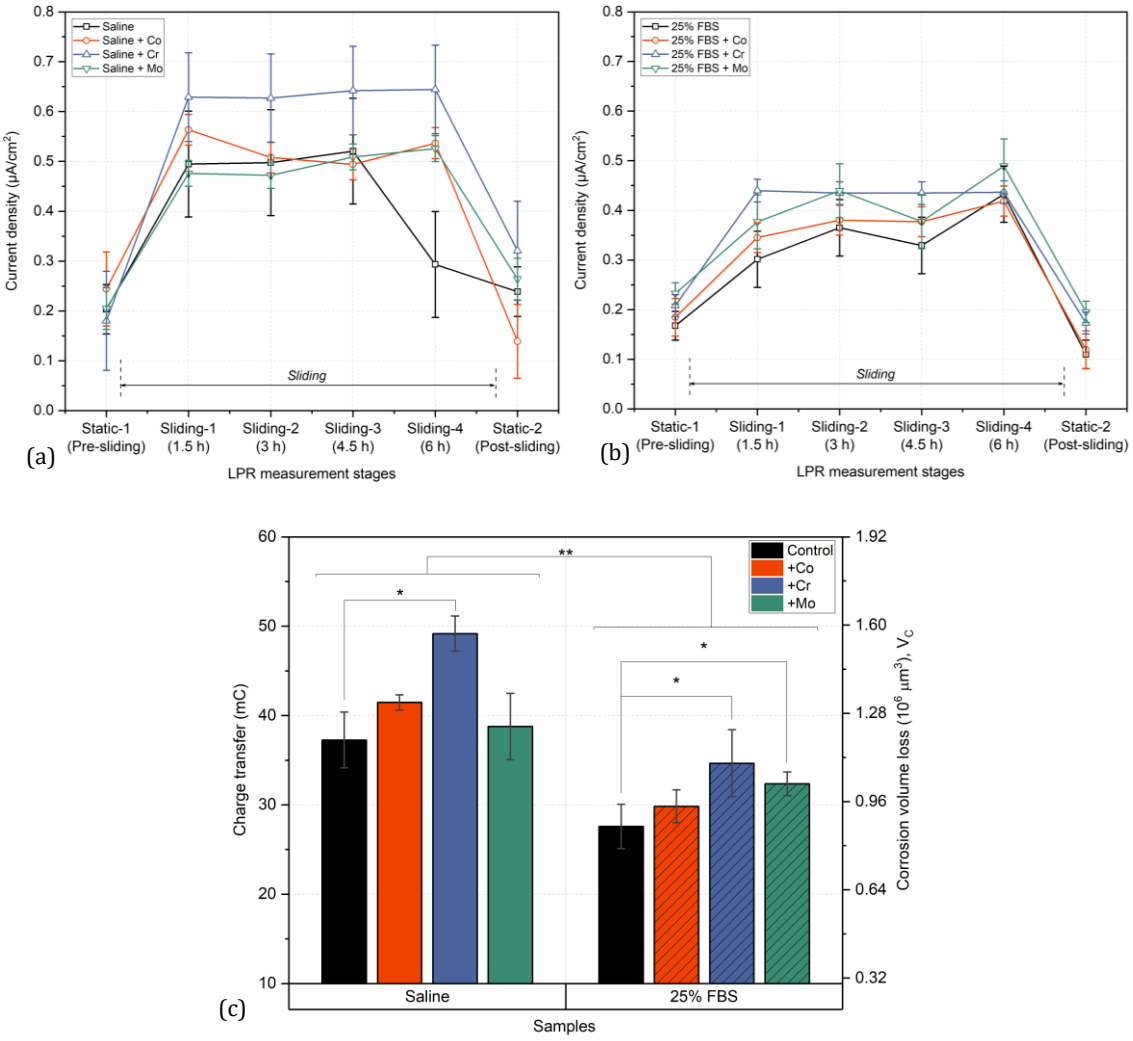

Figure 8.7 The evolution of the c current density measured at the static and tribocorrosion conditions in (a) saline electrolyte and (b) 25% FBS electrolytes; (c) the total charge transfer and corrosion volume loss during tribocorrosion in all electrolytes (n=3; SD bar; p<0.05 for ANOVA as a function of (*)metal ions addition and (**)control electrolyte)

Figure 8.7c shows an average comparison of the total charge transfer during the 6 h of sliding in all electrolytes with the standard deviation (error bar) and ANOVA test. Thus, the corrosion volume loss (V_C) can be estimated and represents the charge transfer behaviour after the 6 h of sliding (refer to Table 8.2). The charge transfers were seen to have significantly higher averages in any saline electrolytes when compared to the samples tested in all 25% FBS electrolytes. The addition of Cr ion was seen significantly to increase the total charge transfer in the saline electrolyte and 25% FBS when compared to their control electrolytes. An increase

in the corrosion volume loss was also observed in the 25% FBS +Mo ion when compared to the 25% as-FBS, whilst no significant difference was seen between the saline electrolyte +Mo ion and as-saline electrolyte samples. On the other hand, the addition of the Co ion tended to increase the charge transfer in both the saline electrolyte and 25% FBS, although no significant difference was observed when compared to samples tested in control electrolytes.

Table 8.2 The total charge transfer and corrosion volume loss (V_C) at the OCP after the 6 h sliding in saline electrolyte, 25% FBS and with metal ions addition (n=3; ±SD)

Electrolytes	Charge transfer, Q (mC)	Corrosion volume loss, V_C (x 10^6 µm^3)
Saline	37.26 ± 3.12	1.17 ± 0.10
Saline + Co	41.46 ± 0.85	1.31 ± 0.03
Saline + Cr	49.17 ± 1.96	1.55 ± 0.06
Saline + Mo	38.77 ± 3.71	1.22 ± 0.12
25% FBS	27.58 ± 2.48	0.87 ± 0.08
25% FBS + Co	29.84 ± 1.85	0.94 ± 0.06
25% FBS + Cr	34.66 ± 3.75	1.09 ± 0.12
25% FBS + Mo	32.36 ± 1.32	1.02 ± 0.04

8.3.4 EIS Measurements

Figure 8.8 presents the Nyquist plot, showing the imaginary impedance ($-Z''$) as a function of the real impedance (Z'), before (pre-sliding OCP) and after the 6-h sliding test in saline and 25% FBS electrolytes. Furthermore, the impedance spectra were measured from high frequency to low frequency. Since the EIS measurements were only conducted once for each variable, the statistical analysis therefore could not be provided.

In all cases, the impedance values were observed to be three-fold higher after the sliding test when compared to the samples before testing. In Figure 8.8a, the

addition of the Cr and Co ions was seen to increase and reduce the imaginary impedance as a function of real impedance, respectively, in the saline electrolyte before sliding test when compared to the as-saline electrolyte. After the 6 h sliding, the CoCrMo tested in saline electrolyte +Cr and +Mo ions tended to have a lower imaginary impedance as a function of real impedance when compared to the as-saline electrolyte and saline electrolyte +Co ion.

In Figure 8.8b, the Mo ion in 25% FBS was observed to reduce the imaginary impedance as a function of the real impedance before the sliding test when compared to the samples in the other 25% FBS-containing electrolytes. The use of the Co ion in the 25% FBS tended to increase the imaginary impedance as a function of the real impedance, whilst this decreased due to the Cr ion addition in the 25% FBS, when compared to the 25% as-FBS and 25% FBS +Mo ion.

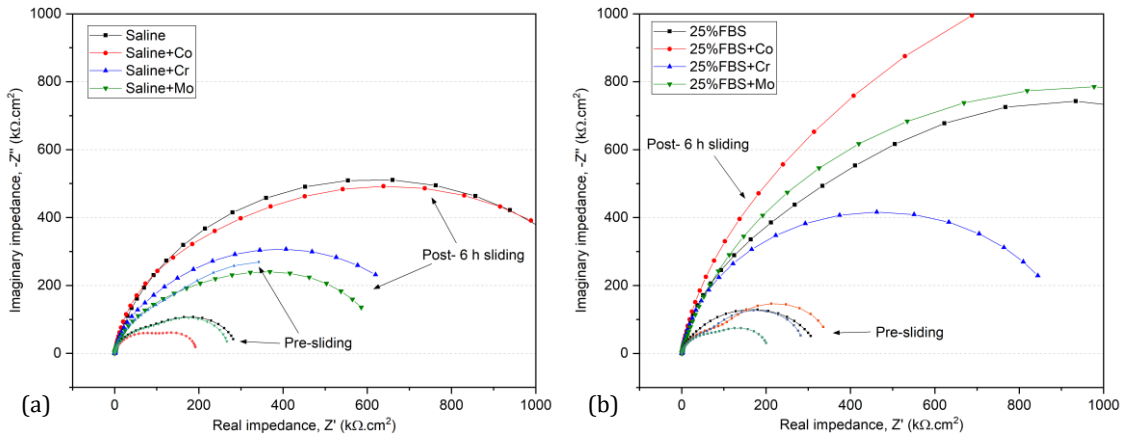

Figure 8.8 Nyquist plot at the pre-sliding OCP and after the 6-h sliding test in (a) saline electrolyte and (b) 25% FBS electrolytes

Figure 8.9 presents the Bode plot, showing the changes in modulus (|Z|) and phase angle (φ) as a function of (high to low) frequency (f), at the OCP before and after the 6-h sliding test in saline and 25% FBS electrolytes. The impedance modulus |Z| was obtained from the resultant imaginary and real impedances through the shifting frequency in Figure 8.8 for all conditions. During the low frequencies, the 25% FBS-containing electrolytes were observed to have a higher modulus |Z| when compared to the saline electrolytes. The double constants were clearly seen for the EIS spectra obtained in all electrolytes, indicated by the slopes/peaks appearing on

the phase angle spectra at mid- and low frequencies before sliding. The first time constant (outer layer) was lower when compared to the second time constant (inner layer), which indicated that the limiting mechanism was correlated to the reactions of the inner layer [163]. However, the shape of the phase angle spectra changed after 6 h sliding when compared to the spectra before the sliding test. The 6 h sliding was observed to omit the phase angle peak at the low frequency (found at before sliding) and extend the peak at the mid frequency. It can be hypothesised that the electrochemical mechanism of the outer and inner layers on the CoCrMo surface is affected during the tribocorrosion condition.

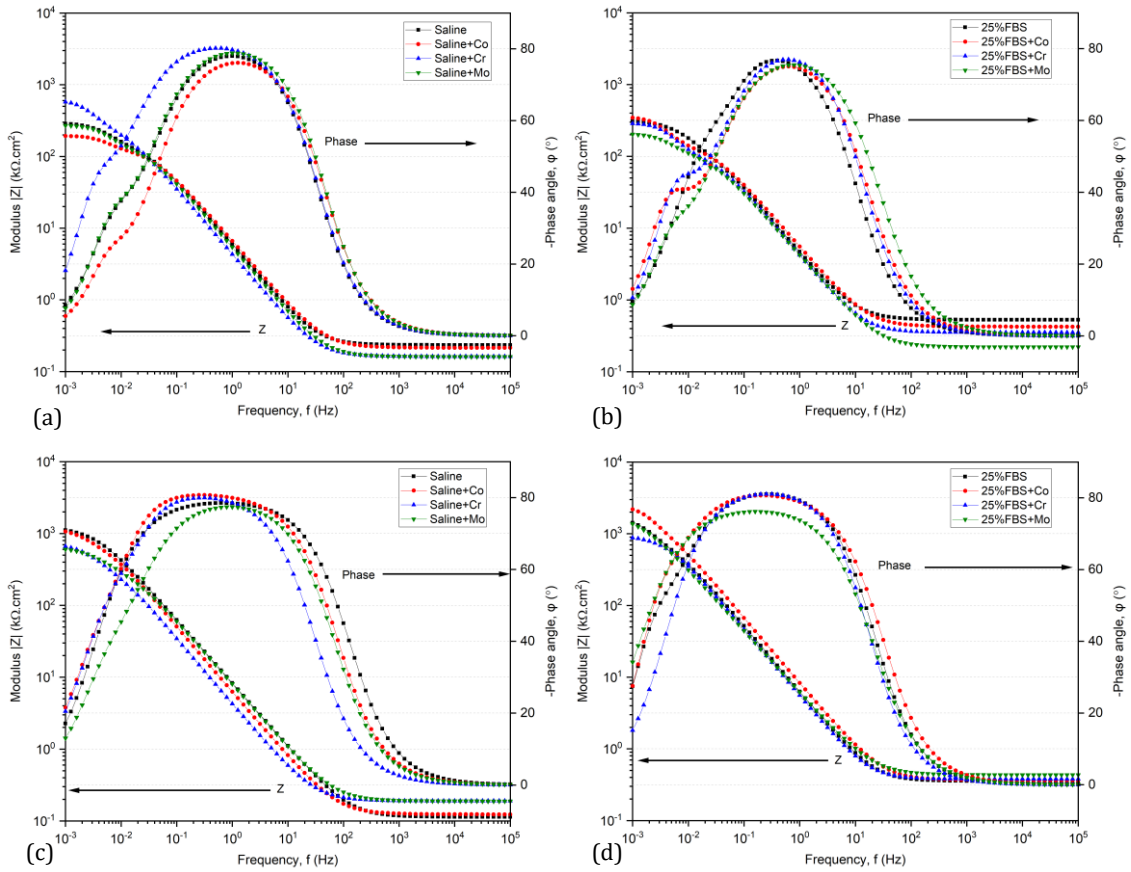

Figure 8.9 Bode plot at (a)(b) the pre-sliding OCP and (c)(d) after the 6-h sliding test in the saline and 25% FBS electrolytes

Table 8.3 compiles the electrical parameters obtained from the fitting process of the experimental data to the suitable equivalent circuit model for the OCP/passive condition (Figure 4.10). The outer layer on the CoCrMo was suggested to be an

inhomogeneous passive oxide film for the CoCrMo tested in saline electrolyte, whilst a biological/protein film if tested in 25% FBS-containing electrolyte. The capacitance parameter (C_{out} and C_{in}) can represent the layer behaviour on the electrolyte-metal interface, that is inversely proportional to the layer thickness, as explained in Equation (2.17). The values of R_s for all of the 25% FBS-containing electrolytes were higher when compared to the saline electrolytes. The Cr and Mo ions tended to reduce the R_s in saline electrolyte, but increase the R_s when added to the 25% FBS electrolyte. However, no clear trend for R_s was observed as the effect of each metal ion addition in both control electrolytes.

Table 8.3 Equivalent electrical circuit parameters of the CoCrMo alloy in all electrolytes at the OCP condition before and after the 6 h tribocorrosion test

Condition/ Electrolytes		R_s	R_{out}	CPE_{out}	n_{out}	C_{out}	R_{in}	CPE_{in}	n_{in}	C_{in}
		$\Omega.cm^{-2}$	$k\Omega.cm^{-2}$	$\Omega^{-1}.s^{n}.cm^{-2}$		$\mu F.cm^{-2}$	$k\Omega.cm^{-2}$	$\Omega^{-1}.s^{n}.cm^{-2}$		$\mu F.cm^{-2}$
PRE	Saline	16.19	7.66	3.7E-05	0.90	42.58	12.46	1.9E-04	1.00	194.40
	+Co	14.82	8.44	3.0E-05	0.89	35.24	4.93	7.0E-04	1.10	490.85
	+Cr	11.22	27.41	2.9E-04	1.10	186.51	13.78	5.0E-05	0.90	63.99
	+Mo	11.13	8.25	3.8E-05	0.90	44.43	10.42	3.2E-04	1.08	240.19
	25%FBS	36.57	21.64	5.0E-05	0.88	73.91	0.87	2.1E-04	1.10	195.16
	+Co	29.44	8.55	3.8E-05	0.89	46.00	15.59	3.8E-04	1.10	254.23
	+Cr	24.48	6.31	5.0E-05	0.91	58.07	13.54	3.4E-04	1.10	229.79
	+Mo	15.28	7.27	4.9E-05	0.88	61.31	6.85	6.3E-04	1.09	451.76
POST	Saline	7.83	91.13	2.8E-05	0.87	47.10	3.36	1.3E-04	1.09	111.15
	+Co	8.53	7.03	1.8E-04	1.10	137.50	79.54	3.6E-05	0.88	60.28
	+Cr	13.15	22.46	5.0E-05	0.89	71.22	26.19	3.2E-04	1.10	207.00
	+Mo	13.01	15.55	3.2E-05	0.87	43.47	28.73	9.5E-05	0.94	118.42
	25%FBS	24.55	37.67	3.5E-05	0.90	49.30	71.97	1.7E-04	1.10	106.42
	+Co	25.35	190.76	2.5E-05	0.89	42.73	7.39	2.3E-04	1.10	169.40
	+Cr	26.41	31.25	3.6E-05	0.92	46.00	36.34	2.4E-04	1.10	153.75
	+Mo	30.15	134.49	4.6E-05	0.91	72.17	4.34	1.0E-04	0.85	137.60

Compared with the control electrolytes, the CoCrMo tested in the 25% as-FBS had a higher R_{out}, C_{out} and lower R_{in} when compared to the as-saline electrolyte in static immersion (before the sliding test). After the 6 h sliding test, the 25% as-FBS had increasing R_{in} and R_{out} and decreasing C_{in} and C_{out} when compared to before sliding. Furthermore, the R_{in} was observed to decrease in the saline electrolyte

after the 6 h sliding test when compared to the 25% as-FBS (after 6 h sliding) and saline electrolyte (before sliding).

In terms of the effect of the metal ions, the Co, Cr and Mo ions were observed to play a role in the CoCrMo surface impedance represented by the electrical parameters when added to both control electrolytes. During static immersion (before sliding), the Co and Mo ions tended to affect the inner layer of the oxide film of the CoCrMo in saline electrolyte, by reducing the R_{in} and layer thickness (higher C_{in}) when compared to the as-saline electrolyte. The addition of the Cr ion tended to have a thinner outer layer (higher C_{out}) but lower C_{in}, representing a thicker passive film or inner layer on the CoCrMo when compared to the as-saline electrolyte. The 6 h sliding tests overall have increased both impedances (R_{in} and R_{out}) in all saline electrolytes when compared to before sliding. For the saline electrolyte +Co ion, the C_{out} was increasing but a reduction was seen for C_{in} after the 6 h sliding test when compared to before sliding. It can be hypothesised that the Co ion has thickened the inner layer and increased its resistance on the CoCrMo sample after sliding when compared to the sample tested in as-saline electrolyte. The CoCrMo tested in the saline electrolyte +Cr ion was observed to have a reduction in C_{out} and increase in C_{in} with relatively lower impedances, indicating a thinner passive inner layer when compared to saline electrolyte +Cr before sliding and as-saline electrolyte after the 6 h sliding. The addition of the Mo ion to the saline electrolyte did not affect the capacitances. However, it tended to increase the R_s and R_{out} on the CoCrMo when compared to the as-saline electrolyte after the 6 h sliding test.

Before the sliding test, all of the metal ions tended to reduce their R_{out} but increase their R_{in} in the 25% FBS when compared to the 25% as-FBS. Furthermore, the Co and Cr ions in the 25% FBS were observed to increase the C_{in} when compared to the 25% as-FBS. The addition of the Mo ion was also seen to increase the C_{in} in the 25% FBS but with two-fold higher when compared to the 25% FBS +Co and +Cr ions. In all of the FBS-containing electrolytes, the 6 h sliding test showed a clear pattern, whereby the R_{out} was higher and C_{in} lower when compared to their values before sliding. It can be hypothesised that the protein content in the FBS increases the outer layer resistance due to the protein tribofilm, as well as the thickness of the inner (passive oxide) film on the CoCrMo surface. The addition of the Co and Mo ions in the 25% FBS was observed to increase the R_{out} but reduce the R_{in} when

compared to the CoCrMo tested in the 25% as-FBS, indicating the role of metal ions on the protein (outer) film resistance. This is in strong agreement with the findings of previous studies [116, 129, 362], showing that Mo tended to interact with protein species and form a resistant outer layer. However, the 25% FBS +Cr ion tended to decrease the resistance of both layers (R_{out} and R_{in}) when compared to the sample tested in the 25% as-FBS. Thus, the dissolved Cr ion in the electrolyte is hypothesised to affect the electrochemical mechanism of the protein tribofilm on the CoCrMo surface. In addition, the 25% FBS +Cr ion had a higher R_{in} but lower R_{out} pre- & post-sliding when compared to the 25% FBS +Co and +Mo ions. It is known that the passive film (inner layer) mostly contained Cr-oxide in the literature. This is hypothesised to be a reason why the Cr ion which tends to increase the resistance of the inner layer more than the other metal ions. It also reduces the resistance of the outer layer, possibly due to the passive film competitive behaviour with protein adsorption.

8.4 Post-Test Wear Analysis

The wear analysis included the chemical analysis (SEM/EDS), surface topography (AFM) and total volume loss (VSI) attributed to the SWR after the tribocorrosion test at the CoCrMo samples.

8.4.1 SEM and Chemical Analysis

Figure 8.10 shows the SEM and EDS analysis of the wear scars for the samples tested in the as-saline electrolyte (control) and 25% as-FBS, while Figure 8.11 to Figure 8.13 show the analysis for the samples tested in the 25% FBS with the addition of metal ions. These SEM images were attributed with EDS mapping to observe the distribution of the elements within the wear scar semi-quantitatively. Several species, i.e., carbon (C) and sulphur (S), appeared, along with metal elements (Co, Cr and Mo) and oxide (O). However, carbon and proteinaceous species were not expected to appear on the CoCrMo tested in saline electrolytes.

The wear scar at 25% as-FBS showed a smaller width ~288 μm (based on SEM scale in Figure 8.10a) when compared to the saline electrolyte sample (width ~734 μm

in Figure 8.10b). EDS confirmed a strong sign of oxide at wear scar edges in saline electrolyte (Figure 8.10a), covering the traces of metal elements. A few oxide signs were also observed inside the wear scar, with less distribution than the wear edge. The traces of oxide indicated a passive reformation dragged onto the wear scar corners during the tribocorrosion test. The EDS analysis at the wear scar edges in the 25% as-FBS (Figure 8.10b) indicated that the carbon and oxygen signals resulted from passive reformation. Traces of sulphur and a few carbons from bovine serum were also seen within the wear scar. The darker layers dominated the corner and edge rather than inside the wear scar due to the tribological condition.

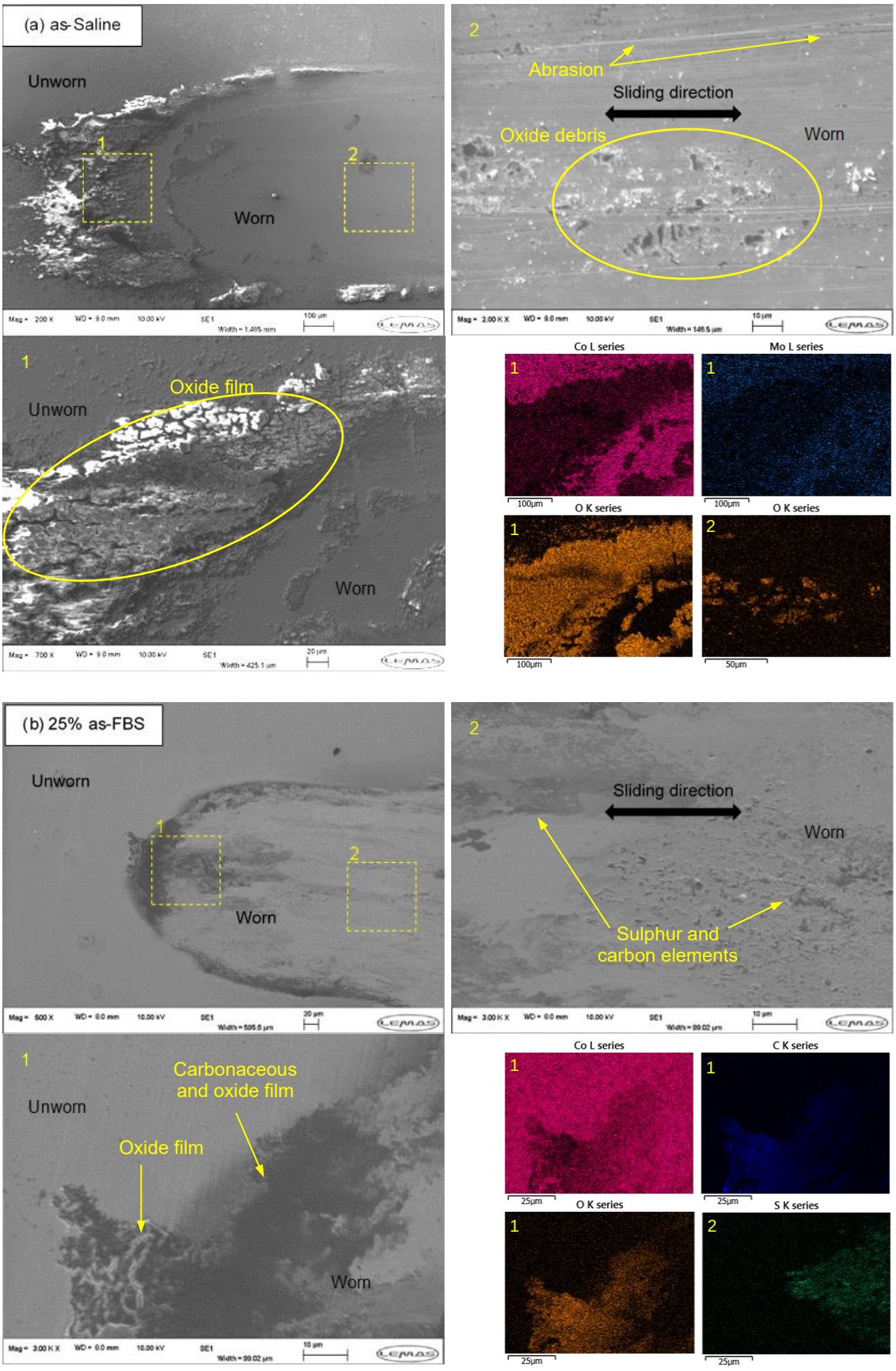

Figure 8.10 The SEM and EDS maps inside the wear scar of the CoCrMo alloys tested in the control electrolytes; (a) saline electrolyte and (b) 25% as-FBS

In the 25% FBS +Co (Figure 8.11), traces of sulphur and carbon from the bovine serum dominated within the wear scar rather than at the edges, suggesting that it covered the abrasion damage on the surface. A few carbons and oxide elements were also seen at the corner by the EDS. Surface pits were seen alongside traces of oxide, carbonaceous and sulphur deposition within the wear scar. An indication of the damaged surface was observed at the outside but parallel to the wear track.

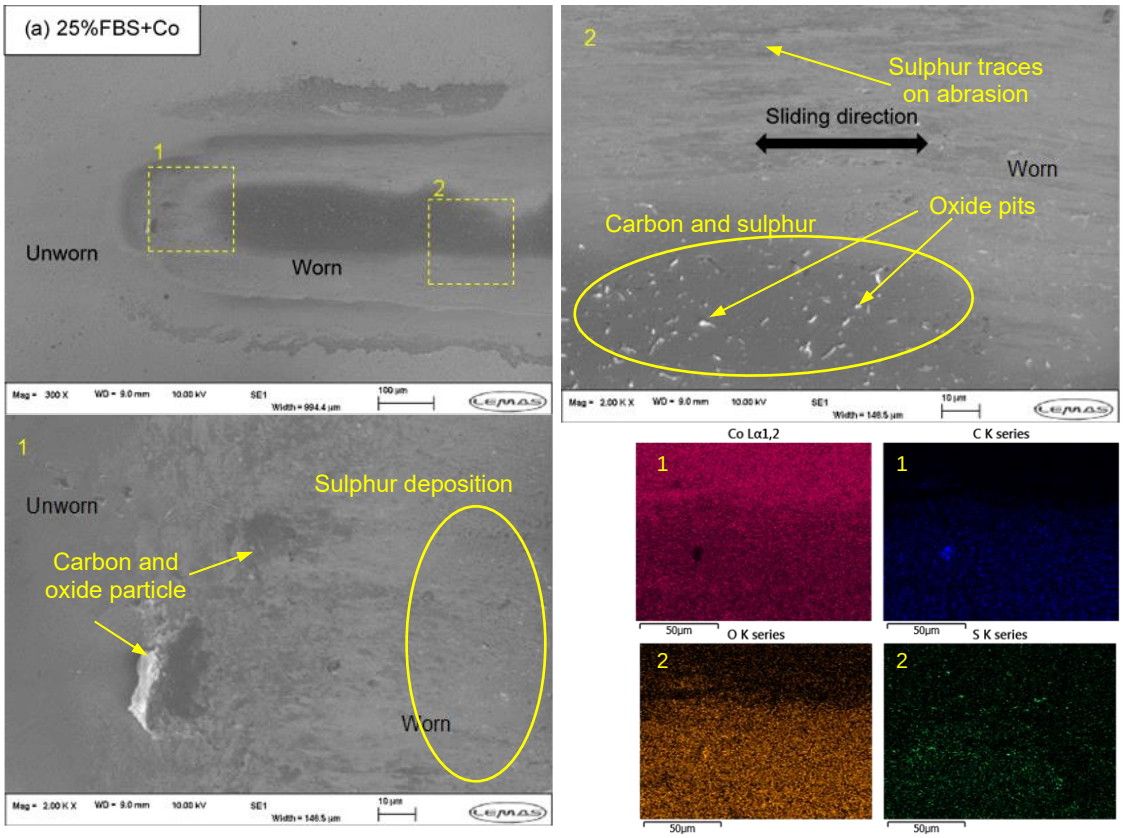

Figure 8.11 The SEM and EDS maps inside the wear scar of the CoCrMo alloys tested in the 25% FBS + Co ion

The wear scar at the 25% FBS +Cr showed a greater width of ~487.7 µm (Figure 8.12) when compared to the samples tested at the 25% as-FBS, 25% FBS +Co and +Mo ions. The EDS confirmed that there was only a small amount of carbon and sulphur from the bovine serum and oxide signals inside the wear area. However, these elements were only observed as precipitating at a few spots and a tribofilm deposition did not appear within nor at the edges of the wear scar. Thus, it can be hypothesised that the Cr ion addition tends to cause less precipitation and tribofilm formation of proteinaceous species. This behaviour can be seen in the SEM image, that shows that no darker layer was found at the wear corner when compared to the SEM images of the other samples.

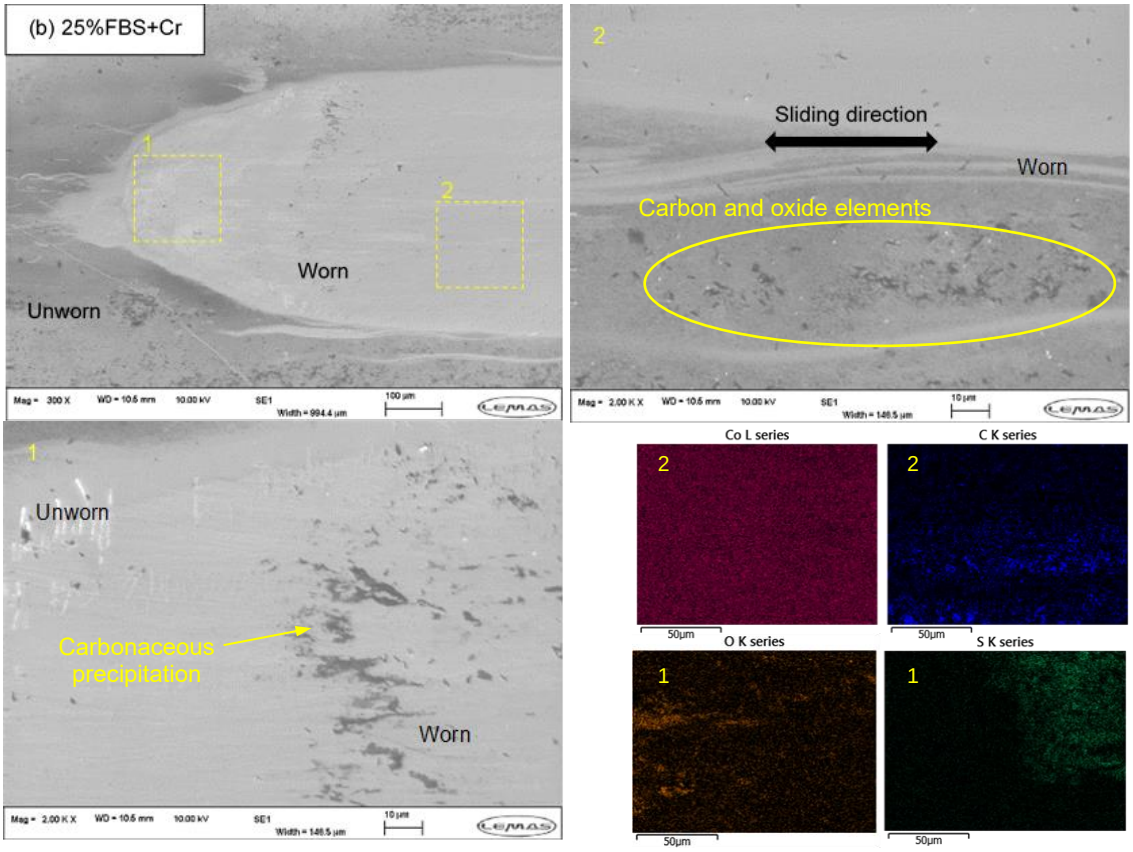

Figure 8.12 The SEM and EDS maps inside the wear scar of the CoCrMo alloys tested in the 25% FBS + Cr ion

In Figure 8.13, the SEM and EDS analysis showed similar wear characteristics (width and elements distribution) between the 25% FBS +Mo and 25% as-FBS samples. A darker layer, consisting of carbons and oxides by EDS, was observed at the wear corner and edge. A trace of sulphur was also observed within the wear track. The speckled appearance within the wear scar was indicated by EDS to be the carbonaceous and sulphur elements. This form of precipitating sulphur and carbon was hypothesised to correlate with the role of Mo ion addition interacting with proteinaceous species from bovine serum.

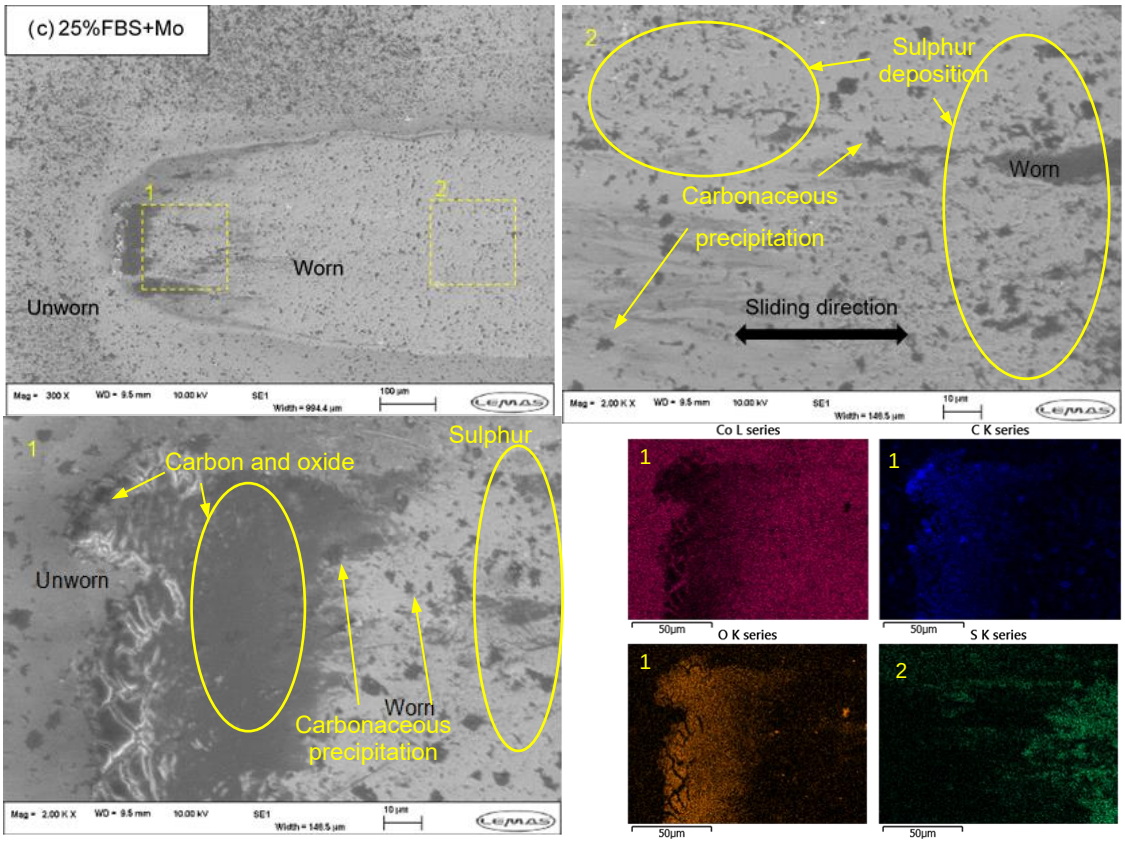

Figure 8.13 The SEM and EDS maps inside the wear scar of the CoCrMo alloys tested in the 25% FBS + Mo ion

Table 8.4 shows that the average atomic percentages (n = two different spots) of carbon, oxide and nitrogen were relatively higher in the sample tested in the 25% FBS +Co when compared to the 25% as-FBS, 25% FBS +Cr and +Mo samples. The sulphur element was found to increase in the wear scar of the 25% FBS +Mo ion when compared to the surface tested in the remaining electrolytes. The oxide was

similar between the 25% as-FBS and 25% FBS +Mo, which was higher when compared to the 25% FBS +Cr sample.

Table 8.4. The EDS atomic percentage of deposited elements at the CoCrMo surfaces tested in the saline electrolyte, 25% FBS and after metal ions addition (n=2; ±SD)

Element	Atomic percentages (at%)				
	Saline	25% FBS	25% FBS + Co	25% FBS + Cr	25% FBS + Mo
Co	50.19 ± 0.95	41.11 ± 0.91	32.62 ± 0.99	48.29 ± 0.44	37.08 ± 0.97
Cr	18.72 ± 0.48	12.80 ± 0.20	8.49 ± 0.32	14.87 ± 0.27	10.60 ± 0.37
Mo	3.36 ± 0.16	6.58 ± 0.07	4.93 ± 0.13	7.79 ± 0.84	6.01 ± 0.11
O	27.73 ± 0.83	13.52 ± 0.95	19.64 ± 0.62	4.39 ± 0.15	15.17 ± 1.17
C	-	19.71 ± 0.74	27.15 ± 0.87	17.02 ± 0.35	22.15 ± 0.49
N	-	2.17 ± 0.07	3.60 ± 0.11	2.26 ± 0.45	2.54 ± 0.66
S	-	4.13 ± 0.58	3.57 ± 0.23	5.38 ± 0.81	6.45 ± 0.89

8.4.2 Surface Topography

Figure 8.14a and Figure 8.14b show the AFM topography of the wear scar after being tested in the control electrolytes. This surface topography measured 1x1 μm, which was a smaller area than the obtained AFM data in Chapter 7 between the saline electrolyte and 25% as-FBS comparison. A sign of abrasion (characterised by grooves/scratches) was seen in the wear scar of the CoCrMo samples tested in saline electrolyte. The AFM analysis of the CoCrMo surfaces tested in FBS electrolytes displayed evidence of film formation and localised build-up, arranged in the direction of the sliding. The CoCrMo surfaces tested in the 25% as-FBS exhibited different behaviour in the nano-scale peak height and force parameters, as well as a smoother texture compared to the sample tested in saline electrolyte. The localised build-up measured ~0.2 μm in width and ~12.5 nm in height in the 25% as-FBS, covering the wear grooves and exposed metal surface. However, the value of the thickness parameter seems to oppose the force behaviour.

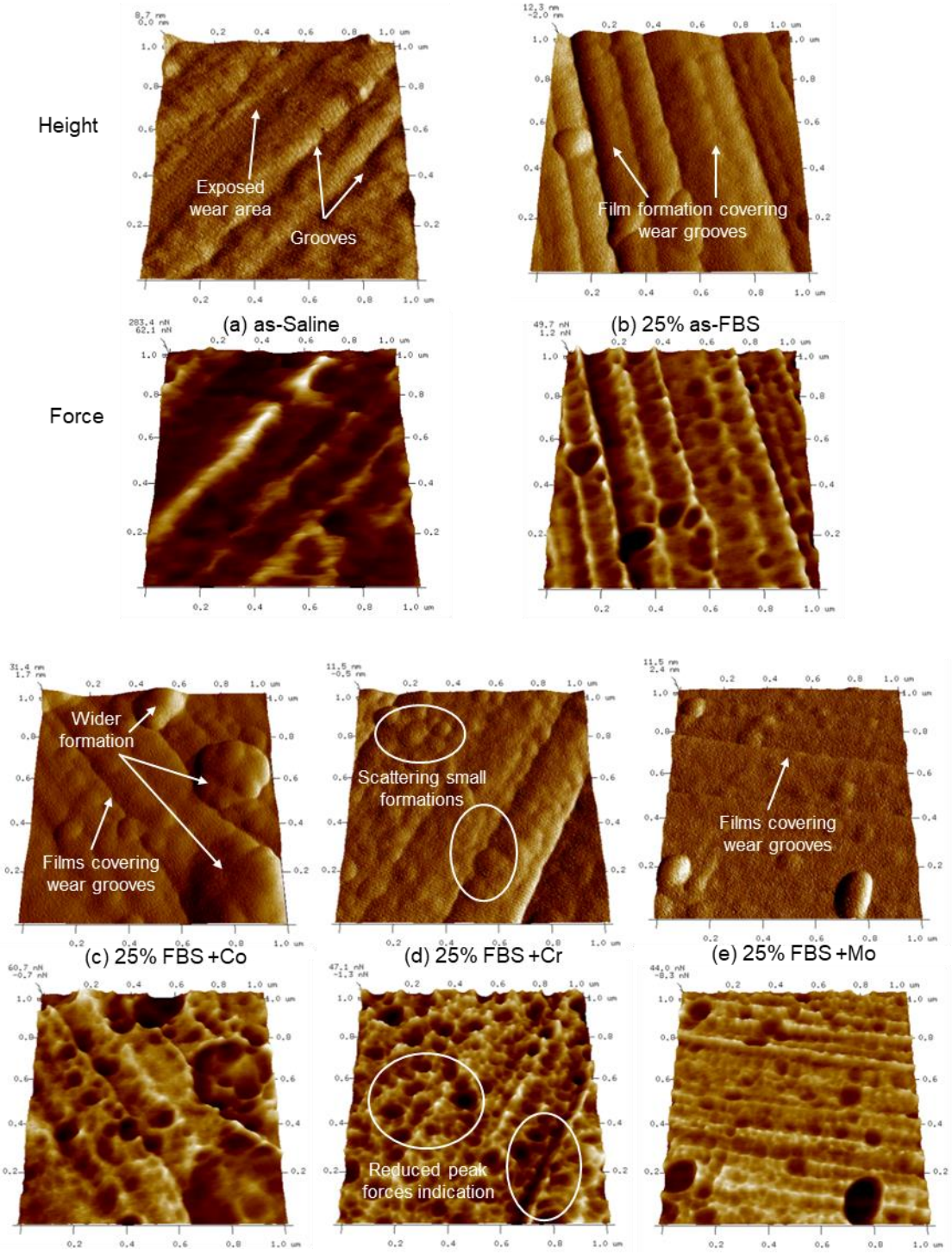

Figure 8.14 AFM 1x1 µm images of wear scar after being tested in (a) as-saline electrolyte, (b) 25% as-FBS, (c) 25% FBS with Co, (d) Cr and (e) Mo ions addition

Figure 8.14c to Figure 8.14e show the AFM 1x1 µm topography of the wear scar after being tested in the 25% FBS with the addition of metal ions. Overall, the behaviour of this AFM topography was seen to be consistent with the sample tested

in 25% as-FBS. However, the AFM analysis of the CoCrMo sample tested in the 25% FBS +Cr was observed to exhibit different behaviour in the peak height and force distributions when compared to the other FBS electrolytes with metal addition. The localised build-up for the 25% FBS + Cr relatively showed the smaller width, peak height and lower force parameter compared to the sample with Co and Mo additions. This behaviour agrees with the obtained SEM/EDS analysis in each sample.

8.4.3 Total Volume Loss

Figure 8.15 shows the total volume loss (V_{total}) after 6 h tribocorrosion tests and SWR for the samples tested in all electrolytes. The addition of Cr and Mo to the saline electrolyte was observed significantly to increase and decrease the V_{total}, respectively, when compared to the CoCrMo surface tested in the as-saline electrolyte. Furthermore, the Co ion tested in the saline electrolyte tended to reduce the V_{total} when compared to the as-saline electrolyte, although not significantly.

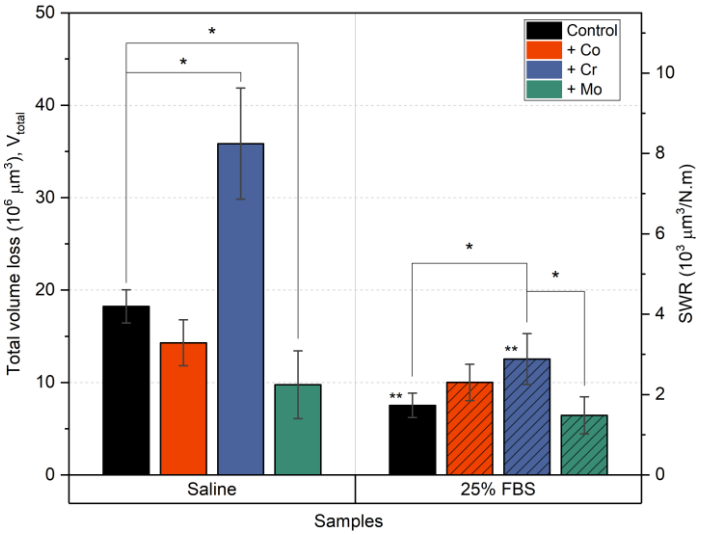

Figure 8.15 The total volume loss after the 6 h tribocorrosion tests and SWR at samples tested in all electrolytes (n=3; SD bar; p<0.05 for the ANOVA as a function of (*)metal ions addition and (**)control electrolyte)

The V_{total} for the CoCrMo tested in the 25% FBS +Cr was significantly higher when compared to the 25% as-FBS and 25% FBS +Mo. An increase of V_{total} was observed

for the Co ion in the 25% FBS when compared to the 25% as-FBS although this difference was not statistically significant. In addition, the Mo ion tested in the 25% FBS tended to reduce the V_{total} when compared to the 25% as-FBS, but this was not significant either.

As a function of the control electrolyte, the CoCrMo tested in the 25% FBS electrolytes were observed to have a lower V_{total} when compared to the saline electrolytes. However, no significant differences were observed for the V_{total} between the saline electrolyte +Co and 25% FBS +Co nor the saline electrolyte +Mo and 25% FBS +Mo.

Table 8.5 Total volume loss at the OCP (V_{total}) and the SWR of CoCrMo after the 6 h sliding in saline electrolyte, 25% FBS and with metal ions addition (n=3; ±SD)

Electrolytes	Total volume loss, V_{total} (x 10^6 µm^3)	SWR (x 10^3 µm^3/N.m)
Saline	18.24 ± 1.79	4.22 ± 0.42
Saline + Co	14.30 ± 2.49	3.31 ± 0.58
Saline + Cr	35.85 ± 6.01	8.30 ± 1.39
Saline + Mo	9.77 ± 3.66	2.26 ± 0.85
25% FBS	7.53 ± 1.32	1.74 ± 0.30
25% FBS + Co	10.01 ± 1.97	2.32 ± 0.46
25% FBS + Cr	12.55 ± 2.76	2.90 ± 0.64
25% FBS + Mo	6.44 ± 2.01	1.49 ± 0.46

8.5 Chapter Discussion

In this study, a novel tribocorrosion test was conducted using metal ion containing simulated electrolytes. The concentration and pH level were adjusted for all dissolved metal ions in both the saline electrolyte and FBS. The objective was to investigate the role of locally high concentrations of metal ions on the material

degradation and surface film behaviour. The addition of each metal ion was demonstrated to affect the friction, corrosion current density and wear behaviour of the CoCrMo surface. The tribofilms were also seen via deposited elements by SEM/EDS within the wear scar at the sample surfaces. Therefore, this sub-chapter discusses the metal ion roles in the tribocorrosion mechanism, based on the experimental results, as a finding of this study. The interaction of the dissolved metal ions and protein species at the tribocorrosion condition was also investigated and discussed with reference to related studies.

8.5.1 The Role of Dissolved Metal Ions in the Tribocorrosion mechanism

Figure 8.16a and Figure 8.16b show the volume loss and %-contribution of the corrosive (V_C) and mechanical wear (V_W) processes towards the total tribocorrosive volume loss (V_{total}) in all electrolytes, respectively. The V_C was estimated using Faraday's Law, allowing the subtraction of V_{total} to obtain V_W (Table 8.6). Overall, the V_W was significantly higher in all electrolytes, contributing at least %-V_W ~84% to the V_{total} when compared to V_C. All FBS-containing electrolytes were observed to reduce the V_W when compared to the saline electrolytes. However, it was statistically significant when compared with the 25% as-FBS and as-saline electrolyte, as well as the 25% FBS +Cr and saline electrolyte +Cr. The addition of Co and Mo ions in the saline electrolyte was observed to decrease the V_W when compared to the as-saline electrolyte, although it was statistically significant only when tested in the saline electrolyte +Mo ion. The CoCrMo tested in the saline electrolyte +Cr ion was seen significantly to increase the V_W when compared to the as-saline electrolyte, saline electrolyte +Co and +Mo ions. On the other hand, the 25% FBS +Co and 25% FBS +Mo were seen to increase and reduce the V_W, respectively, when compare with the 25% as-FBS, although no significant difference was observed. The addition of the Cr ion in the 25% FBS was seen significantly to increase the V_W when compared to the 25% as-FBS and 25% FBS +Mo ion. In both control electrolytes, the addition of the Mo ion tends to increase the proportion of %-V_C, consequently reducing the %-V_W when compared to the as-electrolytes. On the contrary, the Cr ion tends to increase the %-V_W when compared to both of the control electrolytes.

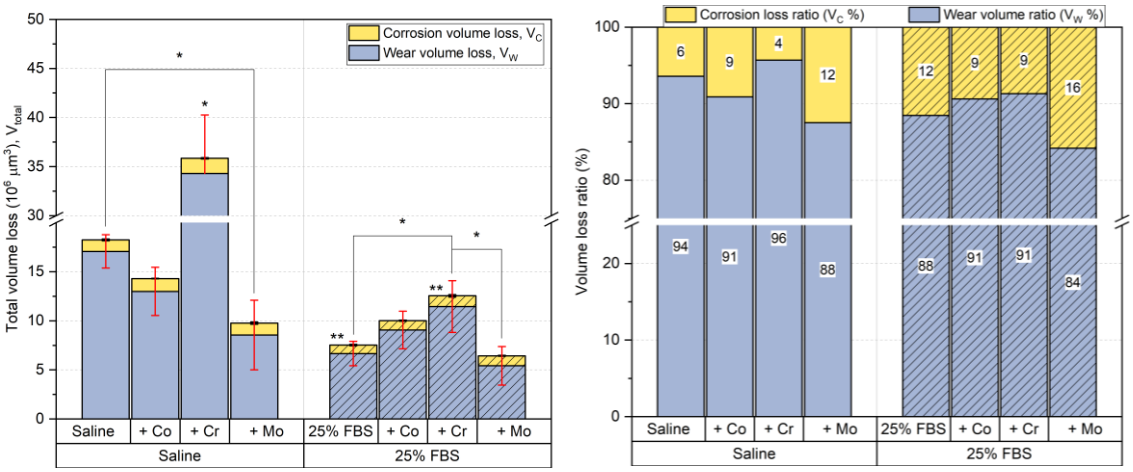

(a) (b)

Figure 8.16 (a) Volume loss of tribocorrosion contributors (n=3; SD bar; p<0.05 for Wear volume loss (V_W) as a function of (*)metal ions addition and (**)control electrolyte) and (b) the ratio of the contributing volume loss components after the 6 h tribocorrosion tests in all electrolytes

The tribocorrosion mechanism was determined by the ratio between the corrosion loss (V_C) over the wear loss (V_W) [327, 328]. Figure 8.17 shows the maps of the tribocorrosive behaviour using the mechanistic approach with respect to the control electrolytes (as-saline electrolyte and 25% as-FBS) and after metal addition. The tribocorrosion process on the CoCrMo tested in the as-saline electrolyte for 6 h was dominated by the mechanical wear mechanism. The addition of the Co and Mo ions in the saline electrolyte shifted the mechanism in the as-saline electrolyte onto wear-corrosion regime. This is because the Co and Mo ions in the saline electrolyte tend to decrease the V_W, so that the corrosive proportion in the total volume loss increases. The addition of the Cr in saline electrolyte was seen to increase both the V_W and V_C, so the wear mechanism was therefore increasing when compared to the as-saline electrolyte.

Table 8.6 The volume loss of each contributor from the tribocorrosion mechanism approach after the 6 h sliding in the saline electrolyte, 25% FBS and with metal ions addition (n=3; ±SD)

Electrolytes	Tribocorrosion mechanistic contributors (x 10^6 µm^3)		
	Total volume loss, V_{total}	Corrosion volume loss, V_C	Wear volume loss, V_W
Saline	**18.24 ± 1.79**	1.17 ± 0.10	17.07 ± 1.73
Saline + Co	**14.30 ± 2.49**	1.31 ± 0.03	13.00 ± 2.49
Saline + Cr	**35.85 ± 6.01**	1.55 ± 0.06	34.30 ± 5.98
Saline + Mo	**9.77 ± 3.66**	1.22 ± 0.12	8.55 ± 3.58
25% FBS	**7.53 ± 1.32**	0.87 ± 0.08	6.66 ± 1.27
25% FBS + Co	**10.01 ± 1.97**	0.94 ± 0.06	9.07 ± 1.94
25% FBS + Cr	**12.55 ± 2.76**	1.09 ± 0.12	11.45 ± 2.68
25% FBS + Mo	**6.44 ± 2.01**	1.02 ± 0.04	5.42 ± 2.00

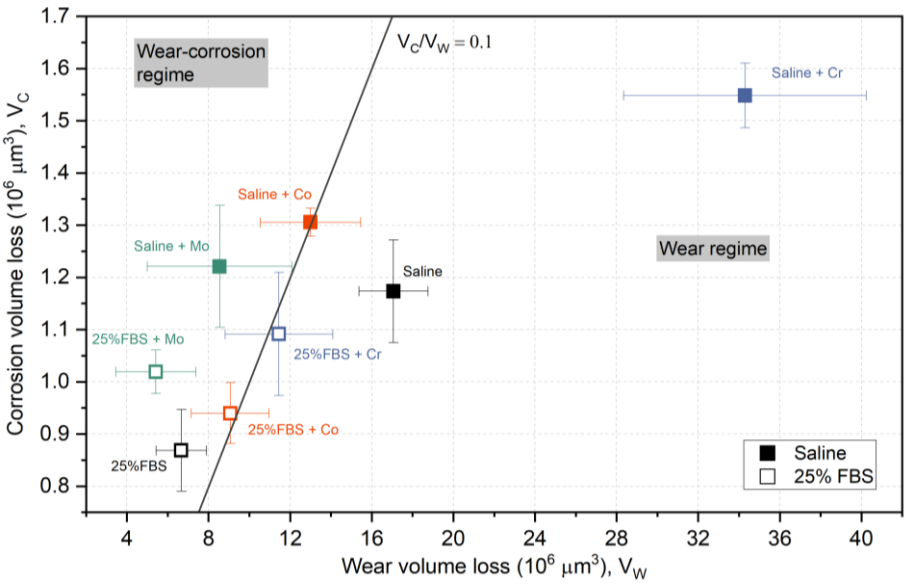

Figure 8.17 The tribocorrosion mechanism after the 6 h sliding in both of the control electrolytes as a function of the metal ion addition (n=3; SD bar)

The tribocorrosive degradation on the CoCrMo tested in the 25% as-FBS for 6 h was dominated by the wear-corrosion mechanism. This is because the use of the FBS

content reduced both the V_W and V_C when compared to the as-saline electrolyte, The addition of the Co and Mo ions in the 25% FBS did not shift the wear-corrosion regime in the 25% as-FBS. The Mo ion was seen to increase the V_C but reduce the V_W when compared to the 25% as-FBS. However, the Co ion was seen to increase both the V_C and V_W when compared to the 25% as-FBS, but these increases were not statistically significant. On the other hand, the addition of the Cr ion 25% FBS was seen to shift the tribocorrosion domain onto the wear regime when compared to the 25% as-FBS. This is because the addition of the Cr in the 25% FBS was seen to increase both the V_W and V_C when compared to the 25% as-FBS.

Based on the results obtained in this study, the dissolved metal ions play a different role in the tribocorrosion mechanism of the CoCrMo surface during the 6 h sliding test in both of the control electrolytes. This difference is hypothesised to be affected by the interaction between the metal ion and the electrolytes species. The addition of the Co ion has a contradictive effect on the total volume loss: reducing the V_{total} in the saline electrolyte but increasing the V_{total} while in the 25% FBS electrolyte. This difference is suggested to be due to the fact that the Co ion effect on the V_W changes depending on the control electrolyte. The Co ion effect in reducing the V_C in both of the control electrolytes is consistent and independent of the electrolyte species. However, none of the effects of the Co ion on the tribocorrosion loss are statistically significant when compared to the control electrolytes. The effect of the Cr ion is consistent in increasing the V_{total} while added in both electrolytes. The addition of the Cr ion is seen significantly to increase both the V_C and V_W contributors during the 6 h sliding test. The increasing trend is hypothesised to be affected by the change in the surface condition of the CoCrMo alloy due to the Cr ion-surface interaction. The addition of the Mo ion has an effect in terms of reducing the V_{total} by decreasing the V_W consistently in both of the control electrolytes, but was statistically significantly observed in the saline electrolyte. Nevertheless, the Mo ion tends to increase the V_C in both of the electrolytes, as significantly observed in the 25% FBS electrolyte. The Mo ion-surface interaction is hypothesised to reduce either the wear degradation or corrosion-wear degradation while dissolved in the saline electrolyte. On the other hand, the interaction between the Mo ion and protein content in the FBS is hypothesised to change the tribochemistry of the CoCrMo by increasing the surface lubricity and corrosion process during sliding.

8.5.2 Metal Ion Effects on Surface Tribochemistry

The dissolved metal ions are hypothesised to change the tribocorrosion and tribochemical reactions at the electrolyte-surface interface, so the material degradation on the CoCrMo surface is thus affected. Studies [107, 129, 363] have attempted to use the Mo ion and a bovine serum to generate proteinaceous film formation and test its friction and corrosion performance. It is thought to be beneficial since the dissolved Mo ion can interact with the protein species in bulk electrolyte, and so affect the protein adsorption and corrosion behaviour at the metal surface. However, this is based on *in vitro* studies at a certain applied potential. The effect of dissolved Co, Cr and Mo ions at the OCP on surface corrosion, tribochemistry and tribocorrosive degradation also remains unexplored. Therefore, tribochemistry is observed in this study to investigate the role of metal ions in CoCrMo tribocorrosion.

The impedance results can represent the condition of the surface layers on the CoCrMo during the 6 h tribocorrosion test. Due to the absence of protein species in saline electrolyte, the sample surface is suggested to rely on an electrical double layer or passive oxide film formation to survive the tribocorrosive degradation. When comparing the control electrolytes, the CoCrMo tested in the 25% as-FBS had a higher R_{out}, C_{out} and lower R_{in} when compared to the as-saline electrolyte in the static immersion test. These differences can be hypothesised as due to the fact that the protein content from the FBS had a thinner outer layer (a higher C_{out} with a higher impedance) and the lower surface impedance of the inner layer (lower R_{in}) when compared to the sample in the as-saline electrolyte at a static condition. This behaviour can also be correlated with the comparison of polarisation resistance during potentiodynamics at the static immersion between the saline electrolyte and 25% FBS + PBS in Chapter 6. After the 6 h sliding, the 25% as-FBS had increasing R_{in} and R_{out} and decreasing C_{in} and C_{out} when compared to before sliding, indicating the presence of a protein film-enhanced electrochemical resistance at the adsorbed outer layer. This may explain why the transient OCP over the sliding cycle in the 25% as-FBS is more noble when compared to the as-saline electrolyte. This is also in line with the findings from the EDS and AFM surface topography, showing the carbonaceous and sulphur traces in the tribofilm. As a result, the total volume

loss was decreased in the 25% as-FBS due to the protective tribofilm when compared to the saline electrolyte.

In the saline electrolyte, the Co and Mo ions tended to affect the inner layer of the CoCrMo by reducing its resistance and thickness. This behaviour may explain the less noble transient OCP observed during the static immersion when compared to the as-saline electrolyte. After the 6 h sliding test, the Co ion is hypothesised to increase the inner layer thickness when compared to the as-saline electrolyte. Thus, this can be related to the role of the Co ion in the saline electrolyte in reducing the volume loss when compared to the as-saline electrolyte, although the difference is not significant. On the other hand, the Mo ion added in saline electrolyte is observed to significantly reduce the volume loss owing to mechanical wear on the CoCrMo after the 6 h sliding when compared to the as-saline electrolyte. The addition of the Mo ion to the saline electrolyte did not affect the capacitances, however it tended to increase the R_s and R_{out} on the CoCrMo when compared to the as-saline electrolyte after the 6 h sliding. These trends may explain the shifting tribocorrosion mechanism in the saline electrolyte onto the wear-corrosion regime following the addition of Co or Mo ions.

The Cr ion in the saline electrolyte tended to reduce the outer layer thickness but thicken the passive inner layer on the CoCrMo when compared to the as-saline electrolyte in the static condition. This explains why there was more noble OCP during the static immersion when compared to all of the saline electrolytes. However, the CoCrMo tested in saline electrolyte +Cr ion was observed to have a thinner passive inner layer after the 6 h sliding when compared to the saline electrolyte +Cr before sliding and as-saline electrolyte after the 6 h sliding. Therefore, the surface condition of the CoCrMo with the addition of the Cr ion in saline electrolyte can be hypothesised significantly to increase both of the tribocorrosion loss contributors during the 6 h sliding test.

For the CoCrMo tested in the 25% FBS-containing electrolytes, the results from EDS, EIS and AFM can be used to understand the effect of the interaction between the metal ion and protein content on the tribocorrosion mechanism. After the 6 h sliding, the Co ion in the 25% FBS was observed to reduce the resistance and thickness of the inner layer when compared to the CoCrMo tested in the 25% as-FBS. This might explain the increasing volume loss after the addition of the Co ion

in the 25% FBS. The surface pits are also seen, along with traces of oxide, within the wear scar. Thus, it tends to increase the total volume loss but had no significant effect on the material degradation mechanism during sliding. In addition, traces of carbon and nitrogen and wider build-up surface topography were observed within the wear scar. These may provide evidence of the interaction between the Co ion and protein species from the FBS which are deposited on the CoCrMo surface during the sliding condition.

During static immersion, the Cr ion tended to increase inner (passive) layer impedance when compared to the other metal ions, which is also in line with the corrosion resistance during anodic polarisation. However, the 25% FBS +Cr ion tended to decrease the resistance of both layers (R_{out} and R_{in}) after the 6 h sliding test when compared to the sample tested in the 25% as-FBS. Thus, the dissolved Cr ion in the electrolyte is hypothesised to affect the electrochemical mechanism of the protein tribofilm on the CoCrMo surface. Due to the competitive behaviour between passive and protein films, thus, carbon an sulphur from the FBS are suggested to be difficult to trace within the wear scar. The trace of oxide is also seen indicating the removal of the unstable formation of passive oxide film during sliding. The reduced build-up topography and force parameter via the AFM can be related to the impedance reduction after sliding. This can explain why the CoCrMo surface is poorly protected during the tribocorrosion condition. As a result, Cr has a significant effect on the material degradation during sliding, which increases both of the tribocorrosion contributors and is dominated by the mechanical wear mechanism.

The effect of the Co and Cr ions while interacting with the protein content in the electrolyte on tribocorrosive behaviour remains largely unknown. The Cr ion has been observed as chromium-oxide composed of the passive film at the CoCrMo surface [30, 136, 300]. The dissolved Co and Cr ion tended to have a more noble OCP in the static condition but more corrosion damage in the tribological condition. The protein species was observed to exhibit competitive behaviour with passive reformation. Therefore, the Co and Cr ions in the electrolytes are hypothesised to interfere in the surface films' stability, facilitating the material degradation during sliding. However, the increasing total volume loss in the 25% FBS +Co ion was not statistically significant when compared to the 25% as-FBS. In addition to the severe

corrosive damage, reduced tribofilm formation and wider scar compared with the other metal ions, the Cr ion also increased the average value of the corrosive volume loss on the CoCrMo surface. The extended wear and corrosive damage with the Cr addition is hypothesised as being due to the mechanism of the wear-corrosion, chloride ion side effects and metal-proteinaceous complexes and metal oxides debris that contribute as a third-body to abrasive wear.

After the 6 h sliding test, the CoCrMo tested in the 25% FBS +Mo ion showed an increasing sulphur trace when compared to the other metal ions. This is in strong agreement with the finding from the XPS signal in this study, that provides evidence of Mo ion-protein interaction and surface tribofilm formation. The Mo ion in the 25% FBS was observed to increase the outer layer resistance but reduce the inner layer resistance when compared to the CoCrMo tested in the 25% as-FBS, indicating the role of metal ions on the protein (outer) film's resistance. Therefore, this evidence of the surface condition may explain the reduce wear volume loss and total volume loss on the CoCrMo tested in the 25% FBS +Mo ion when compared to the 25% as-FBS. The interaction between the protein and metal ions in the electrolyte was suggested to alter the material degradation behaviour. Mo ion and protein observations in the serum electrolyte interaction have been conducted in previous studies [116, 129, 362]. The surface-formed proteinaceous layer stability was enhanced by the addition of the Mo ion in bovine calf serum. The layer was claimed to be metallo-organic complexes, mainly containing metal ions and protein decomposition, as also found in other studies. The increasing protein adsorption layer might reduce the passive oxide layer on the surface, as indicated by the more negative OCP value.

A study by Martin et al. [107] compared the role of Mo ion independently with the Co and Cr ions on protein deposition on the CoCrMo alloys. The protein film was found to have a higher mass gain on molybdenum than cobalt and chromium's presence. It was explained that Mo ions and proteins have a specific affinity to an adhesion process, which might support the film performance. Mo(VI) ion would also be necessary to bind the proteins through cross-links in generating a protein-rich film [107, 363]. The protein adsorption process could have limited the oxygen diffusion to a particular surface area and led to oxide layer dissolution. This might explain the increasing volume loss owing to corrosion observed in the 25% FBS

+Mo ion. A trace of sulphur in the protein layer were also observed via the EDS results within the wear scar in this study. This film formation is hypothesised to have a lubricating effect on the CoCrMo surface Thus, the total volume loss can be decreased due to the reduction in wear volume loss.

8.5.3 Concluding Remarks

By linking all of these findings, the mechanism of metal ions' effect on the tribocorrosion and tribochemistry of tested CoCrMo can be elucidated. Within this thesis and literature, it is well established that the addition of FBS results in a reduction in the total volume loss. However, the reduction in the total volume loss in FBS-containing electrolytes varied with the addition of dissolved metal ions. This outcome suggests that dissolved metal ions have the potential to influence the subsequent tribocorrosive degradation mechanisms. Based on the results of this study, the dissolved metal ions in the electrolyte can affect the material degradation mechanism of the CoCrMo surface. This degradation is because the dissolved metal ions can interact with both the electrical double layer on the surface and species in bulk electrolytes. The interaction can also be hypothesised to be affected by changes in electrolyte conductivity or the chemical diffusion process. The high concentration of dissolved metal ions can cause the chemical diffusion that results in the net mass transport at the electrolyte-surface interface. Although this study did not provide any evidence of the diffusion process, the surface condition and film formation properties were observed to have been altered due to these interactions. In simulated biological fluid, the dissolved metal ions interact with the biological species (protein) in bulk electrolyte, change the surface film formation and cause different material degradation mechanisms during surface articulation.

8.6 Chapter Summary

The role of dissolved metal ions (Co, Cr and Mo ions) in the simulated electrolytes on tribofilm formation and tribocorrosive behaviour, using the mechanistic approach at the CoCrMo surface after the 6 h sliding, was successfully investigated.

To conclude this chapter the following points are highlighted based on the experimental results:

- The addition of Co and Cr ions to the as-received saline electrolyte and 25% FBS increased the OCP (more noble) in the static and sliding conditions. A decrease in the average OCP (less noble) was observed in the 25% FBS +Mo when compared to the 25% as-FBS during sliding.
- The dissolved metal ions in the electrolyte can affect the material degradation mechanism of the CoCrMo surface. This outcome is because the dissolved metal ions can interact with both the electrical double layer (EIS data) on the surface and species in bulk electrolyte.
- The addition of the Cr ion significantly increased the charge transfer and corrosion volume loss in the saline electrolyte and 25% FBS electrolytes. An increase was also observed in the 25% FBS +Mo ion when compared to the 25% as-FBS.
- Each metal ion has a role in the surface tribo-corrosive degradation and chemical behaviour. The dissolved metal ions interact with the biological species (protein) in electrolyte, change the surface film formation and cause different surface degradation mechanisms during articulation.
- SEM/EDS showed higher atomic percentages in carbon, oxide and nitrogen at the wear scar in the 25% FBS +Co when compared to the 25% as-FBS, 25% FBS +Cr and 25% FBS +Mo samples.
- The sulphur element was increased more in the 25% FBS +Mo sample compared to the remaining electrolytes, which is in strong agreement with the finding from the XPS signal in this study. This result provides evidence of Mo ion-protein interaction and surface tribofilm formation to reduce the volume loss owing to mechanical wear.
- The total volume loss increased and reduced after Cr and Mo addition to the saline electrolyte, respectively. A significant increase was observed for the 25% FBS +Cr when compared to the 25% as-FBS and 25% FBS +Mo samples.
- The tribocorrosive process on the CoCrMo tested in the as-saline electrolyte, saline electrolyte +Cr and 25% FBS +Cr for 6 h was dominated by the

mechanical wear mechanism. The tribocorrosive degradation on the CoCrMo tested in the saline electrolyte +Co, saline electrolyte +Cr, 25% as-FBS, 25% FBS +Co and 25% FBS +Mo for 6 h was dominated by the wear-corrosion mechanism.

Chapter 9
Overall Discussion

9.1 Introduction

This thesis details an investigation into the tribocorrosive degradation mechanisms occurring at the CoCrMo alloy surfaces for hip implant applications. The motivation for this researcher was the necessity to understand the interactions between organic species (protein content) in physiological fluid with the metallic surface at the sliding interface of the metallic bearing. The electrolyte-metal interactions under various physiological fluid circumstances were observed to influence the formation of tribochemical films affecting the evolving frictional, corrosion and material loss at the CoCrMo alloy surfaces. The effect of different electrolyte species, electrochemical surface potential, protein conditions (structure and concentration) and dissolved metal ions on the tribochemical and tribocorrosion mechanisms have been investigated *in vitro*. The observations complemented the tribological and electrochemical analysis in various electrolytic natures; an examination also supported by surface chemical analysis of the tested samples. The obtained experimental results were discussed in detail to consolidate the findings. This chapter highlights the key observations and contributions to the current understanding concerning the clinical and pre-clinical challenges of metallic hip bearing. Several key observations are summarised, based on the experimental results, in order to facilitate discussion of the material degradation factors hypothesised in this study.

9.2 Research Highlights

The outcomes of each 'experimental chapter' are summarised to highlight the research findings. This study confirms several hypothesised factors: (a) the electrochemical potential, (b) organic species, (c) protein conditions and (d)

released metal ions in the physiological fluids were observed to affect the electrolyte-metal interaction, tribochemistry and tribocorrosion at the CoCrMo alloy surfaces. The following bullet points highlight the key findings of this study:

- Organic species in electrolyte play an important role in the tribochemical processes on the CoCrMo alloy in the OCP condition. The interaction between the organic species and metal surface during the tribocorrosive condition generates a tribofilm. The tribofilm on a CoCrMo tested in organic-containing electrolyte has a complex chemical structure of metal-organic compounds and passive oxide film. Furthermore, the tribofilm formation plays a protective role in determining the tribocorrosive degradation behaviour at the CoCrMo surface.
- The electrochemical potential condition of the CoCrMo surface affects the electrochemical reactions at the electrolyte-metal interface. The change in surface reaction determines the film formation properties and the interaction between the organic tribofilm and passive oxide film. The cathodic potential tends to increase the adsorption process of the protein species on the metal surface when compared to the OCP condition. The high anodic potential inhibits the cathodic reaction and increases the oxidation process, making the protein tribofilm difficult to form and also less effective. Hence, the tribocorrosion mechanism of the CoCrMo surface is 'potential dependent' due to the change in tribochemistry as a function of the electrochemical potential condition.
- The denaturing structure of protein, and its concentration in simulated electrolyte, is observed to be an important factor in the tribofilm build-up at the CoCrMo surface. The denatured protein conformation has a higher rate of adsorption on the CoCrMo surface, building a protective tribofilm formation to minimise the volume loss owing to mechanical wear. However, the effect of protein concentration in the electrolyte on the corrosion volume loss depends on its concentration in the electrolyte. Therefore, the protein structure and concentrations in the FBS electrolytes are shown to have various effects on the tribocorrosive degradation of the CoCrMo surface, with duration dependent on the tribological condition. These effects are

caused by the change in the tribochemical behaviour on the CoCrMo surface during sliding.

- Dissolved metal ions with a locally high concentration in simulated electrolyte play a different role in the tribocorrosive degradation of tge CoCrMo surface during sliding. This outcome appears due to the fact that the Co, Cr and Mo ions have their own interaction with the electrical double layer on the surface and species in the electrolyte. In simulated biological fluid, the dissolved metal ions interact with the biological species (protein) in bulk electrolyte, change the surface film formation and initiate different material degradation mechanisms while articulating the surfaces. The trace of sulphur in the protein layer observed after the Mo ion addition is hypothesised to have a lubricating effect on the CoCrMo surface, and thus the wear volume loss can be decreased. However, the dissolved Cr ion in the electrolyte is hypothesised to generate less protein tribofilm on the CoCrMo surface, and reduce the build-up topography and force of the tribofilm. The CoCrMo surface is poorly protected during the tribocorrosive condition and thus the Cr has a significant effect on the increasing tribocorrosive degradation.

9.3 Contributions to the Current Understanding

These observations contribute to our current understanding of the metallic alloy degradation mechanism, protein content role, clinical challenges and pre-clinical assessment of hip prosthesis.

9.3.1 Contribution to the Understanding of the Degradation Mechanism

Figure 9.1 illustrates the key factors that should be considered in order to understand tribocorrosive degradation and tribochemical film phenomena for articulating hip implants, based on the findings of this study. The variables used in this study are electrolyte species, surface electrochemical potential, modified

protein conditions and dissolved metal ions in the electrolyte. The effect of these variables on the tribochemistry and tribocorrosive degradation behaviour of the CoCrMo surface is a novelty of this study.

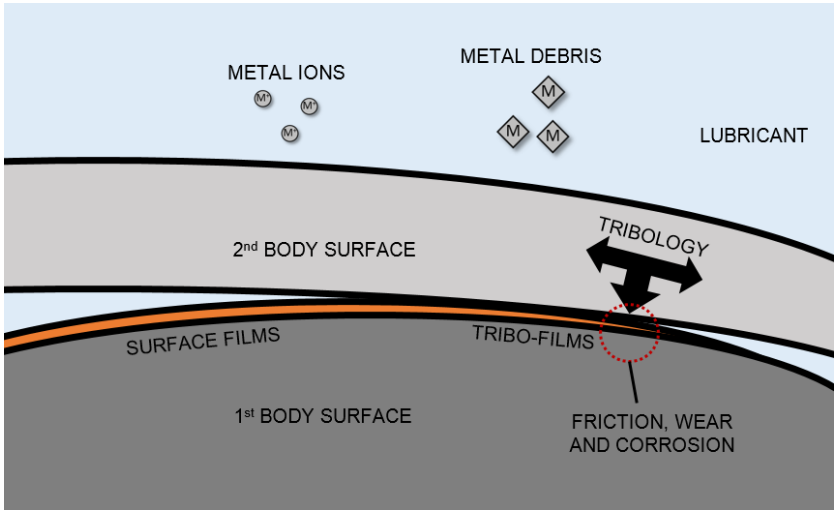

Figure 9.1 Key parameters related to the tribocorrosion and tribochemical film phenomena for articulating the implant surfaces

According to the findings and discussion in this study, a proposed schematic is presented to summarise the holistic tribochemical and tribocorrosion processes, as shown in Figure 9.2. Several interacting parameters are extracted based on the observations made in this and previous studies. The schematic is expected to help readers or other researcher to understand the factors that influence the articulating implant from a wider perspective.

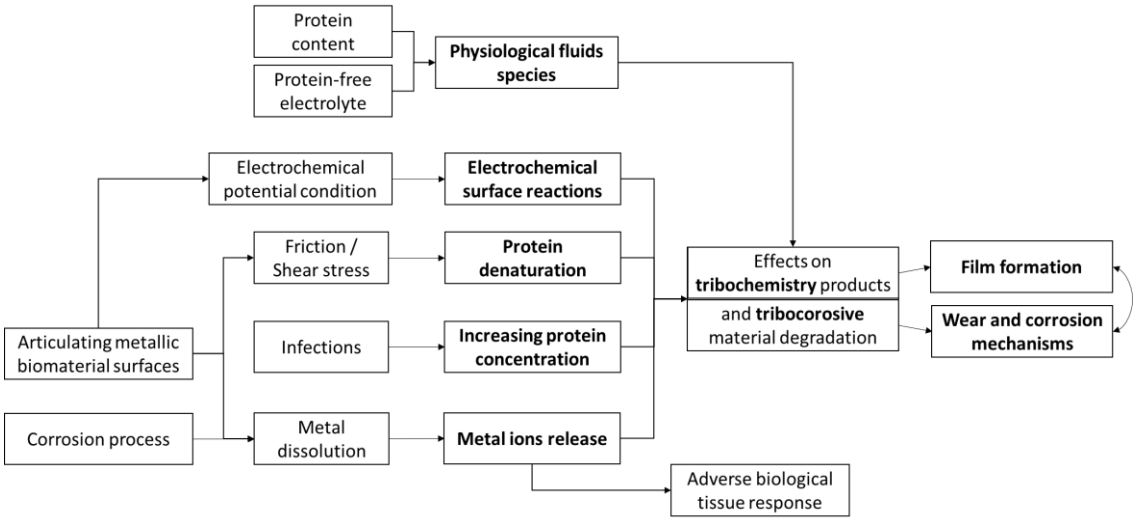

Figure 9.2 Schematic of the overview throughout this present study

The material surface for an implant is immersed in a physiological fluid/electrolyte. The interaction between the exposed surface and electrolyte determines the electrochemical reaction (corrosion) and its products; e.g., metal ion dissolution and passive oxide film. This interaction occurs spontaneously in the static condition; however, the contact load involved in the electrolyte-surface interaction affects the entire electrochemical reaction and generates tribochemical film formation, known as tribofilms, at the contacting surface. The tribochemical film is one of the crucial factors that influence the tribo-system. The presence of tribochemical film formation determines the metal surface response to the tribocorrosion outcomes; e.g., the coefficient of friction (COF), total charge transfer, material degradation, tribocorrosion mechanism, wear debris and ion release. Therefore, this study confirms that the tribochemical behaviour or tribofilm formation on the surface plays the main role since it can be sensitive to the environmental conditions and determines the rate of tribocorrosive degradation.

Another new finding of this study is that the effect of protein structure and metal ions in physiological fluids is not simply to reduce or increase the tribocorrosion volume loss. It has been investigated that these variables have a dependency on the protein content, articulating duration and surface condition before determining the tribochemistry and tribocorrosive behaviour. A novel mechanism revealed in this study is that the corrosive and tribocorrosive products can constitute a drawback for the system by interfering in the electrolyte-metal interaction; thus, the

electrolyte modifies the complex tribochemical film formation. The film formation consequently changes the effects on the tribocorrosion outcomes at the contacting surface. The schematic shows the relationship between the tribochemical process and tribocorrosive behaviour. The generated tribofilm determines the rate of both the corrosion and tribocorrosion products. However, the outcomes will determine the tribofilm's behaviour in the next cycle, and so forth. Furthermore, the mechanism of the tribochemical behaviour is mainly between the electrolyte variables and tribocorrosive degradation.

9.3.2 Contribution to the Understanding of the Protein Content Role

The protein content effect on the corrosion behaviour at the metallic alloy surface remains debatable. The presence of protein accelerated the metal ion dissolution rate under static conditions, which aligns with observations from several other studies [259, 303]. However, the different effect of the protein content on tribofilm was observed to enhance the corrosion resistance [260, 261]. In this study, the role of protein has been investigated and compared to the sample tested in the saline electrolyte and DMEM (protein-free electrolytes). The polarisation curve showed a lower (less noble) E_{corr} and higher I_{corr} at 25% FBS sample in the static condition when compared to the saline electrolyte, whilst the opposite trend under the sliding condition. These trends are aligned with the OCP compared between the static immersion and the sliding in saline electrolyte and 25% FBS.

The concentration of the FBS electrolyte has a role in corrosive inhibition compared to the protein-free environment during sliding [129]. The protein content in bovine serum is suggested to contribute to the protective film generation against the corrosive process during sliding [221]. The presence of protein in the FBS also tends to dominate the CoCrMo degradation with the wear-corrosion mechanism referring to the tribocorrosion mechanistic approach. Moreover, the protein content in the electrolyte tends to reduce the corrosive degradation and COF at applied anodic potentials (E=+0.4 V) when compared to the protein-free electrolytes. In the electrolytes without protein content, the tribocorrosion process is dominated by corrosion and corrosion-wear mechanisms under the OCP condition. The protein content is indicated to have an interaction with the released metal ions in the

electrolyte, which affect the tribocorrosive degradation behaviour. This study shows that the reduction in tribocorrosive loss after the 25% FBS addition to the saline changes with respect to the metal ion addition.

A contradictive role of protein content in the FBS is observed through the electrochemical behaviour in the static and sliding conditions when compared to the saline electrolyte sample. With the presence of the FBS in the electrolyte, the CoCrMo surface had better corrosion resistance at sliding, but less in the static condition when compared to the as-received saline electrolyte. Under static immersion, the protein content tends to increase the corrosion current when compared to the saline electrolyte, as indicated by the less noble OCP, higher corrosion volume loss in all potentials, and lower pseudo-passive potential and transpassive potential. In contrast, the protein at the sliding tribocorrosion tends to have a more noble OCP, increased pseudo-passive and transpassive regimes and a lower corrosion current. This contradictive behaviour is indicated in the polarisation curves between the saline electrolyte and 25% FBS, which is in strong agreement with the bio-corrosion review at the CoCrMo alloy [259, 364]. The difference in protein behaviour in the absence of and with the sliding condition is in strong agreement with a CoCrMo biocorrosion review by Talha et al. [364]. Yan et al. [259] also evaluated CoCrMo and 316 L alloys in saline electrolyte and 50% bovine calf medium in static and tribocorrosion conditions. The results are aligned with the present study, showing the increasing corrosion current in the bovine medium in the static condition. However, the corrosive degradation was reduced in the tribocorrosion test when compared to the NaCl electrolyte.

The protein content in the FBS was also observed significantly to decrease the corrosive material loss during the tribocorrosion test. This decreasing effect was even more apparent at the more anodic potential (E=+0.4 V) when compared to the protein-free electrolytes (saline electrolyte and DMEM samples). The protein's presence was suggested to modify the metallic surface chemistry and affect the degradation mechanism [225, 365]. Therefore, the degradation mechanism between wear and corrosion at the CoCrMo alloy was also influenced during the tribocorrosion. The metal ion dissolution determines the corrosive material loss from the exposed surface at the bulk material, enhanced by mechanical wear [204]. The protein content in the FBS tended to adsorb and minimise the exposed metal

surface, causing the decreasing corrosive volume loss observed in this study. This process also allows more passive reformation to occur. However, the dissolved metal particles are still possible for the electrolyte corrosion process or entrapped as a third-body to disrupt the passive film and increase the tribocorrosion loss [366]. This process is hypothesised to explain the significant increase in volume loss at a pseudo-passive potential, allowing greater metal dissolution.

9.3.3 Contribution to the Clinical Challenges

This study demonstrated several factors in the metallic implant failure mechanism which represent the challenges from the clinical perspective. While used in the body, the implant alloy has various electrochemical potential conditions across the surface. The materials cannot maintain the potential uniformity of the working surface during articulation. In hip bearing, the removal of the passive protective film reduces the potential against the surrounding area in galvanic coupling. Therefore, the unworn site could gain higher potential. The local factors, e.g. biological species, proteins, pH level and coupling materials, can also shift the electrode potential of the implant surface [259, 285]. The change in the surface potential will eventually influence the protein adsorption [257], plastic deformation and surface properties [282]. The mechanisms were claimed to relate to the change in passivation behaviour due to the shifted surface potential. The passive films have effects while interacting with the proteinaceous species into the subsurface deformation of biomedical alloys during tribocorrosion [357, 367, 368].

The articulating implant surfaces facilitate protein in the synovial fluid to denature due to the shear stress. This study shows that the denaturing protein influences the implant surface performance and its protective film against the degradation mechanism. Infections in the human body increase the protein concentration in synovial fluid [277]. Since the protein concentration is uncertain, depending on the physical condition, it is necessary to assess the higher protein concentration's effect on implant performance. This study has successfully indicated that increasing the protein concentration to 51 g/L of protein content would increase the corrosion and wear loss when compared to 17 g/L of protein content, suggesting there may be an increasing risk to implant performance.

This study offers a preliminary report that the released metallic ions from CoCrMo alloys in a relatively high concentration affect its implant surface degradation, thus reducing its longevity. The metal products in synovial fluid will harm the structural integrity [135], adverse tissue responses [304] and accelerate the tribocorrosive surface damage. The metal ions can stay in the surrounding tissues, bind with the proteins to be transferred to remote organs, or influence the tribochemical film and tribocorrosive degradation processes on the metallic bearing surface. The behaviour also suggests that each type of free metal ion plays its own role in the formation of metal-protein complexes or the risk to implant performance. In addition, the mechanisms of tribocorrosion may not change with time.

This study emphasises the importance of tribofilm formation which can drive the tribocorrosive degradation on the metallic alloy. The film formation is generated due to the interaction between a CoCrMo surface and proteins in the synovial fluid or serum at the articulating surfaces during the tribocorrosion condition, as also reported in several studies that used tribometers and simulator tests [280, 369, 370]. Regarding the clinical application, the tribofilm's formation on the metallic implant surface is thought to have a beneficial effect on implant longevity. Based on the previous review [369], the tribofilm is important because it can reduce the transfer of the charge at the electrolyte-metal interface, thus affecting the corrosion-related degradation. The tribofilm also influences the interface mechanics since the film is observed to have a different modulus and hardness upon the base metal. Thus, it will consequently change the shear and wetting characteristics. The wear debris is claimed, in many cases, to originate from the tribofilm formation as the debris is commonly smaller when compared to the thickness. The advanced electron microscopies allow the tribofilm formation, structures and chemical composition to be defined. A study has provided evidence that there are similarities regarding the tribofilm's formation observed from the simulator test and retrieved hip implants [186, 298]. This is because the tribochemical reactions are consistent where the CoCrMo alloy and proteinaceous species are interacting in the tribocorrosion condition.

9.3.4 Contribution to the Pre-Clinical Assessment

The mirror-polished CoCrMo flat surface produced a prominent, well-defined wear scar to gain precision in the interferometry visualisation and volume loss estimation. The use of an alumina ball as the counter-body is reliable for wear resistance and effectively electrochemically localises and isolates the CoCrMo alloy for pre-clinical assessment. Nevertheless, the alumina-CoCrMo configuration needs to consider the contact pressure due to their hardness and mechanical properties. In this study, Foetal Bovine Serum (FBS) is employed for all testing electrolytes. The FBS is observed to have a reliable nature as the protein and organic species in the serum electrolyte. Since the FBS has a complex composition, the chemical analysis of the protein traces deserves more attention. The pH level, salt and chloride concentrations must be carefully adjusted in the testing electrolyte for tribocorrosion assessment.

Currently, many different electrolytes are used in the literature and the standard electrolytes typically consist of NaCl, PBS (ASTM F1875 and corrosion standards) and 17 g/L FBS + DI water (ISO 14242/14243) [309]. The 17gL FBS + DI water was chosen as it brought the MoP wear rates in line with clinical observations when compared to the saline electrolyte and other FBS concentrations [199]. However, the observations in this study have shown that the degradation mechanism and surface chemistry of the metallic alloy is very sensitive to the electrolyte composition. Hence, the current electrolytes used might be deficient and, as such, there is a need to consider this carefully in order to get closer to *in vivo* applications.

Nevertheless, this study can be considered for the modelling variables of tribocorrosive damage in the CoCrMo alloys. This model promotes our understanding of how wear and corrosion interact, an also the volumetric material loss at the tribocorrosion contact can be accounted with all degradation contributors; i.e., chemical/corrosion and mechanical/wear damage. The findings in this study are expected to contribute to the future work designed to predict the mechanisms of the tribocorrosion of CoCrMo alloys tested in such electrolyte conditions by referring to the contribution mapping of degradation due to the wear and corrosion processes.

The use of a reciprocating pin-on-plate tribometer has the advantage of offering a less complicated sample and testing preparations. The 3-electrode instrumentation also allows an *in situ* electrochemistry measurement during the sliding configuration. However, a hip simulator is recommended to achieve the closer replication of contact stress and motion in the human body and compliment the tribometer result. However, many hip simulator tests only focus on wear behaviour without any consideration of the corrosion factor. In order to obtain a fully predictive model, the corrosion measurements are suggested to be involved in pre-clinical testing using a hip joint simulator or another *in vitro* tribometer setup. The inclusion of *in situ* corrosion measurements are thought to be important in order to obtain a further understanding of the tribocorrosive degradation mechanism which is known as a complex synergism of the processes taking place at the metallic bearing surfaces and removed debris [369]. It should be considered that the proportion of the wear volume loss is enhanced by the presence of corrosion and vice versa.

Therefore, this study agrees that a properly predictive modelling can be fulfilled if the corrosion process and its interaction with wear are incorporated in pre-clinical applications. Nevertheless, in order effectively to engineer new surfaces/devices and achieve a closer understanding of *in vivo* applications, several system variables, i.e. electrolyte composition, tribochemical aspects and the corrosion process on hip bearing degradation, must be considered.

Chapter 10
Conclusions and Future Studies

10.1 Conclusions

This present study has successfully observed electrolyte-metal interactions under various physiological conditions in a CoCrMo-based implant application. New insights, as the originality in adding to the existing knowledge and findings, are also demonstrated in terms of the system variables' effects on tribochemical film phenomena and eventually the performance regarding the surface tribocorrosion. The bullet points below are taken out from the findings obtained in all result chapters to conclude the whole study.

- Organic species in electrolytes play an important role in the tribochemical processes, generating a tribofilm which has a complex chemical structure on the CoCrMo alloy under tribocorrosion condition.
- The electrochemical potential condition of the CoCrMo surface affects the electrochemical reactions at the electrolyte-metal interface, determining the film formation properties and the interaction between organic-passive oxide film.
- The protein concentration in simulated electrolyte is observed to be an important factor in the tribofilm build-up at the CoCrMo surface. The denaturing structure of protein is proven to be more interacting on the metal surface.
- Dissolved metal ions with a locally high concentration in simulated electrolyte play a different role in the tribofilm behaviour and tribocorrosive degradation of the CoCrMo surface during sliding.
- A contradictive role of protein content in the FBS is observed through the electrochemical behaviour in the static and sliding conditions when compared to the non-protein electrolyte's sample.

The key findings obtained in this study are expected to: (i) contribute to pre-clinical understanding of more system variables effect on metallic bearing surfaces, (ii) fill the gap in understanding the mechanism of metal-protein interaction via the effect of the denaturing protein and (iii) offer a preliminary report of the released metallic ions effect from CoCrMo on its surface degradation. Moreover, the applicability of the results is that they can be considered for modelling variables of tribocorrosive damage in the CoCrMo alloys. In the end, this model escalates our understanding of how wear and corrosion interact; volumetric material loss estimation at the contacting surfaces can be accounted with the synergistic of degradation components.

10.2 Future Studies

- The tribofilm's behaviour will eventually be changed by the tribochemical reactions with the metal-organic interactions. Exploring the detailed mechanisms of electrolyte-metal interaction in building the film is very important in further study.
- Future studies may need to study *in vivo* using a hip simulator to replicate more accurately the real articulating joint circumstances with more controlled parameters.
- The resistivity and thickness of the film formed, both passive oxide and adsorbed proteins, also need to be further investigated as the function of the proteins' structure and concentration. These suggestions may contribute to a deeper understanding of protein-metal implant interactions in tribocorrosion mechanisms.
- Further investigation is required of the detailed process regarding the metal ions' role in the modifying surface chemistry and responsibility for the change in the wear mechanism. Moreover, the concentration of Cl, Na, or other dissolved ions must be minimised to investigate the more local effect of Co, Cr and Mo ions.

- Conducting the tribocorrosion test with a lower load is essential. It would be even better to use a nano tribometer to give a more accurate result and analysis of the friction behaviour under the particular variable condition.
- The electrochemical reactions on the surface in several conditions require further exploration. The electrochemical reaction aspect turns out to be more critical than explaining many electrolyte-surface phenomena at the contacting surfaces.
- More testing procedures should be carried out using various materials for the bearings; e.g., metal-on-metal, ceramic-on-ceramic, etc. These can broaden our understanding of coupled materials in several possible physiological conditions.

10.3 Closing Statement

Based on all of the evidence presented within this study, it is summarised that the tribochemical film mechanisms and their effect on the tribocorrosive behaviour of CoCrMo biomedical alloys are sensitive to the electrolyte composition used and, therefore, work differently under various physiological conditions. The finding has emerged from the experimental analysis carried out in this study, and is also linked to the previous clinical studies and failure reports. The understanding and conclusions discussed in this study are expected to contribute to further theoretical knowledge, biomaterial design, pre-clinical testing stages' anticipated factors and new insights into metallic-based Total Hip Replacement development.

References

1. Taufiqurrakhman, M., M. Bryant, and A. Neville, *Tribofilms on CoCrMo alloys: Understanding the role of the lubricant.* Biotribology, 2019: p. 100104.
2. *Hip Replacement*. 2019 [cited 2020 30 September]; Available from: https://www.nhs.uk/conditions/hip-replacement/.
3. OECD, *Hip and knee replacement*. 2017.
4. Jared R. H. Foran, M., FAAOS. *Total Hip Replacement*. OrthoInfo 2020 June [cited 2020 1 October 2020]; Available from: https://orthoinfo.aaos.org/en/treatment/total-hip-replacement.
5. *National Joint Registry 17th Annual Report 2020*. 2020, National Joint Registry.
6. Grigoris, P., P. Roberts, and K. Panousis, *The development of the DuromTM metal-on-metal hip resurfacing.* Hip Int, 2006. 16 Suppl 4: p. 65-72.
7. Drummond, J., P. Tran, and C. Fary, *Metal-on-Metal Hip Arthroplasty: A Review of Adverse Reactions and Patient Management.* Journal of functional biomaterials, 2015. 6(3): p. 486-499.
8. Yan, Y., et al., *Tribofilm formation in biotribocorrosion – does it regulate ion release in metal-on-metal artificial hip joints?* Proceedings of the Institution of Mechanical Engineers, Part J: Journal of Engineering Tribology, 2010. 224(9): p. 997-1006.
9. Fan, J., et al., *Synovial fluid lubrication of artificial joints: protein film formation and composition.* Faraday Discussions, 2012. 156: p. 69-85.
10. Hesketh, J., et al., *The composition of tribofilms produced on metal-on-metal hip bearings.* Biomaterials, 2014. 35(7): p. 2113-2119.
11. Espallargas, N., et al., *In-situ generated tribomaterial in metal/metal contacts: Current understanding and future implications for implants.* Biotribology, 2017. 10(Supplement C): p. 42-50.
12. Liao, Y., et al., *Graphitic Tribological Layers in Metal-on-Metal Hip Replacements.* Science, 2011. 334(6063): p. 1687-1690.
13. Liao, Y., et al., *CoCrMo Metal-on-Metal Hip Replacements.* Physical chemistry chemical physics : PCCP, 2013. 15(3): p. 10.1039/c2cp42968c.
14. Williams, D.F., *Definitions in biomaterials*. 1987, Amsterdam: Elsevier. 72.
15. Ghalme, S., A. Mankar, and Y. Bhalerao, *Biomaterials in Hip Joint Replacement*. Vol. 4. 2016. 113-125.
16. Navarro, M., et al., *Biomaterials in orthopaedics.* Journal of the Royal Society Interface, 2008. 5(27): p. 1137-1158.

17. Smith-Petersen, M.N., *Evolution of mould arthroplasty of the hip joint.* J Bone Joint Surg Br, 1948. 30b(1): p. 59-75.

18. Wiles, P., *The surgery of the osteoarthritic hip.* Br J Surg, 1958. 45(193): p. 488-97.

19. *ASTM International, ASTM F138-13a*, in *Standard Specification for Wrought 18Chromium-14Nickel-2.5Molybdenum Stainless Steel Bar and Wire for Surgical Implants (UNS S31673)*. 2013: West Conshohocken, PA.

20. *Metals Handbook Desk Edition, 2nd Ed*, ed. J.R. Davis. 1998: ASM International.

21. Giordano, E., et al., *Electrochemical behavior of two austenitic stainless steel biomaterials.* Rem-revista Escola De Minas - REM-REV ESC MINAS, 2010. 63.

22. Jaimes, R., et al., *New material for orthopedic implants: Electrochemical study of nickel free P558 stainless steel in minimum essential medium.* Materials Letters - MATER LETT, 2010. 64: p. 1476-1479.

23. Willert, H.G., et al., *Crevice corrosion of cemented titanium alloy stems in total hip replacements.* Clin Orthop Relat Res, 1996(333): p. 51-75.

24. Thompson, N.G., R.A. Buchanan, and J.E. Lemons, *In vitro corrosion of Ti-6Al-4V and type 316L stainless steel when galvanically coupled with carbon.* Journal of Biomedical Materials Research, 1979. 13(1): p. 35-44.

25. Brown, S.R., et al., *Long-term survival of McKee-Farrar total hip prostheses.* Clin Orthop Relat Res, 2002(402): p. 157-63.

26. R., T.S., S. D., and L.P. D., *Corrosion of cemented titanium femoral stems.* The Journal of Bone and Joint Surgery. British volume, 2004. 86-B(7): p. 974-978.

27. Gomez, P.F. and J.A. Morcuende, *Early Attempts at Hip Arthroplasty: 1700s to 1950s.* The Iowa Orthopaedic Journal, 2005. 25: p. 25-29.

28. Charnley, J., *The long-term results of low-friction arthroplasty of the hip performed as a primary intervention.* J Bone Joint Surg Br, 1972. 54(1): p. 61-76.

29. *3T PRD, Material Specification: Cobalt Chrome Alloy Co28Cr6Mo*. 2013 [cited 2017 30 August]; Available from: http://www.3trpd.co.uk.

30. Milošev, I. and H.H. Strehblow, *The composition of the surface passive film formed on CoCrMo alloy in simulated physiological solution.* Electrochimica Acta, 2003. 48(19): p. 2767-2774.

31. Antony, K.C., *Wear-Resistant Cobalt-Base Alloys.* JOM, 1983. 35(2): p. 52-60.

32. Betteridge, W. *Cobalt and its alloys*. 1982.

33. Sumner, D.R. and J.O. Galante, *Determinants of stress shielding: design versus materials versus interface.* Clin Orthop Relat Res, 1992(274): p. 202-12.

34. Cottrell, S.A., *An Introduction to Metallurgy*. Vol. 2nd edition. 1997, Leeds, United Kingdom: Maney Publishing.

35. *International Organization for Standardization, ISO 5832-4:2014*, in *Implants for surgery — Metallic materials — Part 4: Cobalt-chromium-molybdenum casting alloy*. 2014: Berlin, Germany.

36. *International Organization for Standardization, ISO 5832-12:2007*, in *Implants for surgery — Metallic materials — Part 12: Wrought cobalt-chromium-molybdenum alloy*. 2007: Switzerland.

37. *ASTM International, ASTM F75 - 12*, in *Standard Specification for Cobalt-28 Chromium-6 Molybdenum Alloy Castings and Casting Alloy for Surgical Implants (UNS R30075)*. 2012: West Conshohocken, PA.

38. Weisse, B., et al., *Failure analysis of in vivo fractured ceramic femoral heads.* Engineering Failure Analysis, 2009. 16(4): p. 1188-1194.

39. Bono, J.V., et al., *Revision Total Hip Arthroplasty*, ed. J.V. Bono, et al. Vol. 1st edition. 1999, New York, US: Springer-Verlag New York.

40. Boutin, P., *Arthroplastie totale de la hanche par prothèse en alumine frittée. Étude expérimentale et premières applications cliniques.* Revue de Chirurgie Orthopédique et Traumatologique, 2014. 100(1): p. 14-21.

41. Firkins, P.J., et al., *A novel low wearing differential hardness, ceramic-on-metal hip joint prosthesis.* Journal of Biomechanics, 2001. 34(10): p. 1291-1298.

42. Brown, C., et al., *Characterisation of wear particles produced by metal on metal and ceramic on metal hip prostheses under standard and microseparation simulation.* Journal of Materials Science: Materials in Medicine, 2007. 18(5): p. 819-827.

43. Figueiredo-Pina, C.G., et al., *Understanding the differences between the wear of metal-on-metal and ceramic-on-metal total hip replacements.* Proceedings of the Institution of Mechanical Engineers, Part H: Journal of Engineering in Medicine, 2008. 222(3): p. 285-296.

44. Affatato, S., et al., *Mixing and matching in ceramic-on-metal hip arthroplasty: An in-vitro hip simulator study.* Journal of Biomechanics, 2009. 42(15): p. 2439-2446.

45. Williams, S., et al., *Comparison of ceramic-on-metal and metal-on-metal hip prostheses under adverse conditions.* Journal of Biomedical Materials Research Part B: Applied Biomaterials, 2013. 101B(5): p. 770-775.

46. Ingham, E. and J. Fisher, *Biological reactions to wear debris in total joint replacement.* Proceedings of the Institution of Mechanical Engineers, Part H: Journal of Engineering in Medicine, 2000. 214(1): p. 21-37.

47. Masson, B., *Emergence of the alumina matrix composite in total hip arthroplasty.* International orthopaedics, 2009. 33(2): p. 359-363.

48. *BIOLOX delta - Scientific Information and Performance Data*. 2015.

49. Dowson, D. and V. Wright, *Introduction to the Biomechanics of Joints and Joint Replacements*. 1st Edition ed. Vol. Vol. 1. 1981, United Kingdom: Wiley–Blackwell.

50. Kumar, K.E.S. and S. Rakshit, *Topology optimization of the hip bone for gait cycle.* Structural and Multidisciplinary Optimization, 2020. 62(4): p. 2035-2049.

51. Glenister, R. and S. Sharma, *Anatomy, bony pelvis and lower limb, hip.* StatPearls [Internet], 2020.

52. Foran, J.R.H. Total Hip Replacement 2015; Available from: http://orthoinfo.aaos.org/topic.cfm?topic=a00377.

53. Singh, A.P. *Synovial Fluid Composition and Functions*. Available from: http://boneandspine.com/synovial-fluid/.

54. Mavraki, A. and P.M. Cann, *Friction and lubricant film thickness measurements on simulated synovial fluids.* Proceedings of the Institution of Mechanical Engineers, Part J: Journal of Engineering Tribology, 2009. 223(3): p. 325-335.

55. Roba, M., *Interaction of Synovial Fluid Components with Artificial Hip-Joint Materials* 2009, ETH Zurich: Zurich.

56. Yan, Y., et al., *Albumin adsorption on CoCrMo alloy surfaces.* Scientific reports, 2015. 5: p. 18403-18403.

57. McCarthy, J.C., J.V. Bono, and P.J. O'Donnell, *Custom and modular components in primary total hip replacement.* Clin Orthop Relat Res, 1997(344): p. 162-71.

58. Toomey, S.D., et al., *Modular component exchange for treatment of recurrent dislocation of a total hip replacement in selected patients.* J Bone Joint Surg Am, 2001. 83(10): p. 1529-33.

59. McKee, G.K. and J. Watson-Farrar, *Replacement of arthritic hips by the McKee-Farrar prosthesis.* J Bone Joint Surg Br, 1966. 48(2): p. 245-59.

60. Dowson, D., *New joints for the Millennium: Wear control in total replacement hip joints.* Proceedings of the Institution of Mechanical Engineers, Part H: Journal of Engineering in Medicine, 2001. 215(4): p. 335-358.

61. Walker, P.S. and B.L. Gold, *The tribology (friction, lubrication and wear) of all-metal artificial hip joints.* Wear, 1971. 17(4): p. 285-299.

62. Jones, D.A., et al., *Cobalt toxicity after McKee hip arthroplasty.* J Bone Joint Surg Br, 1975. 57(3): p. 289-96.

63. Charnley, J., *Arthroplasty of the Hip: A New Operation.* The Lancet, 1961. 277(7187): p. 1129-1132.

64. Oral, E. and O.K. Muratoglu, *Radiation cross-linking in ultra-high molecular weight polyethylene for orthopaedic applications.* Nuclear instruments & methods in physics research. Section B, Beam interactions with materials and atoms, 2007. 265(1): p. 18-22.

65. Galvin, A., et al., *Wear of crosslinked polyethylene under different tribological conditions.* J Mater Sci Mater Med, 2006. 17(3): p. 235-43.

66. Ingham, E. and J. Fisher, *The role of macrophages in osteolysis of total joint replacement.* Biomaterials, 2005. 26(11): p. 1271-86.

67. Tipper, J.L., et al., *Characterisation of wear debris from UHMWPE on zirconia ceramic, metal-on-metal and alumina ceramic-on-ceramic hip prostheses generated in a physiological anatomical hip joint simulator.* Wear, 2001. 250(1): p. 120-128.

68. Rieker, C., R. Konrad, and R. Schoun, *In vitro comparison of the two hard-hard articulations for total hip replacements.* Proceedings of the Institution of Mechanical Engineers, Part H: Journal of Engineering in Medicine, 2001. 215(2): p. 153-160.

69. Tipper, J.L., et al., *Alumina–alumina artificial hip joints. Part II: Characterisation of the wear debris from in vitro hip joint simulations.* Biomaterials, 2002. 23(16): p. 3441-3448.

70. Kumar, P., et al., *Low wear rate of UHMWPE against zirconia ceramic (Y-PSZ) in comparison to alumina ceramic and SUS 316L alloy.* J Biomed Mater Res, 1991. 25(7): p. 813-28.

71. Spinelli, M., et al., *Ceramic-on-ceramic vs. metal-on-metal in total hip arthroplasty (THA): do 36-mm diameters exhibit comparable wear performance? Keramik-Keramik vs. Metall-Metall in Totalprothesen-Hüftgelenkspfanne-. Arthroplastik: zeigen 36-mm Durchmesser ähnliche Verschleißverhalten?* Materialwissenschaft und Werkstofftechnik, 2009. 40(1-2): p. 94-97.

72. Roualdes, O., et al., *In vitro and in vivo evaluation of an alumina-zirconia composite for arthroplasty applications.* 2010.

73. Meng, Q., et al., *The lubrication performance of the ceramic-on-ceramic hip implant under starved conditions.* Journal of the Mechanical Behavior of Biomedical Materials, 2015. 50: p. 70-76.

74. Vassiliou, K., S.C. Scholes, and A. Unsworth, *Laboratory studies on the tribology of hard bearing hip prostheses: Ceramic on ceramic and metal on metal.* Proceedings of the Institution of Mechanical Engineers, Part H: Journal of Engineering in Medicine, 2007. 221(1): p. 11-20.

75. McMinn, D., et al., *Metal on metal surface replacement of the hip. Experience of the McMinn prothesis.* Clin Orthop Relat Res, 1996(329 Suppl): p. S89-98.

76. Daniel, J., P.B. Pynsent, and D.J. McMinn, *Metal-on-metal resurfacing of the hip in patients under the age of 55 years with osteoarthritis.* J Bone Joint Surg Br, 2004. 86(2): p. 177-84.

77. Ball, S.T., M.J. Le Duff, and H.C. Amstutz, *Early results of conversion of a failed femoral component in hip resurfacing arthroplasty.* J Bone Joint Surg Am, 2007. 89(4): p. 735-41.

78. Falez, F., et al., *Results of hip resurfacing.* Int Orthop, 2011. 35(2): p. 239-43.

79. McMinn, D.J.W., et al., *Indications and results of hip resurfacing.* International orthopaedics, 2011. 35(2): p. 231-237.

80. Knight, S.R., R. Aujla, and S.P. Biswas, *Total Hip Arthroplasty - over 100 years of operative history.* Orthopedic reviews, 2011. 3(2): p. e16-e16.

81. Cuckler, J.M., *The rationale for metal-on-metal total hip arthroplasty.* Clin Orthop Relat Res, 2005. 441: p. 132-6.

82. Archibeck, M.J., et al., *The basic science of periprosthetic osteolysis.* Instr Course Lect, 2001. 50: p. 185-95.

83. Boutin, P., *[Total arthroplasty of the hip by fritted aluminum prosthesis. Experimental study and 1st clinical applications].* Rev Chir Orthop Reparatrice Appar Mot, 1972. 58(3): p. 229-46.

84. Osborne, H., *Firm pays out to NHS over defective hip replacements*, in *The Guardian*. 2018: https://www.theguardian.com/.

85. Turner, T. *Hip Replacement*. 2020.

86. Eliaz, N., *Corrosion of Metallic Biomaterials: A Review.* Materials (Basel, Switzerland), 2019. 12(3): p. 407.

87. Balachandran, S., et al., *Atomic Scale Origin of Metal Ion Release from Hip Implant Taper Junctions.* Advanced Science. n/a(n/a): p. 1903008.

88. Cooper, H.J., et al., *Corrosion at the head-neck taper as a cause for adverse local tissue reactions after total hip arthroplasty.* The Journal of bone and joint surgery. American volume, 2012. 94(18): p. 1655-1661.

89. R., W.M., et al., *Adverse local tissue reactions in metal-on-polyethylene total hip arthroplasty due to trunnion corrosion.* The Bone & Joint Journal, 2015. 97-B(8): p. 1024-1030.

90. Yaszemski, M.J., *Biomaterials in orthopedics*. 2003: CRC Press.

91. Hill, D., *Design engineering of biomaterials for medical devices.* Design Engineering of Biomaterials for Medical Devices, by David Hill, pp. 480. ISBN 0-471-96708-4. Wiley-VCH, October 1998., 1998: p. 480.

92. Smith, A.J., et al., *Failure rates of metal-on-metal hip resurfacings: analysis of data from the National Joint Registry for England and Wales.* The Lancet, 2012. 380(9855): p. 1759-1766.

93. Roposch, A., et al., *Functional Outcomes in Children with Osteonecrosis Secondary to Treatment of Developmental Dysplasia of the Hip.* JBJS, 2011. 93(24): p. e145.

94. Espallargas, N., C. Torres, and A.I. Muñoz, *A metal ion release study of CoCrMo exposed to corrosion and tribocorrosion conditions in simulated body fluids.* Wear, 2015. 332(Supplement C): p. 669-678.

95. Muñoz, A.I. and S. Mischler, *Interactive effects of albumin and phosphate ions on the corrosion of CoCrMo implant alloy.* Journal of the Electrochemical Society, 2007. 154(10): p. C562-C570.

96. Vidal, C.V., et al., *Passivation of a CoCrMo PVD alloy with biomedical composition under simulated physiological conditions studied by EQCM and XPS.* Journal of The Electrochemical Society, 2012. 159(5): p. C233-C243.

97. Li, Y.-S., et al., *Surface-enhanced Raman spectroelectrochemical studies of corrosion films on implant Co–Cr–Mo alloy in biosimulating solutions.* Journal of Raman Spectroscopy, 1999. 30(2): p. 97-103.

98. Hedberg, Y. and I. Odnevall Wallinder, *Metal release and speciation of released chromium from a biomedical CoCrMo alloy into simulated physiologically relevant solutions.* Journal of Biomedical Materials Research Part B: Applied Biomaterials, 2014. 102(4): p. 693-699.

99. Yan, Y., D. Dowson, and A. Neville, *In-situ electrochemical study of interaction of tribology and corrosion in artificial hip prosthesis simulators.* Journal of the Mechanical Behavior of Biomedical Materials, 2013. 18: p. 191-199.

100. Hesketh, J., et al., *Biotribocorrosion: Some electrochemical observations from an instrumented hip joint simulator.* Tribology International, 2013. 59: p. 332-338.

101. Bazzoni, A., S. Mischler, and N. Espallargas, *Tribocorrosion of pulsed plasma-nitrided CoCrMo implant alloy.* Tribology Letters, 2013. 49(1): p. 157-167.

102. Alemón, B., et al., *Tribocorrosion behavior and ions release of CoCrMo alloy coated with a TiAlVCN/CNx multilayer in simulated body fluid plus bovine serum albumin.* Tribology International, 2015. 81: p. 159-168.

103. Hodgson, A.W.E., et al., *Passive and transpassive behaviour of CoCrMo in simulated biological solutions.* Electrochimica Acta, 2004. 49(13): p. 2167-2178.

104. Milošev, I., T. Kosec, and H.H. Strehblow, *XPS and EIS study of the passive film formed on orthopaedic Ti–6Al–7Nb alloy in Hank's physiological solution.* Electrochimica Acta, 2008. 53(9): p. 3547-3558.

105. Metikos-Huković, M., et al., *Influence of alloying elements on the corrosion stability of CoCrMo implant alloy in Hank's solution.* Acta Biomater, 2006. 2(6): p. 693-700.

106. Lhotka, C., et al., *Four-year study of cobalt and chromium blood levels in patients managed with two different metal-on-metal total hip replacements.* J Orthop Res, 2003. 21(2): p. 189-95.

107. Martin, E.J., et al., *Dominant role of molybdenum in the electrochemical deposition of biological macromolecules on metallic surfaces.* Langmuir, 2013. 29(15): p. 4813-4822.

108. Milošev, I., *The effect of biomolecules on the behaviour of CoCrMo alloy in various simulated physiological solutions.* Electrochimica Acta, 2012. 78: p. 259-273.

109. Bauer, T.W., *Particles and periimplant bone resorption.* Clin Orthop Relat Res, 2002(405): p. 138-43.

110. Vieira, A.C., et al., *Mechanical and electrochemical deterioration mechanisms in the tribocorrosion of Al alloys in NaCl and in NaNO3 solutions.* Corrosion Science, 2012. 54: p. 26-35.

111. Espallargas, N., et al., *A new experimental technique for quantifying the galvanic coupling effects on stainless steel during tribocorrosion under equilibrium conditions.* Wear, 2013. 307(1): p. 190-197.

112. Matusiewicz, H., *Potential release of in vivo trace metals from metallic medical implants in the human body: From ions to nanoparticles – A systematic analytical review.* Acta Biomaterialia, 2014. 10(6): p. 2379-2403.

113. Agency, M.a.H.p.R., *Metal-on-Metal (MoM) Hip Replacements - Guidance on Implantation and Patient Management Medical Safety Alert*. 2015: GOV.UK.

114. Matharu, G.S., et al., *Adverse reactions to metal debris occur with all types of hip replacement not just metal-on-metal hips: a retrospective observational study of 3340 revisions for adverse reactions to metal debris from the National Joint Registry for England, Wales, Northern Ireland and the Isle of Man.* BMC Musculoskelet Disord, 2016. 17(1): p. 495.

115. Doorn, P.F., et al., *Tissue reaction to metal on metal total hip prostheses.* Clin Orthop Relat Res, 1996(329 Suppl): p. S187-205.

116. Germain, M.A., et al., *Comparison of the cytotoxicity of clinically relevant cobalt-chromium and alumina ceramic wear particles in vitro.* Biomaterials, 2003. 24(3): p. 469-79.

117. Catelas, I., et al., *Cytotoxic and apoptotic effects of cobalt and chromium ions on J774 macrophages - Implication of caspase-3 in the apoptotic pathway.* J Mater Sci Mater Med, 2001. 12(10-12): p. 949-53.

118. Granchi, D., et al., *Sensitivity to implant materials in patients undergoing total hip replacement.* J Biomed Mater Res B Appl Biomater, 2006. 77(2): p. 257-64.

119. Hallab, N.J., K. Mikecz, and J.J. Jacobs, *A triple assay technique for the evaluation of metal-induced, delayed-type hypersensitivity responses in patients with or receiving total joint arthroplasty.* J Biomed Mater Res, 2000. 53(5): p. 480-9.

120. Masse, A., et al., *Ion release and chromosomal damage from total hip prostheses with metal-on-metal articulation.* J Biomed Mater Res B Appl Biomater, 2003. 67(2): p. 750-7.

121. Willert, H.G., et al., *Metal-on-metal bearings and hypersensitivity in patients with artificial hip joints. A clinical and histomorphological study.* J Bone Joint Surg Am, 2005. 87(1): p. 28-36.

122. Kurtz, S.M., et al., *Prevalence of Metal-on-Metal Bearings in the United States*, S. Kurtz, et al., Editors. 2013, ASTM International: West Conshohocken, PA. p. 3-18.

123. Clayton, R.A., et al., *Inflammatory pseudotumor associated with femoral nerve palsy following metal-on-metal resurfacing of the hip. A case report.* J Bone Joint Surg Am, 2008. 90(9): p. 1988-93.

124. Park, Y.S., et al., *Early osteolysis following second-generation metal-on-metal hip replacement.* J Bone Joint Surg Am, 2005. 87(7): p. 1515-21.

125. Dobbs, H.S. and M.J. Minski, *Metal ion release after total hip replacement.* Biomaterials, 1980. 1(4): p. 193-198.

126. Michel, R., et al., *Systemic effects of implanted prostheses made of cobalt-chromium alloys.* Archives of Orthopaedic and Trauma Surgery, 1991. 110(2): p. 61-74.

127. Murgatroyd, S., *Pseudotumor Presenting as a Pelvic Mass: A Complication of Eccentric Wear of a Metal on Polyethylene Hip Arthroplasty.* The Journal of arthroplasty, 2011. 27: p. 820.e1-4.

128. Walsh, A.J., V.S. Nikolaou, and J. Antoniou, *Inflammatory pseudotumor complicating metal-on-highly cross-linked polyethylene total hip arthroplasty.* J Arthroplasty, 2012. 27(2): p. 324.e5-8.

129. Lyvers, M., et al., *Electrochemically induced tribolayer with molybdenum for hip implants: Tribocorrosion and biocompatibility study.* Thin Solid Films, 2017. 644: p. 82-91.

130. Fontana, M.G. and N.D. Greene, *Corrosion Engineering*. 2nd ed. ed. 1993, Japan: McGraw-Hill.

131. Talbot, D. and J. Talbot, *Corrosion science and technology*. 2nd ed. 2007, Boca Raton, Fla;London;: CRC Press.

132. Ratner, B.D., et al., *Biomaterials science: an introduction to materials in medicine*. 2004: Academic press.

133. Kamachimudali, U., T.M. Sridhar, and B. Raj, *Corrosion of bio implants.* Sadhana, 2003. 28(3): p. 601-637.

134. Tait, W.S., *An Introduction to Electrochemical Corrosion Testing for Practicing Engineers & Scientists*. 1994: Pair O Docs Pubns.

135. Bryant, M. and A. Neville, *Corrosion and mechanical properties.* Orthopaedics and Trauma, 2016. 30(3): p. 176-191.

136. Scully, J.R. and K. Lutton, *Polarization Behavior of Active Passive Metals and Alloys*, in *Encyclopedia of Interfacial Chemistry*, K. Wandelt, Editor. 2018, Elsevier: Oxford. p. 439-447.

137. Frankel, G.S., *Pitting Corrosion of Metals: A Review of the Critical Factors.* Journal of The Electrochemical Society, 1998. 145(6): p. 2186-2198.

138. Brox, B. and I. Olefjord, *Preferential dissolution of iron during polarization of stainless steels in acids.* Stainless Steel'84, Chalmers University of Technology, 1984: p. 134-142.

139. Milosev, I. and M. Remskar, *In vivo production of nanosized metal wear debris formed by tribochemical reaction as confirmed by high-resolution TEM and XPS analyses.* J Biomed Mater Res A, 2009. 91(4): p. 1100-10.

140. Kocijan, A., I. Milosev, and B. Pihlar, *Cobalt-based alloys for orthopedic applications studied by electrochemical and XPS analysis*. Vol. 15. 2004. 643-50.

141. Bryant, M., *Fretting-crevice corrosion of cemented metal on metal total hip replacements*. 2013, University of Leeds.

142. Hoar, T., *The production and breakdown of the passivity of metals.* Corrosion Science, 1967. 7: p. 341-355.

143. Uhlig, H.H., *Adsorbed and Reaction-Product Films on Metals.* Journal of the Electrochemical Society, 1950. 97(11): p. 215C.

144. Richardson, J.A. and G.C. Wood, *The Interpretation of Impedance Changes on Oxide-Coated Aluminum Produced by Immersion in Inhibitive*

and Corrosive Aqueous Media. Journal of The Electrochemical Society, 1973. 120(2): p. 193.

145. Pistorius, P.C. and G.T. Burstein, *Metastable pitting corrosion of stainless steel and the transition to stability.* Philosophical Transactions of the Royal Society of London. Series A: Physical and Engineering Sciences, 1992. 341(1662): p. 531-559.

146. *ASTM International, Standard Guide for Examination and Evaluation of Pitting Corrosion*, in *ASTM G46-94(2013)*. 2013, PA: West Conshohocken.

147. Roy, A., D. Fleming, and S. Gordon. *Effect of chloride concentration and pH on pitting corrosion of waste package container materials*. 1996.

148. NACE. *Crevice Corrosion*. [cited 2017 16 August]; Available from: https://www.nace.org/Corrosion-Central/Corrosion-101/Crevice-Corrosion/.

149. Oldfield, J.W. and W.H. Sutton, *New Technique for Predicting the Performance of Stainless Steels in Sea Water and other Chloride-containing Environments.* British Corrosion Journal, 1980. 15(1): p. 31-34.

150. Oldfield, J.W. and W.H. Sutton, *Crevice Corrosion of Stainless Steels: II. Experimental studies.* British Corrosion Journal, 1978. 13(3): p. 104-111.

151. Foundation, A.E., *Hip & Knee Book*, in *TRUNNIONOSIS*. 2017: hipandkneebook.com.

152. Gilbert, J.L., C.A. Buckley, and J.J. Jacobs, *In vivo corrosion of modular hip prosthesis components in mixed and similar metal combinations. The effect of crevice, stress, motion, and alloy coupling.* Journal of Biomedical Materials Research, 1993. 27(12): p. 1533-1544.

153. Gilbert, J.L., et al., *Intergranular corrosion-fatigue failure of cobalt-alloy femoral stems. A failure analysis of two implants.* J Bone Joint Surg Am, 1994. 76(1): p. 110-5.

154. NACE. *Galvanic Corrosion*. Available from: https://www.nace.org/Corrosion-Central/Corrosion-101/Galvanic-Corrosion/.

155. Collier, J.P., et al., *Corrosion at the interface of cobalt-alloy heads on titanium-alloy stems.* Clinical orthopaedics and related research, 1991(271): p. 305-312.

156. Lucas, L.C., R.A. Buchanan, and J.E. Lemons, *Investigations on the galvanic corrosion of multialloy total hip prostheses.* Journal of Biomedical Materials Research, 1981. 15(5): p. 731-747.

157. Serhan, H., et al., *Is galvanic corrosion between titanium alloy and stainless steel spinal implants a clinical concern?* Spine J, 2004. 4(4): p. 379-87.

158. Virtanen, S., et al., *Special modes of corrosion under physiological and simulated physiological conditions.* Acta Biomater, 2008. 4(3): p. 468-76.

159. Mears, D.C., *The use of dissimilar metals in surgery.* Journal of Biomedical Materials Research, 1975. 9(4): p. 133-148.

160. Reclaru, L., et al., *Pitting, crevice and galvanic corrosion of REX stainless-steel/CoCr orthopedic implant material.* Biomaterials, 2002. 23(16): p. 3479-85.

161. Tan, Y., *Homogeneous Electrode Models and Uniform Corrosion Measurements*, in *Heterogeneous Electrode Processes and Localized Corrosion*, R.W. Revie, Editor. 2012, John Wiley & Sons, Inc.: New Jersey, US. p. 1-35.

162. Poursaee, A., *9 - Corrosion measurement and evaluation techniques of steel in concrete structures*, in *Corrosion of Steel in Concrete Structures*, A. Poursaee, Editor. 2016, Woodhead Publishing: Oxford. p. 169-191.

163. Vidal, C.V., *Study of the degradation mechanisms of the CoCrMo biomedical alloy in physiological media by electrochemical techniques and surface analysis*. 2012, Universitat Politècnica de València.

164. Scully, J., D. Silverman, and M. Kendig, *Electrochemical Impedance: Analysis and Interpretation*. 1993.

165. Milošev, I., T. Kosec, and H.-H.J.E.A. Strehblow, *XPS and EIS study of the passive film formed on orthopaedic Ti–6Al–7Nb alloy in Hank's physiological solution.* 2008. 53(9): p. 3547-3558.

166. Moreto, J.A., et al., *Effect of Temperature, Electrolyte Composition and Immersion Time on the Electrochemical Corrosion Behavior of CoCrMo Implant Alloy Exposed to Physiological Serum and Hank's Solution %J Materials Research.* 2018. 21.

167. Namus, R., et al., *The influence of protein concentration, temperature and cathodic polarization on the surface status of CoCrMo biomedical grade alloys.* Applied Surface Science, 2020. 499: p. 143908.

168. Dambatta, M.s., et al., *In vitro degradation and cell viability assessment of Zn-3Mg alloy for biodegradable bone implants.* Proceedings of the Institution of Mechanical Engineers Part H Journal of Engineering in Medicine, 2015. 229: p. 335-342.

169. Growcock, F.B. and R.J. Jasinski, *Time-Resolved Impedance Spectroscopy of Mild Steel in Concentrated Hydrochloric Acid.* Journal of The Electrochemical Society, 1989. 136(8): p. 2310-2314.

170. Olsson, C.O.A. and D. Landolt, *Anodisation of a Nb–Zr alloy.* Electrochimica Acta, 2003. 48(27): p. 3999-4011.

171. Helsen, J.A. and H. Jürgen Breme, *Metals as biomaterials*. 1998.

172. Bommersbach, P., et al., *Formation and behaviour study of an environment-friendly corrosion inhibitor by electrochemical methods.* Electrochimica Acta, 2005. 51(6): p. 1076-1084.

173. STLE. [cited 2017 01 August]; Available from: http://www.stle.org/files/What_is_tribology/Tribology_Applications.aspx.

174. Gohar, R. and H. Rahnejat, *Fundamentals of tribology*. 2nd ed. 2012, London: Imperial College Press.

175. Stachowiak, G.W. and A.W. Batchelor, *Engineering tribology*. Fourth;4;4th; ed. 2014, Oxford: Butterworth-Heinemann.

176. Singer, I., *Surface Analysis*, in *Handbook of Lubrication and Tribology, Volume II*. 2012, CRC Press. p. 1-20.

177. Greenwood, J.A. and J.B.P. Williamson, *Contact of nominally flat surfaces.* Proceedings of the Royal Society of London. Series A. Mathematical and Physical Sciences, 1966. 295(1442): p. 300.

178. Shigley, J.E., *Mechanical Engineering Design*. 5th Edition, Chapter 2 ed. 1989: McGraw-Hill, Inc.

179. Williams, J.A., *Engineering tribology*. 1994, Oxford: Oxford University Press.

180. Hertz, H., *On the Contact of Elastic Solids.* J Reine Angew Math, 1881. 92: p. 156-171.

181. Archard, J.F. and T.E. Allibone, *Elastic deformation and the laws of friction.* Proceedings of the Royal Society of London. Series A. Mathematical and Physical Sciences, 1957. 243(1233): p. 190-205.

182. Williams, J., *Engineering tribology*. 2005: Cambridge University Press.

183. Moore, J., et al. *Mechanics Map - Open Textbook Project*. Engineering Mechanic [cited 2020 2 October]; Available from: http://mechanicsmap.psu.edu/websites/6_friction/dry_friction/dryfriction.html.

184. Association, A.B., *The Principles and Design of Foundation Brake Rigging*. 1921: Air brake association.

185. Hanaor, D.A.H., Y. Gan, and I. Einav, *Static friction at fractal interfaces.* Tribology International, 2016. 93: p. 229-238.

186. Yan, Y., *Corrosion and Tribo-Corrosion Behaviour of Metallic Orthopaedic Implant Materials*. 2006, University of Leeds.

187. Flugsrud, G.B., et al., *The effect of middle-age body weight and physical activity on the risk of early revision hip arthroplasty: A cohort study of 1,535 individuals.* Acta Orthopaedica, 2007. 78(1): p. 99-107.

188. Damm, P., et al., *Friction in Total Hip Joint Prosthesis Measured In Vivo during Walking.* PloS one, 2013. 8: p. e78373.

189. Affatato, S., *7 - Tribological interactions of modern biomaterials used in total hip arthroplasty (THA)*, in *Perspectives in Total Hip Arthroplasty*, S. Affatato, Editor. 2014, Woodhead Publishing. p. 99-116.

190. Totten, G.E. and H. Liang, *Mechanical Tribology*. 2004, New York: Marcel Dekker, Inc.

191. Stachowiak, G.W., *Wear-materials, mechanisms and practice*. 2005, Chichester: Wiley.

192. Stachowiak, G.W. and A.W. Batchelor, *Engineering tribology*. 3rd;3; ed. 2005, Amsterdam;Boston;: Elsevier Butterworth-Heinemann.

193. Stachowiak, G.W. and A.W. Batchelor, *13 - Corrosive and Oxidative Wear*, in *Engineering Tribology (Third Edition)*. 2006, Butterworth-Heinemann: Burlington. p. 573-593.

194. Vingsbo, O. and S. Söderberg, *On fretting maps.* Wear, 1988. 126(2): p. 131-147.

195. Bryant, M., et al., *Galvanically enhanced fretting-crevice corrosion of cemented femoral stems.* Journal of the Mechanical Behavior of Biomedical Materials, 2014. 40: p. 275-286.

196. Oladokun, A., *Mechanism of Fretting Corrosion at the Modular Taper Interface of Hip Prosthesis*. 2017, University of Leeds.

197. Kondo, Y., T. Koyama, and S. Sasaki, *Tribological Properties of Ionic Liquids*, in *Ionic Liquids - New Aspects for the Future*, J.-i. Kadokawa, Editor. 2013, InTech: Rijeka. p. Ch. 05.

198. Neville, A.a.M., A., *Wear and Chemistry of Lubricants*, in *Wear: Materials, Mechanisms and Practice*, G.W. Stachowiak, Editor. 2005, John Wiley & Sons: Hoboken. p. 71–94.

199. Beadling, A.R., *Biotribocorrosion of Hard-on-Hard Bearing Surfaces in Orthopaedic Hip Replacements*. 2016, University of Leeds.

200. Jin, Z., et al., *Analysis and modelling of wear of cobalt-chrome alloys in a pin-on-plate test for a metal-on-metal total hip replacement.* Proceedings of the Institution of Mechanical Engineers, Part H: Journal of Engineering in Medicine, 2000. 214(6): p. 559-568.

201. Sonntag, R., et al., *Hard-on-hard lubrication in the artificial hip under dynamic loading conditions.* PloS one, 2013. 8(8): p. e71622-e71622.

202. Jalali-Vahid, D., et al., *Prediction of lubricating film thickness in UHMWPE hip joint replacements.* J Biomech, 2001. 34(2): p. 261-6.

203. Khaemba, D.N., *Raman spectroscopic studies of friction modifier Molybdenum DialkyldiThioCarbamate (MoDTC)*. 2016, University of Leeds.

204. Mischler, S., *Triboelectrochemical techniques and interpretation methods in tribocorrosion: A comparative evaluation.* Tribology International, 2008. 41(7): p. 573-583.

205. López-Ortega, A., J.L. Arana, and R. Bayón, *Tribocorrosion of Passive Materials: A Review on Test Procedures and Standards.* International Journal of Corrosion, 2018. 2018: p. 7345346.

206. Mathew, M.T., et al., *Significance of Tribocorrosion in Biomedical Applications: Overview and Current Status.* Advances in Tribology, 2009. 2009: p. 250986.

207. Landolt, D. and S. Mischler, *Tribocorrosion of passive metals and coatings*. 2011: Elsevier.

208. Watson, S.W., et al., *Methods of measuring wear-corrosion synergism.* Wear, 1995. 181-183: p. 476-484.

209. Landolt, D., *Electrochemical and materials aspects of tribocorrosion systems.* Journal of Physics D: Applied Physics, 2006. 39(15): p. 3121-3127.

210. Diomidis, N., et al., *Tribocorrosion of stainless steel in sulfuric acid: Identification of corrosion-wear components and effect of contact area*. Vol. 269. 2010. 93-103.

211. Mischler, S. and P. Ponthiaux, *A round robin on combined electrochemical and friction tests on alumina/stainless steel contacts in sulphuric acid.* Wear, 2001. 248(1): p. 211-225.

212. Fuentes, E., et al., *Advanced Surface Treatments on Titanium and Titanium Alloys Focused on Electrochemical and Physical Technologies for Biomedical Applications*, in *Biomaterial-supported Tissue Reconstruction or Regeneration*. 2019.

213. Vieira, A., et al., *Mechanical and electrochemical deterioration mechanisms in the tribocorrosion of Al alloys in NaCl and in NaNO 3 solutions.* Corrosion Science, 2012. 54: p. 26-35.

214. Igual Muñoz, A. and N. Espallargas, *5 - Tribocorrosion mechanisms in sliding contacts*, in *Tribocorrosion of Passive Metals and Coatings*, D. Landolt and S. Mischler, Editors. 2011, Woodhead Publishing. p. 118-152.

215. *ASTM International, ASTM G119-06*, in *Standard Guide for Determining Synergism Between Wear and Corrosion*. 2016, ASTM International: West Conshohocken, PA.

216. Yan, Y., *7 - Growth of passive tribofilms in medical implants*, in *Bio-Tribocorrosion in Biomaterials and Medical Implants*. 2013, Woodhead Publishing. p. 147-168.

217. Zhang, Y., X.-Y. Yin, and F.-Y. Yan, *Tribocorrosion behaviour of type S31254 steel in seawater: Identification of corrosion–wear components and effect of potential.* Materials Chemistry and Physics, 2016. 179: p. 273-281.

218. Ma, F., et al., *Structural, mechanical and tribocorrosion behaviour in artificial seawater of CrN/AlN nano-multilayer coatings on F690 steel substrates.* Applied Surface Science, 2018. 428: p. 404-414.

219. Priya, R., C. Mallika, and U.K. Mudali, *Wear and tribocorrosion behaviour of 304L SS, Zr-702, Zircaloy-4 and Ti-grade2.* Wear, 2014. 310(1): p. 90-100.

220. Stack, M.M. and G.H. Abdulrahman, *Mapping erosion-corrosion of carbon steel in oil exploration conditions: Some new approaches to characterizing mechanisms and synergies.* Tribology International, 2010. 43(7): p. 1268-1277.

221. Mathew, M.T., et al., *Tribocorrosion behavior of CoCrMo alloy for hip prosthesis as a function of loads: A comparison between two testing systems.* Wear, 2011. 271(9): p. 1210-1219.

222. *UNE 112086:2016*, in *Tribocorrosion testing procedure for passivating materials*. 2016, Asociación Española de Normalización (UNE).

223. Bryant, M. and A. Neville, *Fretting corrosion of CoCr alloy: Effect of load and displacement on the degradation mechanisms.* Proceedings of the Institution of Mechanical Engineers, Part H: Journal of Engineering in Medicine, 2017. 231(2): p. 114-126.

224. Mischler, S., et al., *Influence of passivity on the tribocorrosion of carbon steel in aqueous solutions.* Wear, 2001. 251(1): p. 1295-1307.

225. Godet, M., *The third-body approach: A mechanical view of wear.* Wear, 1984. 100(1): p. 437-452.

226. Vinothkumar, K.R. and R. Henderson, *Structures of membrane proteins.* Quarterly reviews of biophysics, 2010. 43(1): p. 65-158.

227. *Protein Concept Map*. 2003: Pearson Education, Inc., publishing as Benjamin Cummings.

228. *Protein-Surface Interactions*, in *An Introduction To Tissue-Biomaterial Interactions*. 2002. p. 37-52.

229. Maskiewicz, V.K., et al., *Characterization of protein degradation in serum-based lubricants during simulation wear testing of metal-on-metal hip prostheses.* J Biomed Mater Res B Appl Biomater, 2010. 94(2): p. 429-40.

230. Parkes, M., et al., *The effect of buffer solution choice on protein adsorption and lubrication.* Tribology International, 2014. 72: p. 108-117.

231. *Malvern Panalytical. Using Raman Spectroscopy to Understand the Conformational Stability of Protein Therapeutics. AZoM, viewed 15 January 2020*. viewed 15 January 2020; Available from: https://www.azom.com/article.aspx?ArticleID=11142.

232. Foley, S., et al., *Photolysis of Bovine Serum Albumin by near UV irradiation.* 2011.

233. Lewis, E.N., et al., *Combined dynamic light scattering and Raman spectroscopy approach for characterizing the aggregation of therapeutic proteins.* Molecules (Basel, Switzerland), 2014. 19(12): p. 20888-20905.

234. Thawornchinsombut, S., et al., *Raman Spectroscopy Determines Structural Changes Associated with Gelation Properties of Fish Proteins Recovered at Alkaline pH.* Journal of Agricultural and Food Chemistry, 2006. 54(6): p. 2178-2187.

235. Zhang, S., et al., *Raman Spectroscopic Characterization of Structural Changes in Heated Whey Protein Isolate upon Soluble Complex Formation with Pectin at Near Neutral pH.* Journal of Agricultural and Food Chemistry, 2012. 60(48): p. 12029-12035.

236. Wang, C.-H., et al., *The effect of disulfide bonds on protein folding, unfolding, and misfolding investigated by FT–Raman spectroscopy.* Journal of Raman Spectroscopy, 2016. 47(8): p. 940-947.

237. Chen, M.C. and R.C. Lord, *Laser-excited Raman spectroscopy of biomolecules. VIII. Conformational study of bovine serum albumin.* J Am Chem Soc, 1976. 98(4): p. 990-2.

238. Wesełucha-Birczyńska, A., et al., *Raman micro-spectroscopy tracing human lymphocyte activation.* The Analyst, 2013. 138.

239. Esmonde-White, K.A., et al., *Raman spectroscopy of synovial fluid as a tool for diagnosing osteoarthritis.* J Biomed Opt, 2009. 14(3): p. 034013.

240. Lin, V.J.C. and J.L. Koenig, *Raman studies of bovine serum albumin.* Biopolymers, 1976. 15(1): p. 203-218.

241. Liang, M., et al., *A simple and direct isolation of whey components from raw milk by gel filtration chromatography and structural characterization by Fourier transform Raman spectroscopy.* Talanta, 2006. 69(5): p. 1269-1277.

242. Qian, W. and S. Krimm, *Vibrational studies of the disulfide group in proteins. VII. Normal mode analysis of the Raman spectra of erabutoxin, γ-II crystallin and immunoglobulin.* Journal of Raman spectroscopy, 1992. 23(10): p. 517-521.

243. Hedberg, Y., et al., *Surface-protein interactions on different stainless steel grades: effects of protein adsorption, surface changes and metal release.* Journal of Materials Science: Materials in Medicine, 2013. 24(4): p. 1015-1033.

244. Oates, K.M.N., et al., *Rheopexy of synovial fluid and protein aggregation.* Journal of the Royal Society, Interface, 2006. 3(6): p. 167-174.

245. Merritt, K., S.A. Brown, and N.A. Sharkey, *The binding of metal salts and corrosion products to cells and proteins in vitro.* Journal of Biomedical Materials Research, 1984. 18(9): p. 1005-1015.

246. Horbett, T.A., *The role of adsorbed proteins in tissue response to biomaterials*, in *Biomaterials Science*. 2004, Elsevier Academic Press: London.

247. Hlady, V. and J. Buijs, *Protein adsorption on solid surfaces.* Current Opinion in Biotechnology, 1996. 7(1): p. 72-77.

248. Gray, J.J., *The interaction of proteins with solid surfaces.* Current Opinion in Structural Biology, 2004. 14(1): p. 110-115.

249. Kopac, T., K. Bozgeyik, and J. Yener, *Effect of pH and temperature on the adsorption of bovine serum albumin onto titanium dioxide.* Colloids and Surfaces A: Physicochemical and Engineering Aspects, 2008. 322(1): p. 19-28.

250. Wang, Z., Y. Yan, and L. Qiao, *Protein adsorption on implant metals with various deformed surfaces.* Colloids and Surfaces B: Biointerfaces, 2017. 156: p. 62-70.

251. Valero Vidal, C., A. Olmo Juan, and A. Igual Muñoz, *Adsorption of bovine serum albumin on CoCrMo surface: Effect of temperature and protein concentration.* Colloids and Surfaces B: Biointerfaces, 2010. 80(1): p. 1-11.

252. Zhu, J., N. Xu, and C. Zhang, *Characteristics of copper corrosion in simulated uterine fluid in the presence of protein.* Advances in contraception, 1999. 15(3): p. 179-190.

253. Li, J., et al., *Comparison of the release behaviors of cupric ions from metallic copper and a novel composite in simulated body fluid.* Journal of Biomedical Materials Research Part B: Applied Biomaterials, 2008. 85B(1): p. 172-179.

254. Ithurbide, A., et al., *XPS and flow-cell EQCM study of albumin adsorption on passivated chromium surfaces: Influence of potential and pH.* Electrochimica Acta, 2007. 53(3): p. 1336-1345.

255. Valero-Vidal, C., et al., *Adsorption of BSA on Passivated CoCrMo PVD Alloy: An EQCM and XPS Investigation.* Journal of The Electrochemical Society, 2014. 161(6): p. C294-C301.

256. Wagner, M.S., T.A. Horbett, and D.G. Castner, *Characterizing multicomponent adsorbed protein films using electron spectroscopy for chemical analysis, time-of-flight secondary ion mass spectrometry, and radiolabeling: capabilities and limitations.* Biomaterials, 2003. 24(11): p. 1897-1908.

257. Muñoz, A.I. and S. Mischler, *Electrochemical Quartz Crystal Microbalance and X-Ray Photoelectron Spectroscopy study of cathodic reactions in Bovine Serum Albumin containing solutions on a Physical Vapour Deposition-CoCrMo biomedical alloy.* Electrochimica Acta, 2015. 180(Supplement C): p. 96-103.

258. Munoz, A.I. and S. Mischler, *Effect of the environment on wear ranking and corrosion of biomedical CoCrMo alloys.* J Mater Sci Mater Med, 2011. 22(3): p. 437-50.

259. Yan, Y., A. Neville, and D. Dowson, *Biotribocorrosion of CoCrMo orthopaedic implant materials - Assessing the formation and effectof the biofilm.* Tribology International, 2007. 40(10-12): p. 1492-1499.

260. Williams, D.F., I.N. Askill, and R. Smith, *Protein absorption and desorption phenomena on clean metal surfaces.* J Biomed Mater Res, 1985. 19(3): p. 313-20.

261. Contu, F., B. Elsener, and H. Bohni, *Characterization of implant materials in fetal bovine serum and sodium sulfate by electrochemical impedance spectroscopy. II. Coarsely sandblasted samples.* J Biomed Mater Res A, 2003. 67(1): p. 246-54.

262. Kerwell, S., et al., *Electrochemically Induced Film Formation on CoCrMo Alloy for Hip Implant Application*. Vol. 3. 2017.

263. Hedberg, Y., *Role of proteins in the degradation of relatively inert alloys inthe human body.* 2018. 2.

264. Yang, J. and J. Black, *Competitive binding of chromium, cobalt and nickel to serum proteins.* Biomaterials, 1994. 15(4): p. 262-268.

265. Hallab, N.J., et al., *Systemic metal–protein binding associated with total joint replacement arthroplasty.* Journal of Biomedical Materials Research, 2000. 49(3): p. 353-361.

266. Jacobs, J.J., et al., *Metal degradation products: a cause for concern in metal-metal bearings?* Clin Orthop Relat Res, 2003(417): p. 139-47.

267. Hedberg, Y.S., *Role of proteins in the degradation of relatively inert alloys in the human body.* npj Materials Degradation, 2018. 2(1): p. 26.

268. Thompson, C., et al., *Impact of Magnetic Stirring on Stainless Steel Integrity: Effect on Biopharmaceutical Processing.* J Pharm Sci, 2017. 106(11): p. 3280-3286.

269. Rosenberg, A.S., *Effects of protein aggregates: an immunologic perspective.* Aaps j, 2006. 8(3): p. E501-7.

270. Hedberg, Y.S., et al., *Can Cobalt(II) and Chromium(III) Ions Released from Joint Prostheses Influence the Friction Coefficient?* ACS Biomaterials Science & Engineering, 2015. 1(8): p. 617-620.

271. Arenas, M., et al., *Electrochemical noise measurements of AISI 316L during wear in simulated physiological media.* Corrosion Engineering, Science and Technology, 2014. 49: p. 656-660.

272. Liang, M., et al., *A simple and direct isolation of whey components from raw milk by gel filtration chromatography and structural characterization by Fourier transform Raman spectroscopy.* Talanta, 2006. 69(5): p. 1269-1277.

273. Mishina, H. and M. Kojima, *Changes in human serum albumin on arthroplasty frictional surfaces.* Wear, 2008. 265(5): p. 655-663.

274. Wimmer, M.A., et al., *The acting wear mechanisms on metal-on-metal hip joint bearings: in vitro results.* Wear, 2001. 250(1): p. 129-139.

275. Bergmann, G., et al., *High-Tech Hip Implant for Wireless Temperature Measurements In Vivo.* PLOS ONE, 2012. 7(8): p. e43489.

276. Myant, C., et al., *Lubrication of metal-on-metal hip joints: The effect of protein content and load on film formation and wear.* Journal of the Mechanical Behavior of Biomedical Materials, 2012. 6: p. 30-40.

277. Ma, L. and W.M. Rainforth, *A study of Biolox® delta subject to water lubricated reciprocating wear.* Tribology International, 2010. 43(10): p. 1872-1881.

278. Li, X., et al., *Depassivation–repassivation behavior of a CoCrMo alloy under Tribological contact in Simulated body Fluids.* Int J Electrochem Sci, 2017. 12: p. 2495-2505.

279. Sun, D., J. Wharton, and R. Wood, *The Effects of Protein and pH on the Tribo-Corrosion Performance of Cast CoCrMo — A Combined Electrochemical and Tribological Study*. 2010. p. 825-826.

280. Hesketh, J.E.T., *Tribocorrosion of Total Hip Replacements*. 2012, University of Leeds.

281. Runa, M.J., M.T. Mathew, and L.A. Rocha, *Tribocorrosion response of the Ti6Al4V alloys commonly used in femoral stems.* Tribology International, 2013. 68: p. 85-93.

282. Wang, Z., et al., *Effect of electrochemical corrosion on the subsurface microstructure evolution of a CoCrMo alloy in albumin containing environment.* Applied Surface Science, 2017. 406: p. 319-329.

283. De Motte, R., et al., *Near surface pH measurements in aqueous CO2 corrosion.* Electrochimica Acta, 2018. 290: p. 605-615.

284. Merritt, K. and S.A. Brown, *Effect of proteins and pH on fretting corrosion and metal ion release.* J Biomed Mater Res, 1988. 22(2): p. 111-20.

285. Valero Vidal, C. and A. Igual Muñoz, *Effect of physico-chemical properties of simulated body fluids on the electrochemical behaviour of CoCrMo alloy.* Electrochimica Acta, 2011. 56(24): p. 8239-8248.

286. Sadiq, K., M.M. Stack, and R.A. Black, *Wear mapping of CoCrMo alloy in simulated bio-tribocorrosion conditions of a hip prosthesis bearing in calf serum solution.* Mater Sci Eng C Mater Biol Appl, 2015. 49: p. 452-462.

287. Heinicke, G., *Tribochemistry*. 1984: John Wiley & Sons.

288. Hsu, S.M., J. Zhang, and Z. Yin, *The Nature and Origin of Tribochemistry.* Tribology Letters, 2002. 13(2): p. 131-139.

289. Fischer, T.E., *Tribochemistry.* Annual Review of Materials Science, 1988. 18(1): p. 303-323.

290. Adams, H.L., et al., *Shear-Induced Mechanochemistry: Pushing Molecules Around.* The Journal of Physical Chemistry C, 2015. 119(13): p. 7115-7123.

291. Jelita Rydel, J., R.H. Vegter, and P.E.J. Rivera-Díaz-del-Castillo, *Tribochemistry of bearing steels: A new AFM method to study the material–tribofilm correlation.* Tribology International, 2016. 98: p. 74-81.

292. Wan, S., et al., *Tribochemistry of adaptive integrated interfaces at boundary lubricated contacts.* Scientific Reports, 2017. 7(1): p. 9935.

293. Meng, Q.E., et al., *Contact mechanics and lubrication analyses of ceramic-on-metal total hip replacements.* Tribology International, 2013. 63: p. 51-60.

294. McEntire, B., et al., *Silicon Nitride Bearings for Total Joint Arthroplasty.* Lubricants, 2016. 4(4): p. 35.

295. Nečas, D., et al., *The effect of lubricant constituents on lubrication mechanisms in hip joint replacements.* Journal of the Mechanical Behavior of Biomedical Materials, 2016. 55: p. 295-307.

296. Vrbka, M., et al., *Study of film formation in bovine serum lubricated contacts under rolling/sliding conditions.* Proceedings of the Institution of Mechanical Engineers, Part J: Journal of Engineering Tribology, 2013. 227(5): p. 459-475.

297. Ghosh, S., et al., *Tribological performance of the biological components of synovial fluid in artificial joint implants.* Science and technology of advanced materials, 2015. 16(4): p. 045002-045002.

298. Wimmer, M.A., et al., *Tribochemical reaction on metal-on-metal hip joint bearings - A comparison between in-vitro and in-vivo results.* WEAR, 2003. 255(2): p. 1007-1014.

299. Pourzal, R., et al., *Micro-structural alterations within different areas of articulating surfaces of a metal-on-metal hip resurfacing system.* Wear, 2009. 267(5): p. 689-694.

300. Pourzal, R., et al., *Characterization of wear particles generated from CoCrMo alloy under sliding wear conditions.* Wear, 2011. 271(9): p. 1658-1666.

301. Zeng, P., et al., *Subsurface characterisation of wear on mechanically polished and electro-polished biomedical grade CoCrMo.* Wear, 2015. 332-333: p. 650-661.

302. Mathew, M.T., J.J. Jacobs, and M.A. Wimmer, *Wear-Corrosion Synergism in a CoCrMo Hip Bearing Alloy Is Influenced by Proteins.* Clinical Orthopaedics and Related Research, 2012. 470(11): p. 3109-3117.

303. Sargeant, A. and T. Goswami, *Hip implants: Paper V. Physiological effects.* Materials & Design, 2006. 27(4): p. 287-307.

304. Jacobs, J.J., J.L. Gilbert, and R.M. Urban, *Corrosion of metal orthopaedic implants.* J Bone Joint Surg Am, 1998. 80(2): p. 268-82.

305. Rabe, M., D. Verdes, and S. Seeger, *Understanding protein adsorption phenomena at solid surfaces.* Advances in Colloid and Interface Science, 2011. 162(1): p. 87-106.

306. Anissian, H.L., et al., *The wear pattern in metal-on-metal hip prostheses.* J Biomed Mater Res, 2001. 58(6): p. 673-8.

307. Smith, S.L., D. Dowson, and A.A.J. Goldsmith, *The lubrication of metal-on-metal total hip joints: A slide down the Stribeck curve.* Proceedings of the Institution of Mechanical Engineers, Part J: Journal of Engineering Tribology, 2001. 215(5): p. 483-493.

308. Beadling, A.R., et al., *Tribocorrosion of hard-on-hard total hip replacements with metal and ceramic counterfaces under standard and adverse loading conditions.* Tribology International, 2016. 103: p. 359-367.

309. *International Organization for Standardization*, in *ISO 14242-1:2002, Implants for surgery -- Wear of total hip-joint prostheses -- Part 1: Loading and displacement parameters for wear-testing machines and corresponding environmental conditions for test*. 2002.

310. *International Organization for Standardization, ISO 14243-3:2004*, in *Implants for surgery - Wear of total knee-joint prostheses - Part 3: Loading and displacement parameters for wear-testing machines with displacement control and corresponding environmental conditions for test 2004.* 2004.

311. Kestin, J., H.E. Khalifa, and R.J. Correia, *Tables of the dynamic and kinematic viscosity of aqueous NaCl solutions in the temperature range 20–150 C and the pressure range 0.1–35 MPa.* Journal of Physical and Chemical Reference Data, 1981. 10(1): p. 71-88.

312. Ponthiaux, P., et al., *Electrochemical techniques for studying tribocorrosion processes.* Wear, 2004. 256(5): p. 459-468.

313. *ASTM International*, in *ASTM Standard G 3–89, Standard Method for Conventions Applicable to Electrochemical Measurements in Corrosion Testing, Annual Book of ASTM Standards*. 2006, ASTM International: West Conshohocken, PA.

314. Bellezze, T., G. Giuliani, and G. Roventi, *Study of stainless steels corrosion in a strong acid mixture. Part 1: cyclic potentiodynamic*

polarization curves examined by means of an analytical method. Corrosion Science, 2018. 130: p. 113-125.

315. Landolt, D., et al., *Third body effects and material fluxes in tribocorrosion systems involving a sliding contact.* Wear, 2004. 256(5): p. 517-524.

316. Yan, Y., et al., *Tribocorrosion in implants—assessing high carbon and low carbon Co–Cr–Mo alloys by in situ electrochemical measurements.* Tribology International, 2006. 39(12): p. 1509-1517.

317. Hsu, R., et al., *Electrochemical corrosion studies on Co–Cr–Mo implant alloy in biological solutions.* Materials Chemistry and Physics, 2005. 93: p. 531-538.

318. Pocock, G. and C.D. Richards, *The human body: an introduction for the biomedical and health sciences*. 2009: Oxford University Press.

319. Thornley, B., et al., *Investigation into the Repassivation Process of CoCrMo in a Simulated Biological Environment.* CORROSION, 2020. 76.

320. Moulder, J.F. and J. Chastain, *Handbook of X-ray Photoelectron Spectroscopy: A Reference Book of Standard Spectra for Identification and Interpretation of XPS Data*. 1992: Physical Electronics Division, Perkin-Elmer Corporation.

321. Cooper, H.J., et al., *Adverse Local Tissue Reaction Arising from Corrosion at the Femoral Neck-Body Junction in a Dual-Taper Stem with a Cobalt-Chromium Modular Neck.* The Journal of Bone and Joint Surgery. American volume, 2013. 95(10): p. 865-872.

322. Windecker, R., et al., *Testing micro devices with fringe projection and white-light interferometry.* Optics and Lasers in Engineering, 2001. 36(2): p. 141-154.

323. Archard, J.F., *Contact and Rubbing of Flat Surfaces.* Journal of Applied Physics, 1953. 24(8): p. 981-988.

324. Sinnett-Jones, P.E., J.A. Wharton, and R.J.K. Wood, *Micro-abrasion–corrosion of a CoCrMo alloy in simulated artificial hip joint environments.* Wear, 2005. 259(7): p. 898-909.

325. Hutchings, I. and P. Shipway, *Tribology: Friction and wear of engineering materials: Second Edition*. 2017. 1-388.

326. Wood, R.J.K., et al., *Electrostatic monitoring of the effects of carbon black on lubricated steel/steel sliding contacts*, in *Tribology and Interface Engineering Series*, D. Dowson, et al., Editors. 2005, Elsevier. p. 109-121.

327. Stack, M.M., M.T. Mathew, and C. Hodge, *Micro-abrasion–corrosion interactions of Ni–Cr/WC based coatings: Approaches to construction of tribo-corrosion maps for the abrasion–corrosion synergism.* Electrochimica Acta, 2011. 56(24): p. 8249-8259.

328. Stack, M.M., et al., *Some views on the construction of bio-tribo-corrosion maps for Titanium alloys in Hank's solution: Particle concentration and applied loads effects.* Tribology International, 2011. 44(12): p. 1827-1837.

329. Di Puccio, F. and L. Mattei, *Biotribology of artificial hip joints.* World journal of orthopedics, 2015. 6(1): p. 77-94.

330. Steinberger, R., et al., *Oxygen accumulation on metal surfaces investigated by XPS, AES and LEIS, an issue for sputter depth profiling under UHV conditions.* Applied Surface Science, 2017. 411: p. 189-196.

331. Jenko, M., et al., *Surface chemistry and microstructure of metallic biomaterials for hip and knee endoprostheses.* Applied Surface Science, 2018. 427: p. 584-593.

332. Ray, S. and A.G. Shard, *Quantitative analysis of adsorbed proteins by X-ray photoelectron spectroscopy.* Anal Chem, 2011. 83(22): p. 8659-66.

333. Vanea, E. and V. Simon, *XPS study of protein adsorption onto nanocrystalline aluminosilicate microparticles.* Applied Surface Science, 2011. 257(6): p. 2346-2352.

334. *Sera Laboratories International Ltd., Certificate of Analysis*, in *Product: Foetal Bovine Serum European Grade*. 2017: Colombia.

335. Van Doveren, H. and J.A.T.H. Verhoeven, *XPS spectra of Ca, Sr, Ba and their oxides.* Journal of Electron Spectroscopy and Related Phenomena, 1980. 21(3): p. 265-273.

336. Hanawa, T. and M. Ota, *Calcium phosphate naturally formed on titanium in electrolyte solution.* Biomaterials, 1991. 12(8): p. 767-74.

337. Demri, B. and D. Muster, *XPS study of some calcium compounds.* Journal of Materials Processing Technology, 1995. 55(3): p. 311-314.

338. Watson, I.M., J.A. Connor, and R. Whyman, *Non-crystalline chromium, molybdenum and tungsten phosphate films prepared by metal organic chemical vapour deposition.* Thin Solid Films, 1991. 201(2): p. 337-349.

339. Moffat, T.P., R.M. Latanision, and R.R. Ruf, *An X-ray photoelectron spectroscopy study of chromium-metalloid alloys—III.* Electrochimica Acta, 1995. 40(11): p. 1723-1734.

340. Di Laura, A., et al., *The Chemical Form of Metal Species Released from Corroded Taper Junctions of Hip Implants: Synchrotron Analysis of Patient Tissue.* Scientific Reports, 2017. 7(1): p. 10952.

341. Payne, B.P., M.C. Biesinger, and N.S. McIntyre, *Use of oxygen/nickel ratios in the XPS characterisation of oxide phases on nickel metal and nickel alloy surfaces.* Journal of Electron Spectroscopy and Related Phenomena, 2012. 185(5): p. 159-166.

342. Guo, L.Q., et al., *Effect of hydrogen on semiconductive properties of passive film on ferrite and austenite phases in a duplex stainless steel.* Scientific Reports, 2017. 7(1): p. 3317.

343. Honna, M., et al., *Effect of friction stroke length on damage and restoration of the passive film of cobalt chromium alloy.* Kitasato Med J, 2017. 47: p. 10-16.

344. Donnet, C., et al., *Super-low friction of MoS2 coatings in various environments.* Tribology International, 1996. 29(2): p. 123-128.

345. Farr, J.P.G., *Molybdenum disulphide in lubrication. A review.* Wear, 1975. 35(1): p. 1-22.

346. Catelas, I., M.A. Wimmer, and S. Utzschneider, *Polyethylene and metal wear particles: characteristics and biological effects.* Seminars in Immunopathology, 2011. 33(3): p. 257-271.

347. Ito, H., et al., *Reduction of polyethylene wear by concave dimples on the frictional surface in artificial hip joints.* J Arthroplasty, 2000. 15(3): p. 332-8.

348. Lee, R., et al., *Scratch and wear performance of prosthetic femoral head components against crosslinked UHMWPE sockets.* Wear, 2009. 267(11): p. 1915-1921.

349. Peaker, A.J.S. and J. Czernuszka, *The Effect of Electric Field on the Formation of Hydroxyapatite Coatings*. Vol. 287. 1996. 174–183.

350. Neville, A., T. Hodgkiess, and A.P. Morizot, *Surface scales in sea water systems: Effects of their formation on corrosion behaviour of engineering steels.* British Corrosion Journal, 1997. 32(4): p. 277-282.

351. Zhang, X. and M. Cresswell, *Chapter 6 - Calcium Phosphate Materials for Controlled Release Systems*, in *Inorganic Controlled Release Technology*, X. Zhang and M. Cresswell, Editors. 2016, Butterworth-Heinemann: Boston. p. 161-187.

352. Shin, J.W., G.R. Stafford, and K.R. Hebert, *Stress in aluminum induced by hydrogen absorption during cathodic polarization.* Corrosion Science, 2015. 98: p. 366-371.

353. Stankovich, M.T. and A.J. Bard, *The electrochemistry of proteins and related substances part III. Bovine serum albumin.* Journal of Electroanalytical Chemistry and Interfacial Electrochemistry, 1978. 86(1): p. 189-199.

354. Kocijan, A., et al., *Electrochemical Study of Co-Based Alloys in Simulated Physiological Solution.* Journal of Applied Electrochemistry, 2004. 34(5): p. 517-524.

355. Moreto, J., et al., *Effect of Temperature, Electrolyte Composition and Immersion Time on the Electrochemical Corrosion Behavior of CoCrMo Implant Alloy Exposed to Physiological Serum and Hank's Solution.* Materials Research, 2018. 21.

356. Perret, J., et al., *EBSD, SEM and FIB characterisation of subsurface deformation during tribocorrosion of stainless steel in sulphuric acid.* Wear, 2010. 269(5): p. 383-393.

357. Bidiville, A., et al., *Effect of surface chemistry on the mechanical response of metals in sliding tribocorrosion systems.* Wear, 2007. 263(1): p. 207-217.

358. Wang, Z., et al., *Effect of proteins on the surface microstructure evolution of a CoCrMo alloy in bio-tribocorrosion processes.* Colloids and Surfaces B: Biointerfaces, 2016. 145: p. 176-184.

359. Wimmer, M., et al., *Investigation on stick phenomena in metal-on-metal hip joints after resting periods.* Proceedings of the Institution of Mechanical Engineers, Part H: Journal of Engineering in Medicine, 2006. 220(2): p. 219-227.

360. Sun, D., J.A. Wharton, and R.J.K. Wood, *Micro-abrasion mechanisms of cast CoCrMo in simulated body fluids.* Wear, 2009. 267(11): p. 1845-1855.

361. Valero Vidal, C. and A. Igual Muñoz, *Electrochemical characterisation of biomedical alloys for surgical implants in simulated body fluids.* Corrosion Science, 2008. 50(7): p. 1954-1961.

362. Luo, L., et al., *Effect of cobalt and chromium ions on MMP-1, TIMP-1, and TNF-α gene expression in human U937 macrophages: A role for tyrosine kinases.* Biomaterials, 2005. 26(28): p. 5587-5593.

363. Dufils, J., et al., *Influence of molybdate ion and pH on the fretting corrosion of a CoCrMo – Titanium alloy couple.* Biotribology, 2017. 11: p. 20-28.

364. Talha, M., et al., *Role of protein adsorption in the bio corrosion of metallic implants – A review.* Colloids and Surfaces B: Biointerfaces, 2019. 176: p. 494-506.

365. Landolt, D., S. Mischler, and M. Stemp, *Electrochemical methods in tribocorrosion: a critical appraisal.* Electrochimica Acta, 2001. 46(24): p. 3913-3929.

366. Barril, S., S. Mischler, and D. Landolt, *Electrochemical effects on the fretting corrosion behaviour of Ti6Al4V in 0.9% sodium chloride solution.* Wear, 2005. 259(1): p. 282-291.

367. Favero, M., P. Stadelmann, and S. Mischler, *Effect of the applied potential of the near surface microstructure of a 316L steel submitted to tribocorrosion in sulfuric acid.* Journal of Physics D: Applied Physics, 2006. 39: p. 3175-3183.

368. Guadalupe Maldonado, S., et al., *Mechanical and chemical mechanisms in the tribocorrosion of a Stellite type alloy.* Wear, 2013. 308(1): p. 213-221.

369. Neville, A., et al., *Incorporating corrosion measurement in hip wear simulators: An added complication or a necessity?* 2016. 230(5): p. 406-420.

370. Yan, Y., et al., *Real-time corrosion measurements to assess biotribocorrosion mechanisms with a hip simulator.* Tribology International, 2013. 63: p. 115-122.

Appendix A

Composition of Testing Electrolytes

Table 10.1 Foetal bovine serum compositions

Foetal Bovine Serum	mg/L
ALAT (SGPT) Alanine transaminase	4.7
ALP Alkaline Phosphatase	249.2
ASAT (SGOT) Aspartate transaminase	25.5
Gamma-Glutamyl Transferase	4.7
Lactate Dehydrogenase	416.1
Bilirubin ($C_{33}H_{36}N_4O_6$)	20
Calcium	140
Cholesterol ($C_{27}H_{46}O$)	340
Creatinine ($C_4H_7N_3O$)	270
Chloride	3580
Glucose ($C_6H_{12}O_6$)	910
Iron	1.58
Phosphorus	97
Potassium	469
Sodium	3127
Triglycerides	660
Urea (CH_4N_2O)	420
Uric Acid ($C_5H_4N_4O_3$)	18
Albumin	15800
Alpha-Globulins	11000
Beta-Globulins	7600
Gamma-Globulins	400

Immunoglobulin IgG	130

Table 10.2. Compositions of PBS tablet

Phosphate Buffered Saline electrolyte	g/L
Sodium chloride	8.0
Potassium chloride	0.2
Di-sodium hydrogen phosphate	1.15
Potassium dihydrogen phosphate	0.2

Table 10.3. DMEM cell culture medium compositions

Amino Acids	mg/L
Glycine ($C_2H_5NO_2$)	30
L-Arginine hydrochloride ($C_6H_{15}ClN_4O_2$)	84
L-Cystine 2HCl ($C_6H_{14}Cl_2N_2O_4S_2$)	63
L-Histidine hydrochloride-H2O ($C_6H_{12}ClN_3O_3$)	42
L-Isoleucine ($C_6H_{13}NO_2$)	105
L-Leucine ($C_6H_{13}NO_2$)	105
L-Lysine hydrochloride ($C_6H_{15}ClN_2O_2$)	146
L-Methionine ($C_5H_{11}NO_2S$)	30
L-Phenylalanine ($C_9H_{11}NO_2$)	66
L-Serine ($C_3H_7NO_3$)	42
L-Threonine ($C_4H_9NO_3$)	95
L-Tryptophan ($C_{11}H_{12}N_2O_2$)	16
L-Tyrosine ($C_9H_{11}NO_3$)	72
L-Valine ($C_5H_{11}NO_2$)	94
Vitamins	**mg/L**
Choline chloride ($C_5H_{14}ClNO$)	4

D-Calcium pantothenate ($C_{18}H_{32}CaN_2O_{10}$)	4
Folic Acid ($C_{19}H_{19}N_7O_6$)	4
Niacinamide ($C_6H_6N_2O$)	4
Pyridoxine hydrochloride ($C_8H_{12}ClNO_3$)	4
Riboflavin ($C_{17}H_{20}N_4O_6$)	0.4
Thiamine hydrochloride ($C_{12}H_{18}Cl_2N_4OS$)	4
i-Inositol ($C_6H_{12}O_6$)	7.2
Inorganic Salts	**mg/L**
Calcium Chloride ($CaCl_2$-$2H_2O$)	264
Ferric Nitrate ($Fe(NO_3)_3$"$9H_2O$)	0.1
Magnesium Sulfate ($MgSO_4$-$7H_2O$)	200
Potassium Chloride (KCl)	400
Sodium Bicarbonate ($NaHCO_3$)	3700
Sodium Chloride (NaCl)	6400
Sodium Phosphate monobasic (NaH_2PO_4-$2H_2O$)	141
Other Components	**mg/L**
D-Glucose (Dextrose) ($C_6H_{12}O_6$)	4500
Phenol Red ($C_{19}H_{14}O_5S$)	15
Sodium Pyruvate ($C_3H_3NaO_3$)	110